UNIVERSIDADE TÉCNICA DE LISBOA
INSTITUTO SUPERIOR TÉCNICO

Measurement of the ^{233}U neutron capture cross section at the n_TOF facility at CERN

Carlos Alberto de Almeida Carrapiço

Supervisor: Doctor José Pedro Miragaia Trancoso Vaz
Co-Supervisor: *Lic.* Isabel Maria Ferro Pereira Gonçalves

Thesis approved in public session to obtain the PhD Degree in
Physics

Jury final classification: **Pass with Distinction**

Jury

Chairperson: Chairman of the IST Scientific Board
Members of the Committee:
Doctor Rui Ferreira Marques
Doctor Frank Gunsing
Doctor Lídia dos Santos Ferreira
Doctor Eric Berthoumieux
Doctor José Pedro Miragaia Trancoso Vaz
Lic. Isabel Maria Ferro Pereira Gonçalves

2012

UNIVERSIDADE TÉCNICA DE LISBOA
INSTITUTO SUPERIOR TÉCNICO

Measurement of the 233U neutron capture cross section at the n_TOF facility at CERN

Carlos Alberto de Almeida Carrapiço

Supervisor: Doctor José Pedro Miragaia Trancoso Vaz
Co-Supervisor: *Lic.* Isabel Maria Ferro Pereira Gonçalves

Thesis approved in public session to obtain the PhD Degree in
Physics

Jury final classification: **Pass with Distinction**

Jury

Chairperson: Chairman of the IST Scientific Board
Members of the Committee:

Doctor Rui Ferreira Marques
Professor Catedrático da Faculdade de Ciências eTecnologia da Universidade de Coimbra.

Doctor Frank Gunsing
Investigador Coordenador do Commissariat á l'Energie Atomique et aux Énergies Alternatives, France.

Doctor Lídia dos Santos Ferreira
Professora Associada (com Agregação), do Instituto Superior Técnico de Lisboa.

Doctor Eric Berthoumieux
Investigador Principal, European Organization for Nuclear Research, Switzerland.

Doctor José Pedro Miragaia Trancoso Vaz
Investigador Principal (com Agregação) do Instituto Tecnológico e Nuclear do Instituto Superior Técnico da Universidade Técnica de Lisboa.

Lic. Isabel Maria Ferro Pereira Gonçalves
Investigadora Auxiliar do Instituto Tecnológico e Nuclear do Instituto Superior Técnico da Universidade Técnica de Lisboa, na qualidade de especialista na área científica em que se insere a tese.

FUNDING INSTITUTION
FUNDAÇÃO PARA A CIÊNCIA E A TECNOLOGIA

2012

Resumo

O ciclo de combustível Tório-Urânio Th-U foi proposto para a produção de electricidade usando reactores nucleares, como uma alternativa ao ciclo de combustível Urânio-Plutónio U-Pu. O Tório pode ser usado como combustível nuclear e diversos estudos e programas de R&D fornecem evidência sobre a sustentabilidade do ciclo de combustível Th-U devido (i) à abundância natural do Tório (ii) à maior resistência a proliferação oferecida pelo ciclo de combustível Tório-Urânio (Th-U) relativamente ao ciclo de combustível Urânio-Plutónio (U-Pu) (iii) à melhor performance neutrónica do ciclo de combustível Th-U relativamente ao ciclo de combustível U-Pu em todo o espectro de energia dos neutrões (iv) ao menor nível de radiotoxicidade dos resíduos nucleares em reactores que utilizam o ciclo de combustível Th-U e consequentemente (v) uma maior economia e aceitação pública dos reactores que utilizam o ciclo de combustível Th-U em comparação com os que usam U-Pu (em referência a reactores nucleares anteriores aos da Generação IV).

No caso dos reactores nucleares que utilizam o ciclo de combustível Th-U, o ^{233}U é um elemento chave que governa a performance neutrónica e consequentemente a economia, a segurança nuclear e a resistência à proliferação.

Desta forma, o conhecimento das secções eficazes de captura netrónica e de cisão do ^{233}U com elevando grau de precisão é de fundamental importância para a determinação da sustentabilidade e do ciclo de combustível Th-U e para o desenvolvimento de reactores que usam este ciclo de combustível.

O presente trabalho detalha a análise de dados referente á medição simultânea da secção eficaz de captura neutrónica de cisão para o ^{233}U efectuada na instalação de Tempo de Voo (n_TOF) no CERN entre 1 eV e 1 keV usando como detector, o Calorímetro de Absorção Total (TAC) 4π de BaF_2.

A instalação "neutron Time-Of-Flight facility (n_TOF)" destaca-se a nível mundial por ser um espectrometro de tempo-de-voo associado a um feixe pulsado de protões de 20 GeV, funcionando num regimo de baixa taxa de repetição e sendo caracterizado por elevados fluxos instantâneos de neutrões, excelente resolução em energia, baixos níveis de ruído ambiente e um sistema de aquisição de dados utilizando electrónica rápida.

A medição da secção eficaz de captura é dificultada pelo facto de competir directamente com a secção eficaz de cisão, a qual possui uma secção eficaz varias vezes superior à de captura neutrónica.

A técnica de absorção total para a detecção de radiação gama for utilizada conjuntamente com a técnica de desconvolução através da análise calorimétrica

do espectro de energia depositada (CSD) pela primeira vez, para distinguir entre reacções nucleares concorrentes.

Várias técnicas de análise e ferramentas computacionais foram desenvolvidas e validadas com dados experimentais.

O sistema de detecção e a resposta do mesmo à radiação gama foi estudada utilizando técnicas de Monte Carlo para determinar as constantes de normalização.

Os resultados mostram o potencial dos métodos desenvolvidos e fornecem importantes informações sobre as secções eficazes medidas.

Palavras chave: ^{233}U, Metodologia de discriminação, Calorimetric Shape Decomposition, Secção eficaz, Captura neutrónica, Cisão, Medição simultânea, Tempo-de-Voo, Calorímetro de Absorção Total, Técnicas de Monte Carlo

Abstract

The Thorium-Uranium (Th-U) fuel cycle has been envisaged as an alternative to the Uranium-Plutonium (U-Pu) fuel cycle for electricity generation using nuclear power reactors. Indeed, thorium can be used as a nuclear fuel, and several studies and R&D programs seem to provide evidence on the sustainability of the Th-U fuel cycle, due to (i) the natural abundance of Thorium, (ii) the improved proliferation resistance offered by the Th-U fuel cycle relative to the U-Pu fuel cycle, (iii) the better neutronics performance of the Th-U fuel cycle throughout the whole neutron energy range compared to the U-Pu fuel cycle, (iv) the lower radiotoxicity of the generated spent fuel in reactors with Th-U fuel cycle and, consequently (v) better economics and public acceptance of the reactors operated using the Th-U fuel cycle compared to those using the U-Pu fuel cycle (prior to the Generation IV nuclear reactors).

In a nuclear reactor operated using the Th-U fuel cycle, ^{233}U is a key nuclide governing the neutronics performance of the system and consequently its economics, nuclear safety and proliferation resistance properties and characteristics.

Therefore, the accurate knowledge of the neutron capture and neutron induced fission cross-sections in ^{233}U are of paramount importance for the assessment of the sustainability of the Th-U fuel cycle and for the design of nuclear reactors using such fuel cycle.

In this work, the neutron capture and neutron induced fission cross sections of ^{233}U have been measured simultaneously at the neutron Time-Of-Flight facility (n_TOF) at European Organization for Nuclear Research (CERN) in the energy range from 1 eV to 1 keV using the 4π BaF_2 Total Absorption Calorimeter (TAC) as a detection device.

The n_TOF facility is a premier neutron spectrometer worldwide, driven by a 20 GeV pulsed proton beam, operated with a low duty cycle and featuring high instantaneously neutron fluxes, excellent neutron energy resolution, low backgrounds and a Data Acquisition System supported by fast electronics.

The measurement of the ^{233}U capture cross section is a very challenging task requiring the discrimination of the neutron capture component from the neutron induced fission component. The neutron induced fission is the main competing reaction, whose cross-section is several times higher than the one for neutron capture.

The total absorption technique has been employed together with the Calorimetric Shape Decomposition (CSD) method for discriminate between competing nuclear reactions for the first time in this work.

A variety of analysis techniques and software tools for the data analysis had to be developed and validated with experimental data.

A complete Monte Carlo study of the detection system has been performed to understand the response to gamma radiation and assess the normalization constants.

The obtained results show the potential of the CSD method and provided unprecedented information about the neutron induced capture and fission cross sections in ^{233}U.

Keywords: ^{233}U, Cross Section, Total Absorber Calorimeter, Discrimination Methodology, Calorimetric Shape Decomposition, Neutron Capture, Fission, Simultaneous measurement, Time-of-Flight, Monte Carlo simulations

Acknowledgements

Foremost, I would like to give a especial thanks to my supervisor, Doctor Pedro Vaz for believing in me and in my work, for all the guidance and for being always there when necessary. With his endless energy, expertise and patience, he contributed to every aspect of this thesis in an irreplaceable way, even in very complicated moments of his life.

I'm forever thankful to Doctor Eric Berthoumieux for supervising all the data analysis work and sharing his endless and outstanding knowledge with me. His tireless work and infinite ingenuity, made possible the accomplishments in this thesis.

I'm deeply thankful to Doctor Isabel Ferro Gonçalves for introducing me to the Monte Carlo techniques, for the open door at all times and availability to help solve problems or discuss whatever was necessary.

Each moment with Doctor Frank Gunsing has translated itself in a learning experience. His ability to clear explain things and outstanding knowledge in nuclear physics makes everything simple. I sincerely thank you for everything.

In summer of 2004 I was given the opportunity of joining the Instituto Tecnológico e Nuclear - Instituto Superior Técnico da Universidade Técnica de Lisboa (IST/ITN) and I started working under the Portuguese participation in the n_TOF Collaboration activities still as a college student. For this opportunity, I must give thanks to Doctors Pedro Vaz, to Doctor Isabel Ferro Gonçalves, to all the n_TOF Collaboration members and to IST/ITN for receiving me.

In the spring of 2007, an idea about a combined effort between the Commissariat à l'Énergie Atomique et aux Énergies Alternatives (CEA) and the IST/ITN for performing the data analysis of the ^{233}U neutron capture cross section, start gaining form. This idea would later on culminate in a two year stay at CEA-Saclay where I started learning the data analysis techniques specific to the work described in this thesis, with Doctor Frank Gunsing and Doctor Eric Berthoumieux. This wouldn't have been possible without their support and support received from the CEA-Saclay.

The work described in this thesis reflects my efforts but also the contri-

butions of many person that are not directly related with it. An endless list of friend and colleagues contributed to it in various forms such as the small things of everyday that make life better and helped me keep going. I will not cite all of them but they know how important they were and are to me, and that I will never forget them.

I am deeply grateful to all my family for all the love and unconditional support, for all the wonderful moments and experiences we passed together.

I give a especial thanks to Joana, my girlfriend and companion in this adventure that has been the last three years of my life. I am deeply grateful to her, for making my life so much happier and letting me be a part of hers.

I thank my grandmother Celeste who has taken care of me and helped me so much when I was growing.

To my uncle, Fernando, who has always been a key figure in my life and contributed so much to the person I am today, I am truly indebted and thankful.

Finally, to my mother, Beatriz, that has sacrificed her wellbeing so I could grow in the best way possible, that made everything at her reach to bring me to this day, that loved me unconditionally, words are short to express all the gratitude, recognition and love, I feel for her.

Contents

List of Tables

List of Figures

Acronym List

ADS Accelerator-Driven System . . . 6
AECL Atomic Energy of Canada Limited . . . 31
AVR Atom Versuchs Reaktor . . . 31
BaF_2 Barium Fluoride . . . xvi
BREST Fast reactors with a nitride fuel and a lead coolant . . . 17
BROND Standard Nuclear Data Files for Russia . . . 44
Btu British thermal unit
C6D6 Deuterated Benzene Liquid Scintillator . . . 63
CAD Computer-Aided Design . . . 155
CAMOT Monte Carlo Transport Code for Simulations of Pulsed Neutron Sources . . . 78
CENDL Chinese Evaluated Nuclear Data Library . . . 44
CERN European Organization for Nuclear Research . . . iii
CPU Central Processing Unit . . . 91
CSD Calorimetric Shape Decomposition . . . iii
DANCE Detector for Advanced Neutron Capture Experiments . . . 56
DAQ Data Acquisition System . . . 63
DST Data Summary Tape . . . 106
ENDF/B-VII.1 Evaluated Nuclear Data File . . . xvi
ENSDF Evaluated Nuclear Structure Data Files . . . 161
EXFOR Experimental Nuclear Reaction Data . . . 56
FBR Fast Breeder Reactor . . . 32
FIC Fission Ionization Chamber . . . 55
Flash ADC Flash Analog to Digital Converter . . . 90
FLUKA Fully integrated particle physics MonteCarlo simulation package . 78
FNR Fast Neutron Reactor . . . 15
FWHM full-width at half-maximum . . . ix
FWTM full-width at a tenth of the maximum . . . ix
GELINA Neutron Time-Of-Flight facility at Institute for Reference Materials and Measurements (IRMM) . . . 82

GFR Gas-cooled fast reactors vii

GIF Generation IV International Forum 17

GANSH Nuclear Reaction Code McGNASH 60

GTMHR Gas Turbine Modular Helium Reactor 18

HEU High-Enriched Uranium 31

HTR-10 High Temperature Reactor-10 MWt 18

HTR-PM High Temperature Reactor-Pebblebed Modules 18

HTTR High Temperature Test Reactor 18

IAEA International Atomic Energy Agency 11

IRMM Institute for Reference Materials and Measurements 1

JEFF Joint Evaluated Fission and Fusion File 44

JENDL Japanese Evaluated Nuclear Data Library 44

LANSCE Los Alamos Neutron Science Center 56

LBE Lead-Bismuth-Eutectic 2

LFR Lead-cooled fast reactors vii

LFTR Liquid Fluoride Thorium Reactor vii

LINAC Linear Accelerator 65

LLFP Long Lived Fission Products 10

LSPR Lead-Bismuth-Eutectic (LBE) Cooled Long-Life Safe Simple Small Portable Proliferation-Resistant Reactor 17

LWBR Light Water Breeder Reactor 32

LWR Light Water Reactor 12

MCNPX Monte Carlo N-Particle Transport Code xvi

MOX Mixed Oxide Fuel 18

MSR Molten salt reactors vii

n_TOF neutron Time-Of-Flight facility i

OECD Organization for Economic Cooperation and Development 7

ORELA Oak Ridge Electron Linear Accelerator Pulsed Neutron Source 53

PBMR Pebble Bed Modular Reactor 18

PHWR Pressurised Heavy Water Reactor 32

PPAC Parallel Plate Avalanche Chambers 63

PS Proton Synchrotron . . . 64
PSD Pulse Shape Discrimination . . . ix
PSF Photon Strength Functions . . . xiii
PTB Physikalisch-Technische Bundesanstalt . . . 68
PWR Pressurized Water Reactor
RMS Root Mean Square . . . 102
RPI Rensselaer Polytechnic Institute . . . 58
RRR Resolved Resonance Region . . . viii
RTR Radkowsky Thorium Reactor . . . 27
SAMMY Multilevel R-Matrix Fits to Neutron and Charged-Particle Cross-Section Data Using Bayes' Equations
SCWR Supercritical Water-cooled Reactors . . . vii
SFR Sodium-cooled fast reactors . . . vii
σ_c Neutron Capture Cross Section . . . 21
σ_f Neutron Induced Fission Cross Section . . . 21
SLFP Short Lived Fission Products . . . 29
STAR Secure, Transportable, Autonomous Reactor . . . 17
TAC Total Absorption Calorimeter . . . iii
Th-U Thorium-Uranium . . . iii
Th-U Tório-Urânio . . . i
THTR Thorium High Temperature Reactor . . . 31
TMSR Thorium-Breeding Molten-Salt Reactor . . . 20
TOF Time-Of-Flight . . . 6
U-Pu Uranium-Plutonium . . . iii
U-Pu Urânio-Plutónio . . . i
URR Unresolved Resonance Region . . . viii
VHTR Very high-temperature gas reactors . . . vii

Context

Nowadays when energy demand and energy sources are a major focus of concern and disputes worldwide, the search for safer, more efficient, environmentally friendly and sustainable energy sources is mandatory. The use of nuclear energy has been a partial solution but not without problems mainly due to the generated radioactive waste, safety concerns and public acceptance. The answer to these problems may not come only in the form of a new solution but also in improving existing solutions or solving problems like the accumulated radioactive waste due to the consumption of electricity produced with nuclear reactors. A more complete answer may consist in the production of electricity using different nuclear fuel cycles that will produce less radioactive waste or at least more easily manageable.

As a possible answer to the question of what to do with the radioactive waste and the need for a clean nuclear energy production, Carlo Rubbia [1], proposed an innovative nuclear reactor system that may permit not only to treat the radioactive waste using a fast neutron spectrum but also to be able to produce nuclear energy using new fuel cycles such as the Th-U. Nevertheless, the design of such kind of reactor requires improved knowledge of key cross sections, not only with higher accuracy but over extended energy ranges. This holds true for any reactor based on the Th-U cycle.

The needs for new and better nuclear data from the points of view of nuclear technology mainly for the present and future generations of reactor lead to a vast effort in the field of nuclear cross section measurements. The list of priority measurements can be found in the report 'Assessment of Nuclear Data Needs for Thorium and other Advanced Cycles' [2].

The n_TOF facility concept and implementation at CERN was a response to the experimental limitations encountered when measuring the neutron capture cross section and other neutron induced reactions for some relevant isotopes which are radioactive.

The facility characteristics allow to measure not only stable isotopes but also radioactive ones with unprecedented accuracy in a broad energy range, very good energy resolution and reduced backgrounds.

Introduction

The work described in this document was performed in the scope of the experimental activities of n_TOF at the CERN. n_TOF is an international collaboration of 40 institutions from European countries, U.S.A., Russia and Japan that work together with the goal of measuring cross sections of neutron capture and neutron induced fission for actinides and other nuclides using the Time-Of-Flight (TOF) spectrometer of CERN. The measurements done are of the highest relevance in the fields of fundamental nuclear physics, nuclear technology ,nuclear waste transmutation using Accelerator-Driven System (ADS) and nuclear astrophysics.

The detailed analysis of the ^{233}U neutron capture cross section will be described in full detail from the data acquisition to the yield assessment together with all the simulation work done to describe and understand the experimental setup.

The final results for the neutron capture yield of ^{233}U are shown together with results obtained for the neutron induced fission cross section also measured at n_TOF.

Chapter 1

Motivations

In our constant evolving world, somethings seem to not change and one that can be pointed out is the growing demand for energy resources. But this demand faces limitations both on the side of availability and usage. Despite the existence of renewable energy sources, which are more environmentally friendly, the energy sources commonly used in large scale are pledged with the byproducts associated with the conversion to electric power. The production of $C0_2$ is one of the most obvious problems but sustainability is not far behind in importance. In the next section, an overview of the global energy demands and future predictions is performed and technological solutions to improve the nuclear energy usage in a cleaner, safer, sustainable and economically viable away are presented. These solutions are discussed and compared with actual nuclear technology.

1.1 Overview on the energy utilization

To understand the problem with the actual energy demand, its necessary to have in mind a global overview of energy utilization in the present days and also an idea of the global energy utilization trend in the medium and long term future. A look at Figure 1.1 shows the current scenario plus the foreseen evolution until 2035 [3]. Nowadays, the energy utilization between nations inside and outside the Organization for Economic Cooperation and Development (OECD) are equally shared but the trend shows an increase of energy utilization by Non-OECD countries. Estimations show that from 2007 to 2035, the energy utilization has increased by 84% in respect to 2007 in Non-OECD countries against 14% in OECD countries.

Looking at the shares that each energy resource represents today and in 25 years (Figure 1.2), it is possible to see that without any substantial political

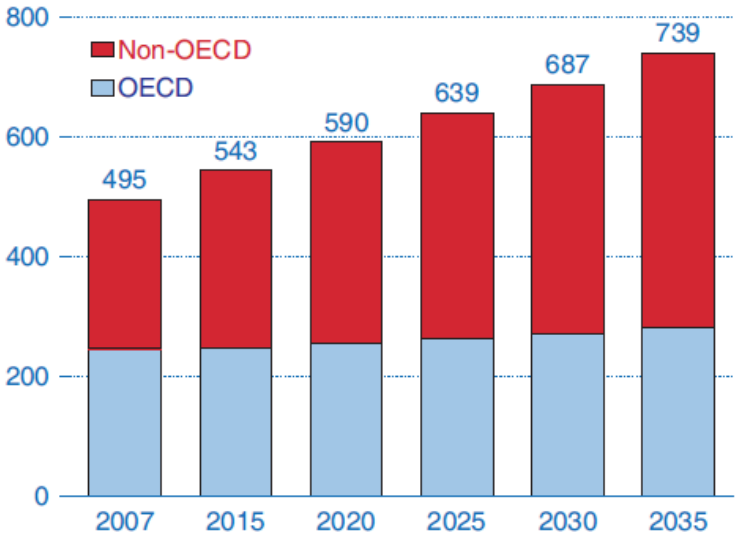

Figure 1.1: World marketed energy utilization, 2007-2035 (quadrillion Btu) [3].

change, the growth of the utilization of carbon free energies is still marginal and the big share belongs to fissile fuels.

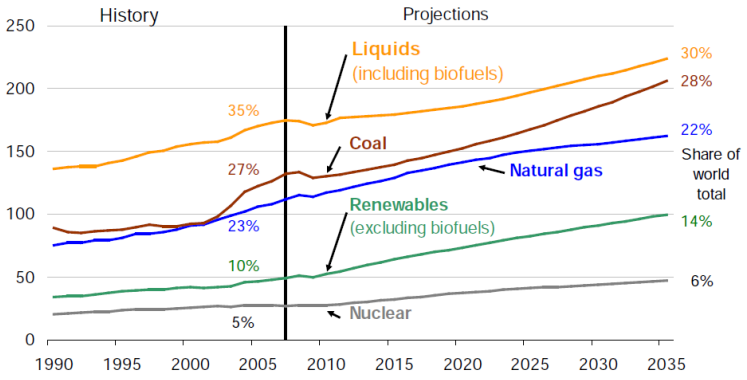

Figure 1.2: History and projections for the share energy sources in overall utilization [3].

Combining the present scenario with the difficulty in changing the world's energy policies and uncertainties in the available natural resources, the prediction of oil prices show very different possibilities but with the reference case showing a significant increase (Figure 1.3).

One thing seems unavoidable and this is the increase in CO_2 emissions. To this contribute the increase on the energy demand (Figure 1.1) and specially

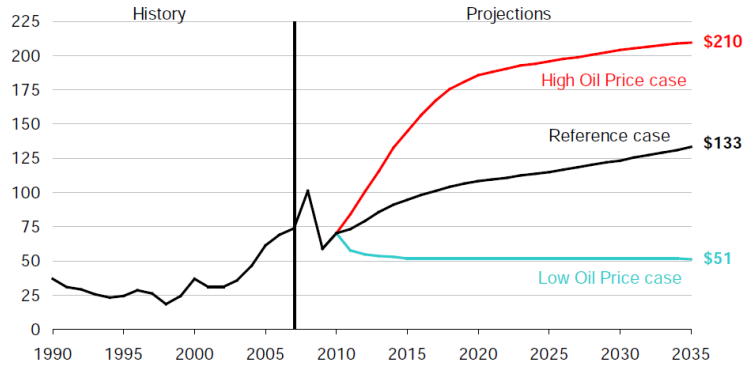

Figure 1.3: Projections for the oil price [3].

the difficulty in increasing the percentage of renewable energies. Although the predictions show only a small increase in the use of nuclear energy, a new, safer, environmentally friendly, proliferation resistant and more efficient generation of nuclear reactors can help to solve some of the world's energy problems.

1.1.1 Nuclear energy overview

Despite the overall small contribution of nuclear energy in the world energy utilization, the scenario is dramatically different specially in some European countries. While nuclear energy accounts only for 6% of the total energy utilization, in countries like France and Lithuania, the nuclear energy contribution can be as high as 80% for electricity production contributing to the total energy utilization with 15%. Although difficult to point out a direct relation between the high percentage of nuclear energy usage in countries like France and Lithuania, some factors can be pointed out such as political strategy, technical knowledge, economical demands, availability of other energy sources, public acceptance, environmental impact, among many others. This factors are common around the globe and one can think that the nuclear energy being economically equivalent to others in many cases and less environmental demanding, would lead to different political strategies and a higher share in the energy sources utilization. The equation isn't that simple and the technical knowledge need to build, operate and deal with the byproducts of a nuclear facility associated with safety concerns of the general public have reduced the acceptance of such technology. In fact, the public concerns play an important role and don't always react in a rational way when confronted with the nuclear energy.

1.2 Addressing the public acceptance problem

The main problems associated with the public acceptance of nuclear energy are related either with the management of radioactive waste or with safety concerns. The management of radioactive waste using the final disposal solution has been scientifically proved to be safe and feasible from the technical point of view, with the use of deep underground repositories. Nevertheless the public opinion demands solutions that don't imply a repository over thousands of years.

Taking this in consideration, transmutation of radioactive waste (it will be discussed is Section 1.2.2) has been proposed as a way to reduce substantially (in a factor of 1/100 or more [4]) the radiotoxicity of long lived component of the nuclear waste, mainly the trans-uranium actinides.

Also, the transmutation of Long Lived Fission Products (LLFP) is foreseen by neutron absorption (mainly by radioactive capture) in thermal and epithermal neutron energy region.

The use of innovative nuclear reactors for radioactive waste transmutation with a fast neutron spectrum to produce short lived fission products and more stable isotopes, can diminish the radiotoxicity by a factor greater than 100 [4].

Despite the important role that radioactive waste management represents in the acceptance of nuclear energy, this represents a fix for past solutions, a look into the future demands more efficient solutions like new fuel cycles and compositions which produce more manageable waste and are based on more abundant isotopes.

Inside a reactor, the nuclear reactions taking place are ruled by the competing cross sections of the fuel's isotopic composition and the neutron energy spectrum. The choice of the neutron energy spectrum together with a specific fuel composition, allows to enhance the desired nuclear reaction and control the isotopic evolution in the reactor.

The reaction path can be chosen with the aim to transmute radioactive waste as described before but also with the aim of producing a certain isotope that is useful in the production of energy (via a breeding cycle) such as ^{233}U as shown in Figure 1.4.

1.2.1 Radioactive waste and disposal

Radioactive waste is normally generated in a nuclear reactor due to neutron induced reactions. Fission reactions generate unstable fission fragments while neutron capture reactions on uranium and higher atomic mass elements give rise to transuranic elements. The fission fragments decay mainly by beta emission and the transuranic elements decay both by alpha and beta emission some

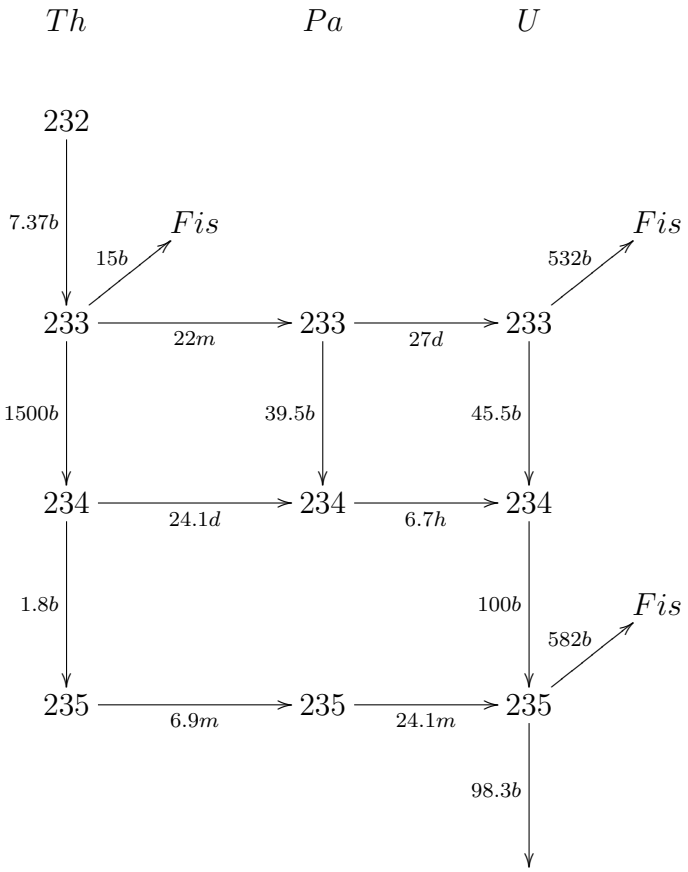

Figure 1.4: ^{233}U breeding cycle and possible branchings

being characterized by relative long half lives.

The radioactive waste is characterized based on its physical and chemical form, specific activity, emitted radiation, and radiotoxicity [5]. Also based on the thermal hazard and requirements for disposal, the International Atomic Energy Agency (IAEA) distinguishes two main classes of waste [6], one denominated high level waste and the other low and intermediate level waste with short and long lifetimes (Table 1.1).

In the particular case of high level waste, specialists have reached a consensual solution being it the deep underground (several hundred meters) geological disposal, taking advantage of the surrounding medium as a radiological barrier to avoid leakage of radioactive isotopes into the environment. Table 1.2 summarizes the amount of relevant nuclides to be disposed of in the repository.

Sustainability principles applied to the nuclear energy field imply a minimization both in volume and radiotoxicity of the high level waste to be dis-

Table 1.1: Classification of radioactive nuclear waste by the IAEA [5].

Waste classes	Typical characteristics	Disposal options
Exempt waste (EW)	Activity levels at or below clearance levels given in [6], which are based on an annual dose to members of the public of less than 0.01 mSv	No radiological restrictions
Low and intermediate level waste (LILW)	Activity levels above clearance levels given in [6] and thermal power below about 2kW/m^3	
Short lived waste (LILW-SL)	Restricted long lived radionuclide concentrations (limitation of long lived alpha emitting radionuclides to 4000 Bq/g in individual waste packages and to an overall average of 400 Bq/g per waste package)	Near surface or geological disposal facility
Long lived waste (LILW-LL)	Long lived radionuclide concentrations exceeding limitations for short lived waste	Geological disposal facility
High level waste (HLW)	Thermal power above about 2kW/m^3 and long lived radionuclide concentrations exceeding limitations for short lived waste	Geological disposal facility

posed in underground repositories. This can be achieved by Partitioning and Transmutation of the radioactive waste.

1.2.2 Partitioning and Transmutation

Partitioning and Transmutation technologies allow a significant reduction of the risk and simplify the conditions for final storage. The RED-IMPACT [4] project study aimed to assess the impact of partitioning and transmutation in the final disposal repositories and in the sustainability of nuclear energy.

In the particular case of a Light Water Reactor (LWR) where the nuclear waste consists mostly of transuranic isotopes and LLFP as shown on Table 1.2,

Table 1.2: Mass of relevant nuclides in the solid waste obtained from the burning of UOX (Uranium dioxide) fuel in a PWR to be disposed of in a repository [4].

Nuclides	Mass of Actinides in solid $[g/TWh(e)]$
U	2302048
Np	2021
Pu	25430
Am	4417
Cm	52
LLFP	125810
Transuranic	31920

a good knowledge of the different cross section for all possible reactions for each isotope is mandatory in order to achieve a sustainable solution both for final disposal or for reuse as nuclear fuel in a transmutation device as an ADS.

The Partitioning and Transmutation of radioactive waste consists in chemically processing the high level waste, isolating the different elements (partitioning) and after with the help of a device capable of irradiate the minor actinide enriched fuel achieve a reduction both in volume and radiotoxicity of the high level waste by transmutation.

Transmutation is a process where nuclear reactions like neutron fission or neutron capture are induced in a reactor core loaded with nuclear waste to create new isotopes that have shorter decay times and being less radiotoxic by comparison with transuranic elements.

The neutron energy spectrum in conventional reactors is governed by the fission reactions that provide the proper neutron multiplication inside the reactor's core. The neutrons produced this way follow a Watt fission neutron energy spectrum that has a maximum around 1.6 MeV and an average of 2.1 MeV corresponding to a fast neutron spectrum. The Watt fission neutron energy spectrum is a good starting point for a desirable neutron spectrum in the scope of transmutation with a fast neutron spectrum but a core full with transuranic isotopes and LLFP works mostly as a neutron absorber and the necessary neutron multiplication doesn't occur, leading to sub-critical working regimes and full stop of the reactor. Therefore, to sustain a reaction, an external source of neutrons is needed. A solution to this problem has been foreseen with the use of and external proton accelerator that is used for neutron production inside the core via spallation reactions. This type of systems that bound

a fast reactor with an external neutron source are called Accelerator-Driven System (ADS).

Transmutation needs, favor the use of a sub-critical reactor like the ADS loaded with specific fuel compositions, highly enriched in high mass transuranic actinides and a fast neutron spectrum in order to increase the ratio of fission to absorption as this increases with neutron energy for most actinide isotopes.

In spite of the possibilities opened by new systems design like ADS and by radioactive waste transmutation, some problems remain, specially the poor knowledge of the involved cross section needed. The actual knowledge on the neutron cross sections of actinides is mainly related to the exploitation of the U-Pu fuel cycle in nuclear reactors with a thermal neutron spectrum and the design and operation of experimental fast U-Pu nuclear reactors.

The precise knowledge of the cross sections for higher neutron energies (typically above 1 keV) is poor or non-existent or very limited to few isotopes and reaction channels. The currently existing nuclear databases can be used for the conceptual design of the transmutation oriented nuclear devices – fast reactors or ADS – and for the first order evaluation of the impact of the transmutation technology in the nuclear waste management. However, the detailed engineering designs, safety assessments and the detailed performance assessment of dedicated transmutation ADS and fast reactors (i.e. with fuels highly enriched in transuranic isotopes) require more precise and complete basic nuclear data.

An example of transmutation with fission is:

$$n + {}^{239}Pu(24000y) \xrightarrow{Fission} {}^{134}Cs(2y) + {}^{104}Ru(stable) + 2n + 200MeV$$

And by capture:

$$n + {}^{129}I(15.7Million\ years) \xrightarrow{Capture} {}^{130}I(12h)$$

Or by combination of several reactions:

$$n + {}^{240}Pu(6600y) \xrightarrow{Capture} {}^{241}Pu(14y)$$
$$n + {}^{241}Pu(14y) \xrightarrow{Fission} {}^{134}Xe(stable) + {}^{105}Rh(35h) + 3n + 200MeV$$

Transmutation can also be used for energy production by breeding fissile isotopes like the case of the Th-U cycle where fissile ^{233}U is produced from the abundant ^{232}Th via a breeding process. The breeding process consists in consecutive neutron captures followed by beta decay. This permits to convert

a non-fissile nucleus in to fissile one and will be discussed in more detail in the next chapters.

To cope with demands for improve nuclear safety, improve proliferation resistance, minimize waste and natural resource utilization, and decrease the cost to build and run nuclear reactors, the Generation IV International Forum (GIF) was started to conduct the research on a new generation of reactor [7].

1.3 Generation IV reactors

Why do we need a new generation of nuclear reactors? The answer is readily available in the current generation of reactors where a relatively inefficient fuel cycle is present together with big volumes of high radiotoxicity and high level waste. More, many of the current generation reactors have not addressed the problem of proliferation-resistance problem or are no longer considered secure by today's standards.

To address this problems, an international task force is developing six nuclear reactor technologies for deployment between 2020 and 2030.

From the six reactor designs, four are fast neutron reactors, all of these operate at higher temperatures than today's reactors and four are designated for hydrogen production [8].

More important, all six systems represent advances in sustainability, economics, safety, reliability and proliferation-resistance and most of the six systems employ a closed fuel cycle to maximize the resource base and minimize high-level wastes to be sent to a repository. There were originally six technologies chosen, but development on one has gone in two directions and therefore seven are listed in Table 1.3.

1.3.1 Overview of the different designs

Three of the six are Fast Neutron Reactor (FNR) and one can be built as a fast reactor, being one described as epithermal, and only two operating with slow neutrons like today's plants.

From the six reactor designs, only one is cooled by light water, two are helium-cooled and the others have lead-bismuth, sodium or fluoride salt coolant. Three operate at low pressure, with significant safety advantage. The one has the uranium fuel dissolved in the circulating coolant.

Temperatures range from 510°C to 1000°C, which is a significant change compared with less than 330°C for today's light water reactors, and this means that four of them can be used for thermo-chemical hydrogen production.

The sizes range from 150 to 1500 MWe (or equivalent thermal) , with the lead-cooled one optionally available as a 50-150 MWe "battery" with long core life (15-20 years without refueling) as replaceable cassette or entire reactor module. This is designed for distributed generation or desalination.

At least four of the systems have significant operating experience already in most respects of their design, which provides a good basis for further R&D and is likely to mean that they can be in commercial operation well before 2030.

However, it is significant that to address non-proliferation concerns, the fast neutron reactors are not conventional fast breeders, i.e. they do not have a blanket assembly where ^{239}Pu is produced. Instead, plutonium production takes place in the core, where burn-up is high and the proportion of plutonium isotopes other than ^{239}Pu remains high. In addition, new reprocessing technologies will enable the fuel to be recycled without separating the plutonium.

1.3.1.1 Gas-cooled fast reactors (GFR)

Like other helium-cooled reactors which have operated or are under development, GFR will be a high-temperature unit - 850°C. This reactor employ similar reactor technology to the VHTR (discussed in Section 1.3.1.5), suitable for power generation or thermo-chemical hydrogen production. The reference GFR unit is 1200 MWe, with thick steel reactor pressure vessel and three 800 MWt loops [9]. It would have a self-generating (breeding) core with fast neutron spectrum and no fertile blanket. Robust nitride or carbide fuels would include depleted uranium and any other fissile or fertile materials as ceramic pins or plates, with plutonium content of 15 to 20%. As with the SFR(discussed in Section 1.3.1.3), used fuel would be reprocessed on site and all the actinides recycled repeatedly to minimize production of long-lived radioactive wastes. This is the only Gen IV design with no operating antecedent, so a prototype is not expected before 2025.

1.3.1.2 Lead-cooled fast reactors (LFR)

The LFR is a flexible fast neutron reactor which can use depleted uranium or thorium fuel matrices, and burn actinides from LWR fuel. Liquid metal (Pb or Pb-Bi eutectic) cooling is at low pressure by natural convection (at least for decay heat removal). Fuel is metal or nitride, with full actinide recycle from regional or central reprocessing plants. Operating temperature of 550°C is readily achievable but 800°C is envisaged with advanced materials to provide lead corrosion resistance at high temperatures and this would enable thermochemical hydrogen production[10].

Table 1.3: Generation IV reactor's design and characteristics [8].
* high = 7-15 Mpa
+ = with some ^{235}U or ^{239}Pu
** 'battery' model with long cassette core life (15-20 yr) or replaceable reactor module

Reactor designation	Neutron spectrum	Coolant	Temperature (°C)	Pressure*	Fuel	Fuel cycle	Size (MWe)	Applications
Gas-cooled fast reactors	fast	helium	850	high	^{238}U +	closed, on site	1200	electricity and hydrogen
Lead-cooled fast reactors	fast	lead or Pb-Bi	480-800	low	^{238}U +	closed, regional	20-180** 300-1200 600-1000	electricity and hydrogen
Molten salt fast reactors	fast	fluoride salts	700-800	low	UF in salt	closed	1000	electricity and hydrogen
Liquid Fluoride Thorium Reactors	thermal	fluoride salts	750-1000		UO_2 particles in prism	open	1000-1500	hydrogen
Sodium-cooled fast reactors	fast	sodium	550	low	^{238}U & MOX	closed	30-150 300-1500 1000-2000	electricity
Supercritical water-cooled reactors	thermal or fast	water	510-625	very high	UO_2	open (thermal) closed (fast)	300-700 1000-1500	electricity
Very high temperature gas reactors	thermal	helium	900-1000	high	UO_2 prism or pebbles	open	250-300	electricity and hydrogen

This corresponds with Russia's Fast reactors with a nitride fuel and a lead coolant (BREST) and builds on 80 reactor-years experience (accumulated in several reactors) of lead or lead-bismuth cooling, mostly in submarine reactors. Its fuel is U+Pu nitride. More immediately the Generation IV International Forum (GIF) proposal appears to arise from two experimental designs: the USA Secure, Transportable, Autonomous Reactor (STAR) and Japan's LBE Cooled Long-Life Safe Simple Small Portable Proliferation-Resistant Reactor (LSPR), these being lead and lead-bismuth cooled respectively.

1.3.1.3 Sodium-cooled fast reactors (SFR)

The SFR uses liquid sodium as the reactor coolant, allowing high power density with low coolant volume. It builds on some 390 reactor-years experienced with

sodium-cooled fast neutron reactors over five decades and in eight countries, and is the main technology of interest in GIF. Most plants so far have had a core plus blanket configuration, but new designs are likely to have all the neutron action in the core. Other R&D is focused on safety in loss of coolant scenarios, and improved fuel handling [11].

The SFR utilises depleted uranium as the fuel matrix and has a coolant temperature of 500-550°C enabling electricity generation via a secondary sodium circuit, the primary one being at near atmospheric pressure. Three variants are proposed: a 50-150 MWe type with actinides incorporated into a U-Pu metal fuel requiring electrometallurgical processing (pyroprocessing) integrated on site, a 300-1500 MWe pool-type version of this, and a 600-1500 MWe type with conventional Mixed Oxide Fuel (MOX) fuel and advanced aqueous reprocessing in central facilities elsewhere.

1.3.1.4 Supercritical Water-cooled Reactors (SCWR)

This is a very high-pressure water-cooled reactor which operates above the thermodynamic critical point of water (374°C, 22 MPa) to give a thermal efficiency about one third higher than today's light water reactors from which the design evolves. The supercritical water (25 MPa and 510-550°C) directly drives the turbine, without any secondary steam system, simplifying the plant. Two design options are considered: pressure vessel and pressure tube. Passive safety features are similar to those of simplified boiling water reactors. Fuel is uranium oxide, enriched in the case of the open fuel cycle option. However, it can be built as a fast reactor with full actinide recycle based on conventional reprocessing [12].

1.3.1.5 Very high-temperature gas reactors (VHTR)

These are graphite-moderated, helium-cooled reactors, based on substantial experience. The core can be built of prismatic blocks such as the Japanese High Temperature Test Reactor (HTTR) and the Gas Turbine Modular Helium Reactor (GTMHR) under development by General Atomics and others in Russia, or it may be pebble bed such as the Chinese High Temperature Reactor-10 MWt (HTR-10) or High Temperature Reactor-Pebblebed Modules (HTR-PM) and the Pebble Bed Modular Reactor (PBMR) under development in South Africa, with international partners. Outlet temperature of over 900°C and aiming for 1000°C enables thermochemical hydrogen production via an intermediate heat exchanger, with electricity cogeneration, or direct high-efficiency driving of a gas turbine (Brayton cycle). There is some flexibility in fuels, but no recycle initially. Modules of 600 MW thermal are envisaged. The VHTR

has potential for high burn-up (150-200 GWd/t), completely passive safety, low operation and maintenance costs, and modular construction [13].

1.3.1.6 Molten salt reactors (MSR)

In an MSR, the uranium fuel is dissolved in the sodium fluoride salt coolant which circulates through graphite core channels to achieve some moderation and an epithermal neutron spectrum. The reference plant is up to 1000 MWe. Fission products are removed continuously and the actinides are fully recycled, while plutonium and other actinides can be added along with ^{238}U, without the need for fuel fabrication. Coolant temperature is 700°C at very low pressure, with 800°C envisaged. A secondary coolant system is used for electricity generation, and thermochemical hydrogen production is also feasible.

Compared with solid-fuelled reactors, MSR systems have lower fissile inventories, no radiation damage constraint on fuel burn-up, no spent nuclear fuel, no requirement to fabricate and handle solid fuel, and a homogeneous isotopic composition of fuel in the reactor. These and other characteristics may enable MSRs to have unique capabilities and competitive economics for actinide burning and extending fuel resources.

During the 1960s the USA developed the molten salt fast reactor as the primary back-up option for the conventional fast breeder reactor, and a small prototype was operated for about four years. Recent work has focused on lithium and beryllium fluoride coolant with dissolved thorium and ^{233}U fuel. The attractive features of the MSR fuel cycle include: the high-level waste comprising fission products only, hence shorter-lived radioactivity; small inventory of weapons-fissile material (^{242}Pu being the dominant Pu isotope); low fuel use (the French self-breeding variant claims 50kg of thorium and 50kg ^{238}U per billion kWh); and safety due to passive cooling up to any size [14].

1.3.1.7 Liquid Fluoride Thorium Reactor (LFTR)

A quite different concept is the LFTR, utilizing ^{233}U which has been bred in a liquid thorium salt blanket.

The core consists of fissile ^{233}U tetrafluoride in molten fluoride salts of lithium and beryllium at some 700°C and at low pressure within a graphite structure that serves as a moderator and neutron reflector. Fission products dissolve in the salt and are removed progressively – xenon bubbles out, others are captured chemically. Actinides are less-readily formed than in fuel with atomic mass higher than 235, and those that do form stay in the fuel until they are transmuted and eventually fissioned [15].

The blanket contains a mixture of thorium tetrafluoride in a fluoride salt

containing lithium and beryllium, made molten by the heat of the core. Newly-formed ^{233}U forms soluble uranium tetrafluoride (UF_4), which is converted to gaseous uranium hexafluoride (UF_6) by bubbling fluorine gas through the blanket solution (which does not chemically affect the less-reactive thorium tetrafluoride). Uranium hexafluoride comes out of solution, is captured, then is reduced back to soluble UF_4 by hydrogen gas in a reduction column, and finally is directed to the core to serve as fissile fuel.

The LFTR is not a fast reactor, but with some moderation by the graphite is epithermal (intermediate neutron speed). Safety is achieved with a freeze plug which if power is cut allows the fuel to drain into subcritical geometry in a catch basin. There is also a negative temperature coefficient of reactivity due to expansion of the fuel.

The China Academy of Sciences in January 2011 launched an R&D program on LFTR, known there as the Thorium-Breeding Molten-Salt Reactor (TMSR), and claimed to have the world's largest national effort on it, hoping to obtain full intellectual property rights on the technology [16].

1.3.2 Summary of the Generation IV reactors

The several studies and R&D programs confirm that the various engineering concerns can be met and that running reactors on thorium could indeed forestall clandestine efforts to use the spent fuel for making bombs. It is estimate that thorium-based fuels could cost anywhere from 10 % less to about 10 % more than conventional nuclear fuels [17]. The wide range stems from fundamental uncertainties about the cost of the seed uranium (which must be four times more enriched in ^{235}U than is the case with typical nuclear fuels), the cost of fabricating the fuel assemblies and the savings that might accrue in the future as a result of the reduction in the amount of spent fuel in need of disposal.

Although it seems unlikely that economics alone could drive the adoption of thorium fuels, there are no technical "show-stoppers" here. Modifications to the existing commercial infrastructure would clearly be needed, but no fundamentally new technology is required. And the fact that the relevant materials (thorium and enriched uranium) have a long record of experimental use in reactors (see Section 1.4.4) lends credibility to the notion that this scheme could one day find widespread application, should policymakers push the nuclear industry in that direction.

1.4 Thorium as nuclear fuel

Thorium, as well as uranium, can be used as a nuclear fuel. Although not fissile itself, ^{232}Th will absorb slow neutrons to produce ^{233}U, which is fissile and long-lived. The irradiated fuel can then be unloaded from the reactor, the ^{233}U separated from the thorium, and fed back into another reactor as part of a closed fuel cycle. Alternatively, ^{233}U can be bred from thorium in a blanket, the ^{233}U separated, and then fed into the core [18].

In one significant respect ^{233}U is better than ^{235}U and ^{239}Pu, because of its higher neutron yield per neutron absorbed. Given a start with some other fissile material (^{233}U, ^{235}U or ^{239}Pu) as a driver, a breeding cycle similar to but more efficient than that with ^{238}U and plutonium (in conventional, slow neutron reactors) can be set up. (The driver fuels provide all the neutrons initially, but are progressively supplemented by ^{233}U as it forms from the thorium.) However, there are also features of the neutron economy which counter this advantage. In particular the intermediate product ^{233}Pa which is a neutron absorber and diminishes the ^{233}U yield.

Over the last 40 years there has been interest in utilizing thorium as a nuclear fuel since it is more abundant in the Earth's crust than uranium. Also, all of the mined thorium is potentially usable in a reactor, compared with the 0.7% of natural uranium in today's reactors, so some 40 times the amount of energy per unit mass might theoretically be available (without using fast neutron reactors). But this relative advantage vanishes if fast neutron reactors are used for uranium [16].

1.4.1 Breeding, comparison between the Th-U and U-Pu cycles

In the U-Pu Cycle, the fertile element is ^{238}U, the fissile element it can produce is ^{239}Pu.

$$^{238}U \xrightarrow{n-capture} {}^{239}U \xrightarrow[23.4\ m]{\beta-decay} {}^{239}Np \xrightarrow[2.35\ d]{\beta-decay} {}^{239}Pu$$

An ^{238}U nucleus captures a neutron, it becomes a ^{239}U nucleus; this is radioactive by β-decay with a half life of 23.4 minutes. The ^{239}U nucleus decays to ^{239}Np, which is radioactive by β-decay with a half life of 2.35 days. The ^{239}Np nucleus decays to ^{239}Pu which has a very long half life. The ^{239}Pu nucleus fissions with a Neutron Induced Fission Cross Section (σ_f) or captures a neutron and becomes ^{240}Pu with a Neutron Capture Cross Section (σ_c). The fission reaction yields fission products and neutrons. The neutrons can be captured by a ^{238}U nucleus or captured by a ^{239}Pu nucleus.

On the chart of elements, and taking in account the possible production of minor actinides through successive neutron captures, the process can be represented as shown below in Figure 1.5.

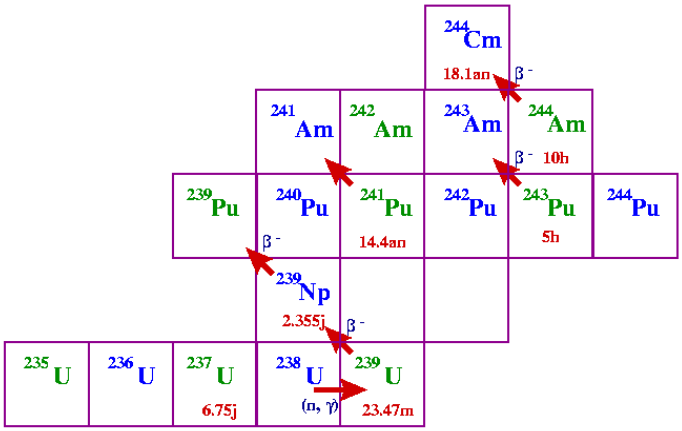

Figure 1.5: Partial isotope chart for the U-Pu cycle. Shown in green, the fissile nuclei. The arrows pointing up-left show the β-decay of isotopes creating isotopes of different elements and leading to the need for successive neutron captures to achieve a fissionable isotope. If β-decay or neutron capture occurs instead of fission, the production of minor actinides will be favored.

In the case of the Th-U Cycle, the fertile element is ^{232}Th, the fissile element it can produce is ^{233}U.

$$^{232}Th \xrightarrow{n-capture} {}^{233}Th \xrightarrow[22.3\ m]{\beta-decay} {}^{233}Pa \xrightarrow[27\ d]{\beta-decay} {}^{233}U$$

A ^{232}Th nucleus captures a neutron, it becomes a ^{233}Th nucleus; this is radioactive by β-decay with a half life of 22.3 minutes. The ^{233}Th nucleus decays to ^{233}Pa, which is radioactive by β-decay with a half life of 27 days. The ^{233}Pa nucleus decays to ^{233}U which has a very long half life. The ^{233}U nucleus fissions with cross section σ_f or captures a neutron and becomes ^{234}U with cross section σ_c. The fission reactions yields fission products and neutrons which can be captured by a ^{232}Th, induce fission or be captured in the ^{233}U nucleus.

On the chart of the elements, and taking in account the possible production of minor actinides through successive neutron captures, the process can be represented as shown below in Figure 1.6.

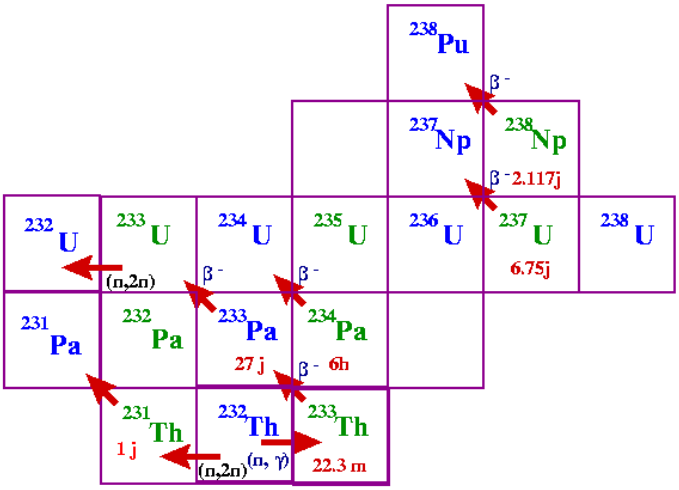

Figure 1.6: Partial isotope chart for the Th-U cycle. Shown in green, the fissile nuclei. Due to the smaller mass of the ^{232}Th, the production of minor actinides via the β-decay and successive neutron captures is mitigated.

1.4.2 Conversion versus Breeding

With the set of reactions described, starting from ^{238}U or from ^{232}Th, it is possible to obtain:

- Conversion if, at equilibrium, exactly as many fissile nuclei are produced as are consumed.
- Breeding if, at equilibrium, more fissile nuclei are produced than are consumed.

In either case, the fuel that the reactor receives is a mixture of fissile and fertile nuclei. The fissile element releases their energy in the form of γ radiation, α particles and neutrons. Some neutrons will trigger fission events for the next generation and others will induce transmutation reactions. The fertile nuclei are progressively transmuted to fissile nuclei and the entire fuel is eventually consumed. The fissile nuclei in the reactor at start up can be different from those that the fertile element will produce. Let us take, as an example, the Th-U cycle. There is no ^{233}U in nature. The cycle can be started with Plutonium taken from the spent fuel of today's reactors. There is plenty of that Plutonium in the world and the aim is to get rid of it. As the Plutonium is used in the reactor, it is replaced with ^{233}U. ^{239}Pu would thus serve as a "match" for the Th-U cycle, the additional advantage being, then, the destruction of otherwise cumbersome Plutonium stocks coming from today's reactors which cannot burn all their Plutonium for safety reasons. The ability of Th-U reactors

to operate safely with both ^{233}U and ^{239}Pu will have to be ascertained. The computer simulations of a Thorium reactor done at ISN (Institut des Sciences Nucléaires de Grenoble) [19] have confirmed that Plutonium could indeed be used to initiate a Thorium cycle.

1.4.3 Th-U cycle advantages over the U-Pu cycle

It was previously mentioned that the capture and fission cross sections of nuclei depend on the neutron energies. This holds also for the ratio of the capture and fission cross sections. They can become so nearly equal that, in a given step of our cycles, a capture is almost as likely as a fission.

Such is the case in the U-Pu cycle for thermal neutrons (neutron energy less than 1 eV). For these energies, the cross section ratio (see Figure 1.7), favors fission reactions over neutron capture. For fast neutrons (neutron energy around 200 keV), the ratio is close to 90/10 (see Figure 1.7). With thermal neutrons, too many neutrons are wasted in captures and conversion cannot be obtained. Moreover, a capture on ^{239}Pu gives ^{240}Pu and one more neutron will have to be lost in a capture in order to reach ^{241}Pu which is fissile. But ^{241}Pu itself is liable to capture a neutron without fissioning. It is thus possible to climb repeatedly towards heavier minor actinides. It is with this kind of capture that minor actinides are produced in reactors [20].

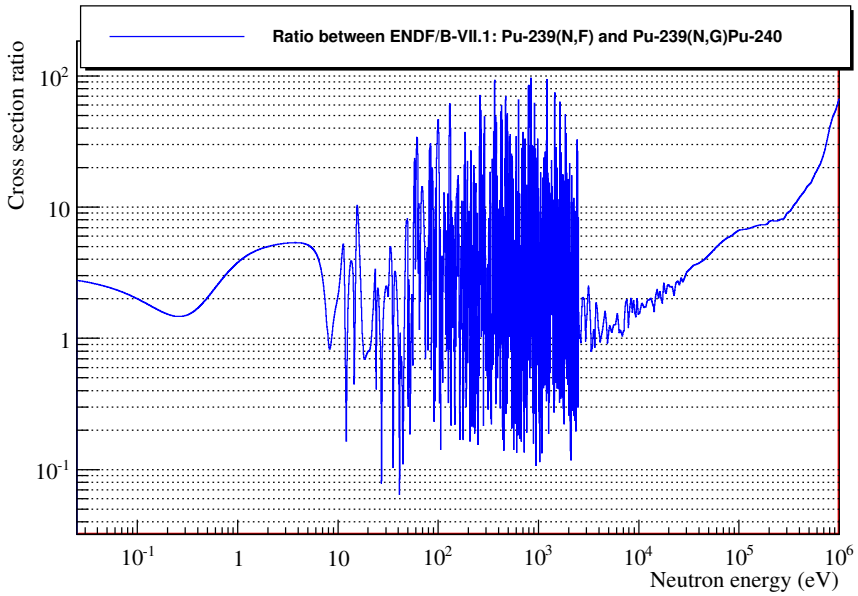

Figure 1.7: Fission to neutron capture cross sections ratio for ^{239}Pu as a function of neutron energy [21]

As can be seen in Figure 1.7, fission is about two times more probable than capture for thermal neutrons while, for fast neutrons, capture has a very low probability.

The Th-U cycle behaves quite differently. The cross section ratio (see Figure 1.8), is closer to 90/10 over the full energy range of neutrons in a reactor. For 100 neutron interactions with ^{233}U nuclei, 90 will yield a fission, and 10 will lead to a simple capture. For all energies, an average of 1.1 neutrons are needed per fission, the latter producing an average of 2.5 neutrons.

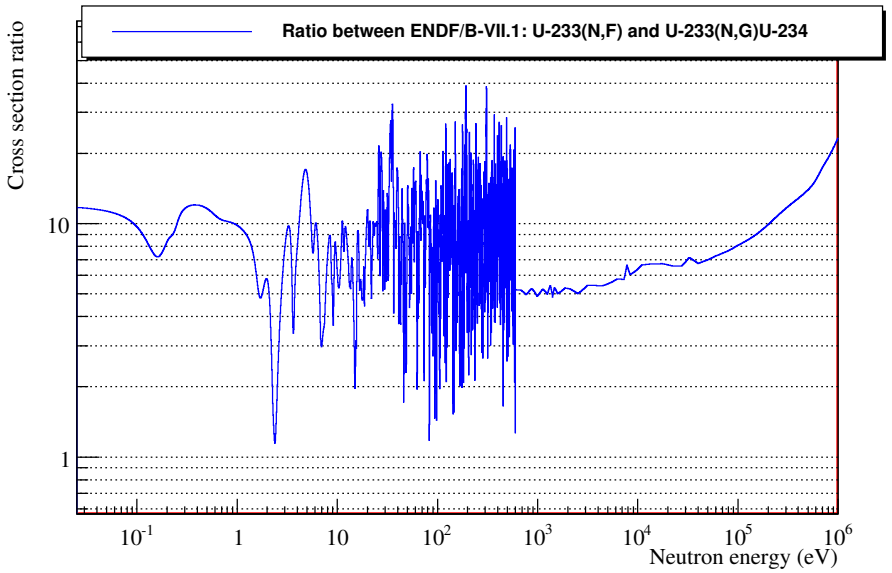

Figure 1.8: Fission to capture cross sections ratio for ^{233}U as a function of neutron energy [21].

As can be seen in Figure 1.8, the fission cross section is about 10 times larger than that of capture over the full energy range. Multiple resonances occur between 1 eV and 100 eV. Because of its poor cross section ratio for low neutron energies, a reactor based on the U-Pu cycle cannot operate as a converter with thermal neutrons, it can achieve conversion only with fast neutrons. On the contrary, with the Th-U cycle, the ratio of cross sections is favorable to conversion both for fast neutrons and for thermal neutrons as shown in Figure 1.9, a reactor based on the Th-U cycle can operate as a converter (or breeder) with thermal neutrons or with fast neutrons.

The difficulty connected with the Th-U cycle is that ^{233}Pa has a relatively

long 27 days half life: It can well capture neutrons, producing ^{234}Pa before decaying to the fissile ^{233}U. ^{234}Pa decays to ^{234}U (with a half life of 6 hours) which is fertile and an additional neutron capture will be needed to reach ^{235}U which is fissile. Computer simulations show that the neutron losses due to captures on Protactinium and ^{232}U formation can jeopardize breeding.

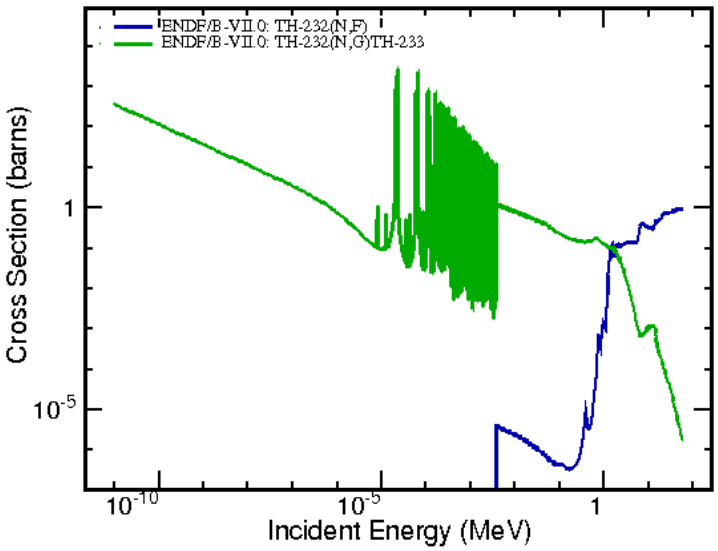

Figure 1.9: Fission and neutron capture cross sections (barns) for ^{232}Th as a function of neutron energy [21].

1.4.3.1 Proliferation

As previously mentioned, the lack of ^{233}U in nature necessitates using a different fissile material, such as ^{235}U (or perhaps ^{239}Pu), to prime a reactor running on thorium. Given the present-day proscription against commercial fuels that are too highly enriched in ^{235}U, a considerable amount of (non-fissionable) ^{238}U would clearly need to be included in the primer; current standards require at least 80 percent, and more is typical. As is the case with conventional reactors, this would make it impossible to use the fresh fuel for a bomb without first having to go through the technically difficult step of isotropically enriching the uranium.

The main advantage of using a combination of thorium and uranium is the significant reduction in plutonium content of the spent fuel compared with what comes out of a conventionally fueled reactor.

Indeed, the approach undergoing the biggest effort in investigation nowadays is a combination that keeps a uranium-rich "seed" separated from a

thorium-rich "blanket" [22]. The chief proponent of this concept was the late Alvin Radkowsky.

Radkowsky's idea was to construct special fuel assemblies that could be used in typical water-cooled reactors with very little modification. These units are made up of a central seed region containing fuel rods filled with reactor-grade uranium (that is having no more than 20 percent ^{235}U). Surrounding the seed is a blanket region with fuel rods containing thorium and a small amount of uranium. Having ^{238}U in the blanket prevents anyone from withdrawing these rods and using only chemical means to separate out the fissionable ^{233}U that is created over time.

Radkowsky and his colleagues had calculated that their scheme would reduce the amount of plutonium produced by 80 % compared with what goes on in a conventionally fueled reactor of the same energy output. Moreover, they found that the mix of plutonium isotopes generated, mostly in the seed fuel, would not be particularly desirable for military use, because a bomb made from it would be extremely unlikely to give much explosive yield. Also, the plutonium has such a high content of the ^{238}Pu isotope that its decay heat may be sufficient to melt or damage the other materials used in constructing a weapon.

The work at Shippingport was developed by Alvin Radkowsky, who was the chief scientist of the United States Navy's nuclear propulsion program from 1950 to 1972 and headed the team that built the Shippingport plant. The Radkowsky Thorium Reactor (RTR) addresses the aspects of the thorium fuel cycle that are considered sensitive from the point of view of weapons proliferation. In particular, the RTR avoids the need to separate ^{233}U.

Radkowsky proposed the use of a heterogeneous seed-blanket fuel assembly geometry, which separates the uranium (or plutonium) part of the fuel (the seed) from the thorium part of the fuel (the blanket). In the blanket part, ^{233}U is generated and fissioned, while the seed part supplies neutrons to the blanket. Either uranium enriched to 20% ^{235}U or plutonium can be used in the seed region. One method of increasing the proliferation resistance of the design is to include some ^{238}U in the thorium blanket. Any uranium chemically separated from it (for the ^{233}U) would not be usable for weapons. Used blanket fuel would also contain ^{232}U, which decays rapidly and has very active γ-emitter daughters creating significant problems in handling the bred ^{233}U and hence conferring proliferation resistance. Plutonium produced in the seed will have a high proportion of ^{238}Pu, generating a lot of heat and making it even more unsuitable for weapons than normal reactor-grade plutonium [22].

The calculations made for the plutonium production do, however, support Radkowsky's assertions that the spent fuel would contain appreciable amounts

of ^{238}Pu, a highly radioactive isotope, which thus produces a lot of heat.

The production of such large amounts of ^{238}Pu comes about because more of the fuel is consumed than is the case in conventional uranium-fueled reactors. An equivalent amount of ^{238}Pu could be created using an all-uranium fuel, but this would require a higher initial amount of fissile uranium (^{235}U) than is typical in today's practice, and the economic projections for that are discouraging.

1.4.3.2 Radiotoxicity of the waste

$^{232}_{90}$Th and $^{238}_{92}$U are separated by 6 mass units and 2 charge units. Neutron captures lead to heavier actinides in the U-Pu cycle than in the Th-U cycle. Heavier actinides have shorter half lives so that, for the same amount of fuel, the radioactivity of a U-Pu fuel is larger than that of a Th-U fuel. The consequences are negligible as long as the fuel is in the reactor.

It affects reprocessing significantly, in the way that more care must be taken in the handling, transportation and physico-chemical processing of the fuel. It is even more important when reprocessing and losses are considered: neither chemistry nor physics can achieve 100 % efficiency, some heavy nuclei are lost during reprocessing. Theses losses are small, they are estimated at 0.1% but they are not equal to zero. The radiotoxicity of nuclear waste produced by converter reactors can be so low that these fuel reprocessing losses can end up dominating the residual toxicity. The nature and amount of actinides produced can thus become a determining factor in the choice of the fuel cycle on one hand, and in the choice between fast or thermal neutrons, on the other hand.

Concerning the fuel, as we have just seen, the Th-U cycle produces fewer cumbersome actinides, in this respect, it is a better choice than the U-Pu cycle.

As shown before, a reactor based on the Th-U cycle can operate as a converter either with fast neutrons or with thermal neutrons. Let us examine how these differ in the actinides they generate. A reaction which we have not yet mentioned because its probability is very low has a significant incidence on actinide production. It is a so called "threshold" reaction, because it can occur only if the energy of the captured neutron is large (larger than a few MeV). It is the (n,2n) reaction, in which the nucleus, having captured a neutron, emits 2 neutrons. This reaction is a cause for additional actinide production in a fast neutron reactor [23, 20].

Thus, actinide production in the Th-U fuel cycle is lower in a reactor with thermal neutrons, because of the very low probability of (n, 2n) reactions in these circumstances. The reaction probability is very small but not zero, because the fast neutrons emitted during a fission can be captured before they are slowed down (moderated) by successive scattering interactions.

The reactor liable to produce the least actinides would then be a thermal neutron reactor based on the Th-U cycle. There are two reasons for reducing the production of minor actinides.

1. They increase the fuel's radioactivity (in the reactor and during reprocessing).
2. They increase the radiotoxicity of losses.

In Figure 1.10, a graphic representation of the radiotoxicities generated for a given amount of energy produced by the various technologies as a function of time gives a better understanding of the phenomena. The radiotoxicity due to the fission products is roughly the same for all the technologies, it dominates in the short term, because of the contribution of Short Lived Fission Products (SLFP). After a few hundred years, the radiotoxicity due to fission products falls to a relatively low level, very much below that of the natural Uranium used in the PWR case, then remains flat; that is the contribution of very LLFP. The radiotoxicity of the spent fuel from a PWR reaches the radiotoxicity level of the natural Uranium used for that PWR one million years after fuel unloading. The other curves are far below that of the Th-U cycle with thermal neutrons being the lowest. It reaches the radiotoxicity level of the Thorium used after a little more than ten thousand years.

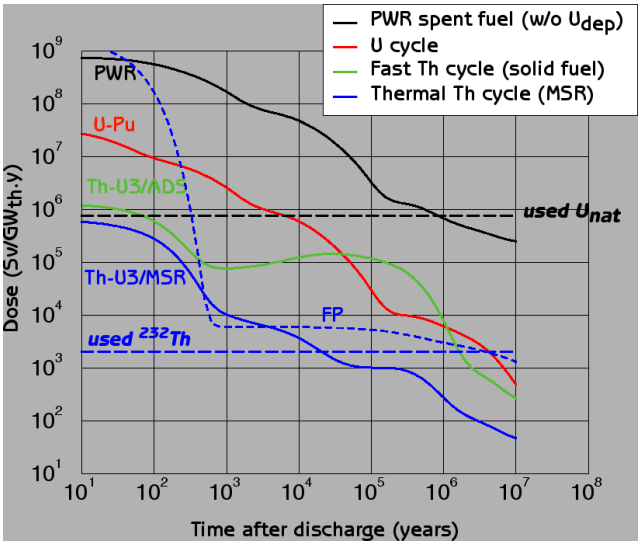

Figure 1.10: Radiotoxicity as a function of time (logarithmic scales). FP: fission products without transmutation. PWR; spent fuel from a PWR excluding depelted Uranium; U-PU: fast neutron U-Pu fuel cycle; TH-U/ADS: fast neutron Th-U fuel cycle; Th-U/MSR: slow neutron Th-U fuel cycle [23].

It is customary to represent the radiotoxicity at one thousand years, as on

Figure 1.11. It is the time when the radiotoxicity due to the fission products becomes small and the time when the actinides begin to dominate. That is the time when it becomes interesting to compare the technologies using a representation that allows more precise reading, at a specific time. Moreover, while the time curves the global values were shown in Figure 1.10, the losses and inventories are shown in Figure 1.11.

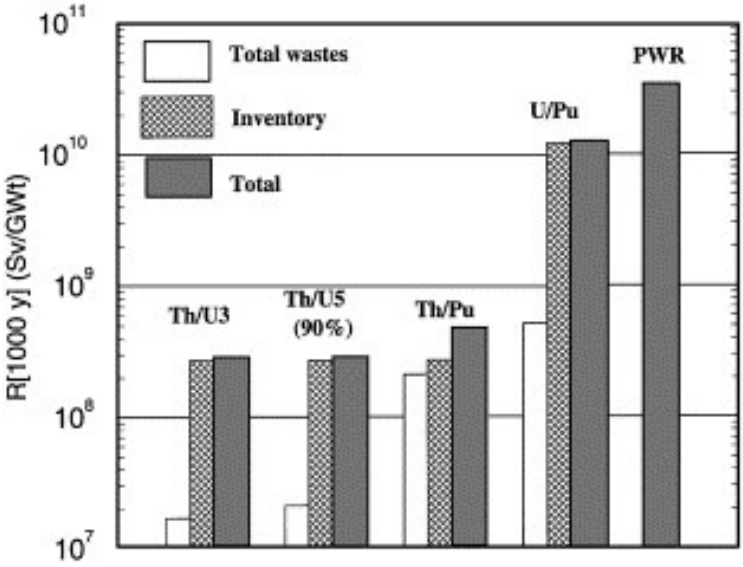

Figure 1.11: Radiotoxicities for the different technologies at 1000 years after discharge, due to the actinides in the wastes generated by 200 yr of energy generation and in the final inventory for different reactors simulated in this study, assuming the type-A waste regeneration scenario. For comparison, the radiotoxicity of the non-reprocessed wastes from a PWR reactor is included. All values are normalized to the installed thermal capacity [24]

1.4.4 Past experience - Thorium R&D History

The use of thorium-based fuel cycles has been studied for about 40 years, but on a much smaller scale than uranium or uranium/plutonium cycles. Basic research and development has been conducted in Germany, India, Japan, Russia, in the UK and in the USA. Test reactor irradiation of thorium fuel to high burn-ups has also been conducted and several test reactors have either been partially or completely loaded with thorium-based fuel [25].

Noteworthy experiments involving thorium fuel include the following, the first three being high-temperature gas-cooled reactors:

- Between 1967 and 1988, the Atom Versuchs Reaktor (AVR) (Nuclear Test Reactor), experimental pebble bed reactor at Jülich, Germany, operated for over 750 weeks at 15 MWe, about 95% of the time with thorium-based fuel. Overall a total of 1360 kg of thorium was used, mixed with High-Enriched Uranium (HEU). Burn-ups of 150,000 MWd/t were achieved.
- Thorium fuel elements with a 10:1 Th-U HEU ratio were irradiated in the 20 MWth Dragon reactor at Winfrith, UK, for 741 full power days. The Th-U fuel was used to 'breed and feed', so that the ^{233}U formed replaced the ^{235}U at about the same rate, and fuel could be left in the reactor for about six years.
- General Atomics Peach Bottom high-temperature, graphite-moderated, helium-cooled reactor in the USA operated between 1967 and 1974 at 110 MWth, using HEU with thorium.
- In Canada, Atomic Energy of Canada Limited (AECL) has more than 50 years experience with thorium-based fuels, including burn-up to 47 GWd/t. Some 25 tests were performed until 1987 in three research reactors and one pre-commercial reactor, with fuels ranging from ThO_2 to that with 30% UO_2, though most were with 1-3% UO_2, the U being high-enriched [26].
- In India, the Kamini 30 kWth experimental neutron-source research reactor using ^{233}U, recovered from ThO_2 fuel irradiated in another reactor, started up in 1996 near Kalpakkam. The reactor was built adjacent to the 40 MWt Fast Breeder Test Reactor, in which the ThO_2 is irradiated [27].
- In the Netherlands, an aqueous homogeneous suspension reactor operated at 1 MWth for three years in the mid-1970s. The HEU/Th fuel was circulated in solution and reprocessing occurred continuously to remove fission products, resulting in a high conversion rate to ^{233}U.

Much experience has been gained in thorium-based fuel in power reactors around the world, some using high-enriched uranium HEU as the main fuel:

- The 300 MWe Thorium High Temperature Reactor (THTR) in Germany was developed from the AVR and operated between 1983 and 1989 with 674,000 pebbles, over half containing Th/HEU fuel (the rest being graphite moderator and some neutron absorbers). These were continuously recycled on load and on average the fuel passed six times through the core.
- The Fort St. Vrain reactor was the only commercial thorium-fuelled nuclear plant in the USA, also developed from the AVR in Germany, and operated 1976-1989. It was a high-temperature (700°C), graphite-

moderated, helium-cooled reactor with a Th/HEU fuel designed to operate at 842 MWth (330 MWe). The fuel was in microspheres of thorium carbide and Th/^{235}U carbide coated with silicon oxide and pyrolytic carbon to retain fission products. It was arranged in hexagonal columns ('prisms') rather than as pebbles. Almost 25 tonnes of thorium was used in fuel for the reactor, and this achieved 170,000 MWd/t burn-up.

- Thorium-based fuel for PWRs was investigated at the Shippingport reactor in the USA.
- In India, thorium has been used for power flattening in the initial cores of the two Kakrapar pressurised heavy water reactors (PHWRs).
- The 60 MWe Lingen Boiling Water Reactor (BWR) in Germany utilised Th/Pu-based fuel test elements.

1.4.5 The experimental confirmation of breeding in a power reactor using Th

The Light Water Breeder Reactor (LWBR) concept is a major potential application for conventional Pressurized Water Reactor (PWR) and was successfully demonstrated at the Shippingport reactor in the USA. Shippingport commenced commercial operation in December 1957 as the first large-scale nuclear power reactor to be operated solely for electricity production. In 1965 the Atomic Energy Commission began designing a ^{233}U/Th core for the reactor and in 1976, the Energy Research and Development Administration established the Advanced Water Breeder Applications programme to evaluate the LWBR concept for commercial-scale applications. Shippingport operated as an LWBR between August 1977 and October 1982. During this period, the demonstration LWBR operated for over 29,000 effective full power hours with an availability factor of 76 % and had a gross electrical output of over 2.1 billion kWh. Following operation, inspection of the core found that 1.39 % more fissile fuel was present at the end of core life than at the beginning, proving that breeding had occurred [28].

1.4.6 India's plans for thorium cycle

With about six times more thorium than uranium, India has made utilization of thorium for large-scale energy production a major goal in its nuclear power programme, utilising a three-stage concept:

Pressurised Heavy Water Reactor (PHWR) fuelled by natural uranium, plus light water reactors, producing plutonium. Fast Breeder Reactor (FBR) using plutonium-based fuel to breed ^{233}U from thorium. The blanket around

the core will have uranium as well as thorium, so that further plutonium (particularly ^{239}Pu) is produced as well as the ^{233}U. Advanced heavy water reactors burn the ^{233}U and this plutonium with thorium, getting about 75 % of their power from the thorium. The used fuel will then be reprocessed to recover fissile materials for recycling. This Indian program has moved from aiming to be sustained simply with thorium to one 'driven' with the addition of further fissile uranium and plutonium, to give greater efficiency. In 2009, despite the relaxation of trade restrictions on uranium, India reaffirmed its intention to proceed with developing the thorium cycle.

Another option for the third stage, while continuing with the PHWR and FBR stages, is the use of sub-critical accelerator driven systems.

1.4.7 Thorium and accelerator driven systems

In an Accelerator-Driven System (ADS), high-energy neutrons are produced through the spallation reaction of high-energy protons from an accelerator striking heavy target nuclei (lead, lead-bismuth or other material). These neutrons can be directed to a sub-critical reactor containing thorium, where the neutrons breed ^{233}U and promote the fission of it. There is therefore the possibility of sustaining a fission reaction which can readily be turned off, and used either for power generation or destruction of actinides resulting from the U-Pu fuel cycle. The use of thorium instead of uranium reduces the quantity of actinides that are produced [29].

1.4.8 Issues in the development of a Thorium based fuel cycle

Despite the thorium fuel cycle having a number of attractive features, development has always run into difficulties.

The possibility of utilizing a very abundant resource which has hitherto been of so little interest that it has never been quantified properly. The production of power with few long-lived transuranic elements in the waste and a radioactive waste richer in short lived nuclides.

The problems include:

- The high cost of fuel fabrication, due partly to the high radioactivity of ^{233}U chemically separated from the irradiated thorium fuel.
- Separated ^{233}U is always contaminated with traces of ^{232}U (69 year half-life but whose daughter products such as ^{208}Tl are strong gamma emitters with very short half-lives). Although this confers proliferation resistance

to the fuel cycle by making ^{233}U hard to handle and easy to detect, it results in increased costs.

- Some concern over weapons proliferation risk of ^{233}U (if it could be separated on its own), although many designs such as the Radkowsky Thorium Reactor address this concern [22].
- The technical problems (not yet satisfactorily solved) in reprocessing solid fuels. However, with some designs, in particular with the MSR, these problems are likely to largely disappear.
- Much development work is still required before the thorium fuel cycle can be commercialized, and the effort required seems unlikely while (or where) abundant uranium is available.

Nevertheless, the thorium fuel cycle, with its potential for breeding fuel without the need for fast neutron reactors, holds considerable potential in the long-term. It is a significant factor in the long-term sustainability of nuclear energy.

Chapter 2

Theoretical introduction

In this chapter an overview of the theoretical background needed for the full understanding of the particular data analysis process described in this document will be performed.

The concept of neutron cross section will be introduced together with the compound nucleus theory and the R-matrix formalism.

The main features of the principal neutron induced reactions will be explained as well as the technique used for measuring the cross sections in this work.

2.1 Nuclear reactions induced by neutrons

2.1.1 Neutron interactions with matter

With the exception of hydrogen, nuclei of atoms consist of protons and neutrons, which are therefore collectively referred to as nucleons. The neutral charge gives to neutrons the ability of interact directly with the nucleus as they are insensitive to the Coulomb barrier [30]. Even a very low energy neutron is able to trigger a reaction with a nucleus. The lack of charge also leads to the ability that neutrons possess to cross large thickness of materials without interacting.

In a free state (without being bound in a nucleus) the neutron will β-decay within a half life of approximately 10.2 minutes releasing 0.78 MeV of energy [31].

$$n \rightarrow p + e^{-} + \overline{\nu}$$

In an energy range that goes from a few tenths of meV to tenths of MeV, 11 minutes is a long time allowing for a free neutron to interact. In this energy

range, neutrons can interact with matter by two types of reactions, direct and formation of compound nucleus.

In the case of a direct reaction, the neutron interacts directly with one or several nucleons of the target nucleus within a very short time interval of the order of 10^{-22} s without forming a compound nucleus. This reaction is important for neutrons in the energy range of the MeV where the De Broglie wavelength of the neutron becomes comparable to the size of nucleons but negligible for less energetic ones specially in the case of heavy nucleus like the actinides ($_{89}$Actinium, $_{90}$Thorium, $_{91}$Protactinium, $_{92}$Uranium..., $_{103}$Lawrencium). At lower neutron energies, mainly for light mass or closed shell nuclei, direct reactions may contribute significantly to the total reaction cross section. In general for neutrons with energies below 1 MeV, the here discussed compound nucleus reactions prevail.

In a compound nucleus reaction a neutron interacts with a nucleus to form a temporary compound nucleus, which is characterized by a longer interaction time in comparison with direct reactions. In fact, these reactions take place in a time interval thousands of times larger. This longer interaction time allows the incident neutron to interact with the nucleons until the available binding energy plus the kinetic energy is shared by all the nucleons including the incoming neutron. This new equilibrium state corresponds to the compound nucleus. At this moment, the compound nucleus is in a excited state and several alternatives become available to release the energy surplus. Typically the compound nucleus will release the energy by emission of γ-rays, or by fission, or by neutron emission which will therefore modify the initial target nucleus leading to the formation of a new isotope or new elements [32].

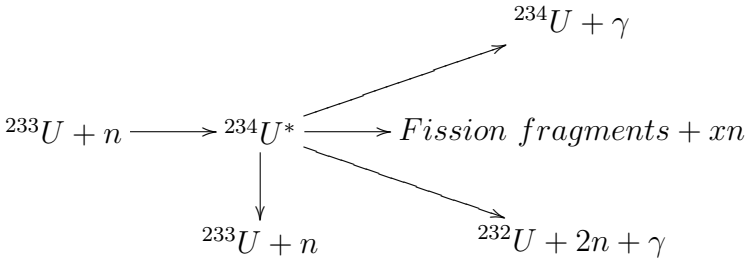

Another possible way for the neutron to interact with the target nucleus is by potential scattering. In this case, the incident neutron will not penetrate the target nucleus, instead, it is reflected due to the so called hard sphere effect of the nucleus. In this reaction, the total kinetic energy is conserved and the scattered neutron is the same as the incident. The process is denominated by potential elastic scattering.

From the energetic point of view, the scattering reaction can be differ-

entiated in elastic and inelastic reactions. Also the incident neutron can be absorbed or not by the target nucleus.

The inelastic scattering is very similar to the elastic scattering except in the fact that some of the kinetic energy of the incident neutron is transfered to the target nucleus leaving it in an excited state. The target nucleus will go back to the ground state by emitting a number of γ-rays depending of the excited state achieved.

Other possible reactions like neutron capture or radiative capture, fission, (n, p), (n, α), (n, xn) are characterized by the absorption of the neutron.

A decomposition of the total cross section in the basic nuclear reactions can be found in Table 2.1. The direct reaction contribution was omitted due to the fact of occurring at higher energies that the ones discussed and of interest to this work.

Table 2.1: Decomposition of the total cross section in the basic nuclear reactions

<table>
<tr><td colspan="6">Total cross section</td></tr>
<tr><td>No compound nucleus formation</td><td colspan="5">Compound nucleus formation</td></tr>
<tr><td colspan="3">Scattering</td><td colspan="3">Absorption</td></tr>
<tr><td colspan="2">Elastic</td><td colspan="4">Inelastic</td></tr>
<tr><td>Potential elastic scattering</td><td>Resonant elastic scattering</td><td>Resonant inelastic scattering</td><td>Radiative capture</td><td>Fission</td><td>(n, p)
(n, α)
(n, xn)</td></tr>
</table>

The neutron capture and neutron induced fission are the reactions of most interest for the work here discussed.

In the case of neutron capture, the incident neutron will be absorbed by the target nucleus forming a compound nucleus which is an excited state with energy equal to the sum of the incident neutron kinetic energy plus the binding energy of a nucleon on the compound nucleus. This energy can be released by the emission of several γ-rays until the nucleus (X^{A+1}) reaches the ground state. The γ-rays energy spectrum is defined by the selection rules which depend on the spin, parity and excited level energies in the compound nucleus, leading to a discrete spectrum.

The neutron fission leads also to the incident neutron absorption. The result is a deformed, unstable nucleus which will brake in more stable fragments, neutrons and accompanied by the emission of energy in the form of

γ-rays. This reaction is most relevant for heavy nucleus and is for some isotopes characterized by a low energy threshold for the incident neutron.

Finally, the reactions which leads to the emission of particles depend most of the incident neutron energy. If the neutron's kinetic energy is enough, the compound nucleus will release the excitation energy by emitting charge particles like protons or an α or several neutrons in the case of a (n, xn) reaction.

The life time of an excited state in the compound nucleus τ is finite and follows the Heisenberg uncertainty principle

$$\tau \cdot \Gamma \approx \hbar \tag{2.1}$$

where Γ represents the energetic width of the excited level and therefore the resonance width.

In Table 2.1 where the possible compound nucleus reactions induced by neutrons are enumerated, several 'channels' are available for the de-excitation of the compound nucleus. An incident neutron in a ^{233}U target can react with the target nucleus by neutron capture, neutron induced fission, elastic and inelastic scattering. The total cross section for a given excited state is therefore defined by by the partial widths associated with the available channels $(\Gamma_\gamma, \Gamma_f, \Gamma_n, \Gamma_{n'})$.

$$\Gamma = \Gamma_\gamma + \Gamma_f + \Gamma_n + \Gamma_{n'} + ... \tag{2.2}$$

The excited states correspond to quantum states with a finite life time. The decay time probability of this states is given by a negative exponential function. The probability distribution as a function of the energy associated to this states is given by the square of the absolute value of the Fourier transform of the exponential.

$$P(E) = \frac{\Gamma/2\pi}{(E - E_0)^2 + \Gamma^2/4} \tag{2.3}$$

2.2 Resonant behavior of the neutron interaction cross section

One of the most striking features of neutron-nucleus interactions is the resonance structure observed in the reaction cross sections at incident neutron energies typically below 1 keV for most heavy nuclei [33]. Since the electrically neutral neutron has no Coulomb barrier to overcome, and has a negligible

interaction with the electrons in matter, it can directly penetrate and interact with the atomic nucleus, even at very low kinetic energies in the order of electron-volts.

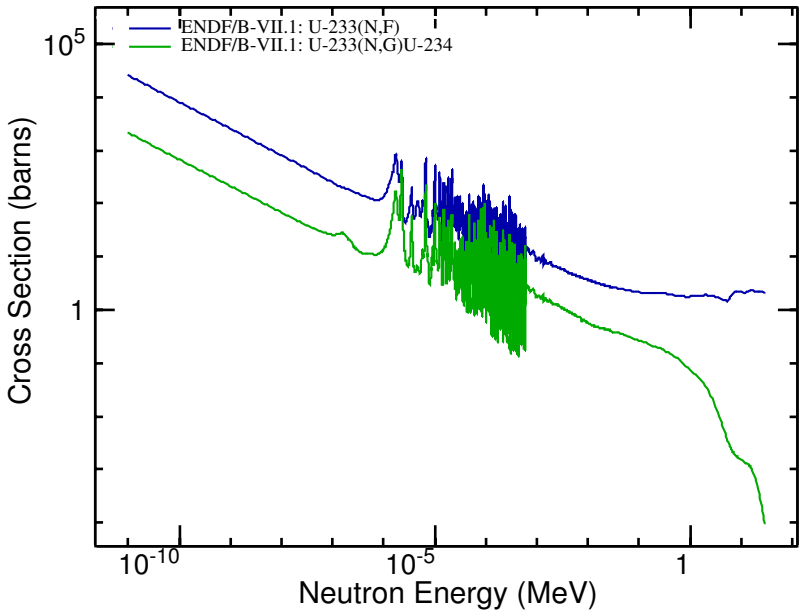

Figure 2.1: Neutron capture (green) and neutron induced fission (blue) cross section for the ^{233}U form ENDF/B-VII.1

The need to quantify the probability of a given incident particle to react with a target nucleus led to the introduction of the "cross section" concept. As the name suggests, this concept is based on the idea that an incoming particle sees a given target area which could be the geometrical cross section. As will be shown later, this is not realistic in terms nor conceptually but works as a simplistic introduction. This quantity depends on the target nucleus, on the type of reaction occurring and on the incident particle kinetic energy. The unit associated with this quantity is the barn (1 barn = 10^{-24} cm^2) and corresponds approximately to the geometrical cross section of a nucleus. Against the classical idea, the cross section for a incident neutron on a target nucleus can vary by several orders of magnitude on an energy scale of only a few eV. This can be clearly seen in Figure 2.1 where the neutron capture and neutron induced fission for the ^{233}U is shown over a large interval of incident neutron energies. The deviation from the pure geometrical collision factor and the variations with the incident neutron energy, target nucleus, and reaction type

are related with the formation of a compound nucleus. Looking at Figure 2.1, its easy to remark that the fission and capture cross section variations occur at the same neutron energies. The origin of the resonances is well understood: they are related to the excitation of nuclear states in the compound nuclear system formed by the neutron and the target nucleus, at excitation energies lying above the neutron binding energy typically several MeV. This specific energies correspond to excited states of the compound nucleus.

The compound nucleus model was introduced by Niels Bohr [34] to explain the observed resonances in neutron-nucleus reactions. The wavelength of low energy neutrons is comparable to the size of the nucleus. Typical widths (Γ) of measured resonances are in the order of electron-volts. According to Heisenberg's uncertainty principle, the corresponding life time of the compound nucleus is in the order of $\tau = \hbar/\Gamma \simeq 10^{-15}s$, several orders of magnitude larger than the typical time needed by a neutron to cross a nucleus without interaction. In this picture, the neutron binding energy which becomes available to the compound nucleus, is rearranged among all nucleons, and gives rise to a complex configuration corresponding to a well defined nuclear state with an energy, spin and parity. Within Fermi's description of excitations of particle-hole configurations, such a state would correspond to an extremely complicated configuration of a many particle, many hole state. The compound nucleus may then decay through the energetically allowed channels. The type of decay and the decay probability of the compound nucleus is considered to be independent from the way how the compound nucleus was formed, but respecting conservation of energy and angular momentum. The decay probability is equal to the branching ratio Γ_x/Γ where Γ_x is the width related to the decay by emission of a particle x, which at low energy is mainly a gamma ray or a neutron.

In Figure 2.2 a picture of the compound nucleus reaction is sketched. After the formation of the highly excited state by an incident neutron, the compound nucleus can decay by emission of gamma radiation, which is called radiative neutron capture, or by emission of a neutron, which is elastic scattering. If the kinetic energy of the neutron is high enough, threshold reactions are possible, like inelastic scattering, leaving the target nucleus in an excited state. If the excitation energy is higher than the fission threshold, fission is energetically allowed. Due to the pairing effect, the neutron binding energy for even compound nuclei is considerably lower than for odd compound nuclei, which for some of the heavy nuclei results in a fissionable nucleus even if the incident neutron has nearly zero kinetic energy. All these reactions show resonances at the same energies corresponding to the excitation of the nuclear levels in the compound nucleus. The shapes of the resonances are different and related to the involved widths and their quantum numbers.

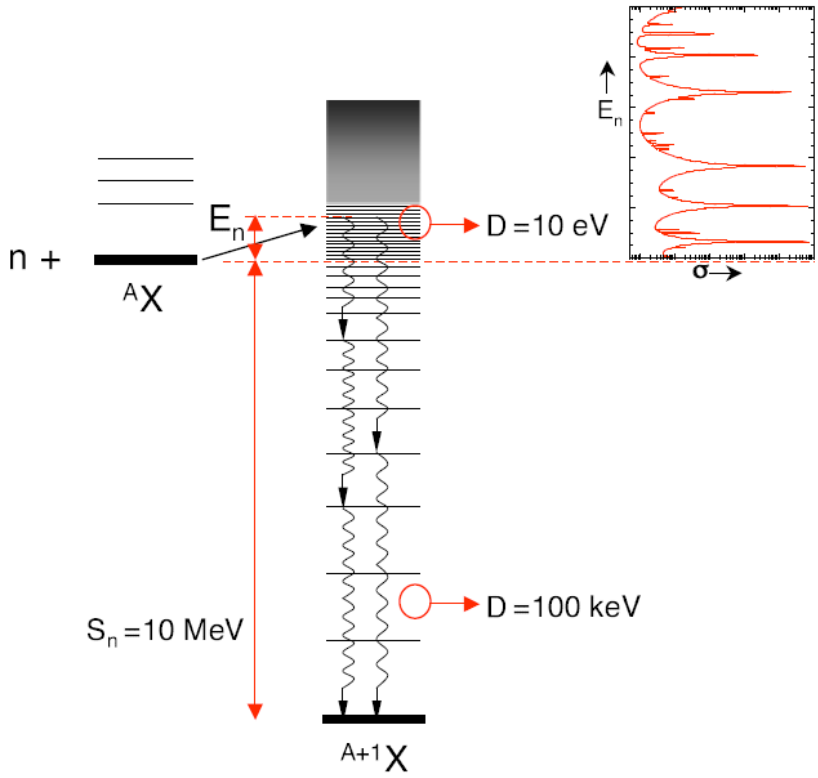

Figure 2.2: Schematic view of the formation and decay of a compound nucleus with typical values of level spacing and neutron separation energy. The resonances observed in the reaction cross section correspond to the excitation of nuclear levels.

The possible neutron-nucleus reactions vary with incident neutron energy. The nuclear reaction that is always present if a reaction is energetically allowed is elastic scattering. This may be scattering from the nuclear potential, also called shape elastic or sometimes hard sphere scattering, without forming a compound nucleus. In addition resonant elastic scattering through a compound nucleus may be present. The potential scattering is a smooth and nearly energy independent cross section as a function of energy but interferes with the resonant scattering cross section.

The shape of isolated resonances in reaction cross sections have in good approximation a Breit-Wigner shape [35]. The squared absolute value of the Fourier transform of $\Phi(t)$ gives the energy distribution $P(E)$ (Eq. (2.3)) having the Breit-Wigner form which is the typical shape for any quantum-mechanical state with a finite lifetime. This equivalence in the time and energy domain is illustrated in Figure 2.3.

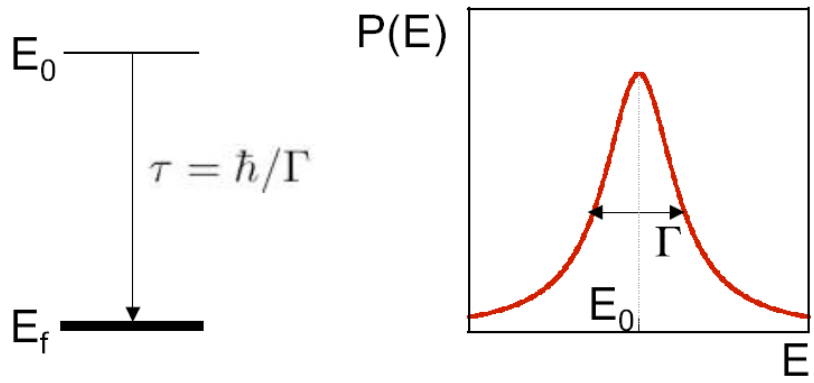

Figure 2.3: The Breit-Wigner shape of the energy profile (right) of a quantum state with a finite life time τ (left)

In the limiting case of a single, isolated resonance with orbital momentum $\ell = 0$ at low energy E_0 and with capture, fission and elastic scattering as the only open channels, the total cross section can be expressed in the single level Breit-Wigner formula as:

$$\sigma_T(E) = 4\pi R'^2 + \pi\lambda^2 g \left(\frac{4\Gamma_n(E - E_0)R'/\lambda + \Gamma_n^2 + \Gamma_n\Gamma_\gamma + \Gamma_n\Gamma_f}{(E - E_0)^2 + (\Gamma_n + \Gamma_\gamma + \Gamma_f)^2/4} \right) \tag{2.4}$$

where Γ_n is the neutron width, Γ_γ the radiative width, Γ_f the fission width, g the statistical spin factor and λ the reduced de Broglie wave length of the neutron. The first term in the sum is the potential scattering cross section $\sigma_p = 4\pi R'^2$, where R' is the effective nuclear radius, with a value close to the channel radius a_c and is defined as:

$$a_c = a_0 A^{1/3} \tag{2.5}$$

a_0 is approximately 1.4 and $A = A_{particle\ 1} + A_{particle\ 2}$ is the total number of nucleons.

The boundary a_c is the limit between the internal region, where there is an unknown potential and the wave functions can not be found by solving the Schrödinger equation, and the external region, where the potential is known (zero or Coulomb) and the wave functions can be calculated. Although there is no sharp limit, in practice the channel radius a_c can be taken just slightly larger than the nucleus radius.

At the high excitation energies above the neutron binding energies, for most nuclei the nuclear system is extremely complex and no nuclear model is

capable of predicting the position and other properties of these excited states [36]. Cross sections can therefore be accessed only by measurements. For a heavy nucleus the wave function describing such a highly excited state may have as much as 10^6 components. Also the level density in this region is consequently very high. A neighboring eigenstate can be excited by only a small change in excitation energy and may have a completely different wave function. This is a manifestation of what is also called chaotic behavior. Due to extreme configuration mixing, the nucleus in this regime above the neutron threshold has a statistical behavior. This is expressed by the assumption that the matrix elements relating nuclear states have a random character, governed by a Gaussian distribution with zero mean. This statistical model of the compound nucleus is referred to as the Gaussian Orthogonal Ensemble (GOE) [37, 38, 39, 40, 41].

The statistical model has direct consequences on the observables of the reaction cross sections. The channel widths are proportional to the square of the matrix elements and have therefore a χ^2 distribution with one degree of freedom, also called the Porter-Thomas distribution [42]. The observed gamma width of a resonance is the sum of many several tens of thousand individual gamma widths for medium and heavy nuclei and tends therefore more to a Gaussian distribution. Observed fission widths correspond to a relatively small number of fission channels, at maximum three or four. The resulting distribution can be approximated by an effective chi-squared distribution with a small, fractional number of degrees of freedom [43].

2.3 Non-resonant behavior of the neutron interactions

With increasing excitation energy the widths of the states start to overlap and the resulting cross sections become smooth. The properties of the eigenstates, like the decay widths, fluctuating from one state to another, become apparent as values averaged over many resonances. These average values on the contrary can be predicted by nuclear models, parametrized with average properties. Measured average cross sections can therefore fine tune the parametrization of these models.

At even higher excitation energies, many more decay channels open up and cross section measurements become very difficult or impossible. Reaction cross sections may therefore only be accessible by nuclear model calculations.

2.4 Neutron energy distributions

As an example, in Figure 2.4 the neutron capture cross section of ^{238}U is shown on an energy scale spanning more than ten decades. The resonance structures, given by resonance parameters, are clearly visible in the low energy part while the smooth cross section at higher energies is parametrized in the libraries by interpolation tables. The sudden transition between these two regimes is therefore not physical but related to these different descriptions.

In order to appreciate the importance of the cross sections at different energies, typical energy distributions of neutron fluxes are also shown in the Figure 2.4. The energy region around a few tens of meV is called the thermal region and is of importance in reactor physics where the water moderated neutrons are in thermal equilibrium with the water and have Maxwell-Boltzmann distributed velocities peaked at an equivalent kinetic energy k_BT. For a temperature of nearly 300 K this corresponds to 25.3 meV or a velocity of 2200 m/s. The thermal cross section at 25.3 meV is an important quantity and can be measured accurately with only small amounts of material in reactor experiments.

A different energy distribution is found for neutrons in certain stars and responsible for the synthesis of the isotopes heavier than A = 60 in the universe. The neutrons are present as a hot gas and also have a Maxwellian kinetic energy distribution but now at temperatures with k_BT ranging from 5 to 100 keV.

Several distribution functions describe in a satisfactory way the kinetic energy distribution of neutrons from the nuclear fission process. The neutrons from ^{235}U thermal neutron induced fission follow well a Maxwellian kinetic energy distribution, peaked at about 1 MeV. This distribution is also shown in Figure 2.4 (fission spectrum).

Neutron induced reaction data are of great importance for nuclear reactor physics. In several other fields, including astrophysics and fundamental symmetries, neutron induced reactions play also an important role. Some items will be discussed in the following sections. In addition, important information on level densities, a key ingredient in many nuclear reaction codes, can be obtained directly from neutron resonance spectroscopy [44]. Many of the experimental data have been compiled [45, 46, 47] and once evaluated, made available through nuclear data libraries like Standard Nuclear Data Files for Russia (BROND) [48], ENDF/B-VII.1 [21], Joint Evaluated Fission and Fusion File (JEFF) [49], Japanese Evaluated Nuclear Data Library (JENDL) [50] and Chinese Evaluated Nuclear Data Library (CENDL) [51].

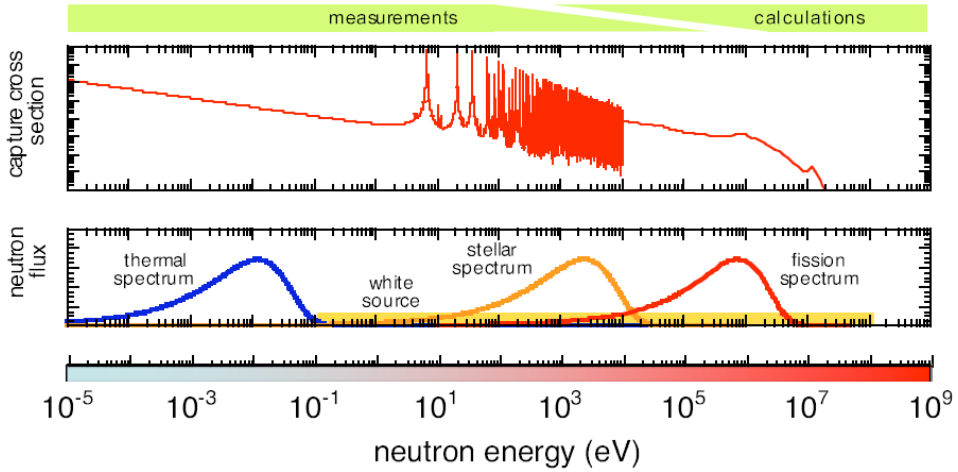

Figure 2.4: The neutron capture cross section of ^{238}U together with several different neutron source energy distributions in a wide energy range [36].

2.5 Nuclear cross sections and reaction rates

The microscopic physical quantity used in determining the nuclear reaction rate and therefore, the interaction of a neutron with a specific nucleus is the cross section. Moreover, the total cross section is the sum of all the reactions (partial cross sections) allowed between the incoming neutron and target nucleus.

$$\sigma_{total} = \sigma_{capture} + \sigma_{fission} + \sigma_{scattering} + ... \tag{2.6}$$

This concept can actually be easily understood from the experimental point of view. Considering a beam of neutrons with intensity I(neutrons/cm^2/s) incident on a very thin plate of a given isotope with area A(cm^2), density of nuclei N(nuclei/cm^3) and thickness Δ_x(cm). In this case, the collision reaction rate R(reactions/s) must be proportional to the intensity of the neutron beam (I) and the number of target nuclei ($N*\Delta_x*A$), with proportionality constant:

$$R = \sigma * I * (N * \Delta_x * A) \tag{2.7}$$

This constant (σ) has the dimension of an area (cm^2) and if neutrons were classical point particles and nuclei were solid spheres, σ would simply be the cross-sectional area of each nucleus.

2.5.1 Typical cross section behavior vs energy

The partial cross sections are very different depending on the specific reaction and the energy of the incident neutron. Furthermore, neutron cross sections are completely different from one isotope to another because they are related to the nuclear structure of the nucleus under neutron bombardment.

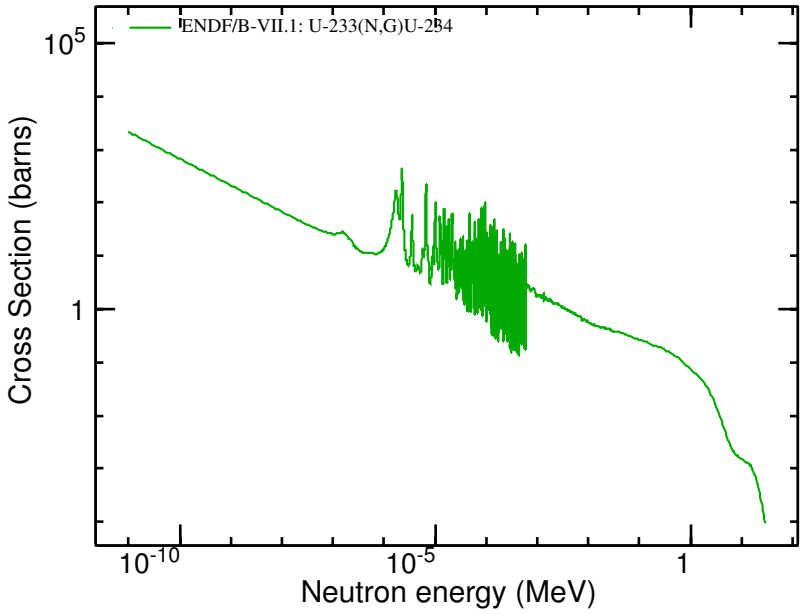

Figure 2.5: Neutron capture cross section for the ^{233}U

Figure 2.5 shows the neutron capture (n,γ) cross section of ^{233}U on an energy scale spanning more than ten decades. At first sight it is observed that there is a very wide range of five orders of magnitude between the smallest and largest cross section values.

The examination of the Figure 2.5 allows distinguishing two well differentiated energy regions attending to the shape of the neutron cross sections:

- Resolved Resonance Region (RRR) which includes the thermal and epithermal regions, located between 0.025 eV (thermal point) and the first resonant structure in the eV region. The cross sections are found to be smooth and inversely proportional to the square root of the energy ($\sigma \sim 1/ E^{1/2} \sim 1/v$), that is proportional to the time that the incident neutrons spend in the vicinity of the target nucleus. Between a few eV and several keV, depending on the specific isotope, the cross sections show

well resolved resonances with large peak to valley variations. The nature of these resonant structures is related to the existence of quasi-stationary levels of the Compound Nucleus (n + ^{A}Z −> $^{A+1}$Z*).

- Unresolved Resonance Region (URR). With increasing excitation energy the resonances start to overlap, because their intrinsic widths become comparable to the distance between neighboring resonances. At higher energies, the distance between resonances is much smaller than their intrinsic widths and resonant structures can not be observed any more. In addition, more and more reaction channels corresponding to threshold reactions open up.

The point wise cross sections displayed in Figure 2.5 correspond to the ENDF/B-VII.1 evaluated data library [21] for ^{233}U neutron capture.

Usually, the cross sections are provided in a point-wise basis but can also be parameterized in the appropriate theoretical formalisms (R-matrix) as is the case with the ENDF/B-VII.1 in the RRR. For instance, the resonant structures are usually described using the R-matrix formalism in which the shape of each resonance is given by its energy and spin as well as several widths Γ_i related to each open reaction channel and corresponding particular cross section.

In this way a large number of data points is reduced to just a few parameters for each resonance and also to plot the cross section at various temperatures.

The 1/v region comes from the tails of all resonances and is always present. Furthermore, to match the thermal value one or more resonances with negative energies can be used. The R-matrix formalism can be further extended to the URR which can be represented as a large number of overlapping resonances described by a reduced set of average resonance parameters.

As the energy increases, the cross sections are described using complex models, such as the Optical Potential, based on nuclear structure theory and the information from the cross sections at lower energies.

2.6 R-matrix formalism

The large peaks correspond to excitations of eigenstates in the compound nucleus. In order to describe the cross sections in a satisfactory way, the R-matrix formalism is the most accurate way.

The R-matrix theory has been first introduced by Wigner and Eisenbud [52]. A most extensive and detailed overview has been given by Lane and Thomas [53] and by Lynn [37]. More recently Fröhner [54] summarized the R-matrix formalism together with other useful considerations on nuclear data evaluation. Other related references of interest can be found elsewhere [55, 56,

57, 58, 59, 60, 61, 62, 63]. In the following only a brief outline of the formalism is given in order to understand the principle without giving the full details.

If the wave functions of the nuclear system before and after the reaction were known, one could calculate the cross section with the usual concepts of reaction theory. Where the incoming waves are known, the reaction modifies the outgoing wave functions in a generally unknown way. The idea behind the R-matrix formalism is to use the wave function of the nuclear system of two particles when they are so close that they form a compound nucleus.

Although the wave function of the compound nucleus is extremely complicated, one can expand it in its eigenstates. Matching then the incoming and outgoing waves to the internal wave function provides a way to describe the cross section of the reaction in terms of the properties of the eigenstates of the compound nucleus. These properties are basically the energy, spin, parity, and a set of partial widths related to the widths of the decay modes of the compound nucleus.

This method of describing a reaction cross section using only the properties of nuclear excitation levels, is at the same time also the most important limitation. No information of the forces inside the nucleus are needed or can be extracted.

The nucleus is treated as a black box of which the properties of the eigenstates have to be measured in order to describe the cross sections. The binary nuclear reactions proceeding from one system of two particles to another system of two particles can be described with the general R-matrix theory. For neutron induced reactions, but also in other cases, such a reaction goes often through the formation of a compound nucleus X^*.

$$A + a \rightarrow X^* \rightarrow B + b \tag{2.8}$$

The R-matrix formalism does not only apply to compound nucleus reactions. Both direct and indirect reactions can be described with it. The inclusion of the Coulomb interaction allows to use it also for charged particle reactions. But the theory is applicable only in a general way for binary reactions which is appropriate for neutron induced reactions up to energies of several tens of MeV.

In a very general way, the cross section of a two-body nuclear reaction could be calculated if the nuclear wave functions were known. The wave functions could be calculated by solving the Schrödinger equation for the nuclear system. This requires that the nuclear potential is known. When the two particles are far away, the interaction can be considered absent for neutral particles or to be the Coulomb interaction for charged particles. In these cases it is indeed possible to calculate the wave functions. When the two particles are so close

to each other that a nuclear reaction takes place, the potential of the interaction is extremely complicated. For certain energy ranges and reactions this potential can still be approximated or calculated [64] and the wave functions and cross sections can be calculated. In other cases however, and especially in the resolved resonance region, the complexity of the reacting system does not allow this.

The first step is to consider that the reaction process can be split up geometrically into two regions for each channel where a channel is the precise constellation of particles and their spins. The channel radius value has to be chosen in such a way that outside the channel radius, the potential is well known and nuclear forces have no longer action.

If the separation is smaller than the channel radius a_c, all nucleons involved in the reaction are close to each other and form a compound nucleus. Although the wave function of the compound nucleus is extremely complicated, it can be expanded as a linear combination of its eigenstates without solving explicitly the Schrödinger equation of the system.

In the external region, at distances larger than a_c, the potential is zero for neutral particles or is the Coulomb interaction for charged particles and the Schrödinger equation of the system can be solved. The properties of the eigenstates of the compound nucleus are taken together in the R-matrix. Equating the values and derivatives of the wave functions at the boundary of the internal and external region assures a smooth wave function and the cross sections can be calculated. The exact internal wave function is not needed, only the values and derivatives at the nuclear surface.

Chapter 3

Status of the ^{233}U nuclear data available

To understand the reason why the available capture cross sections on ^{233}U, ^{237}Np, ^{240,242}Pu, ^{241,243}Am and ^{245}Cm are not sufficient for the optimization of a transmutation device and for Generation IV of nuclear reactors, one has to consider the two steps previous to the release of the corresponding evaluated files:

- First, the available data sets for ^{233}U, ^{237}Np, ^{240,242}Pu, ^{241,243}Am and ^{245}Cm are not accurate enough, are incompatible in some cases, do not cover the necessary neutron energy range and the resolution provided is not sufficient.
- Second, the available evaluated cross section files do not agree between themselves either. More often than it would be desirable, the evaluators are forced to question and re-investigate the accuracy of specific data sets in order to reach a self-consistent result in their evaluation for all the reaction channels.

Thus, the result on the evaluation depends strongly on the decisions adopted by the evaluator. More accurate measurements are necessary in order to constrain the parameters (such as level densities or optical potential parameters) of the physics models applied.

In the particular case of the work described here, which is dedicated to the ^{233}U(n,γ) cross section data, an in depth description of the actual status of the neutron capture cross section will be made in this chapter.

The focus of the discussion will be on the capture and fission cross section around the Resolved Resonance Region (RRR) and the Unresolved Resonance Region (URR) of ^{233}U (Figure 3.1). The RRR is the energy region where the resonances in cross-section can be separately recognized while the URR is the region where the resonances in cross-section can no longer be individually

resolved either due to the resonance overlapping (resonance width comparable with the space between resonances) or due to experimental limitations.

In the following discussion, the cross section data and information included in the ENDF/B-VII.1 library [21] will be taken as reference. Notice that the ENDF/B-VII.1 library is based on many of the same experimental data sets as other standard libraries differing sometimes only in the evaluation done. Taking this in consideration we can now look at the latest changes and improvements done to the ^{233}U capture and fission cross sections.

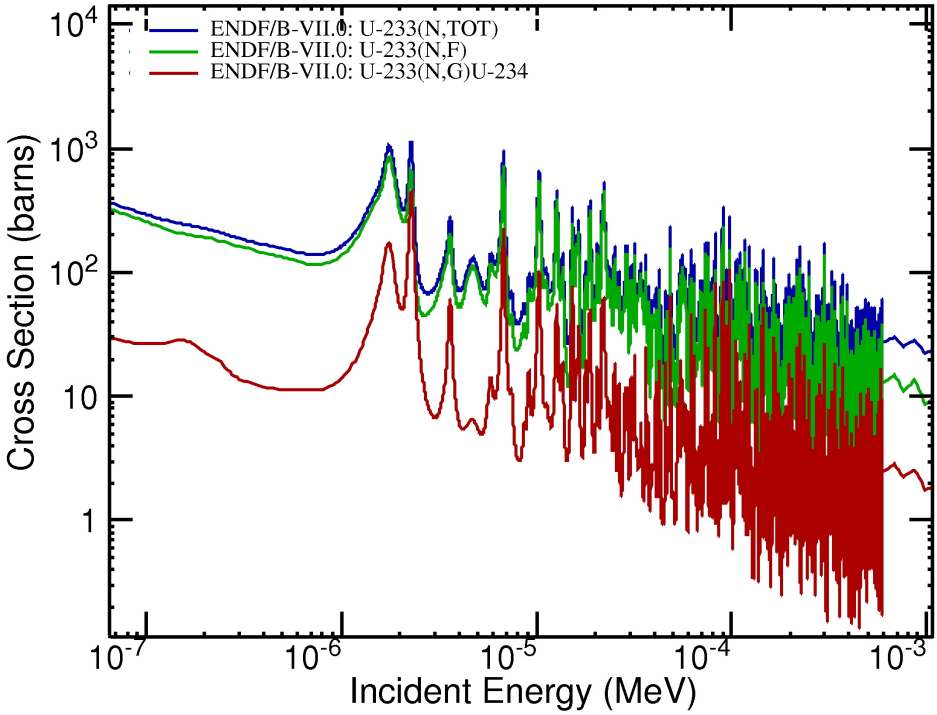

Figure 3.1: ENDF/B-VII.1 evaluation of the total, fission and capture cross section for ^{233}U

3.1 Cross Sections

In the sequence, the discussion of the cross section evaluation in the RRR and URR will be performed separately.

3.1.1 Resolved Resonance Region (RRR)

The data used to obtain the ENDF/B-VII.1 evaluation for the ^{233}U came from the measurements listed in Table 3.1 where it is possible to see that the only measurements dedicated to capture are the ones done by Weston et al. in 1968 [65]. In the evaluation [66], twelve measurements were included but the ones considered more relevant and used as primary data by the evaluators were the ones done at the Oak Ridge Electron Linear Accelerator Pulsed Neutron Source (ORELA) [67] by Guber et al. [68] due to better resolution and broader energy range covered. This measurements were done only for the transmission and fission and therefore the capture cross section was deduced using the transmission and fission data.

With the use of the Guber et al. data together with the other data sets, the ^{233}U RRR was extended from 1 to 600 eV while the unresolved resonance region covers the energy range from 600 eV to 40 keV (Figure 3.1).

The present cross section evaluation in the resolved resonance region goes up to 600 eV. This limitation has either to do with TOF measurements suffering from poor energy resolution or due to a strong overlapping of resonances which make the resonance analysis almost impossible to perform. The flight-path used in the Guber et al. measurement was 80 m and to achieve better resolution, the sample was cooled down to 11 K leading to resonances widths being reduced by a factor two comparing to room temperature measurements.

3.1.1.1 Fission cross section in the RRR

The fission cross section for ^{233}U has been measured widely in several different laboratories. One common feature in these measurements is the measurement being done as a ratio to the ^{235}U fission cross section or normalized to other measurements. Notwithstanding all the measurements done, the uncertainties and discrepancies are still bigger than what is needed for the feasibility study and design of nuclear systems based on the Th-U cycle which is a major point of interest of this cross section.

Data with uncertainties around 1% [2] are needed as also an increase in the resolved energy range which stops at 600 eV.

New fission data measured at n_TOF [75] that took advantage of the high instantaneous neutron flux in a very wide neutron energy spectrum and of the excellent energy resolution of the neutron beam, which is particularly suited for measurements on radioactive isotopes, allowed to refine the resonance analysis up to 1 keV.

For the first time, the whole energy range from thermal to 1 MeV is covered in a single measurement, thus minimizing possible systematic uncertainties

Table 3.1: Selected measurements for the ^{233}U evaluation [66]

Author	Energy Region Analyzed (eV)	Main Features
Moore et al., 1960 [69]	0.020 - 15.0	Transmission: chopper, TOF 15.7 m Sample 0.0037 and 0.0213 at/b
Pattenden and Harvey, 1963 [70]	0.080 - 15.0	Transmission: chopper, TOF 45 m Sample 0.00057, 0.00308, 0.01219 at/b
Weston et al., 1968 [65]	1.0 - 600.0	Simultaneous measurements of capture and fission, Linac TOF 25.2 m
Weston et al., 1968 [65]	0.020 - 1.0	Simultaneous measurements of capture and fission, Linac TOF 25.6 m
Blons, 1973 [71]	4.0 - 600	Fission, Linac, TOF 50.1 m, Sample at Liquid Nitrogen Temperature
Deruyter and Wagemans, 1974 [72]	0.020 - 15.0	Fission, Linac, TOF 8.1 m
Harvey et al., 1979 [73]	0.020 - 1.2	Transmission, Linac, TOF 17.9 m Sample 0.00605 and 0.0031 at/b
Wagemans et al., 1988 [74]	0.002 - 1.0	Fission, Linac, TOF 8.1 m
Guber et al., 1998 [68]	1.0 - 80.0	Transmission, Linac, TOF 80 m Cd filter, Sample Temperature 11K Sample thickness 0.00298 at/b
Guber et al., 1998 [68]	7.0 - 600.0	Transmission, Linac, TOF 80 m Cd filter, Sample Temperature 11K Sample thickness 0.0119 at/b
Guber et al., 1998 [68]	1.0 - 80.0	Fission, Linac, TOF 80m Cd filter
Guber et al., 1998 [68]	7.0 - 600	Fission, Linac, TOF 80 m ^{10}B filter

related, for example, to the absolute normalization of the cross section. The results can be seen in Figure 3.2 and Figure 3.3.

It is important to stress that more accurate resonance data help to improve predictions of the Doppler reactivity coefficient of advanced reactor systems that use ^{233}U as fuel [76].

The data taken in n_TOF takes advantage of the very long flight-path of 185 m and has been measured using Fission Ionization Chamber (FIC), [77], specifically built for fission cross section measurements of radioactive U isotopes and other actinides at n_TOF. The detector consists of a stack of ionization chambers, assembled along the direction of the neutron beam, thus allowing the simultaneous measurement on several isotopes. In the measurement, four ^{233}U and two ^{235}U samples were used.

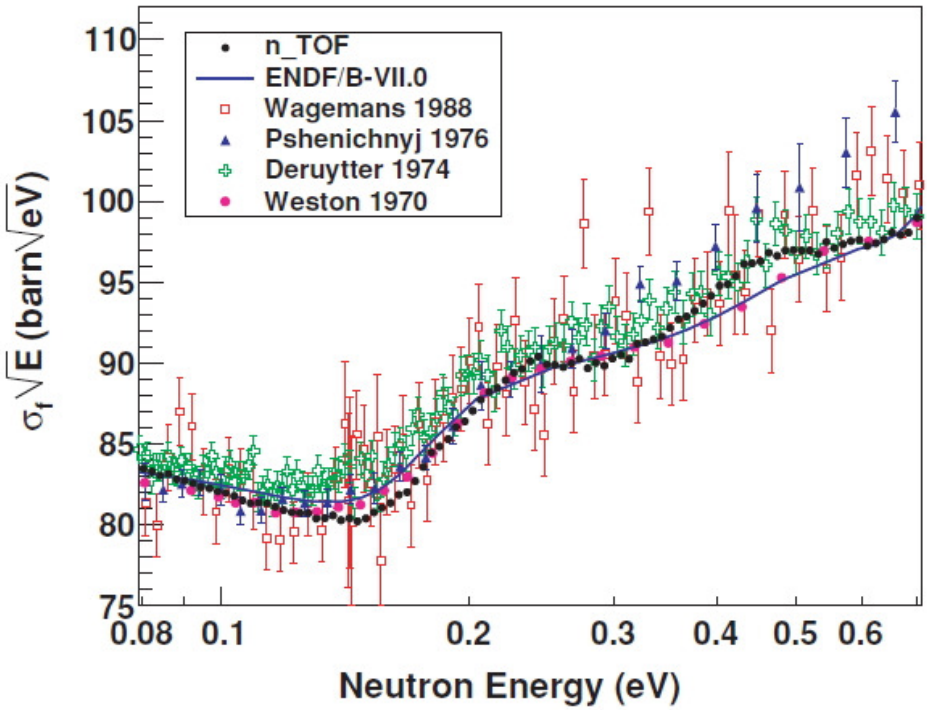

Figure 3.2: ^{233}U(n,f) cross section measured with FIC chambers at n_TOF compared with other data sets below resolved resonance region [75].

The ^{233}U fission cross section is normalized to the ^{235}U fission cross section also measured at the same time in equal experimental conditions. It is important to stress that the data are not normalized to any previous result, but rely only on the standard ^{235}U(n,f) cross section.

In Figure 3.2 two resonances at 0.25 and 0.45 eV are visible in the n_TOF data thanks to the better resolution and uncertainties while in Figure 3.3 one can see the resolved resonance range extended relative to the ENDF/B-VII.1

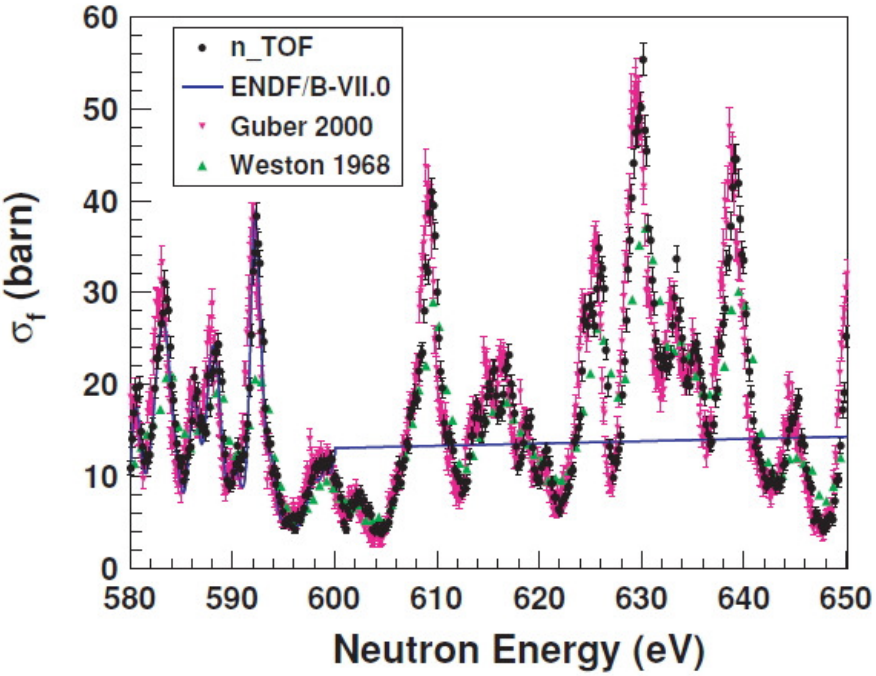

Figure 3.3: ^{233}U(n,f) cross section measured with FIC chambers at n_TOF compared with other data sets in the resolved resonance region [75].

library.

Also from n_TOF there are data taken from a simultaneous measurement of the neutron capture and fission yields (Figure 3.4) [78].

3.1.1.2 Capture cross section in the RRR

The data used in the evaluation for the neutron capture in ^{233}U comes from the measurement performed by Guber et al. mainly, although a preliminary data set from capture and fission simultaneous measurement from n_TOF facility at CERN [78] exist in the Experimental Nuclear Reaction Data (EXFOR) data base [79] with the entry numbers 23071004 and 23071002 respectively.

Up to now only two other measurements are available for the neutron capture in ^{233}U in the resonance region. The first one performed by Brooks et al. [80] up to 10 eV with a poor energy resolution. Another measurement has been performed by Weston et al. [65] up to 1 keV using the fission veto technique. A similar fission technique is being developed at Los Alamos Neutron Science Center (LANSCE) using Detector for Advanced Neutron Capture Experiments (DANCE) [81, 82, 83] but no data on ^{233}U has been reported so

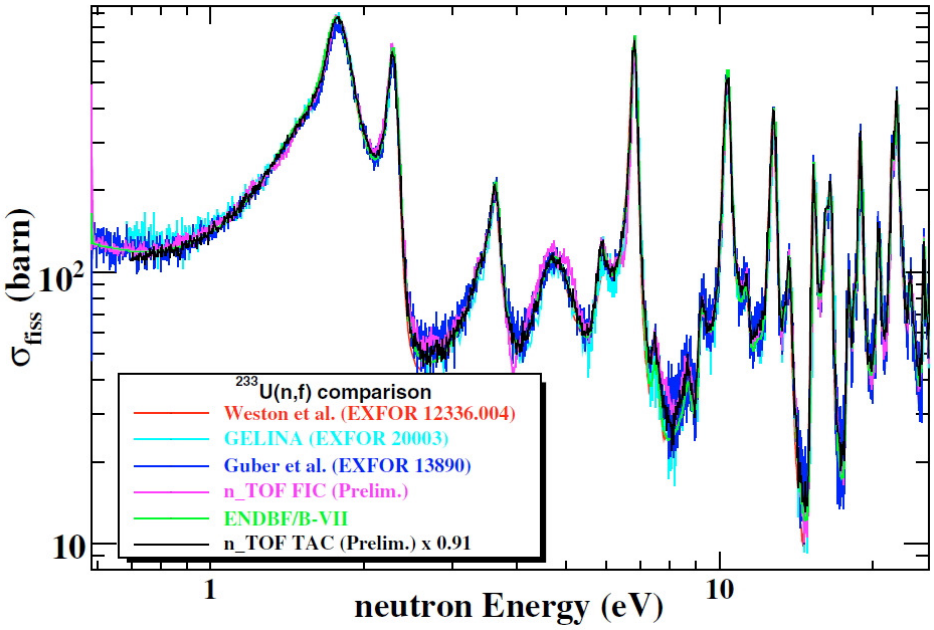

Figure 3.4: ^{233}U(n,f) measured with the TAC compared with several data sets [78].

far. Recently, a new measurement of the ^{233}U capture cross section has been planed at the neutron time-of-flight facility GELINA [84, 85] at Geel, but no results have been reported yet [86].

The preliminary data for the neutron capture and neutron induced fission simultaneous measurement from n_TOF, released to the EXFOR data base suffer from some experimental effects that were not correctly treated at that time and was not used in the latest evaluation of the JENDL4.0 [50].

This work reports on the evolution of the data analysis that led to data with improved accuracy and in an extended energy range.

The measurement done at n_TOF have better energy resolution, wider energy range and both capture and fission cross sections are measured simultaneously. The fission cross section which is better known, can be used in the resonance parameter analysis together with other ^{233}U (n,f) measurements done at n_TOF [75], allowing therefore to minimize systematic uncertainties by making a combined analysis of several data sets.

Looking at Figure 3.5, a resonance can be seen in the Weston data around 10.1 eV, but not in n_TOF data neither reported in the evaluation. The origin of this resonance is not clear and can be related with a contamination of the sample. n_TOF resonances also shows a deeper fall-off on the low energy side

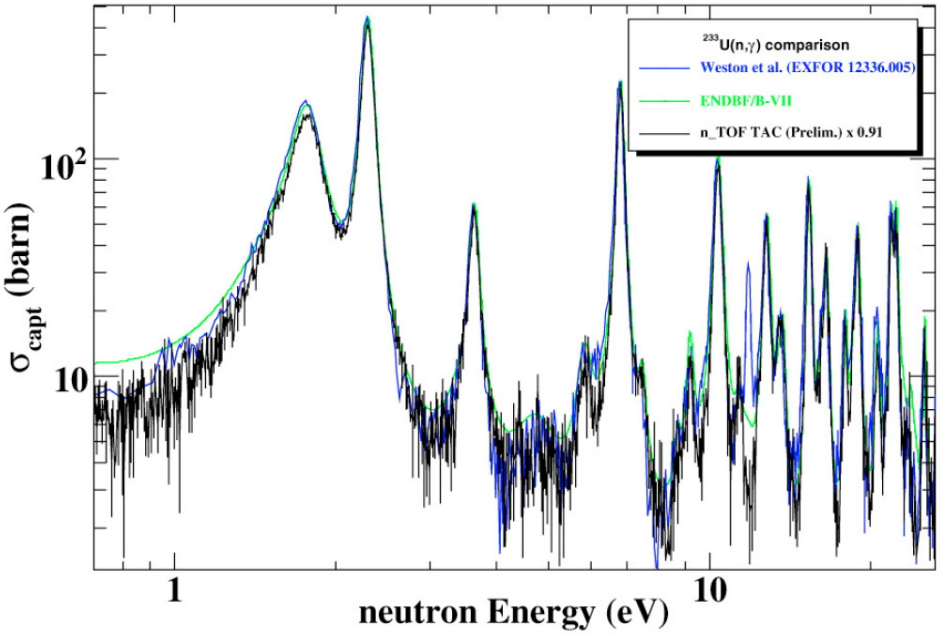

Figure 3.5: ^{233}U(n,γ) measured with the TAC compared with several data sets [78]

that could be attributed to the better energy resolution of the n_TOF facility compared to the Rensselaer Polytechnic Institute (RPI) facility.

3.1.2 Unresolved Resonance Region (URR)

The evaluation performed for the ENDF/B-VII.1 library in URR covers the energy range from 600 eV to 40 keV. In this energy range, the evaluation included high resolution transmission data [87] and fission cross section data [68] measured at ORELA.

3.1.2.1 Fission cross section in the URR

The new results obtained in n_TOF [75] using FIC show that above 1 keV the evaluated cross section is lower by as much as 12% in certain energy ranges (Figure 3.6). This finding is confirmed by another measurement performed at n_TOF with a different experimental setup [88] and is in agreement with recent data from Guber et al. 2000 [68]. All these observations point out to a problem even in the most recent evaluations, which can most probably be attributed to the normalization procedure adopted to reproduce the results of integral measurements. A comparison between different libraries is shown in

Figure 3.7. Important to note that evaluation for the ^{233}U(n,f) cross section present in the library ENDF/B-VII.1 is the same as in the previous .0 version.

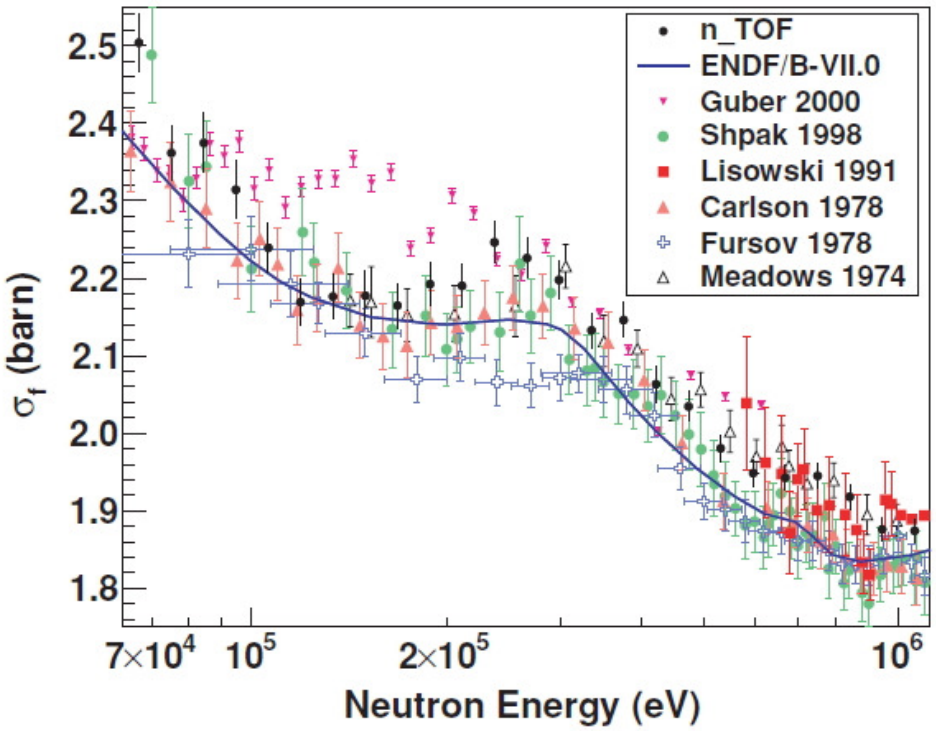

Figure 3.6: ^{233}U(n,f) cross section measured with FIC chambers at n_TOF compared with other data sets in the unresolved resonance region [75].

In the present evaluation, all ^{233}U(n,f) ratio and cross section data were converted to ENDF/B-VII.1 standards [89], and a covariance analysis of the data was performed. The results were smoothed and used for the (n,f) cross section, after small modifications. The somewhat higher ^{235}U fission cross section in the fast spectrum region produces better agreement with fast critical benchmark experiments.

On the basis of these new experimental results, a revision of the evaluations at least in the energy region between 100 eV and 10 keV seems mandatory.

3.1.2.2 Capture cross section in the URR

No measurement prior to the one done in n_TOF [78] was performed in the URR energy range (above 600 eV) for the ^{233}U capture cross section. Between 40 keV and 30 MeV:

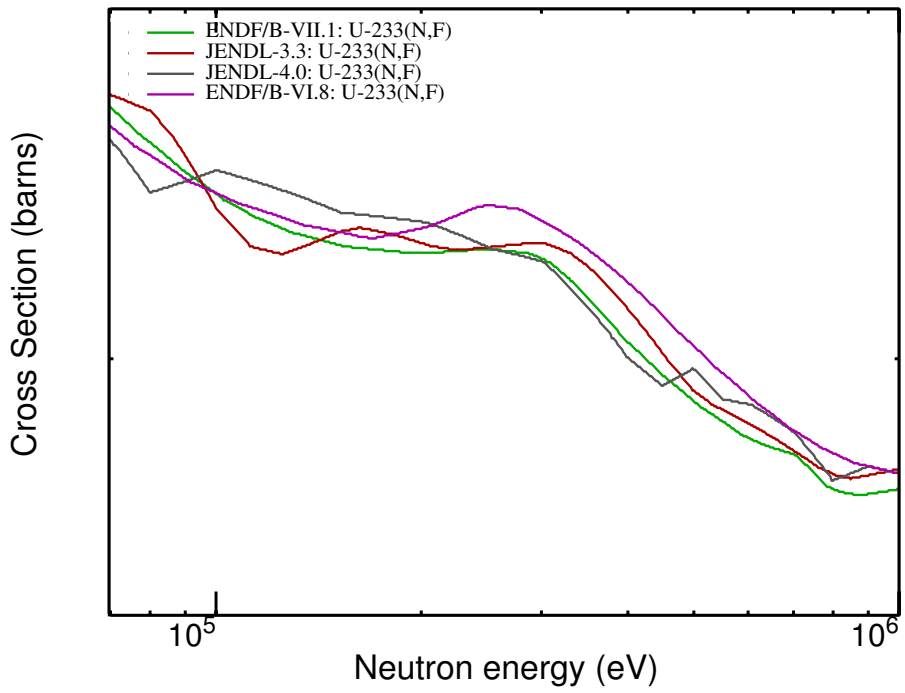

Figure 3.7: ^{233}U(n,f) cross section comparison between different libraries in the keV region.

- The Nuclear Reaction Code McGNASH (GANSH) code system [90] was utilized to calculate the (n,γ) cross section from 1 keV to 16 MeV.
- The γ-ray strength function and level densities were adjusted so that the calculation reproduced the experimental data of Hopkins and Diven [91].
- The results were used from 0.04 to 16 MeV for the (n,γ) cross section, with a smooth extrapolation to 30 MeV.

The measurement done simultaneously for the ^{233}U neutron capture and fission cross section at the n_TOF facility is the only data available in this energy range for capture cross section.

3.2 Cross section summary

The evaluated total, fission, and capture cross sections present in the ENDF/B-VII.1 library are based all or in part on experimental data. The data sets used

for the evaluation come mainly from the EXFOR data base. The evaluation includes high resolution transmission data, fission cross section data measured at the ORELA in addition to other experimental data.

Much of the ^{233}U fission cross section data was taken in the form of ratios relative to ^{235}U which is a standard. To benchmark the ^{233}U fission cross section data, all ^{233}U(n,f) ratios and cross section data were converted to ENDF/B-VII.1 standards [89] and a covariance analysis of the data was performed. The results were smoothed and used for the (n,f) cross section, after small modifications.

Important to note that in order to achieve better agreement with fast critical benchmark experiments the ^{235}U fission cross section (present in the evaluated nuclear data libraries) in the fission spectrum region was increased.

This artificial increase in the ^{235}U fission cross which is later used as a standard in the ^{233}U measurement can be a source of systematic errors.

The evaluated data now present in the ENDF/B-VII.1 library both in the resolved and unresolved resonance region must be improved with measurements that are independent of other cross sections. The measurements done with high resolution n_TOF using the FIC detector have shown improvements in the uncertainties. Also this measurements have extended the resolved resonance region in the fission cross section.

The capture cross section for the ^{233}U is the less measured due to all experimental difficulties and also where bigger improvements are needed. New preliminary data [78] show the possibility of extending the resolved resonance region and also offer for the first time information in the unresolved resonance region above 1 keV. Moreover, the type of measurement where a high flux, high resolution, broad neutron spectrum source is used, decreases the uncertainties and discrepancies between neutron energy regions and due to the samples activity.

These findings, lead to the motivation and justification of the present analysis, specially in the case of the ^{233}U capture cross section where no high quality data in a wide energy range is available or foreseen to be taken.

Chapter 4

The neutron time-of-flight (n_TOF) facility at CERN

The Time-Of-Flight (TOF) of CERN became operative during 2001 and is a unique spectrometer worldwide to perform cross-section measurements relevant to Nuclear Technology, Nuclear Astrophysics, fundamental Nuclear Physics and eventually other applications, featuring the following characteristics:

- Very high instantaneous flux of neutron per burst
- Low duty cycle,
- Excellent neutron energy resolution and
- Low background
- Fast electronics and Data Acquisition System (DAQ)

In the neutron Time-Of-Flight facility (n_TOF), neutrons in the wide range from thermal to approximately 1 GeV are generated via spallation reactions triggered by 20 GeV/c protons impinging on a lead spallation target. After traveling inside the beam tube, the neutron beam reaches the measuring station located 185 meters downstream the spallation target. The measuring station houses the samples made of materials which neutron induced cross-sections are measured and a set of detectors such as:

- Silicon detectors, to measure and monitor the neutron beam fluence.
- Micromegas detectors to determine the neutron beam spatial characteristics and fluence.
- Parallel Plate Avalanche Chambers (PPAC) and Fast Ionization Chambers FIC, to detect the fragments from fission reactions in the sample.
- Deuterated Benzene Liquid Scintillator (C6D6) detectors to measure neutron capture cross section in cases where the scattering to capture ratio is very high and detectors with low neutron sensibility are required.
- A 4π calorimeter consisting of 40 BaF_2 crystals to measure neutron cap-

ture cross section in non-radioactive and radioactive samples.

The energy of the neutrons incident on the samples is determined using the Time-Of-Flight (TOF) method.

This facility is used by a consortium of 40 laboratories in European countries, Russian Federation, Japan and U.S.A.

The aforementioned facility performance parameters and detectors are described in the sequence.

In this chapter a detailed description of the experimental setup and all the major components is performed.

4.1 Facility description

The setup is composed by the Proton Synchrotron (PS) facility, a spallation target, the TOF beam line, the experimental area where the detectors are placed and the data acquisition system.

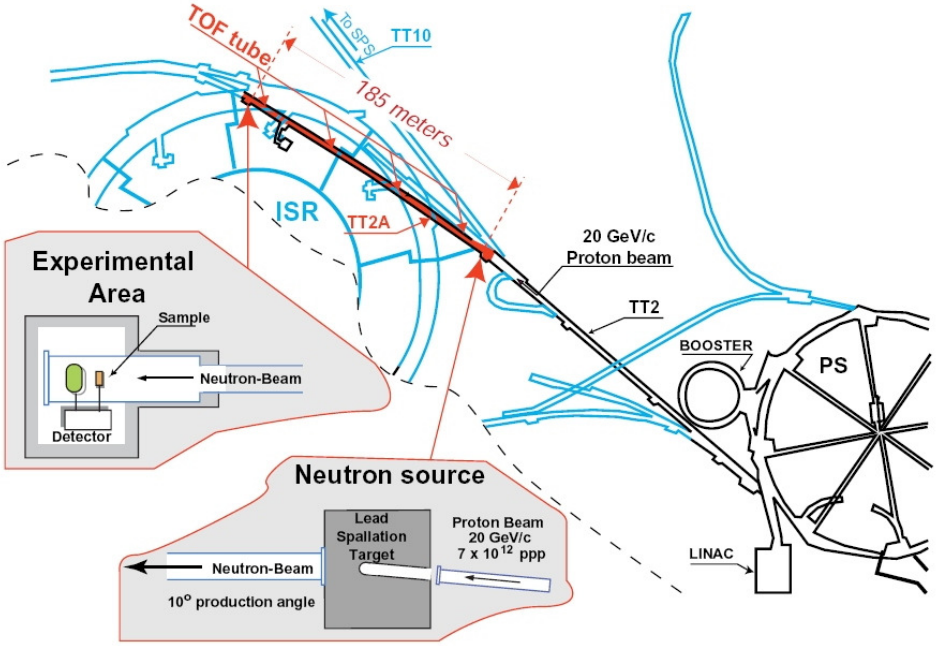

Figure 4.1: Layout of the n_TOF spectrometer including the Proton Synchrotron, position of the neutron source (lead target) and experimental area [92].

The PS facility delivers a pulsed proton beam which interacts via spallation reactions with a lead target to create a pulsed neutron source capable of de-

livering high instantaneous fluxes. The lead target is surrounded by water for both cooling and moderation purposes. The spallation mechanism is a powerful source of neutrons and lead has a high transparency for neutrons bellow 1 MeV. The produced neutron beam follows by a 185 m neutron flight path to reach the measuring station where the detection system is installed, namely a Total Absorption Calorimeter (TAC) composed by 40 BaF_2 crystals together with other detection systems. The combination of a long flight path which allow us to have a very good neutron energy resolution together with high count rate due to the intense neutron source, makes possible to measure cross section of low mass radioactive samples. The large enough solid angle and granularity characteristic of the TAC allow to detect and identify the nuclear reactions taking place in the sample. The overall arrangement of the facility can be seen in Figure 4.1.

4.1.1 The proton beam

The pulsed neutron source essential to the measurement of the cross sections is powered by the protons accelerated in the PS facility. The proton beam is primarily accelerated in a Linear Accelerator (LINAC) and afterwards in a booster witch allows to reach higher energies. Finally the proton beam is injected in the synchrotron to achieve a maximum momentum of 20 GeV/c. The beam is then extracted to the TT2 proton extraction line (Figure 4.1) that delivers the beam to the n_TOF spallation target.

To achieve a high neutron energy resolution demanded by the experimental needs, the proton beam is compressed in figure before interacting with the spallation target. The compression yields a proton bunch with a width of 7 ns RMS.

When the PS operates in dedicated mode to the n_TOF spectrometer, the proton beam is characterized by a momentum of 20 GeV/c in a bunch of 7 x 10^{12} protons with a 7 ns pulse width. The pulses are delivered with a minimum interval of 1.2 s. The PS capabilities for delivering proton bunches are only limited by its power consumption (5 MW) while the n_TOF spallation target is limited by the cooling system capabilities. To avoid exceeding the nominal maximum power dissipated in the spallation target, the number of bunches per super-cycle is reduced to 5.

The PS facility also delivers less intense beams with a a typical fluence of 4 x 10^{12} protons that correspond to a parasitic mode. The remaining characteristics rest unchanged although the timing performance is inferior. The reasons for the second type of proton bunches has to do with the demands of sharing the proton beams with other experimental facilities needing different beam characteristics and also with the optimization of proton beam use.

4.1.2 The spallation target

The n_TOF target system (Figure 4.2) was designed with an 80x80x60 cm^3 spallation core made of lead. The target core is surrounded by water that serves both for cooling and neutron moderation purposes.

The design of the spallation target system followed closely the experimental demands which include a neutron spectrum with high fluences in a broad energy range. To achieve this, the lead target is impinged by a pulsed proton beam that gives rise to neutrons via spallation reactions. The spallation reactions generate a neutron spectrum with maximum energy of ∼20 GeV. To better populate the neutron energy spectrum in the energy region bellow 1 MeV, the spallation target system has a moderation layer of water with 5 cm thickness between the lead core and the window connecting to the neutron tube.

Figure 4.2: Pool containing the spallation target and showing the start of the neutron beam pipe

The outcome is a broad energy neutron source with very high number of neutrons (2 x 10^{15}) per bunch outside the spallation target system.

Another experimental challenge is the low background levels. To avoid that the high energetic particles created together with the neutrons in the spallation

process reach the measuring station, a tilt of 10 degrees in the horizontal plane was introduced between the neutron tube and the proton beam line. The high energetic particles are generated mostly in the forward direction and therefore will follow a divergent direction in respect to the neutron tube. More details about background suppression are given in Section 4.1.4.

4.1.2.1 Spallation reactions

Spallation reactions are triggered when a high energy projectile (proton, neutron, or light nucleus) with kinetic energy from several hundreds of MeV to several GeV interacts with a heavy nucleus (in our particular case lead) and causes the production of a large number of hadrons and mesons or fragments.

As the projectile loses energy (∼100 MeV), all interactions occur just between nucleons and the process is called nucleon cascade [93].

With growing incident particle energy, the threshold energies for particle production in nucleon-nucleon collisions are being exceeded. Initially, pions come up (at energies of about hundreds of MeV), at higher energies (∼2 to 10 GeV) heavier hadrons and mesons are being produced. They can also participate in the intra-nuclear cascade and interact between each other, originating an hadron cascade [93]. Particles that obtain energy high enough to escape from the nucleus are being emitted mainly in the direction of the incident particle. The rest of the energy is equally distributed among nucleons in the nucleus which is left in a highly excited state.

Finally, the equilibrium stage comes up ($\sim 10^{-16}$ s). Energy is equally distributed throughout the nucleus that is in a highly excited state with small angular momentum. The nucleus loses its energy by evaporation of neutrons or light charged fragments (like d, t, α) with energies up to ∼40 MeV . The particles are emitted in a good approximation isotropically (angular distribution less forward peaked) in contrast to the spallation mechanism.

A competitive process to evaporation is fission. Fission products also undergo evaporation depending on their excitation energy.

4.1.2.2 The neutron energy spectrum

The neutron energy spectrum at the measuring station has a characteristic distribution due to the spallation and moderation processes as shown in Figure 4.3. In this distribution, there are three identifiable energy regions concerning the shape of the neutron fluence.

- At higher energy (∼MeV), the shape of the spectrum behaves as a typical neutron evaporation spectrum, having a maximum at ∼1.6 MeV due to evaporation and other at higher energies due to intra-nuclear cascade.

- In the region in between 1 eV and 10 keV it presents itself flat following an isolethargic distribution. This corresponds to the partially moderated neutrons.
- At energies below 0.1 eV one can see a peak corresponding to neutrons that have been fully thermalized

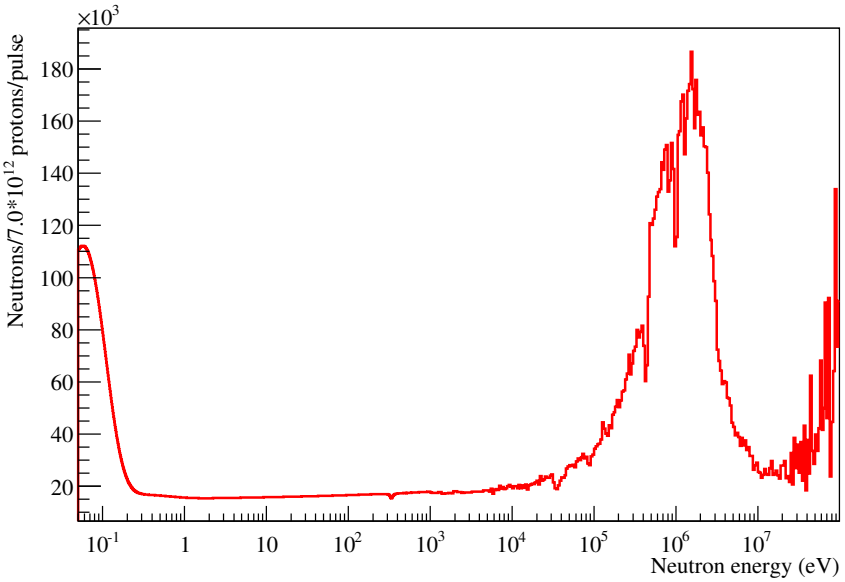

Figure 4.3: Neutron energy spectrum at the experimental area for the 2004 year

4.1.2.3 Neutron fluence

The fluence is the flux integrated over time. It can be defined as the total number of particles that intersect a unit area in a specific time interval of interest and has units of m^{-2}. In the particular case of n_TOF, the fluence is given by the neutron beam intensity integrated over the time of a neutron bunch.

The neutron fluence at the measuring station, $\phi_n(E_n)$, which dependents of the incident neutron energy (E_n), is given by the assessed neutron beam intensity for the experimental conditions used during the measuring campaign. The assessment was performed using two calibrated fission chambers from Physikalisch-Technische Bundesanstalt (PTB) [94] and other auxiliary detection systems such as a silicon detector associated with a ^{6}Li foil, C6D6 detectors [95] and Parallel Plate Avalanche Chambers (PPAC) [92].

The PTB detection system consisted of two identical parallel plate ionization chambers with deposits of ^{238}U and ^{235}U with 436 and 444 $\mu g/cm^2$ respectively. With such thin targets, it is possible to assume the thin target approximation and the measured counting rate $C_{(n,f)}(E_n)$ should be directly proportional to the incident neutron fluence $\phi_n(E_n)$ and to the fission cross section $\sigma_f(E_n)$ of ^{235}U, which is a standard in the range of interest. The neutron fluence can be calculated from the counting rate using the following relation where n is the sample thickness in atoms per barn:

$$\phi_n(E_n) = \frac{C_{(n,f)}(E_n)}{n \cdot \sigma_f(E_n)} \tag{4.1}$$

Important to note that the neutron fluence per pulse at the n_TOF facility is the largest among the time-of-flight facilities around the world and this feature is a great advantage when measuring radioactive samples because the signal to noise ratio is greatly favorable to the signal being the signal the neutron induced reactions and the noise respectively the sample's activity.

4.1.3 The neutron beam tube

In order to allow the propagation and energy separation of the neutrons exiting the source and reaching the sample without any interaction in between, a 185 m long evacuated neutron tube has been implemented. The neutron tube is equipped with two collimators, several tube diameter reductions, and a sweeping magnet. The several diameter reductions witch serve also as collimator are followed by barriers acting as beam stoppers to avoid that the neutrons traveling outside the beam pipe reach the experimental area [92]. The neutron beam line and components are shown in Figure 4.4.

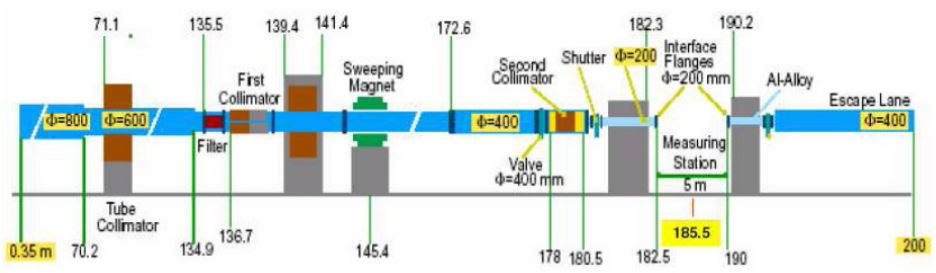

Figure 4.4: Neutron beam line after the target system. (All distances are given having the target system as the origin.)

The first section of the neutron beam line has a diameter of 80 cm and extends for 70 m. The second section with a diameter of 60 cm extends through

68,4 m and the third and last section with a diameter of 20 cm extends for 61,4 m passing through the sweeping magnet and reaching the second collimator witch reduces the beam pipe diameter to 1.8 or 8 cm depending if performing capture or fission measurements. The neutron beam enters the experimental area where the measurements are performed and interacts with the samples at approximately 185 m from the lead target just before continuing to the escape lane.

4.1.4 Shielding and background suppression

To avoid the propagation of neutron and other particles outside the neutron beam pipe and reduce the background due to neutron interactions in the measuring station, several shielding element were implemented. This shielding elements are located after each tube reduction and are made of 2 m of iron which moderates the very high energy neutrons. In addition, after each collimator, a shielding element composed of 3 m of concrete is placed and an additional shielding element was positioned after the sweeping magnet being composed of 3 m of iron to avoid the background due mostly to muons (not shown in Figure 4.4).

4.1.4.1 Collimation systems

To shape the neutron beam that reaches the experimental area, two collimators where implemented. The first collimator (Source Screening Collimator) limits the neutron source area seen by the sample and limits the number of neutrons reaching the second collimator. This permits to select form the total population of neutrons in the source, those that have smaller flight paths inside the target and thus increase the energy resolution [92].

This collimator is composed of 1 m of iron followed by 1 m of concrete having a inner diameter of 11.5 cm and is located at 137.7 m from the target system.

The second collimator (Beam Shaping Collimator) limits the amount of beam intersecting the sample avoiding also interactions with components very near the sample and limiting the background in the experimental area. This collimator is located just before the measuring station being at 178 m from the target system and can be tunned for capture or fission measurements to fulfill the experimental need in terms of beam shape. When used in fission mode, it is composed of 50 cm of 5% borated polyethylene followed by 125 cm of iron and another 75 cm of 5% borated polyethylene having an inner diameter of 8 cm. In capture mode, it is composed of 235 cm of iron and followed by 50 cm of 5% borated polyethylene having an inner diameter of 1.8 cm.

4.1.4.2 In beam shielding (Sweeping Magnet)

During the spallation processes, a great amount of charged particles are emitted in the forward direction. This charged particle background will travel through the flight path tube and reach the experimental area. To eliminate this background, a sweeping magnet was installed before the experimental area at 145 m from the lead target.

4.2 Energy resolution of the spectrometer

With the implementation of the above mentioned setup, the n_TOF spectrometer has unique characteristics that make it a very good neutron induced reactions cross section measuring facility.

The high instantaneous fluence makes possible to measure very small mass samples of radioactive isotopes by enhancing the capture count rate, making possible to see the cross section signal above the radioactive background.

The 185 m long flight path allows to resolve the neutron energy with high accuracy and resolution using the time-of-flight technique.

The characteristics of the neutron source with a relative small energy resolution function (discussed in Section 4.4) permits to measure cross sections in a broad energy spectrum with a high energy resolution.

4.2.1 The TOF Technique

In order to perform neutron time-of-flight measurements, it is important that the neutron source is pulsed. In a relatively short time, typically a few nanoseconds (higher if thermalization processes are involved), the neutrons with a broad energy spectrum are created at the reference start time t_0.

The time of detection t_n of the reaction product serves as a stop signal to determine the time of flight $t = t_n - t_0$ of the neutron having induced the reaction. The kinetic energy E_n of neutrons with a speed $v = L/t$ can be expressed relativistically as

$$E_n = E_{tot} - mc^2 = c^2p^2 + m^2c^4 - mc^2 = mc^2(\gamma - 1) \tag{4.2}$$

with $\gamma = (1 - v^2/c^2)^{-1/2}$ and where c is the speed of light. The first term of the series expansion gives the classical expression for the neutron kinetic energy.

$$E_n = \frac{1}{2}mv^2 = \alpha^2\frac{L^2}{t^2} \tag{4.3}$$

Taking the definition of the speed of light $c = 299792458$m/s and taking $m = 939.6\text{MeV}/c^2$ for the neutron mass, we get $\alpha \approx 72.3$ when L is expressed in meters and t in microseconds [96].

4.2.2 Experimental considerations

The reaction yields that are obtained in this way are, after background and dead time corrections, not directly related to the cross section formula. The resonance profiles are broadened by two effects: Doppler broadening and resolution broadening.

The fraction of incident neutrons on a sample with thickness n atoms per barn, undergoing a reaction, is given by the reaction yield $Y_r(E) = R(E)/\Phi(E)$ where $R(E)$ is the reaction rate and $\Phi(E)$ the incident particle rate. In a first approximation the reaction yield is related to the cross sections by

$$Y_r = \left(1 - e^{-n\sigma_T(E)}\right) \frac{\sigma_r(E)}{\sigma_T(E)} \tag{4.4}$$

where $\sigma_r(E)$ is the reaction cross section and $\sigma_T(E)$ the total cross section. In experiments at non-zero temperature the cross sections need to be convolved with Doppler broadening.

Doppler broadening is the effect of the thermal motion of the target nuclei in their atomic structure. Due to the movement of the target nucleus, a neutron approaching the nucleus with constant speed in the laboratory system, will have a spread in its velocity in the center of mass system. In a good approximation, for metallic samples this movement can be described by the free gas model [97], resulting in a Gaussian broadening of the resonances with a standard deviation

$$\sigma_D = \sqrt{\frac{2k_bT}{M/m}E} \tag{4.5}$$

with M/m the ratio of the masses of the target nucleus and the incident particle. For crystalline lattices a more complicated description is sometimes needed [98, 99]. Doppler broadening is always present in the interaction of neutrons with liquids or solids and cross sections are usually given at a specific temperature.

In addition to the Doppler broadening of the cross sections, the reaction yield is broadened by the experimental resolution. Resolution broadening is an experimental effect and reflects the distributions in the neutron flight time or flight length, originating from the finite primary beam pulse duration, the moderation distance, and all other experimental conditions. These effects are

different for each experimental facility and have to be carefully modeled and included in the resonance analyses [100].

The two broadening effects are important for resolved resonances. For unresolved resonances, where the cross sections appear smooth, broadening has not much effect. On the contrary, if a resonance structure is still present, one cannot extract in a straightforward way the average cross section from the average yield, as can be seen from equation (4.4) by taking averages. The factor $\left(1 - e^{-n\sigma_t(E)}\right)$ gives rise to what is known as the self-shielding effect. Corrections based on Monte Carlo simulations have to applied for both the multiple scattering and the self-shielding effect.

4.3 The Total Absorber Calorimeter (TAC)

The TAC (shown in Figure 4.5) design followed closely the experimental demands associated with the measurement of neutron capture cross section [101].

In order to measure the capture cross section of an isotope with multiple reaction channels competing and be able to perform a data analysis based on the reaction characteristics to discriminate between competing reactions, one has to be able to detect the several gammas emitted following neutron capture in order to be able to reconstruct the event.

- Have detectors capable of fully absorb the energy of a gamma ray up to 10 MeV.
- Have excellent time resolution ($\Delta\tau \simeq 1\ ns$).
- And be rather insensitive to the neutron and alpha background.

To fulfill this experimental requirements, several detection materials were studied (NaI, BGO and BaF_2) considering the experimental needs at n_TOF for performing the measurements of the isotopes related with the Th-U fuel cycle.

4.3.1 Neutron sensitivity

The high neutron sensitivity of the NaI due to the iodine content, the not so fast timing of light emission (0.23 μs) and low total efficiency for high energy gammas ruled out this material.

The BGO has a very small neutron sensitivity, a high stopping power for gamma radiation but a not so good timing characteristics and the binding energy characteristic of the constituent isotopes of this material is very close to the ones aimed to be measured. The very close binding energies of the detector's constituents and sample measured would lead to a background component difficult to eliminate.

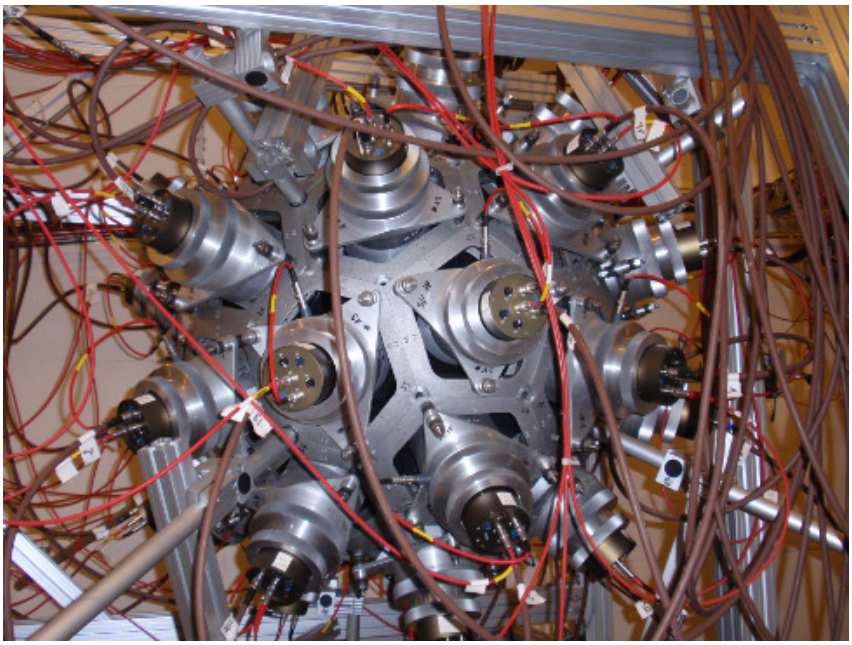

Figure 4.5: The Total Absorber Calorimeter at n_TOF

The BaF_2 has a small neutron sensitivity, high stopping power for gamma radiation, very good time resolution, acceptable energy resolution and from the point of view of implementation, it's available in the necessary dimensions to form a detector with 4π solid angle coverage and ability of stopping a 10 MeV gamma ray [102].

Although the BaF_2 features a small neutron sensitivity, two layers of neutron absorber materials were added between the sample and the crystals to reduce this source of background.

The first layer consists of a neutron absorber in the form of two spherical shells composed of ^{6}Li salt surrounding the sample. The $^6Li + n$ reaction gives a alpha particle and a tritium, both characterized by small mean free paths that are fully stopped inside the neutron absorber.

The second absorber consists of carbon shells doped with boron wrapping each scintillator crystal. The ^{10}B will capture a neutron to give a alpha plus a ^{7}Li both particles with a short mean free paths.

4.3.2 Solid angle and event detection efficiency

The division of a sphere in individual volumes is not new problem and one solution consist of a polyhedral geometry with a fix number (12) of pentagonal volumes followed by a variable number of hexagonal volumes. A single crystal

is shown in Figure 4.6.

Figure 4.6: Single crystal of the Total Absorber Calorimeter at n_TOF and respective carbon capsule

To decide the number of hexagonal volumes and overall dimension of the crystals, several factors were considered such as:

- The necessary depth to stop the gamma radiation (15 cm of BaF_2 for 10 MeV gammas).
- The available crystal dimensions and the granularity necessary to be able to detect separately all the gammas from the nuclear cascade.

The typical multiplicity of a capture gamma cascade is around 3 or 4 gammas and a good granularity to study these types of events consists of 5 times the multiplicity leading to a TAC with 20 or more individual crystals.

In fact the polyhedral geometry has magic numbers like 32, 42, 72, 92. A TAC with 32 crystals would be sufficient for measuring the capture cross sections as it would diminish the cross talk between individual detectors compared with a 42 crystal setup but due to constrains with the biggest commercial BaF_2 crystal size being 17.5 cm by 14 cm, the 42 crystal configuration was adopted.

The final assembly of the detection system is therefore composed by 40 BaF_2 scintillators arranged to form a honeycomb sphere covering 4π of the

solid angle as shown in Figure 4.5. The two missing crystal correspond to the symmetrical openings to let the beam in and out [103, 92, 101].

4.3.3 Alpha and gamma discrimination

The BaF_2 scintillator is characterized not only by the fast time resolution but also by the different responses to different types of radiation. In the case of gamma radiation, the response is characterized by a signal with two different components one having a very short time constant typically of the order of 0.7 ns (fast component) and a second one with a time constant of 630 ns (slow component) as shown in Figure 4.7. In the case of a alpha particle and because the process involved in the energy deposition in the crystal is different, the short component is not present [92, 101]. The alpha background comes from the contamination of the BaF_2 with ^{226}Ra, which decays emitting an alpha particle.

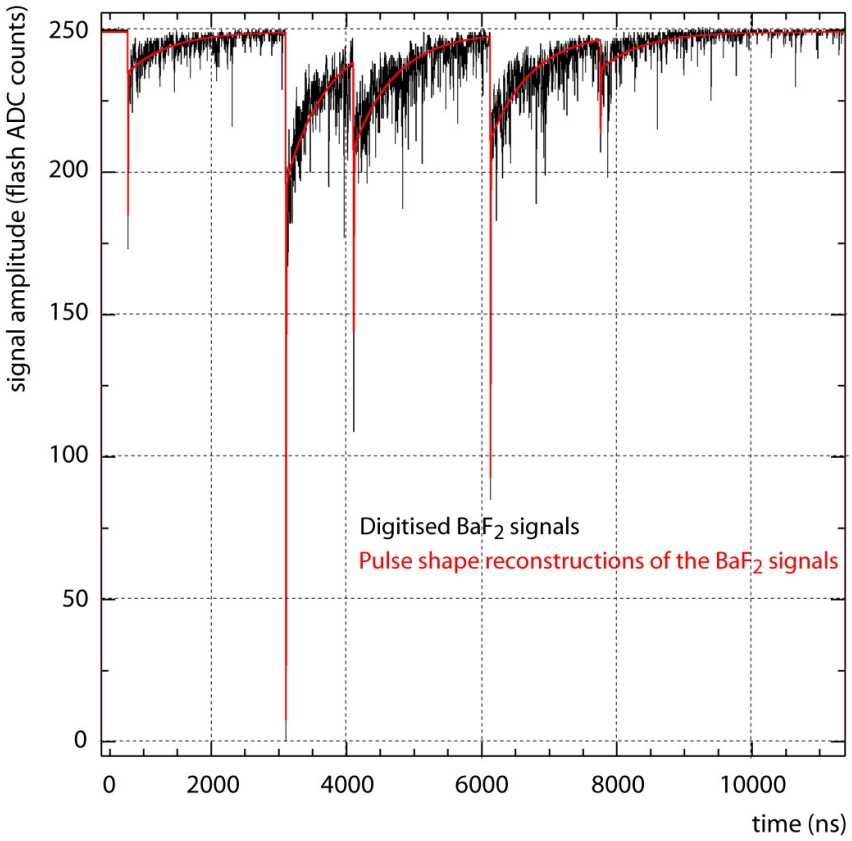

Figure 4.7: Digitized signal of a BaF_2 detector (black) and the reconstruction of the same signals using the Pulse Shape routine (red).

The analysis of the pulse shape give us the information needed to set apart the contributions of both radiations (gamma or alpha) allowing the tracking of the detectors gain by looking at the detectors alpha spectrum (discussed in detail in Sections 5.2.6).

The Figure 4.7 shows the typical signal of the BaF_2 for gamma radiation.

The two contributions are clearly visible in Figure 4.8 separated by the threshold line.

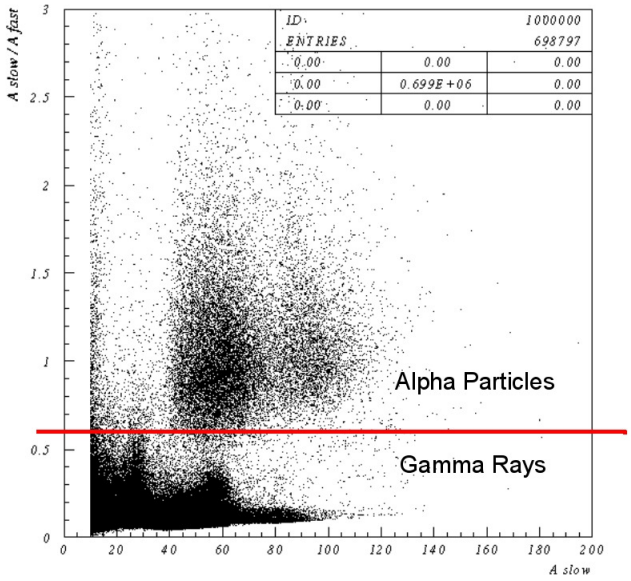

Figure 4.8: Discrimination between γ and α particles.

4.3.4 Granularity

The granularity of the detection system allows to characterize events by the number of gammas involved in the reaction and therefore identify the nature of the nuclear reactions and disentangle competing reactions occurring at the same time.

Uncorrelated background is characterized by a single gamma while capture has a multiplicity distribution that averages at 3 or 4 and fission multiplicity tends to have a broader multiplicity distribution with higher average [101].

4.4 Study of the neutron energy resolution function of the n_TOF Facility

The n_TOF target [104] was designed with an 80 X 80 X 60 cm^3 spallation core made of lead surrounded by water that serves to cool and moderate the exiting neutrons. Two studies have been done using distinct simulation programs to assess the performance of the n_TOF spectrometer concerning its resolution function. In one of the studies [100], the resolution function was simulated for energies below 20 MeV using the code Monte Carlo Transport Code for Simulations of Pulsed Neutron Sources (CAMOT) and implementing the geometry described in [105]. In the other study, described in [106], the Fully integrated particle physics MonteCarlo simulation package (FLUKA) code [107] was used with the same geometry. Both studies consider a moderation thickness of 5 cm. The resolution function is calculated at the sample position, which is located at approximately 185 m from the moderation target. Because of the large geometric factor involved in the problem, the resulting statistics were limited. Recently, when performing a check of the spallation target, it was found that during the construction, a supplementary O-ring was introduced just behind the aluminum windows that seal the target system from the Time-Of-Flight (TOF) spectrometer increasing the moderation thickness to approximately 5.8 cm at the center of the target. The knowledge of the effects of this extra moderation depth and its influence on the energy resolution function as well as the neutron energy spectrum is crucial for the data analysis. The accurate knowledge of the energy resolution function is essential for the analysis in the resolved resonance region. To study the effect of the increased moderation depth from 5 cm to 5.8 cm with high statistics, we performed new simulations with the MCNPX. To study the consistency of our results, we also performed the simulation with a moderation depth of 5 cm and compared the results with the resolution available from the two previous simulations.

4.4.1 Resolution function

Neutrons are generated by spallation reactions in the target and are afterwards moderated until they reach the evacuated neutron tube. The unknown path followed by the neutrons inside the target and associated moderation system impacts the assessment of the neutron energy using the TOF technique by introducing an intrinsic uncertainty. The goal for determining the neutron energy resolution function is to describe and include the energy-dependent resolution. The analytical description of the resolution function used in this work is already implemented in the R-matrix analysis code SAMMY [108] with

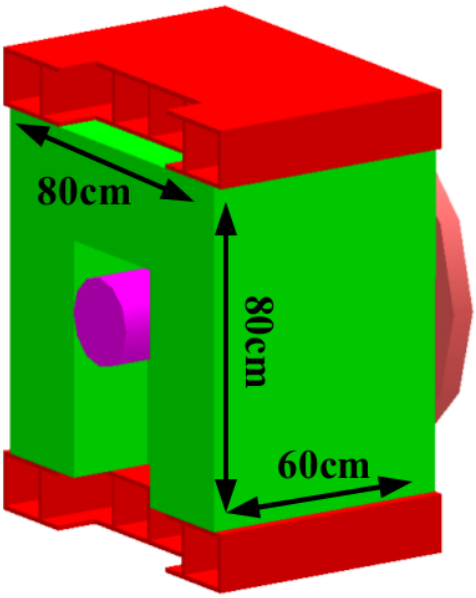

Figure 4.9: Target system accompanied by the supporting structure and aluminum entrance window on the right. The proton beam impinges from the left side.

the Rensselaer Polytechnic Institute (RPI) broadening function. Many of the parameters of this analytical function are energy dependent. The simulated resolution function can be adapted to this function by adjusting the energy dependence of the parameters. The effect of the resolution is most visible in the reaction cross sections in the resolved resonance region, where the overall shape of the resonance is deformed and the resonance energy is shifted. The RPI function used has the form of Eq. (4.6),

$$R(\delta t) = A_0 \left(\frac{(\delta t + \tau)^2}{2\Lambda^3} e^{\left(-\frac{\delta t+\tau}{\Lambda}\right)} + A_1 \left[A_2 e^{-A_3(\delta t+t_0)} + A_4 e^{-A_5(\delta t+t_0)} \right] X(\delta t) \right) \tag{4.6}$$

where δt is the time need for a neutron to exit the target system and is equivalent to the delayed distance, $X(\delta t)$ is a function which takes 0 or 1 as value and determines the exponential tail inclusion in the fit. In Eq. (4.6) the χ^2 distribution (first term) is related with the neutron moderation effect and its contribution to the energy resolution, while the two exponential tails are associated with the combined target-moderator system. Although the above mention equation seems to be only time dependent (1D function), one should take care that the parameters $\Lambda, \tau, A1, A3$, and $A5$ have a dependency on the

neutron energy. Considering both dependencies, the RPI functions assumes the 2D form for the neutron energy resolution. To assure that the RPI function doesn't return valueus without physiscal meaning, the parameter $A1$ is constrained to equal zero if the sum of the two exponentials is negative.

Figure 4.10 shows how the χ^2 and exponential tails contribute to the overall RPI function shape.

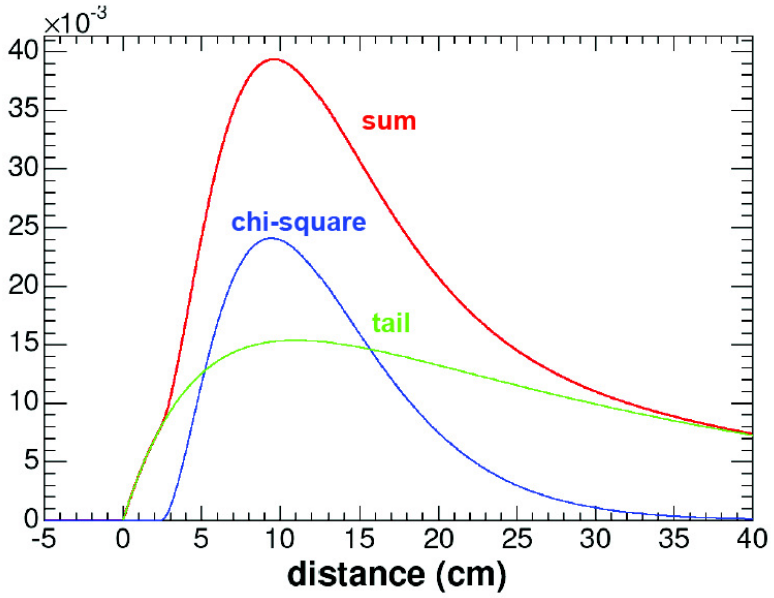

Figure 4.10: χ^2 and exponential tails components of the RPI function. Arbitrary units in the vertical axis.

Monte Carlo simulations with the code MCNPX have been performed in order to assess the differences introduced by the increased moderation thickness. A detailed geometric description of the neutron production system considering all the components inside the target container was used (Figure 4.9). The neutron beam pipe used for the TOF spectrometer was also implemented. In addition, two ideal tube collimators and two ideal beam collimators were included to fully describe the experimental conditions encountered in the experimental area. The first tube collimator is located at approximately 71 m from the exit plan of the target system and the second at approximately 140 m, and they serve the purpose of killing particles traveling outside the beam tube. The beam collimators are located at approximately 137 and approximately 175 m. A detailed description of the beam pipe and the positions of the collimators can be found in [104]. The transport of the particles from the target system until the experimental area is performed using a deterministic

approximation.

4.4.2 Monte Carlo simulations

4.4.2.1 Physics models used

The neutrons were generated by spallation reactions triggered by 20 GeV/c protons impinging on a lead block (the target). The pre-equilibrium and evaporation physics associated with the spallation processes were simulated using the CEM2k [109] model implemented in MCNPX 2.6e [110]. The CEM2k model is able to describe fission reactions and the production of light fragments heavier than ^{4}He, using the Generalized Evaporation Model code [111, 112]. It also contains a number of improvements and refinements in the cascade and Fermi breakup models compared with previous models used in MCNPX simulation. All these features allowed us to describe quite well a large variety of spallation, fission, and fragmentation reactions necessary for the simulations performed.

4.4.3 Simplifications in the simulation

The interaction of a 20 GeV/c proton with a lead block produces a huge number of particles, including neutrons. The neutron production per proton is approximately 320 neutrons. This large neutron production ratio combined with the cascade of nuclear reactions produced inside the target and the associated particles produced yields a heavy and lengthy simulation problem. The problem is characterized by a very high multiplicity of particles and a reduced solid angle. However, the neutrons that are relevant to our studies are those produced in the forward direction in a very narrow solid angle. To increase the simulation speed without compromising the realistic approach of the simulation concerning the experimental conditions, several simplifications have been made. Considering that we are interested only in neutrons with energies comprehended between 1^{-9} and 10 MeV, only hadronic particles were tracked in the simulation. In addition, we used one DXTRAN sphere [110, 113]. The DXTRAN sphere consists in the deterministic transport of particles to a zone (comprehended inside the the sphere) which is not being adequately sampled because particles have a very small chance of reaching that region. In our case, where a very small solid angle (approximately 1 mrad) due to the 185 m length of the neutron beam pipe and collimators are present, the use of DXTRAN sphere allows to achieve good statistics. The DXTRAN variance reduction technique available in MCNPX is capable of dealing with the large geometric factor related to the transport of particles over large distances without interactions in simple geometries like the TOF tube. This technique is based on the

angle-biasing technique together with deterministic transport of the neutrons inside the pipe [113]. Particles traveling outside the target system or beam pipe are killed and don't contribute.

4.4.4 Simulated results

The neutron energy and equivalent distance or delay distance (path length equivalent to the time spent by a neutron of a given outgoing velocity inside the target-moderator system) were tallied using a user-defined tally used in similar calculations [85] for the facility Neutron Time-Of-Flight facility at IRMM (GELINA) [84]. These quantities are stored in a two-dimensional matrix (Figure 4.11) to facilitate the analysis. The tally binning consists of one bin per millimeter for the equivalent distance and of ten bins per decade of energy. The equivalent distance was tracked from -10 to 300 cm, and the energy range considered is between 1 meV and 10 MeV.

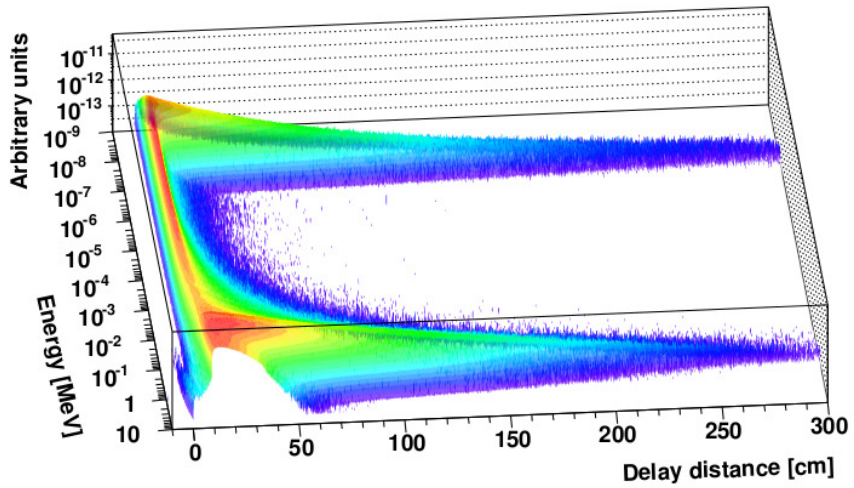

Figure 4.11: Two-dimensional matrix of the tallied quantities in MCNPX, showing their dependence for a moderation thickness of 5.8 cm.

4.4.5 Analysis procedure and methodology

The simulated data for 5 and 5.8 cm of moderation depth were fitted using the RPI resolution function, and the results were compared with two previous

simulation's data assessed for 5 cm using the FLUKA and CAMOT Monte Carlo simulation codes. The fit was done using two different energy bins (two and ten bins per decade) for the data of FLUKA and MCNPX. Although it was necessary to rebin the FLUKA data in the equivalent distance axis to achieve reasonable statistics, the results showed that the fit with ten bins per decade agrees very well with the fit using two bins per decade. The same was observed for the data from MCNPX. For the data obtained with CAMOT, the fit was processed using two bins per decade in the energy scale due to statistical constraints. We have compared the FWHM and the FWTM of the fitted energy resolution function for each energy interval. To determine the parameters of the resolution function, we have fitted the equivalent distance for each energy bin using the RPI function with all parameters free in order to obtain the best description of the simulated data but all parameters were initialized with values that already reproduced to a certain extent the distribution. The fitted RPI function for each energy bin is analyzed and the quantities FWHM and FWTM are extracted. Figure 4.12 displays the RPI-fitted function for the 80 eV bin overlayed on the 5 cm data simulated with MCNPX. The resolution function is fitted throughout the whole energy range and analyzed.

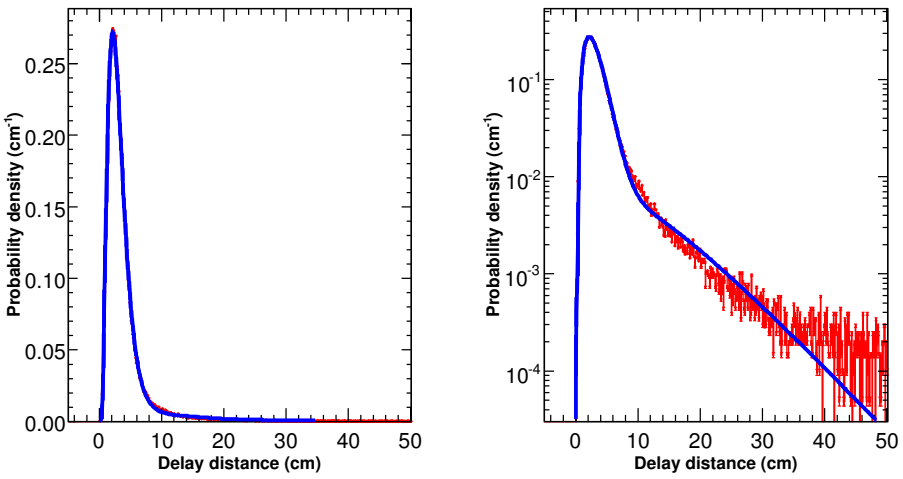

Figure 4.12: Fit of the data simulated with MCNPX at 80 eV for a moderation depth of 5 cm in linear(left) and logarithm (right) vertical scales

4.4.6 Analysis of the FWHM and FWTM

The procedure used to assess the differences between the resolution functions assessed with different codes and for the different depths of moderation was the comparison of the full-width at half-maximum (FWHM) and the full-width at a tenth of the maximum (FWTM) for each energy bin between the different sets of data. The plotted data of the FWHM and FWTM variation with the energy are provided in Figures 4.13, 4.14 and 4.15, respectively. From Figures 4.13 and 4.14 it is possible to see that the results from previous simulations are different at higher neutron energies. Also the results of this work are not consistent with any of the two previous simulations. Concerning the simulated equivalent distance using MCNPX and moderation depths of 5 and 5.8 cm with water, the behaviors are almost identical for the equivalent distance spectrum. This can be seen in Figure 4.15, where the simulated data are displayed both on a linear and logarithmic scale. The FWHM and FWTM (Figure 4.16) assessed show very small differences over the energy range for the two different moderation depths.

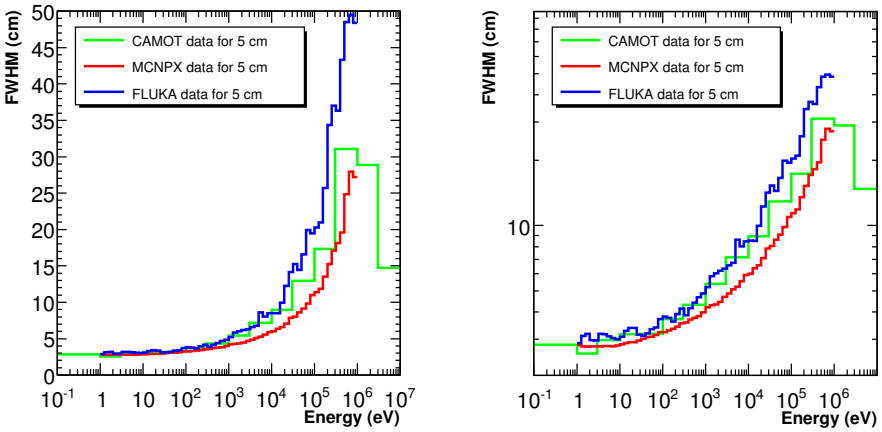

Figure 4.13: The FWHM for the three parameterizations for 5 cm of water.

4.4.7 Conclusion

The results obtained in this study show the existence of important differences between the different simulations done to assess the resolution of the n_TOF spectrometer. The reason behind these differences is not clear and may be

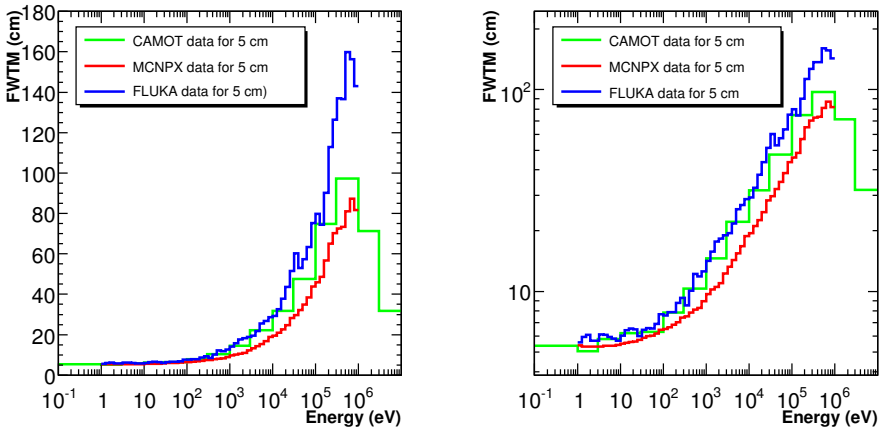

Figure 4.14: The FWTM for the three parameterizations for 5 cm of water.

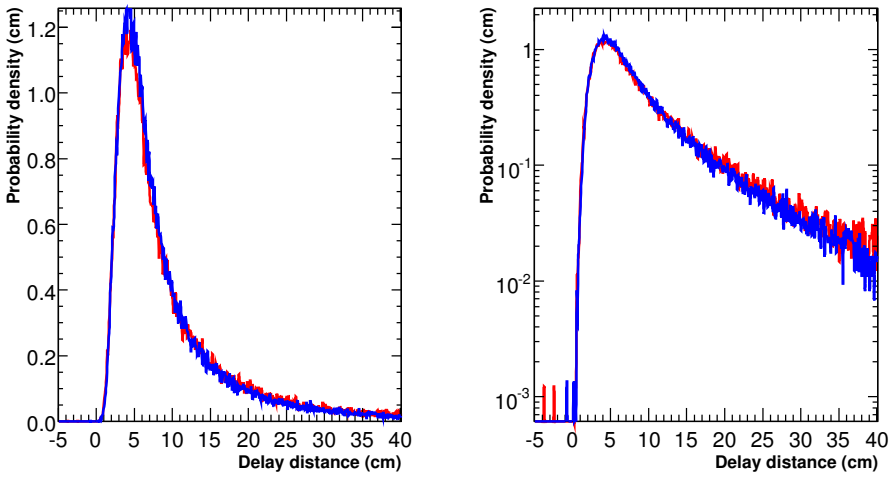

Figure 4.15: Comparison of the equivalent distance between two different moderation depths for 8 keV (red for 5 cm and blue for 5.8 cm).

related to the different codes, libraries, and methodologies used. The transportation of the particles through the TOF tube can be a cause, as all codes and methodologies were different. With MCNPX, the transport of the particles in the TOF tube was done during the simulation using the code's variance

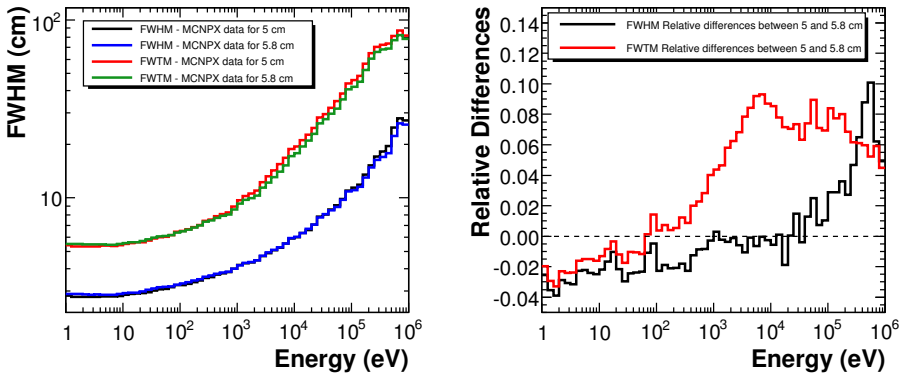

Figure 4.16: Comparison of the equivalent distance between two different moderation depths for an arbitrary neutron energy of 8 keV (red for 5 cm and blue for 5.8 cm).

reduction techniques. For the FLUKA simulation, the neutron spectra were tallied just outside the target system and then transported with a separate code through the TOF tube. Results obtained in this study using MCNPX show that an increase in moderation depth introduces almost no changes in the equivalent distance shape. This leads to the importance of validating the simulations and determining which one reflects the characteristics of the n_TOF spectrometer. As one can see from Figure 4.17, the energy resolution function dominates the broadening of the resonance shape above several keV. A change in the resolution function used in the analysis of resolved resonances will certainly affect the extracted resonance parameters. On the other hand, since the area of the resonance is conserved, an integrated quantity like the Maxwellian averaged capture cross section will not change with a different resolution function.

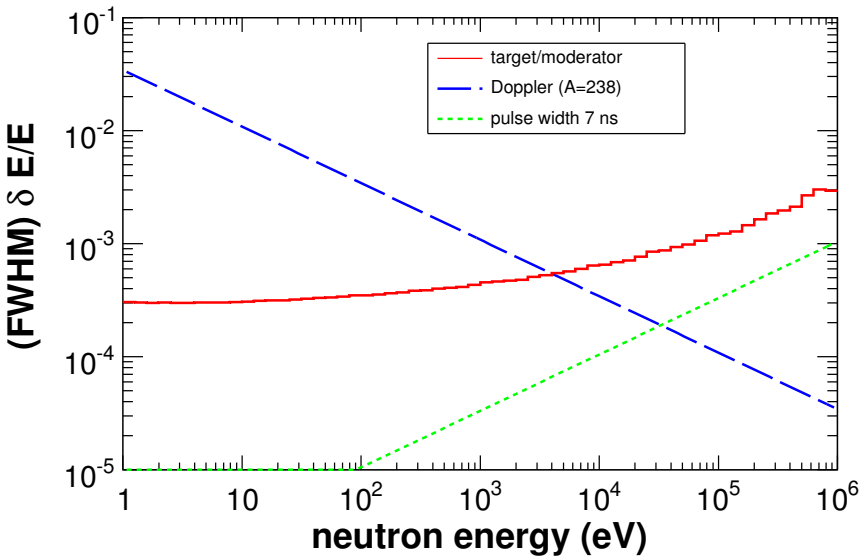

Figure 4.17: Different contributions for the broadening of the resonances. The target/moderator curve represents the results obtained for the FWHM with MCNPX using a moderation depth of 5 cm

Chapter 5

Data extraction

Before addressing all the specificities of the data reconstruction and data analysis it is important to understand the challenges behind the measurement of the capture cross section for the particular nuclide here discussed.

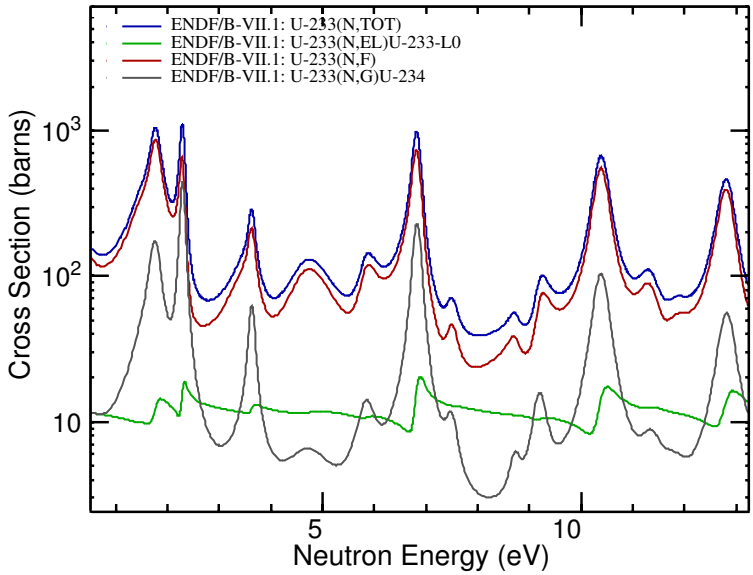

Figure 5.1: ^{233}U total, neutron induced fission, neutron capture and elastic cross sections from ENDF/B-VII.1.

The data analysis of the neutron capture in ^{233}U is entangled directly with the fission data analysis because both nuclear reactions are competing in the energy range of interest, as shown in Figure 5.1 for the energy interval between

1.5 and 13 eV. Moreover, both reactions are characterized by the emission of gamma rays covering a broad energy range. Additionally, gamma rays from fission can originate from three components: prompt gamma, neutrons emitted during fission interacting in the surrounding materials and delayed gamma emission from fission fragments. Besides, the fission cross section is one order of magnitude higher in comparison with the capture contribution. The contributions from neutron scattering and the sample's related activity due to the isotopic impurity must also be considered, as will be shown later.

5.1 The TAC's data acquisition system

The method employed to perform the ^{233}U neutron capture measurement using the time of flight Time-Of-Flight (TOF) technique, consists for the work here described in the use of a high efficiency, almost 4π γ-ray detector made of 40 individual BaF_2 detector modules. The 40 detector modules assembled together are denominated as Total Absorption Calorimeter (TAC). The capture yield is then obtained by counting events where the total deposited energy in the TAC corresponds to the neutron binding energy. This method is particularly suitable when dealing with fissionable samples, or when only low mass (tens of mg) is available. The choice of BaF_2 as scintillating material [102] was explained before and is due to:

- Its very good timing properties.
- Good pulse shape discrimination properties.
- Previous experience [114] in using such material at FZK, which has proven to be very beneficial.

In order to be able to take advantage of the full features of the BaF_2 crystals and to take into account the experimental requirements of measuring samples that can induce counting rates as high as few counts per μs when irradiated with the neutron beam, [115] it was decided to use an acquisition system based on Flash Analog to Digital Converter (Flash ADC) modules. It is necessary upon the digitalization of the BaF_2 signals to sample with enough detail to be able to reconstruct the fast component of the BaF_2 crystals which gives information on the time of the signal. This component is of the order of 6 ns (corresponding to the photomultiplier response and not to the real timing of the fast component) and accordingly with Nyquist–Shannon sampling theorem, the acquisition system has to obey the following:

If a function $x(t)$ contains no frequencies higher than B Hertz, it is completely determined by giving its ordinates at a series of points spaced $1/(2B)$ seconds apart.

This leads to the need of having sample rates of 400 MHz or higher. The acquisition system chosen is based upon 8 bits flash Flash ADC that can operate up to 1 GHz with internal memory of 8 Msamples. The 8 bits gives enough precision in each sampling and the 500 MHz sampling rate permits to sample for a time long enough to measure the cross section in an energy range from above the MeV region to eV. This translates in a sampling time ($T_{sampling}$) of approximately 16 ms which gives time for 1 eV neutron and slightly less energetic ones to travel the 185 m flight path.

$$T_{sampling} = \frac{M_{8Msamples}}{500MHz} = 16ms \tag{5.1}$$

5.1.1 Shape of the signals from the BaF_2 crystals

The signals from the BaF_2 are characterized by two decay components as shown in Figure 5.2. One that has a (fast) 6 ns decay constant and another with a (slower) 630 ns decay constant. Because every signal is very noisy, a reference pulse shape for γ response is obtained by:

- Selecting more than 50 γ signals per detector, with no pile-up and each signal having more than 40 and less than 150 Flash ADC channels for fast amplitude.
- The signal's maximum amplitude is normalized to unity, and the corresponding time set to 1000 ns. The baseline is removed. The final pulse shape is averaged over all selected signals.

Even though the resulting reference pulse shapes are similar (Figure 5.2), one can not superimpose the response of one detector to another. The ratio between the maximum amplitude and the slow component amplitude varies between 5 to 8 and an unexpected second bump comes about 600 to 800 ns after signal starting. The reason for this bump is related with the high voltage divider circuit and has no physical meaning.

5.1.2 Peak characterization algorithm

The use of Flash Analog to Digital Converter (Flash ADC) allows to record the full signal and thanks to this, a pulse analysis routine can be as simple as pulse rise-time or time over threshold analysis [116] or much efficient, but very Central Processing Unit (CPU) time consuming, signal correlation analysis [117]. For the particular case of neutron Time-Of-Flight facility (n_TOF), peak finding is based upon the derivative of signal while the pulse analysis is based upon both signal integration and signal fitting.

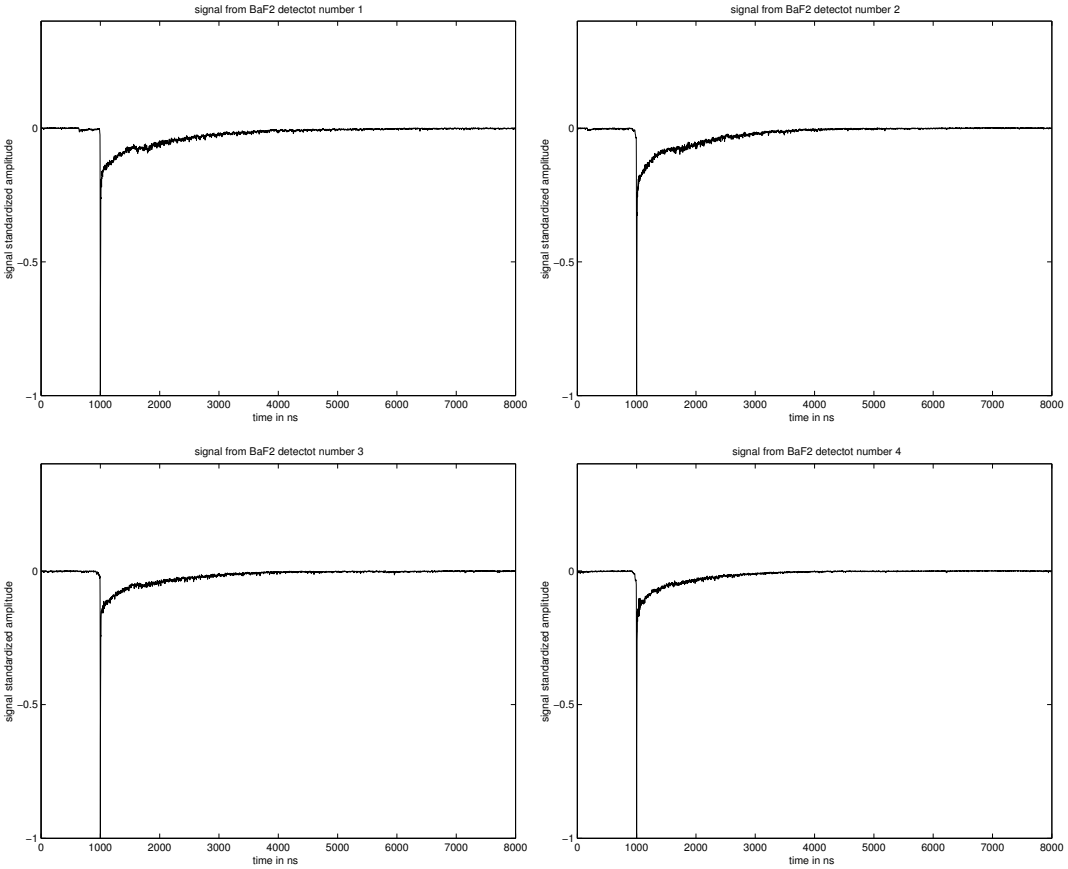

Figure 5.2: Reference pulse shape for BaF_2 crystals 1 to 4. Although all crystals show a very similar pulse shape, small differences are present and are characteristic of each crystal.

5.1.2.1 Finding a peak

When trying to find a peak, one of the problems is the possible moving baseline. To overcome this problem, the peak finding algorithm does not work on the direct signal but on its "time-derivative". In order to search and to characterize the peaks, the following quantities are computed for each sample j:

- The second derivative, $\partial^2(j)$ is used for triggering the validation of the peak finding.
- The mean, $M_{left}(j)$, and variance, $V_{left}(j)$, of data averaged over a 200 ns window on the left side of the current point are computed.
- The computed $M_{left}(j)$ is used for baseline determination while $V_{left}(j)$ is used as triggering threshold.
- The mean, $M(j)$ of data averaged over a 200 ns window centered on the

current point is also computed . $M(j)$ is used to determine peak ending.

To accept a peak, two thresholds are considered. The first one is related to the input threshold (the one given to perform the zero suppression) and denominated as ∂ti. The second which is a derivative trigger is related to the expected background for the current sample. The expected background value is give by $\partial tn \propto -\sqrt{\frac{V_{left}}{Range}}$ where $Range = 3samples$.

The detected peak must fulfill 4 conditions to be accepted:

- The signal derivative must be inferior to the Flash ADC threshold (negative voltage is used) $\partial(j) < \partial ti$
- The signal derivative must be inferior to the background derivative (negative voltage is used) $\partial(j) < \partial tn(j)$
- $D(j) \geq 200$ where $D(j)$ is the Flash ADC value for sample j
- Not in another peak triggering. Condition "Not in another peak triggering" is false until derivative becomes positive again.

Once a peak is detected and validated, it is important to assess several quantities that indicate the peak quality and method to analyze it. This is achieved by:

- Checking if more than 3 consecutive samples are saturated. If so the peak will not be fitted and flag called "LongPeak" is switched on.
- Estimating rise time.
- Estimating maximum peak ending time.

The peak's amplitude relative to the baseline is integrated during 20 ns giving the "fast charge", Q_{fast} and also until the peak ended giving the "total charge", Q_{tot}. Last, the pile-up order is computed as the difference between the number of peaks (not rejected) found when the peak ended and the number of peaks found at peak starting.

Peak rejection: Peaks are rejected if one of these two conditions is fulfilled:

- Peak estimated time based on the known slow decay constant and slow amplitude is much bigger that the measured peak end time.
- The fast to slow amplitude ratio is bigger than 30.

5.1.2.2 Pile-up treatment

When a peak is detected before the previous one ended, the baseline corresponding to the last detected peak can not be considered constant anymore. In our case an exponential decaying baseline is considered, with 630 ns decay constant. So two corrections have to be made to the slow component amplitude and the A_{slow} is calculated differently:

- To correct bias induced by moving average, the baseline value is taken as the previous peak baseline plus an exponential decay component which

represents the tail of the first peak.

- If a new peak is detected before the previous one ended, then the slow component amplitude, A_{slow}, of the previous peak is computed without waiting the peak ending, to avoid to integrate inside the newer signal.
- Corrections terms are similar to the ones used for a no pile-up case, except that time corresponding to the end of the first signal in the exponential term have to be replaced by the time corresponding to the new peak detection.

5.1.3 Fitting the signals

In order to improve the characterization of peaks, a fitting procedure is performed. Firstly a fit is performed to determine the baseline. Then a fit is made for each found peak. Fitting is made using the Levenberg-Marquadt method [118] for both baseline and peak characterization. Peaks having a non null LongPeak flag are not fitted, so only initial guess parameters are given for these peaks.

5.1.3.1 Baseline treatment

Determining the baseline region while two consecutive normal (i.e. LongPeak=0) peaks are distant by less than 3.5 μs + 512 ns (peak duration plus pre-sample length), they are associated with the same baseline. When a peak having a non null LongPeak flag is found a new baseline region is defined. Two baseline fit regions are considered, one before the first considered peak, and another one after the last considered peak. The first baseline fit region starts 512 ns before the first peak and stop one channel before the considered peak starting. The second baseline region begins at the last considered peaks starting plus 3.5 μs, and finishes 512 ns later.

Determining the baseline shape, two cases have to be considered for determining the baseline shape:

- If the baseline is inside a long peak then the baseline is supposed to have an exponential tail shape.
- Else the baseline shape is considered linear.

5.1.3.2 BaF_2 signal's integration and fitting

Once a peak is accepted, and the baseline has been determined, the following integral quantities are recomputed for each peak:

- Integral (relative to baseline shape) from peak starting to 20 ns later

- Maximum amplitude and corresponding baseline value found in this 20 ns time window width.
- Integral (relative to baseline shape) from peak starting to 3.5 μs later

The number of peaks fitted simultaneously is given by the pile-up parameter. Nevertheless if the pile-up order is greater than 12, no fitting will be performed to avoid consuming too much CPU time. The fitting region begins one channel before the first peak starting and ends at the maximum value between estimate and real time ending of the last considered peak.

5.1.4 Extracted parameters

For each peak 8 integer parameters and 9 floating point parameters are extracted:

Integer parameters:

1. Peak starting time [ns] (see also float parameter n. 4)
2. Peak maximum time [ns]
3. Peak end time [ns]
4. Peak number in the movie (movie is the consecutive data points after applying the zero suppression)
5. Pile-up order
6. LongPeak flag (0 : normal peak, 1 : long peak, 2 : movie ended before peak return to baseline)
7. threshold (unused)
8. Baseline type (0 : linear , 1 : exponential tail)

Floating point parameters:

1. Fitted baseline value at peak maximum [Flash ADC units]
2. Fitted Fast component amplitude [Flash ADC units]
3. Fitted Slow component amplitude [Flash ADC units]
4. Start time adjustment [ns] (true fitted starting time is given by adding integer parameter no 1 with this parameter)
5. Fitted exponential rise time and fast component decay constant [ns]
6. Best reduced χ^2 value obtained when fitting this peak.
7. Measured maximum amplitude relatively to the fitted baseline [Flash ADC units]
8. Measured integration during 20 ns relatively to the fitted baseline [Flash ADC units $\times$ ns]

9. Measured integration during 3.5 μs relatively to the fitted baseline [Flash ADC units $\times$ ns]

5.2 BaF_2 crystal's performance

In this section the description of the comprehensive study to assess the BaF_2 crystals performance in terms of pile-up recovering, Pulse Shape Discrimination (PSD), signal to energy conversion, resolution, linearity and stability is done.

5.2.1 Pile-up recovering

Since the pulse shape is reconstructed, pile-up should be treated properly. Figure 5.3 shows a typical BaF_2 train of pulse shapes for a gold sample in the 5 eV saturated resonance region. The black histogram is the measured raw signal and red curve corresponds to the reconstructed one using the method described previously.

The signal shape due to γ interaction in BaF_2 has already been described in the previous section. Moreover one can see that slow component signal fluctuates a lot. On the contrary, the signal corresponding to the baseline is very stable, indicating that these oscillations do not originate from intrinsic background, but are associated with the γ interaction within the detector.

Figure 5.3 shows that four interactions occurred before the signal returns to its baseline. This shows the need to implement a reconstruction algorithm able to deal properly with pileup. As can be found in Ref. [115] and since one can have more than one reaction per μs, it is important to be able to reconstruct event distant by a fraction of μs.

For randomly incoming events, following a poissonian distribution, the time interval between two successive events follows an exponential distribution. Figure 5.4 shows the time interval spectrum for a given detector obtained during a ^{235}U sample measurement. Since the ^{235}U content in the sample was very low, the counting was mainly dominated by the γ background, and so this measurement is a good approximation for randomly incoming events.

For time interval values above 800 ns both histograms follow an exponential shape. From 600 to 800 ns, the single spectra is slightly above the exponential law. This overshoot is due to the wrong BaF_2 shape occurring around 600 ns after a true signal and generating sometimes false triggering.

Moreover one can also see that the 600 ns bump is not present in the red histogram. This indicates that this problem, should not affect significantly TAC performance. Below 500 ns, interval time spectra drops significantly.

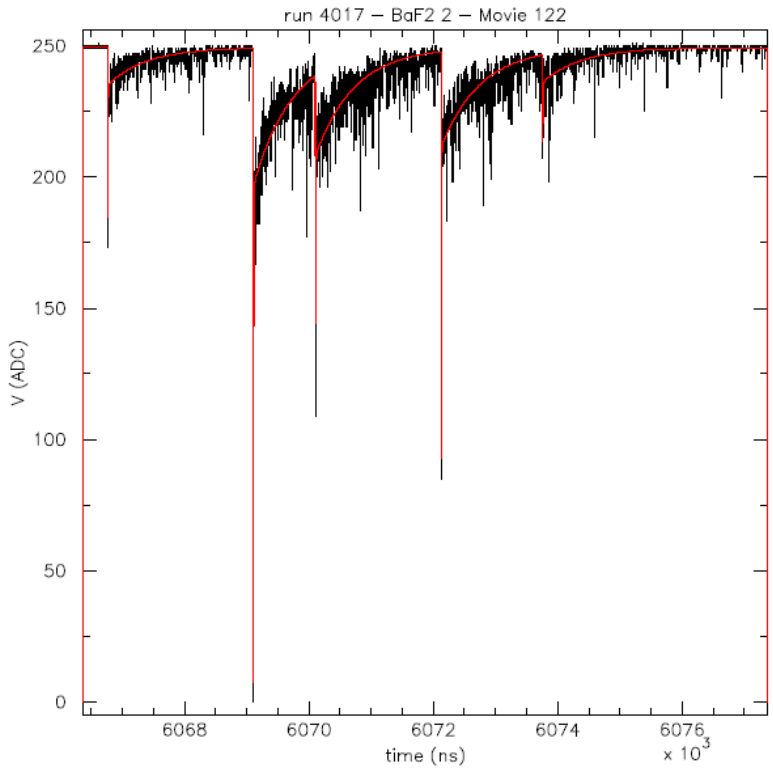

Figure 5.3: BaF_2 measured (black) and reconstructed (red) pulse shape.

As already noticed, a signal induces a lot of fluctuation and threshold for signal discrimination becomes higher in the tail of the first signal. Because γ rays from capture events have a higher energies than background γ rays, this drop is strongly reduced in coincidence (red) spectra. Nevertheless below 400 ns, one would have to correct data due to this loss of efficiency. Finally below 150 ns one can see a peak in both single and coincidence spectra. This is probably due to strong oscillations after the fast component signal.

5.2.2 Pulse Shape Discrimination (PSD)

The PSD can be understood by looking at Figure 5.5 which is a 2-dimensional plot where the horizontal axis represents the ratio between fast amplitude (A_{fast}) and fitted signal integral, Q_{fit}, divided by the slow component (A_{slow}) decay time (630 ns). For α particles the fast component signal is strongly reduced, so the ratio is expected to be below 1. For γ rays the ratio may vary from one detector to another. In our case it was found to be widely spread around 5. The vertical axis represents ratio between the real signal duration

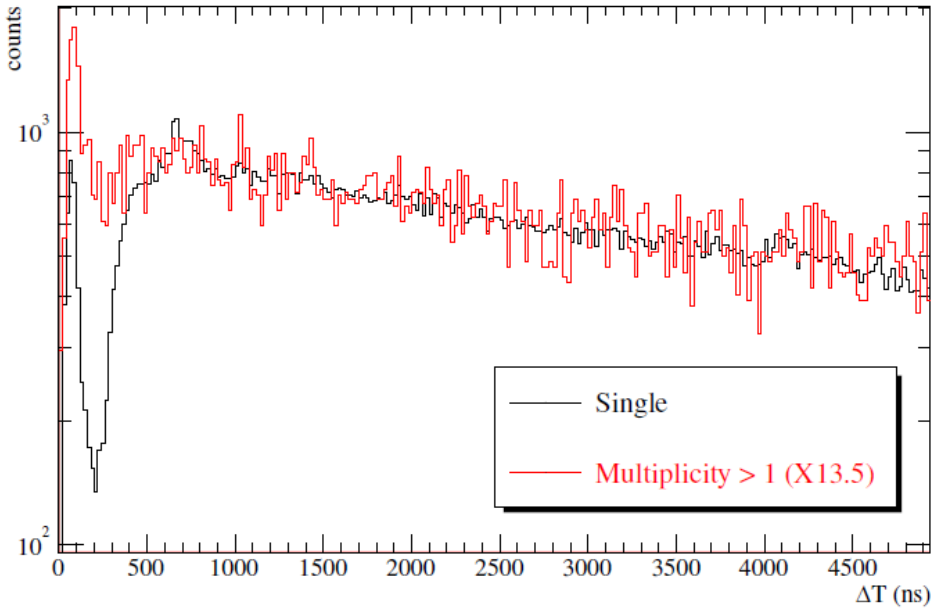

Figure 5.4: Time interval spectrum for two consecutive events (ΔT) in a given detector. The black histogram corresponds to events in single mode (multiplicity = 1). The red histogram is filled only if an interaction, at least, occurs in another BaF_2. The red histogram is scaled by a factor 13.5 to superimpose it on the black one.

and the expected one $t_{expected}$, given by:

$$t_{expected} \simeq t_0 + \tau \ \ln\left(\frac{A_{slow}}{y}\right) \tag{5.2}$$

Where t_0 is the scintillation time, y is the difference between the baseline value and pulse shape value and τ is the decay component.

For good signals the ratio between real signal duration and the expected one, should be around one. Low value indicates that peaks return to baseline too fast and these signals are probably due to noise. On Figure 5.5 three regions are clearly isolated.

- The α particles are associated with fast amplitude to integral ratio below 1.6 and real to expected duration ratio above 0.3.
- γ rays are associated with fast amplitude to integral ratio above 1.6 and real to expected duration ratio above 0.3.
- Finally signals with real to expected duration below 0.3 are rejected.

Results of this selection can be seen on energy spectra shown on Figure 5.6.

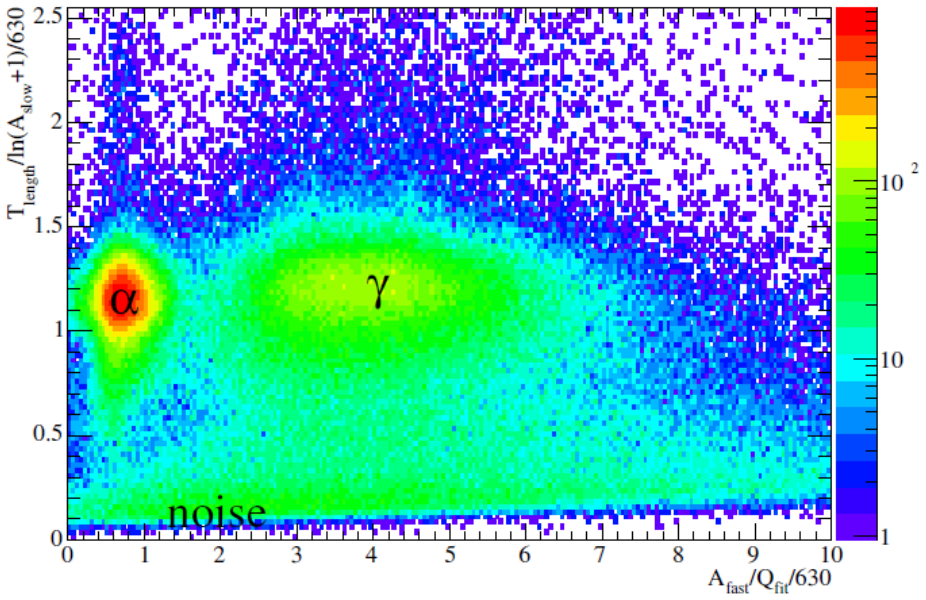

Figure 5.5: Pulse Shape Discrimination between γ and α particles based on the characteristics of the A_{fast} and A_{slow} components for each event on a detector module.

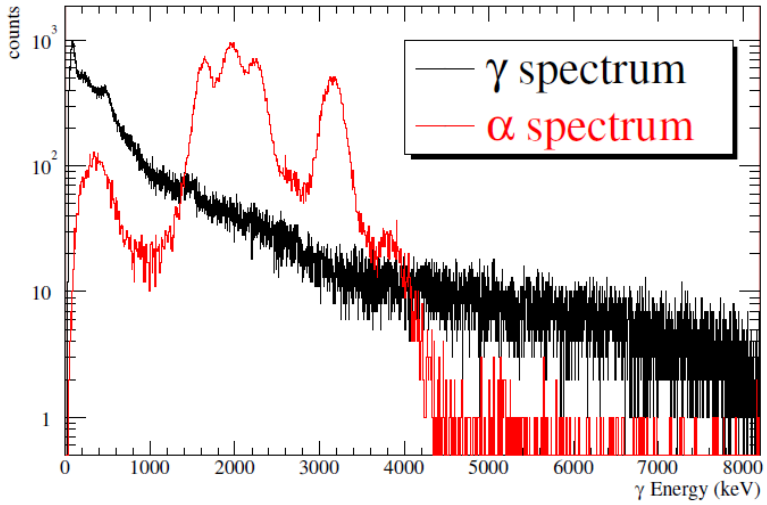

Figure 5.6: Energy spectrum for γ and α particles obtained using the PSD algorithm.

The γ energy spectrum is shown on black. The α energy spectrum is in red.

Energy calibration has been performed for γ rays, but the same scale has been used for α spectrum in order to compare both spectra. Figure 5.6 doesn't show any structure of the α spectrum in the γ spectrum leading us to believe that the here above selection criteria was successful in separating both contributions.

5.2.3 Signal to energy conversion

Each individual detector module (crystal plus photomultiplier) is calibrated using standard radioactive sources of ^{88}Y (898 and 1836 keV) and ^{137}Cs (662 keV) allowing for a calibration in an energy spectrum large enough to account for possible non linearity of the detector. The BaF_2 crystals feature typically a good linearity and it was found that the use of a linear function for calibration is adequate.

Calibrations are performed at the beginning and end of a measurement and repeated approximately once a week. The energy calibration of the experimental data is performed by fitting the characteristic peaks in the calibration sources spectrum and produce an individual detector module calibration function.

A byproduct of the calibration is the determination of the characteristic α peak position due to the crystals impurity with radium isotopes and subsequent decay chain. This reference will be used to check for gain drifts that can happen during data acquisition.

Taking advantage of the discrimination features of the BaF_2 crystals, during the calibration we also look at the alpha spectrum for each detector. The goal of this procedure is to establish a long term gain stability check. The details of the stability check are explained later.

The whole information about the resolution and fitting errors of the calibration spectra are calculated and stored for later checking.

After performing the PSD, the γ-ray energy is obtained using one of the two following methods:

- Measured signal integral (integration time 3.5 μs)
- Fitted signal integration.

After performing the energy calibration for each detector module, the following characteristics are studied:

- Resolution
- Linearity
- Stability

5.2.4 Energy resolution

The energy resolution has been measured using a ^{60}Co source and at various sampling rates. To avoid a de-convolution problems, the resolution given in Table 5.1 corresponds to the FWHM averaged on the 1173 and 1332 keV γ ray lines of ^{60}Co. Figure 5.7 shows the fractional energy resolution of all detectors for the three different energies of the calibration sources.

Table 5.1: Fractional energy resolution for a ^{60}Co source at various sampling rates and using the measured or fitted signal integral.

Sampling rate (MHz)	Measured integral	Fitted integral
100	15.3%	15.0%
200	13.2%	12.1%
500	13.0%	10.9%

At 100 MHz, because of the too low sampling rate, the fast component signal is strongly suppressed, and so the PSD does not work. As a result, this sampling rate can definitively not be used in future experiment. As expected, the measured signal integral is almost sampling rate independent.

The FWHM is about 13% at both 200 and 500 MHz. On the contrary, the fitted signal results depend on the sampling rate. Because one adds a constraint on the pulse shape, resolution using the fitted signal is about 20% better at 500 MHz than the one obtained using the measured signal. From these results, all the following studied, will be performed by operating at 500 MHz, and by looking at the fitted signal. *These are the conditions used to acquire the ^{233}U data.*

Also, from the studies performed, it was found that the resolution is worse by about 10% for pile-up events.

5.2.5 Linearity

To assess the linearity of the each detector module, an energy calibration has been performed by computing the fitted signal integral, Q_{fit}, given by equation:

$$Q_{fit} = e\ A_{fast}\ \tau + A_{slow}\ (630 - \tau) \tag{5.3}$$

The following radioactive sources have been used:

- 511 keV γ ray line
- ^{137}Cs (662 keV)

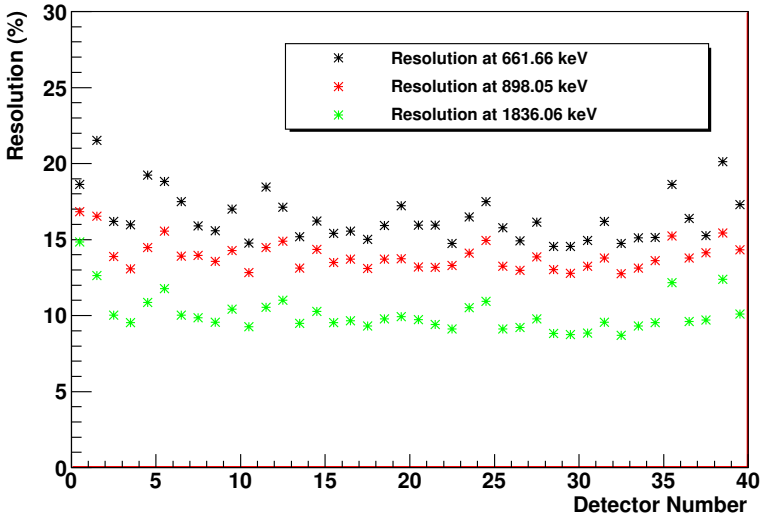

Figure 5.7: Resolution at three different energies for each individual detector module obtained with the Cs and Y calibration sources.

- ^{60}Co (1173 and 1332 keV)
- PuC (6130 keV)

The linearity has been estimated by looking at the regression coefficient, r^2, when performing a linear regression. For the all detectors, r^2 is better than 0.9999 indicating that non-linearities should be below 1%.

5.2.6 Stability

The energy stability has been checked for, using the 7.7 MeV α line coming from ^{214}Po decay shown in Figure 5.8 as red area. The ^{214}Po originates due to the Ra decay which is present in the BaF_2 crystals as an impurity. The energy resolution (FWHM) at this energy is about 12% and our goal is to detect an about 0.25% (Root Mean Square (RMS)) energy variation. The uncertainty on mean energy value, σ_E is given by:

$$\sigma_E = \frac{\sigma}{\sqrt{N}} \tag{5.4}$$

where σ corresponds to the RMS associated with the 7.7 MeV α peak ($\simeq 12/2.35\%$), and N is the number of counts inside the peak. The number of counts needed to obtained the desired accuracy is then:

$$N = \left(\frac{\sigma}{\sigma_E}\right)^2 = \left(\frac{12/2.35}{0.25}\right)^2 \simeq 420\ counts \tag{5.5}$$

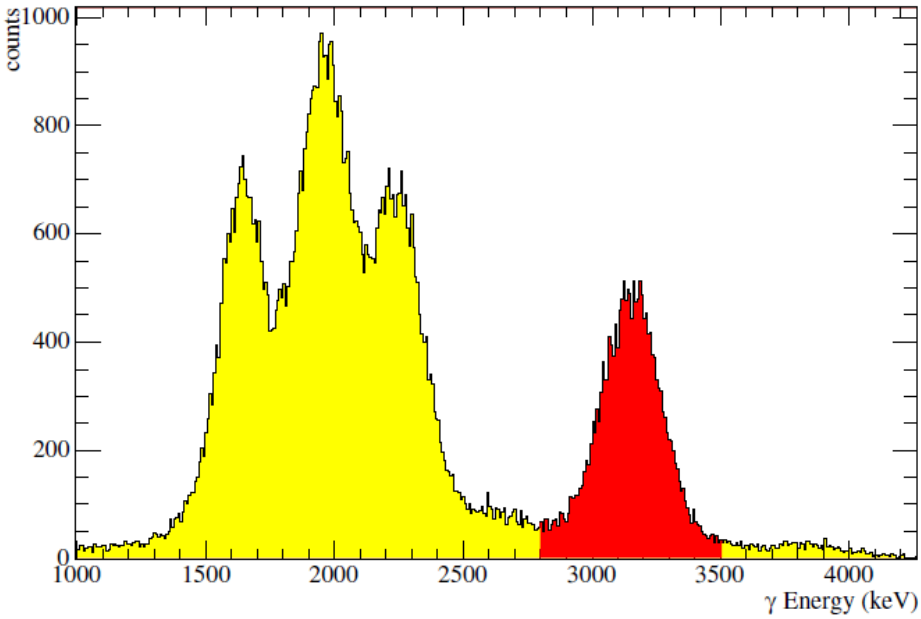

Figure 5.8: Alpha energy spectrum used (red area) to check for energy calibration stability.

Since the α counting rate for each detector is about 200 counts/s [114] and about one quarter are associated with the 7.7 MeV α peak, the time, T, needed to reach this number of counts is:

$$T = \frac{N}{200/4} = 8.4\ s \tag{5.6}$$

At 500 MHz the signal is recorded during 16 ms. The number of proton pulses, N_P , needed is:

$$N_p = \frac{T}{16 \times 10^{-3}} = 525\ pulses \tag{5.7}$$

Following this rough study, we have recorded the mean energy associated with the 7.7 MeV α peak from ^{214}Po decay, every 500 proton pulses. α particles having energies (given by γ calibration) from 2.8 to 3.5 MeV have been considered (red area in Figure 5.8). If one assumes an average value of 2 pulses per super-cycle (16.4 s) 500 pulses is about one hour measurement.

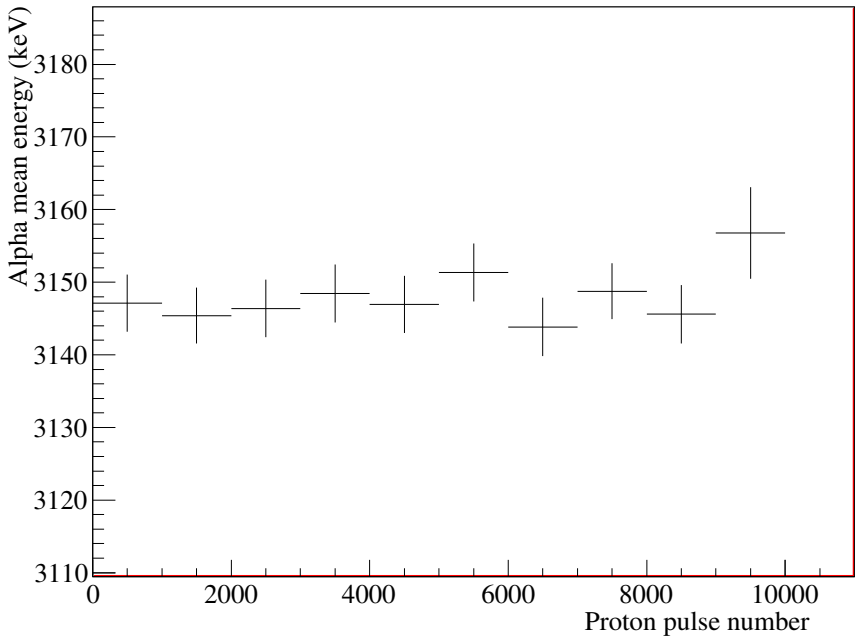

Figure 5.9: Alpha mean energy spectrum for detector 3.

As can be seen on Figure 5.9, the uncertainty on the 7.7 MeV α peak mean energy is about 6 keV, for an average value of about 3150 keV (relative to γ calibration), corresponding to gain variations below 0.25%.

5.3 TAC performance

5.3.1 Coincidence using the time window technique

When using the time window coincidence technique, one must assess which is the time window where real event coincidences exist. This is assessed by analyzing the time between consecutive events (Figure 5.10) in any of the detection modules of the TAC and looking for the minimum time distribution between all detectors. Figure 5.10 shows this distribution obtained during a ^{233}U sample measurement with a nominal (i.e. 7×10^{12} protons/pulse) proton beam.

Two regions can be clearly seen on Figure 5.10. From 0 to 6 ns the distribution decrease by more than one order of magnitude. This fall-of is characteristic of coincidence events. Above 6 ns it becomes almost flat, as expected

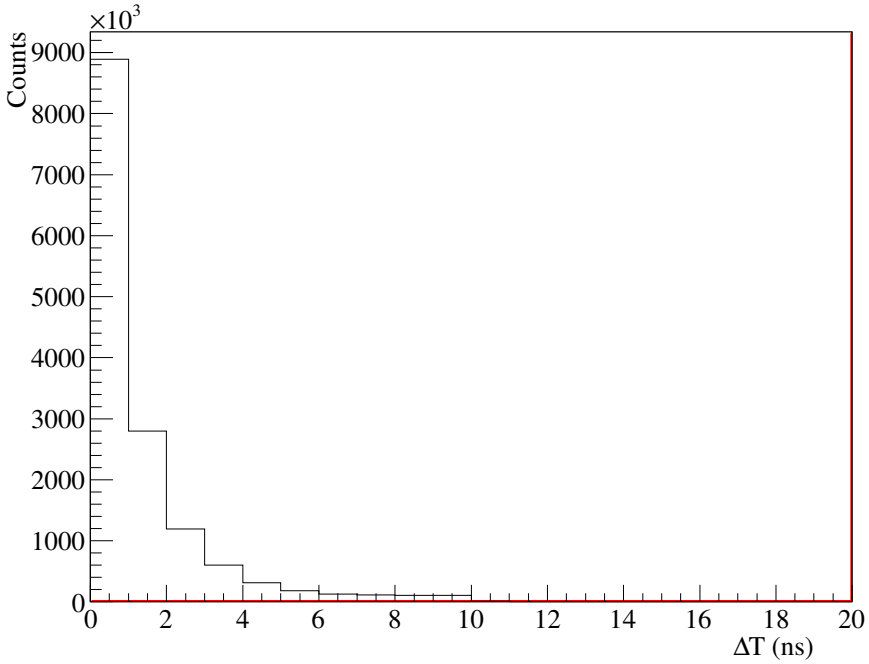

Figure 5.10: Coincidence time window spectrum. The spectrum is truncated at 10 ns due to data analysis selection criteria.

for uncorrelated events. A coincidence window longer than 10 ns would favor only the addition of uncorrelated events with correlated events leading to the distortion of the real signal.

5.4 Event reconstruction in the TAC

5.4.1 Zero suppression algorithms

The first step in acquiring data is to record the signals seen in the TAC. This is done for each individual detector module by digitalizing the signals and store them in local disk servers. The digitalization, produces a "movie" that should be understood in this context as the full recording of each detector module output without any cuts or analysis, showing signals (any interaction with the detector module) or the baseline for all the time where the acquisition system is active. Despite the advantages that this procedure can bring to the analysis of problems with the acquisition system, it is very memory consuming as many time regions of the "movie" have no signals. To save memory without loosing

information, a data reduction algorithm called Zero-Suppression, analyzes the movie of each detector module and removes all regions below a given threshold. In the regions with signals, a part of the base line is kept before and after the signal.

The resulting raw data is stored in the CASTOR facility [119] at CERN where the raw data is transformed in Data Summary Tape (DST) using analysis routines specific for each detector as is the case of the PSD for the TAC. The DST contains all the physical quantities assessed upon the signal analysis and fitting but in a compressed binary form. For analysis purposes, the data is retrieve using a routine called DST2ROOT which migrates the data to a easier readable format (ROOT files [120]) used in the analysis containing only the necessary variables. The ROOT files contain all the extracted parameters associated with the signal processing as given in section 5.1.4 by using the TTree format of ROOT:

In Figure 5.11 a diagram of the data management and pre-analysis steps is shown until the events are reconstructed and ready for analysis.

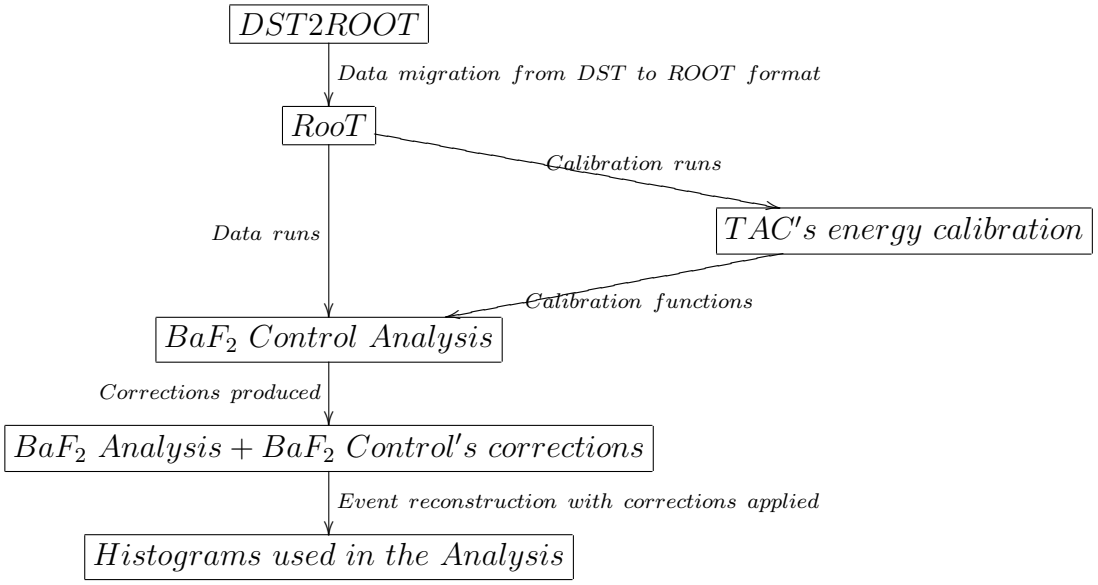

Figure 5.11: Scheme of the ^{233}U data processing from DST data to the histograms used in the analysis.

The first step performed once the data is in the form of a ROOT TTree which is a storage format native of ROOT, is to assess the energy calibration correlating the area of a signal detected with the specific energy. To do so, a

calibration is done using the data in the calibration runs which is acquired for standard calibration sources like Cs, or Y.

The previously assessed calibration will be used but not applied when doing the first loop over the ^{233}U data or other auxiliary data like empty canning, using the BaF_2 Control analysis routine.

5.4.2 BaF_2 Control routine

When starting to process the data, the BaF_2 Control routine, performs a check of the data using the energy calibration assessed previously and creates a correction factor for any possible gain drift. The corrections assessed are not applied immediately. Instead, the information is stored and applied using the BaF_2 Analysis routine.

5.4.3 BaF_2 Analysis routine

Is at this point that the signals are calibrated in energy and correct for any gain drift. The BaF_2 Analysis routine is the main routine for reconstructing the neutron capture and fission events from individual signals applying the time coincidence technique to the events. Some important parameters are recomputed for each event in the coincidence window namely:

- The TOF of an event is recomputed from the corrected (clock adjustments) time minus the pick-up time. The time is assessed from the time of the first signal that opens the coincidence window.
- Energy deposited in the crystal corrected by any known gain drift.
- Number of crystals with hits within the coincidence window.
- Total energy deposited in the TAC from hits within the coincidence window.

The events are reconstruct and stored in Histograms. A list of the main histograms produced and used in the analysis is shown below:

- 1D histogram with the TOF spectra in the vicinity of the gamma flash to have a precise determination of the gamma flash.
- 1D histogram with the total number of counts in the TAC vs TOF without any correction except for the noise rejection criteria as explained in section 5.2.2. This is used to assess the count rate for each TOF bin.
- 2D histogram with counts as function of the TOF and Total energy deposition for a given multiplicity criteria.

5.4.4 Single detector module analysis

From now on, the data analysis is performed only by looking at γ rays. At this point, the first thing to do is to check if each individual detector module has the expected behavior. A look at the gamma spectrum of a single detector module is a quick and efficient check and can help understand the whole analysis procedure.

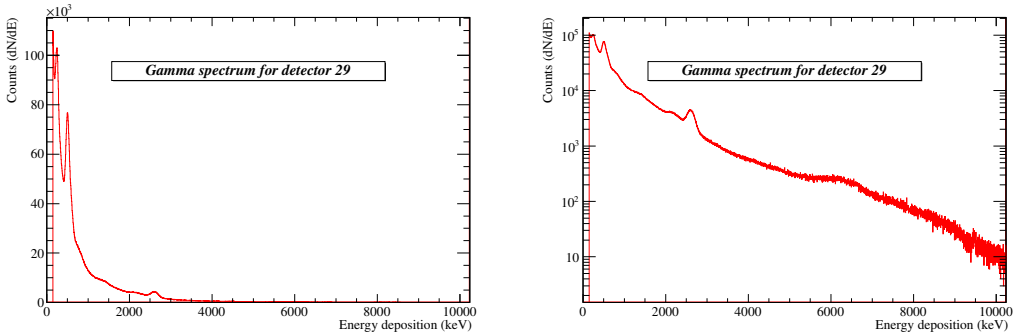

Figure 5.12: Gamma spectrum for a single detector displayed in linear (left) and logarithm (right) scale.

When looking at a single detector without any correlation or time coincidence analysis, all the events with multiplicity equal to 1 but also single gammas from events with higher multiplicities are scored. Assuming that gamma emission is isotropic, this spectrum must be similar in all detector modules.

In Figure 5.12 (left) its possible to see a set of peaks being the most energetic one the contribution from ^{208}Pb (2.614 MeV) which is a decay product of the ^{208}Tl and is related with the sample activity as will be detailed later. The peak at approximately 500 keV can be attributed to pair production and also to the $^{10}B(n, \alpha + \gamma)^{7}Li$ reaction which has a gamma with 478 keV. Moreover, (in the right plot) we can see the existence of some γ rays with higher energy than the sample related activity γ rays and the capture binding energy (approximately at 6.9 MeV) . This is due to capture in structural materials, fission and even cosmic background.

5.4.5 Total energy deposition in the TAC

Once all 40 detector modules are checked to be working as expected, one can start looking at the whole TAC system data analysis as a single detector. With the possibility of correlating signals between individual detector modules, the event analysis can achieve a higher level of discrimination.

In the case of neutron capture, events are characterized by the emission of gamma radiation during the deexcitation of the compound nucleus to the ground level. The γ rays (more than one) are emitted in a very small time interval of the order of few ns. The number of emitted γ rays is denominated "capture event multiplicity".

5.4.5.1 Total energy deposition and multiplicity assessment using the coincidence time window

Neutron capture, fission and sample related activity events are also characterized by higher than 1 multiplicities. To detect and reconstruct such events and clearly identify them, we take advantage of the TAC's 4π solid angle and the good segmentation given by the 40 BaF_2 detector modules. The solid angle permits to detect almost all the gammas emitted in an event while the segmentation of the detection system allows the identification of background events with energies close to the binding energy, due to the characteristic multiplicity equal to 1.

The event reconstruction algorithm consists of:

- order the events in time
- Taking the first gamma ray detected in the TAC and identify the time and detection module where it occurred.
- Search the remaining 39 detection modules for events occurring in the same time plus the time coincidence window (10 ns).
- Add the number of detection modules with signals to calculate the event multiplicity.
- Add the energy of all individual gamma rays to assess the total energy deposition.
- Search for a new event by looking for the next gamma ray detected after the time of the previous gamma ray plus the time window.

The time interval used to search for coincident detected gammas in each detector modules is denominated as "time window" for coincidences.

A scheme of the time window application to the data flow can be seen in Figure 5.13. The assessment of the event multiplicity is also displayed. Important to note that for every signal, a time window is opened except if the signal is already inside a previous time window due to coincidence. In Figure 5.13, some time windows have been omitted to simplify the understanding.

All events are "tagged" with multiplicity equal to the number of gammas detected in the TAC. If more than one gamma is found while the coincidence time window is open, the event is "selected'.

To be sure to detect all the gammas from the capture events, one should opt for the largest possible coincidence time window. This is constrained by the

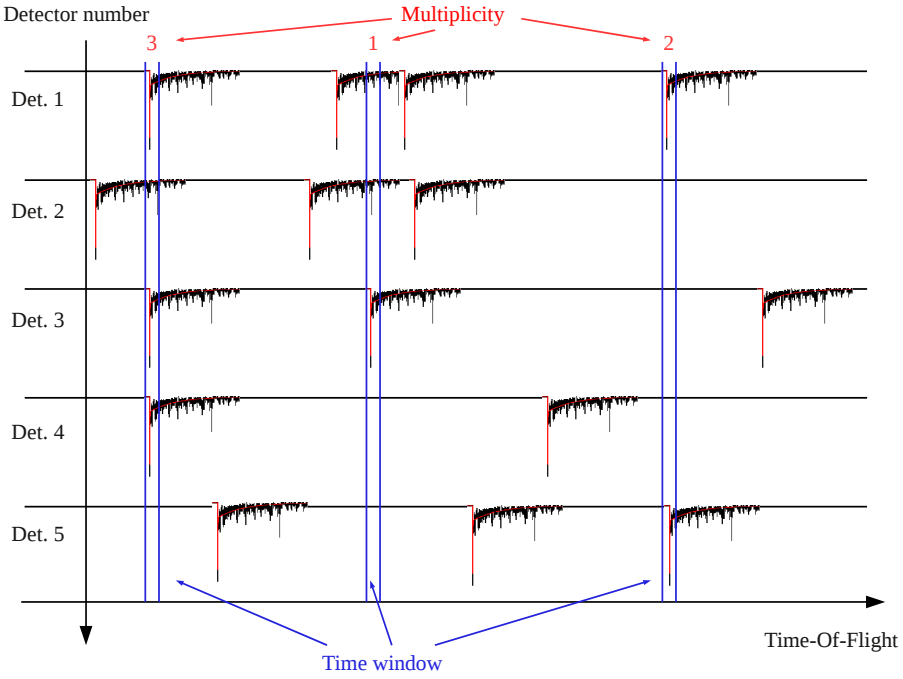

Figure 5.13: Scheme of the coincidence window applied in the TAC's data analysis.

rate of events happening as we aim to isolate each event instead of adding them all. The coincidence time window is as large as possible avoiding being too large to count more than one event. In the particular case of n_TOF, where capture, fission, sample related activity and scattering events compete, the time window must be scaled down to avoid the addition of background events with other events. The value found that optimizes the number of detected capture and fission events without losing many due to pile up with background was 10 ns.

If one applies the multiplicity selection criteria to remove uncorrelated background events and reconstruct the events with higher multiplicity, this leads to a new spectrum corresponding to the total energy deposition in the TAC (40 detector module system) as a function of time. Unfortunately, the spectrum is contaminated with background (non-capture events), and we can see many contributions from other reactions as shown in Figure 5.14).

Looking at the total energy spectrum for all the 40 detectors (Figure 5.14), and taking in consideration that multiplicity higher than 1 is used in the analysis, one can see:

- The sample related activity peak at approximately 3.2 MeV.
- The capture binding energy for the ^{233}U at approximately 6.9MeV.

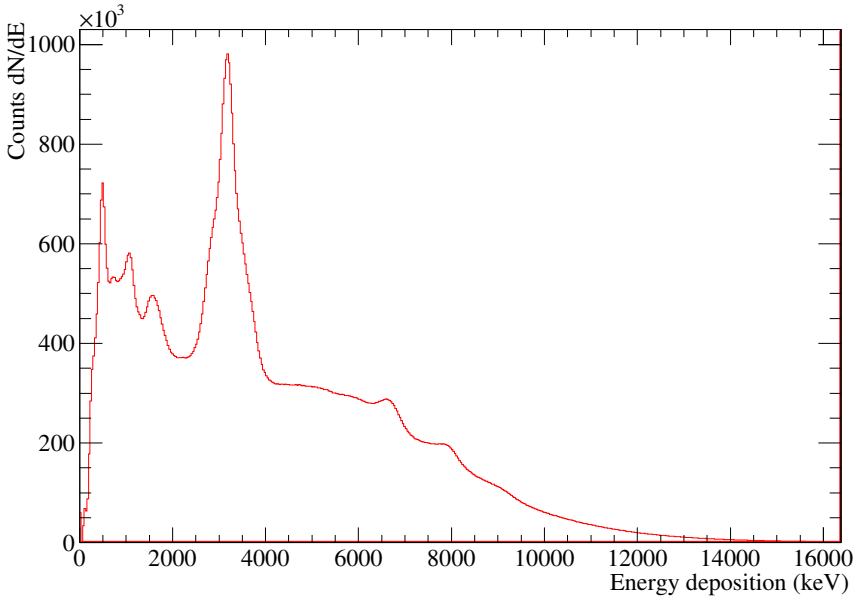

Figure 5.14: Total energy deposition in the TAC (40 BaF_2 detector modules) with multiplicity higher than 1.

- The neutron capture in the Barium of the detectors at approximately 8 and 9 MeV.
- The exponential tail at energy deposition higher than 9 MeV due to the fission events.

The sample related activity presents itself as narrow peak and fission has the shape of an exponential tail.

5.5 Event selection criteria

A typical way to discriminate between events originating from different nuclear reactions is to apply selection criteria to the physical quantities extracted from the signals detected to separate the contribution of one nuclear reaction from the other. These selection criteria can be applied to any physical quantity. A good example is the discrimination between α and γ signals applying selection criteria on the magnitude of the fast and slow component of each signal. To continue, it's important to understand which selection criteria can be applied to the detection modules or to the TAC in order to improve our signal to background ratio where the signal corresponds to the gammas emitted by capture events and the background are all competing reactions. The set of selection

criteria that optimize the signal to background ratio have been studied in terms of multiplicity and detections threshold and is detailed in the next sections.

5.5.1 Event gamma multiplicity

The gamma multiplicity used in the analysis has been addressed before and defined as higher than 1 but not discussed. This choice has to do with the nature of the capture events that we want to isolate from the background. The background definition for the analysis process here discussed can be defined as the uncorrelated events detected. This includes all detected γ rays that occur at a given time and for which there is no other gamma detection occurring within the coincidence window. In the case of ^{233}U capture, the multiplicity equal to one is highly improbable due to the high number of nuclear levels available to be populated during the deexcitation process.

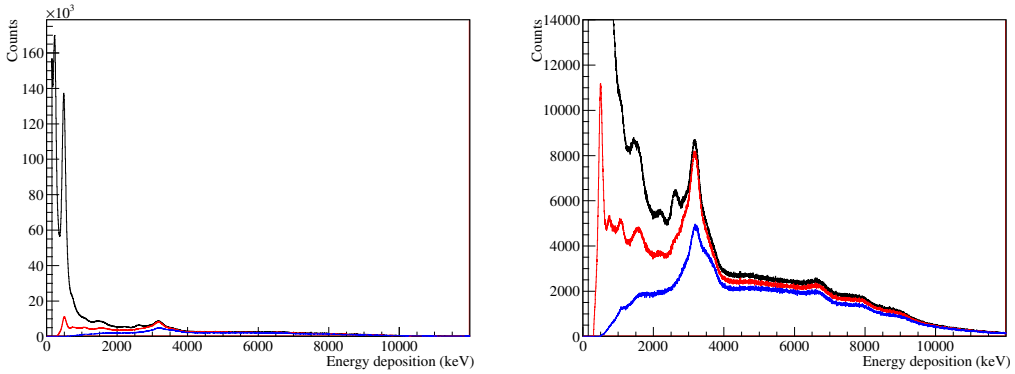

Figure 5.15: Different selection criteria in gamma multiplicity applied to the energy deposited spectrum. No selection criteria in multiplicity (black). Multiplicity higher than 1 (red) and higher than 2 (blue). Right plot is a zoom of the left plot along the y axis.

In Figure 5.15, the total energy deposition in the TAC is shown for different selection criteria applied on the gamma multiplicity.

For multiplicity, the condition that increases the signal to background ratio was found to be higher than 1 as shown in Figure 5.15.

5.5.2 Single gamma energy threshold

The energy threshold can be applied to each single detector module or to the total energy deposited in the TAC. Based on the analysis done and shown in Figure 5.16, the threshold for single gamma that improves the signal (top of

the resonances) to background (deep part between resonances) ratio without loosing the characteristic signature of capture events was 150 keV.

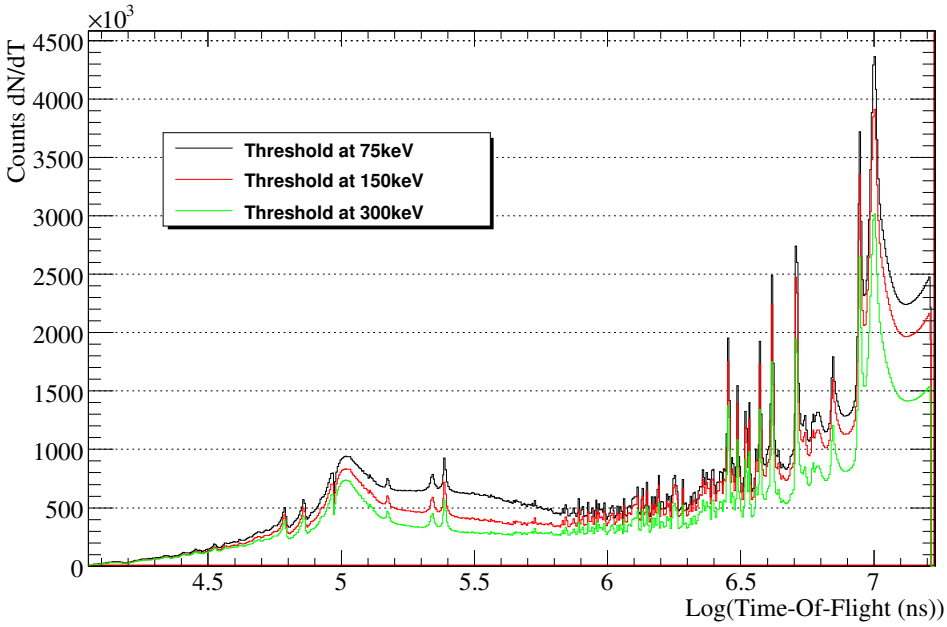

Figure 5.16: Time spectrum showing the resonant behavior of the data and the effect of different gamma energy detection thresholds.

Looking at Figure 5.16 the introduction of a 300 keV threshold seems to be the best choice but Figure 5.17 shows that it excludes too many gammas coming from capture events. This threshold excludes important part of the background but the removal of capture contributions is also significant, causing the binding energy peak to disappear from the energy deposition spectrum.

Its important to stress that a higher threshold can improve the signal to background ratio but completely change the energy deposition signature of each competing reaction and affect the ability to discriminate between competing reactions. This can be seen in Figure 5.17.

5.5.3 Thresholds in minimum and maximum total energy deposition

The imposition of minimum and maximum thresholds for total energy deposition was foreseen as a way to separate the capture events from fission events together with other selection criteria. The goal of the thresholds in minimum and maximum total energy deposition is to completely isolate the capture

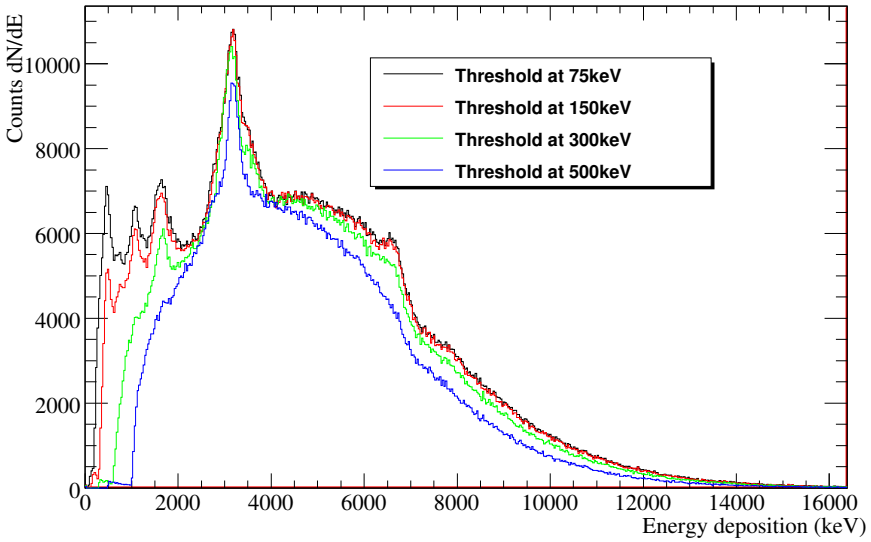

Figure 5.17: Effect of different gamma energy detection thresholds in the energy deposition spectrum.

contribution from the fission and activity contributions. The results obtained using this methodology are shown and discussed in Section 5.8.

5.6 Sample characterization

The ^{233}U sample used in n_TOF to measure the neutron capture cross section has the dimensions of a 10 mm diameter disc. The ^{233}U mass is deposited on an aluminum backing and encapsulated with Titanium. The final sample assembly can be seen is Figure 5.18 together with the sample holder made of kapton foil used to center the sample inside the TAC and avoid as much as possible the interaction of the neutron beam with structural materials. Figure 5.19 shows the sample assembly layout.

The ^{233}U sample although highly enriched is not a pure isotopic sample (as shown in Table 5.2) and this together with the significant amount of other materials like Al and Ti constituents of the sample backing and canning respectively, intersect the neutron beam and lead to an increase in the complexity of the data analysis and also to the need of informations about the competing reactions cross sections and background in the Total Absorber Calorimeter (TAC).

Due to the results obtained with the analysis of the measured sample re-

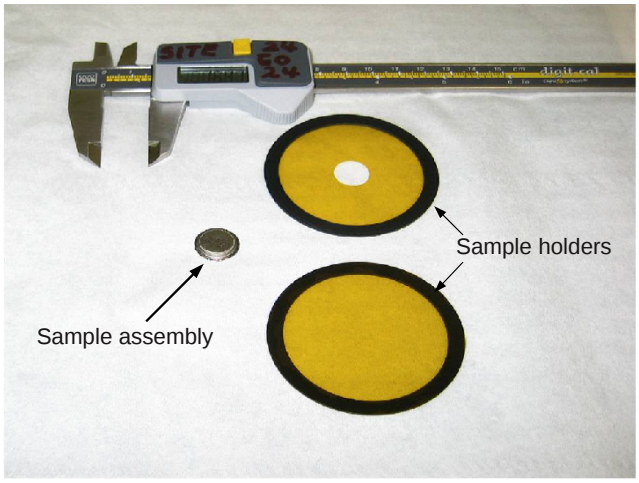

Figure 5.18: ^{233}U sample assembly (1 cm diameter) and sample holders.

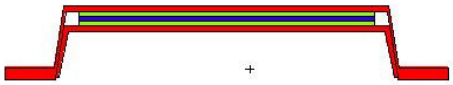

Figure 5.19: Sample assembly scheme showing the ^{233}U mass (blue), Ti encapsulation (red) and Al backing (green).

Table 5.2: Details of the sample assembly used.

Sample		Isotopic Composition		Canning	
Property	Value	Isotope	Atomic %	Material	Mass (mg)
U_3O_8 mass	108 mg	^{233}U	99.01	Ti mass	277.1
^{233}U mass	91 mg	^{234}U	0.74	Al mass	70
Diameter	10 mm	^{235}U	0.23		
Thickness	n.a.	^{238}U	0.04		
atoms/barn	10^{-3}	^{232}U	n.a.		

lated activity in n_TOF, it was decided to add an impurity of ^{232}U to the Table 5.2. The amount of the impurity is unknown and the origin will be discussed in the next section.

5.6.1 Sample's activity

As mentioned before, the ^{233}U is highly enriched but not pure, containing an unquantified impurity of ^{232}U which is a radioactive isotope with a half-life of 70 years. The origin of the ^{232}U is related probably with the way the ^{233}U mass/sample was build from ^{232}Th by irradiation in a nuclear reactor.

The ^{232}U decay mode is typically α emission although it can undergo spontaneous fission. In the case of α emission, the decay path is complex as shown in Figure 5.20.

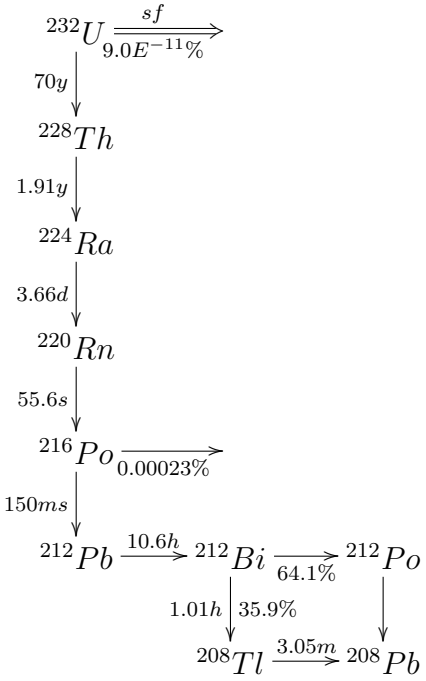

Figure 5.20: ^{233}U sample's activity resulting from ^{232}U impurity. The main source of the activity seen is the ^{208}Tl which comes from the ^{232}U probable impurity.

The sample related activity is dominated, with the applied multiplicity criteria (M>1), by the ^{208}Tl decay to ^{208}Pb which have high energetic γ lines

as can be seen in Figure 5.21. Note that the better TAC resolution is due to the use of only 8 detection modules instead of 40.

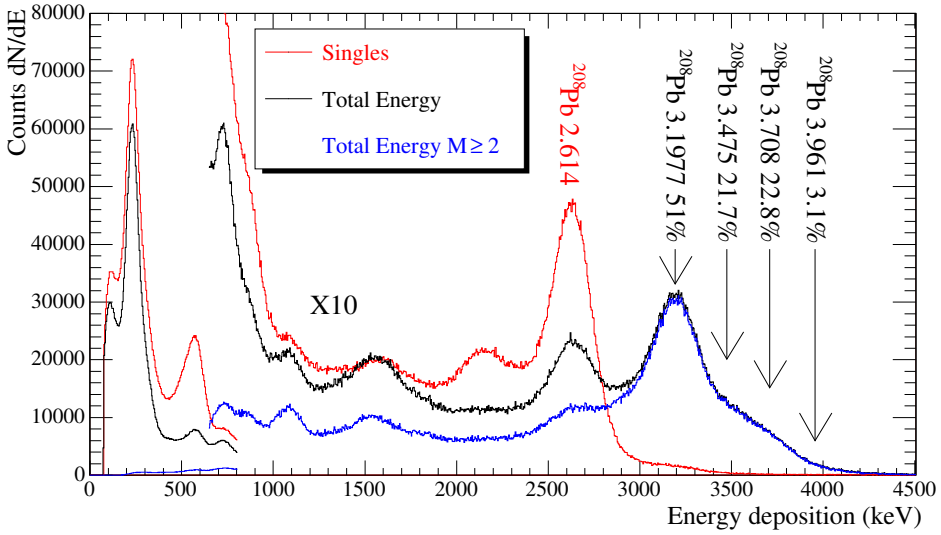

Figure 5.21: Activity measurement of the ^{233}U sample with the TAC and a simple analysis of the same spectrum imposing selection criteria in multiplicity (M=1 and M>=2.

5.6.2 Sample's homogeneity

One very important factor when measuring neutron cross sections is the beam intersection with the sample and therefore two important factors that must be taken into account. One being the neutron beam profile which will be discussed later and the other is the sample's homogeneity. In the case of the ^{233}U sample and to investigate the distribution of the U mass inside the canning assembly, an X-ray picture was taken as shown in Figure 5.22. No analysis was performed to assess the U mass thickness and distribution and therefore its only possible to speculate about this. On the other hand, the results obtained from the X-ray image show a size approximately of 10.2 and 10.0 mm for the horizontal and vertical profile respectively which is acceptable. Moreover, the same 0.2 mm difference is present in all samples measured, leading to the conclusion that it may by related with the measurement rather than with the sample.

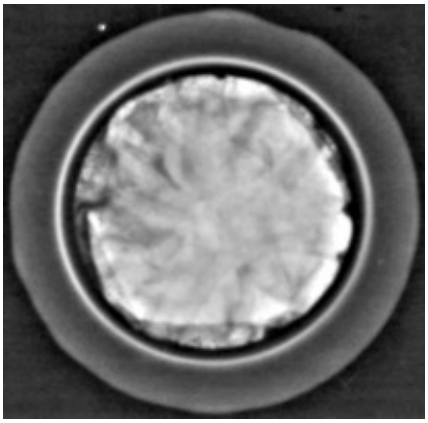

Figure 5.22: X-ray picture of the ^{233}U sample plus canning.

5.7 Detector's gain monitoring

As mentioned before, the neutrons coming out from the spallation target are preceded by relativistic radiation coming directly from the spallation processes and due to many interactions and second order particles produced in the shielding and collimation systems, the effect in the detectors is overkilling making then blind to the following nuclear reactions happening in the sample. This relativistic radiation burst is denominated as γ-flash and it takes about 100 μs for the detectors to recover the base line. Once the detectors recover enough to be able to detect the desired nuclear reactions, there is no guarantee of an accurate energy determination. The way found to check the gain stability of the detectors was by looking at the activity peak energy (3.1977 MeV) which should always be constant despite the neutron energy (or TOF).

In the particular case of the ^{233}U, the sample has an impurity of ^{232}U which increases the sample radioactivity. The activity measurement of the sample shows a spectrum with several lines characteristic of the decay scheme of the above mentioned isotope (Figure 5.21).

Considering the particular selection criteria used in the ^{233}U analysis (Multiplicity >1) and the high activity rate, the activity peak at 3.1977 MeV with 57% intensity can serve as reference for gain shifts along the period of the neutron energy spectrum. This peak is clearly visible and possible to be tracked in most of the neutron energy range of interest for the ^{233}U cross section analysis.

A routine has bean implemented to fit the activity peak and determine the variations in the activity peak energy vs the neutron energy. The variations in the energy of the activity peak are related with gain variations and plotting this against the neutron energy shows the time dependence as neutron energy

is related with time-of-flight.

An energy shift induced by the higher count rate at the resonance was already foreseen and the correction implemented in the energy deposition analysis routine. Even with this correction implemented a significant amount of energy shift was still present.

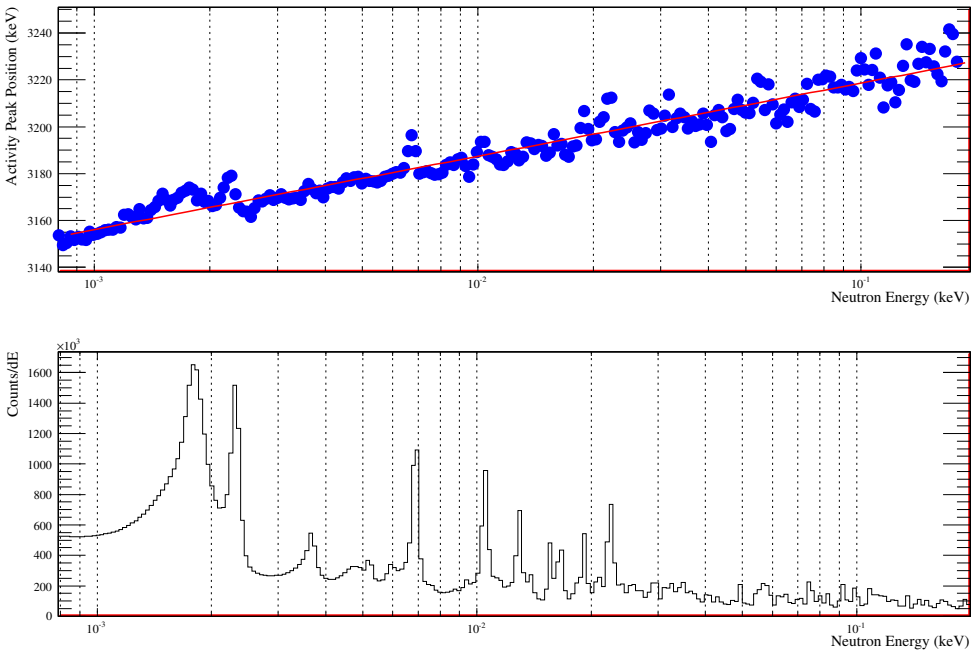

Figure 5.23: Activity peak shift in energy vs the neutron energy.

Figure 5.23 shows the evolution of the activity peak energy with the neutron energy in each neutron beam pulse. The results are very interesting and show a long gain decay constant associated with the already expected effect due to higher count rate in the resonances.

This effect has been studied and a correction patch was added in the "BaF2Analysis" routine to correct the energy deposition spectrum.

The gain variation with the count rate has been studied and found to be too small to correct (0.5% variation) as shown in Figure 5.24 and to have any effect in the decomposition routine.

5.8 Event analysis - first attempt

The methodology here discussed to reconstruct the neutron capture yield is based on a series of imposed selection criteria to increase the capture to fission

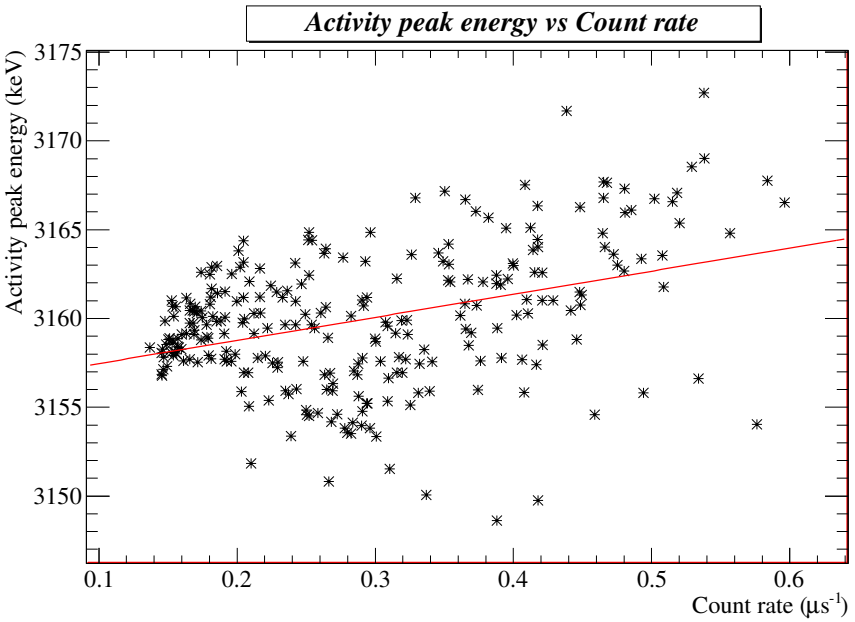

Figure 5.24: Variation of the TAC's gain with the count rate.

ratio and also to reduce the contribution due to the sample related activity.

Several selection criteria where studied and implemented. The detection threshold at 150 keV was kept from the previous analysis (Figure 5.16). A new threshold for the lower total energy deposition (Edep) was implemented at 4 MeV. With this threshold, the contribution from the sample activity is removed.

An upper energy deposition threshold was also implemented in order to mitigate the contribution from fission and from capture events occurring in the structural materials that are characterized by a higher binding energy. This threshold cuts every event having a energy deposition above 7 MeV as can be seen in Figure 5.25.

Figure 5.25, shows a comparison of the total energy deposition spectra for the applied selection criteria in gamma energy threshold, total energy deposition and multiplicity (red spectrum).

Multiplicity selection criteria have been implemented taking in consideration the different multiplicity distributions for capture and fission. Capture has a lower average multiplicity comparing to fission in the particular case of ^{233}U. With a higher multiplicity cut at 5 the capture contributions are left almost unaffected. On the contrary, the fission is affected allowing to improve the capture to fission ratio as can be seen by the variation of the ratio of the first and second (counting from the right) resonance in Figure 5.26. The lower

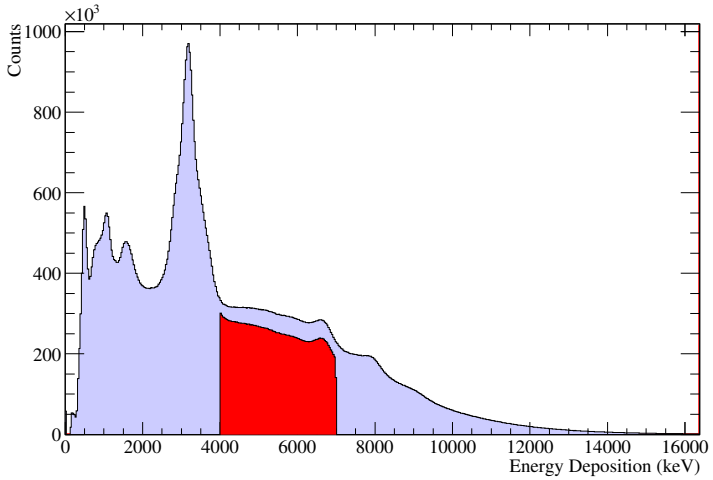

Figure 5.25: Comparison of the total energy deposition spectra for the applied selection criteria in gamma energy threshold, total energy deposition and multiplicity. The red spectrum corresponds to the selection criteria in energy deposition ($4 < \text{Edep(MeV)} < 7$) and multiplicity ($1 < \text{M} < 6$). The light blue spectrum as only selection criteria in multiplicity ($\text{M} > 1$).

multiplicity threshold is kept at 1 to avoid severe rejection of events from the capture contribution.

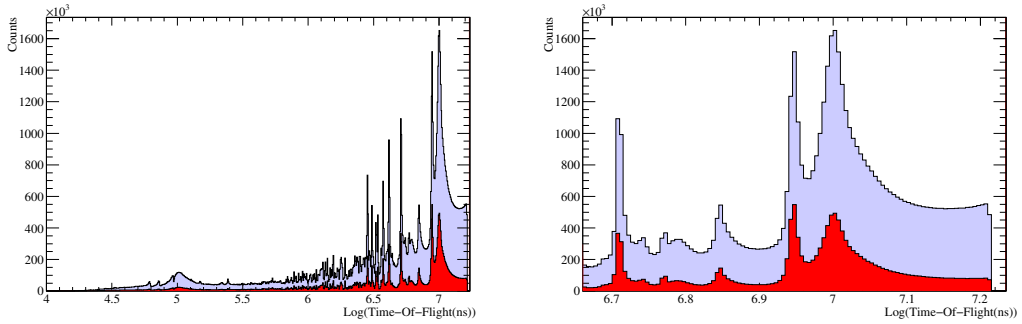

Figure 5.26: Time-Of-Flight spectrum comparison for applied selection criteria in total energy deposition and multiplicity. The red spectrum has condition in energy deposition ($4 < \text{Edep(MeV)} < 7$) and multiplicity ($1 < \text{M} < 6$). The light blue as only selection criteria in multiplicity ($\text{M} > 1$).

The major problem with this methodology is related with the need to completely isolate the capture contribution from the rest of the contribution such as fission, and scattering. With the set of selection criteria previously

applied this seems out of reach. A possibility would be to use the ENDF/B-VII.1 neutron induced fission cross section which is relatively well known to subtract the fission component. Despite of the possibility of obtain results with this methodology, this would imply that the neutron capture measurement at n_TOF would depend on previous measurement and the goal of this measurement was exactly the opposite as it was aimed at determining a completely independent and highly accurate cross section in a broad energy range. Moreover, the scattering effect must also be accounted for, leading to another dependency on a previous measurement.

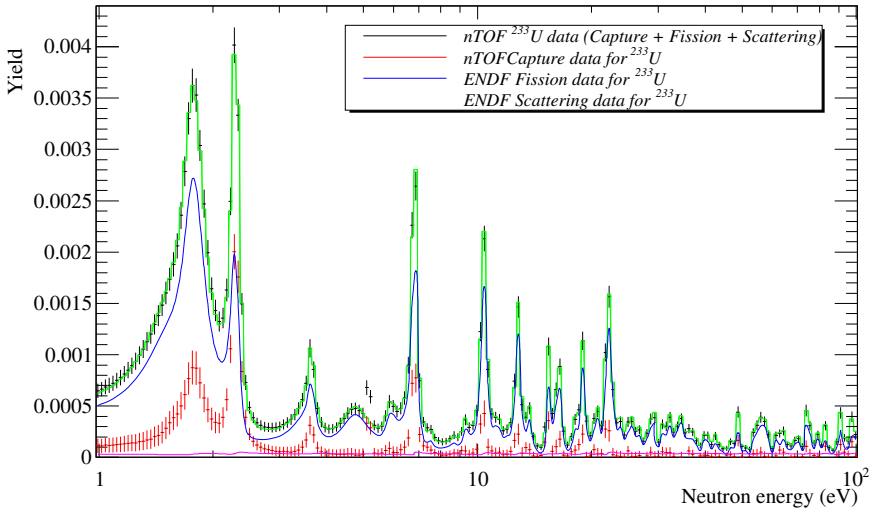

Figure 5.27: Reconstruction of the ^{233}U neutron capture yield using the fission and scattering cross section from ENDF/B-VII.1 library.

Figure 5.27 shows the extraction of the ^{233}U capture cross section by reconstructing the n_TOF data based on the knowledge of the fission and scattering cross sections from the ENDF/B-VII.1. A good agreement can be observed between the experimental data and the reconstruction except at 5.5 eV where a contribution from ^{234}U capture cross section is visible.

A comparison of the ^{233}U capture cross section obtained in n_TOF with the ENDF/B-VII.1 library shows agreement despite the limitation of the methodology as shown in Figure 5.28. As mentioned before this methodology depends strongly on the good knowledge of the fission and scattering cross sections and the results are highly correlated with the ENDF/B-VII.1 data which is not desirable. A methodology to measure the capture and fission cross sections highly independent on available data is of paramount importance if one aims at adding new information or strong validation to the already existent data.

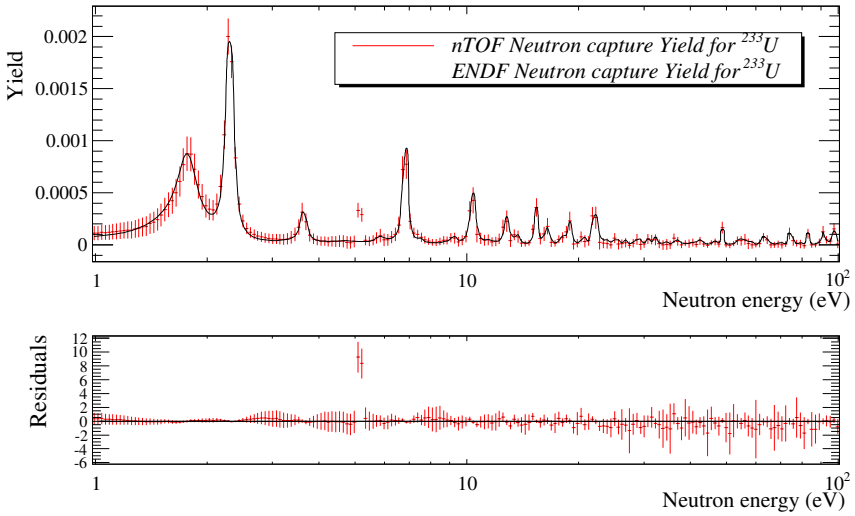

Figure 5.28: Comparison of the ^{233}U capture cross section obtained in n_TOF with the ENDF/B-VII.1.

Chapter 6

CSD - A new methodology for the ^{233}U data analysis

Using the ^{233}U sample data taken in the energy range up to about 5 keV, a preliminary analysis showed that the TAC response provided the information for reconstructing the γ cascades from neutron-induced capture and fission events properly. It also showed that a traditional approach, where the applied selection criteria are based on cuts in γ multiplicity and on the total deposited energy would not suffice to discriminate between neutron capture and fission for determining an accurate neutron capture cross section, mainly due to the very broad range in multiplicity and in total deposited energy of the fission γ-rays that dominate the capture channel.

Apart from the γ-ray cascades emitted in (n, γ) and (n, f) reactions, backgrounds are due to:

- γ-rays from neutron capture of neutrons scattered in the sample assembly.
- Sample related activity.
- An uncorrelated component composed of in-beam γ-rays scattered by the sample.
- Ambient background in the experimental area.

All these components have to be considered in the analysis of the ^{233}U data.

First, a short time window of 10 ns was chosen for selecting γ-ray cascades from capture events. With this choice, the number of detected capture events was optimized with respect to background by pile-up of uncorrelated γ-rays. During data acquisition, for each BaF_2 module an electronic threshold corresponding to a minimum energy of 150 keV for single γ-rays was imposed to improve the signal to noise ratio without loosing the characteristic multiplicity information of capture and fission events. In the following, the term *multiplicity* denotes the number of BaF_2 modules contributing to an event.

Backgrounds due to uncorrelated events, particularly the in-beam γ-ray component, which consists mostly of single low energy γ-rays below 2 MeV, could be efficiently reduced by rejecting events with multiplicity of one.

With these selection criteria, the TAC energy response to the interaction of neutrons with the ^{233}U sample is displayed in the bottom right panel of Figure 6.1. The pronounced peak in the total energy deposition at approximately 3.2 MeV corresponds to the γ activity of the sample (Figure 6.1, bottom right). The signature of the sum energy of the capture cascade in ^{233}U, which corresponds to the Q-value, appears at approximately 6.9 MeV. At higher energies, capture events in the barium crystals contribute around 8 and 9 MeV, while the high energy part of the γ-rays from neutron induced fission extends up to 16 MeV.

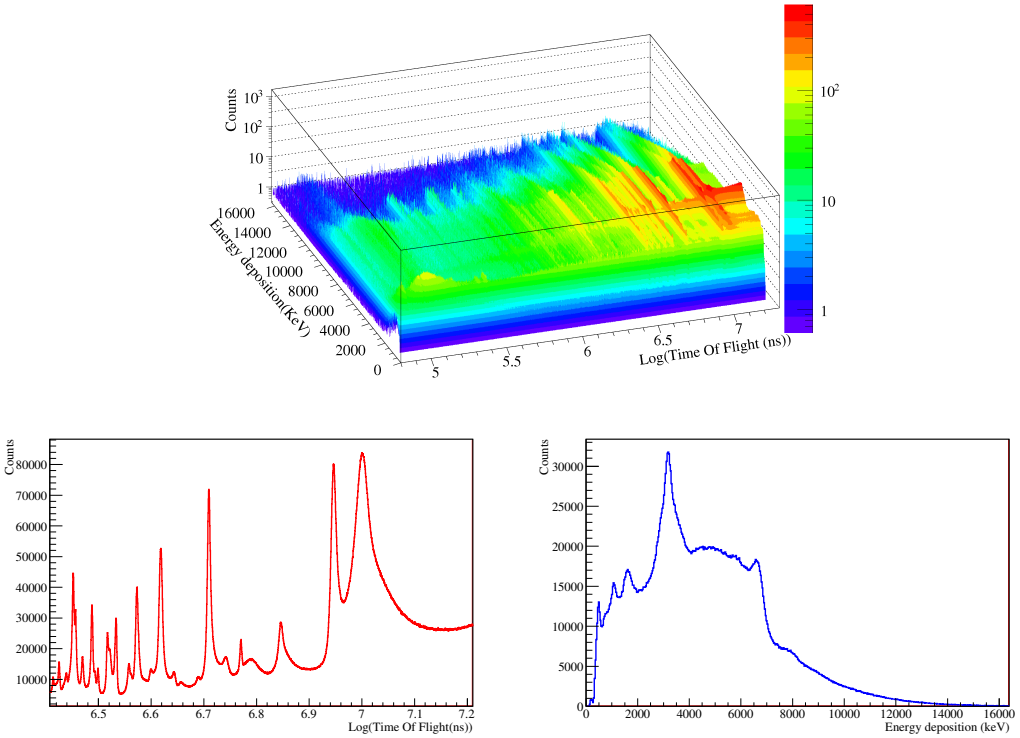

Figure 6.1: Plot of the data in a 2D histogram (top) and projections on the time-of-flight (bottom left) and total energy deposition (bottom right) axes.

6.1 Calorimetric Shape Decomposition (CSD) method

The identification of neutron capture events is complicated because multiplicity and total energy distributions are strongly dominated by the neutron induced fission channel. Additionally, the capture/fission ratio is only about 1/10 on average in the energy range studied here. Therefore, selection criteria based on energy deposition and multiplicity alone are not sufficient to discriminate between the two reactions. This leads to the need of a different analysis method based on characteristics that are unique for each reaction [121].

The specific features of the γ-ray cascades from capture and fission reactions studied in this work are summarized in Table 6.1.

Table 6.1: Neutron capture and neutron induced fission characteristics for energy deposition (Edep) and multiplicity (Mult) distributions. Data obtained from the analysis and constrained by the here-above mentioned event selection criteria.

	Low Edep keV	High Edep keV	Average Edep keV	Low Mult	High Mult	Average Mult
Capture	300	6900	4630	2	6	3.69
Fission	300	16000	4955	2	20	5.5

The characteristic feature found to be unique and useful was the shape of the total energy distribution in the TAC, to which capture and fission events contribute linearly independent from each other. Using the CSD method, the contributions of the different reactions are discriminated solely by the TAC energy response, independent of selection criteria. It only requires to know the open reaction channels and the respective energy deposition spectra, because these are reflecting the specific physics of each reaction. Even if the mean energy deposition for capture and fission are similar, the shape of both spectra are different.

The following assumptions must be verified in order to use the CSD method:

- The TAC energy response to neutron capture and neutron induced fission is assumed to be the same for each resonance (i.e. neutron energy independent). The reason behind this is that the large intrinsic efficiency of the TAC makes the total energy deposition highly independent from the electromagnetic de-excitation pattern.
- The coincidence time window is small enough to avoid the addition of

different contributions. There are two distinct effects: the summing due to the coincidence window and pile-up in each individual crystal. By reducing the coincidence time window, one can mitigate the sum of γ-rays from two distinct events occurring very close in time. The low counting (below 1 keV the count rate remains below 1.2 counts/μs and below 100 eV the count rate does not exceed 0.7 counts/μs) rate in the neutron energy region of interest contributes also to mitigate the possibility of pile-up in the crystals.

- The shape of each contribution is linearly independent from the others and the total energy deposition spectrum can be expressed as a linear combination of the individual contributions.

Figure 6.2 shows the data analysis procedure using the aforementioned CSD method.

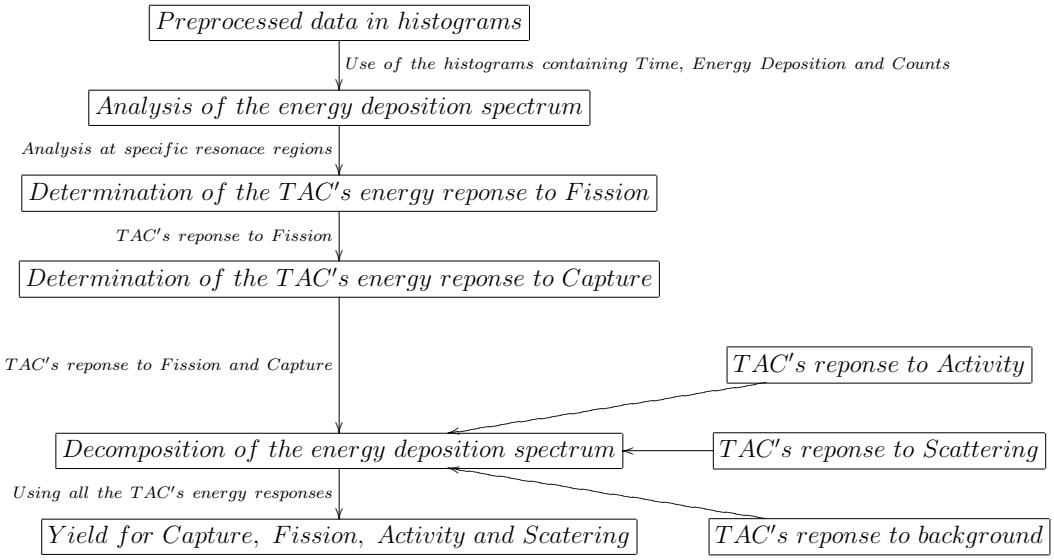

Figure 6.2: Methodology scheme for the ^{233}U data analysis.

The first step of the analysis consists in determining the TAC energy response to each competing reaction. Once all the characteristic TAC energy responses are known, one can express the TAC's total energy deposition spectrum as a linear combination of the TAC's response to the individual components.

More detailed information will be given in section 6.3 where the method is applied to ^{233}U with the TAC.

6.1.1 TAC's energy response for each competing reaction

To obtain the characteristic TAC energy response for each reaction, it is necessary to measure it alone or with applying a set of selection criteria that allows the discrimination. This is possible for most of the background components such as sample related activity, neutron scattering, ambient background of the facility without sample nor beam. The main difficulty rests in the neutron capture and neutron induced fission events.

To assess the difference between the response of the TAC for neutron induced fission and capture events, the energy deposition spectrum was studied at neutron energies where the resonant behavior of the cross sections leads to an enhancement of the fission or capture reaction.

Because the analysis of the TAC response is made by looking at the total energy deposition at given neutron energies, the data has been stored in a 2D histogram displaying the number of counts for each time-of-flight and energy deposition bin (Figure 6.1 top panel). This allows to analyze the energy deposition spectrum as function of the neutron energy (related to the time-of-flight) and study the resonant behavior of the data.

Figure 6.1 illustrates the resonant behavior as a function of time-of-flight. The distribution of the energy deposited in the detector for a time-of-flight corresponding to the 2.28 eV resonance is shown in the bottom right panel of Figure 6.1. The left panel is the distribution of the time-of-flight independent of the energy deposition in the detector. Selection criteria applied in energy deposition to discriminate between reactions occurring will provide the means to determine the individual cross sections.

It is important to stress that in the vicinity of a resonance, the non resonant contribution is supposed to remain constant in time, and therefore will not change from one time bin to another. The neutron scattering cross section of ^{233}U follows closely the resonant structure of the neutron capture and neutron induced fission cross section but due to the smaller amplitude of the resonant component can be considered constant (see Figure 5.1). A comparison of the projections of two different time bins will show differences only in the resonant fission and capture contributions, while the non-resonant components due to the sample activity and other uncorrelated backgrounds will be constant. The differential analysis of the projections of different time bins can then be used to isolate only the resonant components.

Because the capture and fission channels contribute to the resonances of ^{233}U, one needs an additional criteria for their separation. The evaluated ^{233}U neutron capture and fission cross-section data in the ENDF/B-VII.1 library [21] (Figure 6.3) clearly indicate that the fission component is always larger

than the capture component in the range comprehended from meV to MeV.

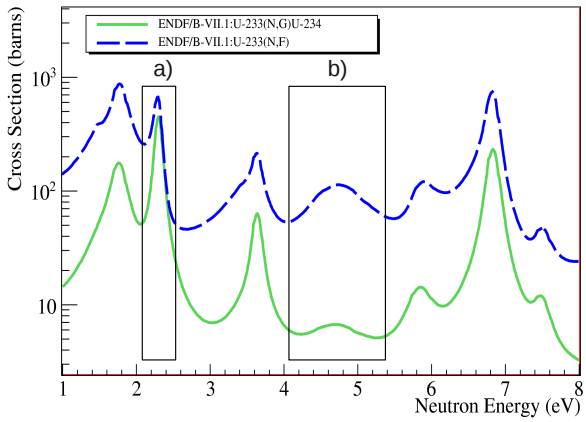

Figure 6.3: Evaluated neutron capture and fission cross sections for ^{233}U extracted from the ENDF/B-VII.1 library [21]. Resonances used to assess the TAC response to capture and fission events are indicated by boxes (a) and (b), respectively.

On average, the ratio between the fission and capture cross section is approximately 10, except for the second resonance at 2.28 eV, a) where capture and fission contributions are approximately equal. Another exception occurs at the 4.5 eV resonance, b) where the cross section is strongly dominated by the fission channel. This "fission only" resonance allows to assess the TAC energy response to fission.

6.1.2 TAC's energy response to neutron induced fission

To determine the energy response of the TAC to fission, the energy deposition pattern in the 4.5 eV resonance and in the surrounding deeps between the neighboring resonances have been analyzed as shown in Figure 6.4. The counts in the resonance are due to fission events, superimposed by time-independent background from the sample related activity and other uncorrelated backgrounds.

It should be stressed that in the energy range of interest (1 ev to 1 keV) also the effect of sample-scattered neutrons belongs to this time-independent component, which can be obtained in the regions outside the resonance, where the fission contribution is less important and the non-resonant contribute in a more significant way to the data in the form of a constant background as shown in Figure 6.5.

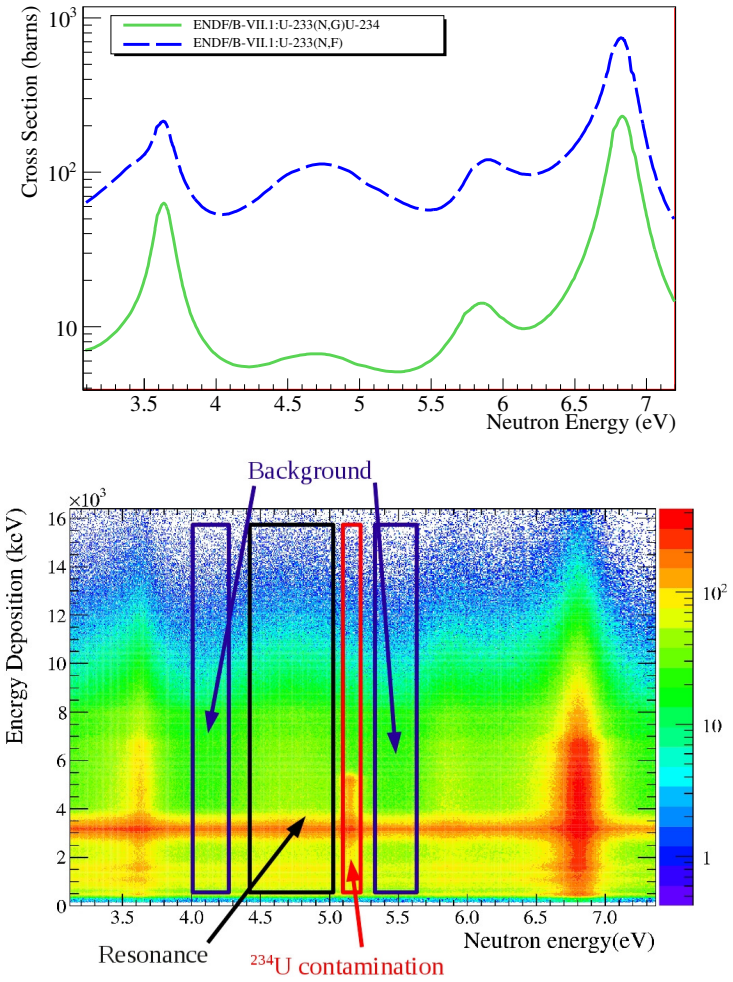

Figure 6.4: The evaluated neutron capture and fission cross sections of ^{233}U from the ENDF/B-VII.1 library [21] in the neutron energy range between 3 and 7 eV showing the fission-dominated resonance at 4.5 eV (top), and the adopted analysis scheme for the determination of the energy deposition pattern of fission events (bottom).

The TAC response to this background can be subtracted from the events in the resonance region after proper normalization to equivalent TOF bins in the resonant and non-resonant part. (This normalization was applied to all other background components accordingly.) With this subtraction, the non-resonant components are completely removed from the spectrum, yielding the TAC energy deposition response to neutron induced fission shown in Figure 6.6.

In order to reduce the statistical fluctuations, a smoothing was done to

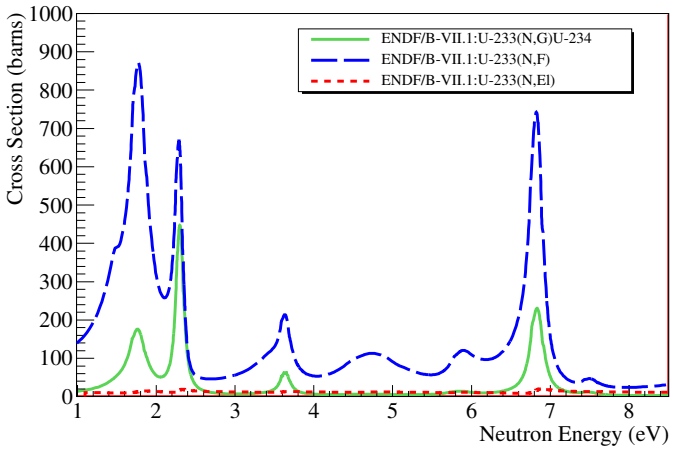

Figure 6.5: The evaluated neutron capture, fission and elastic scattering cross sections of ^{233}U from the ENDF/B-VII.1 library[21].

the obtained TAC energy response to neutron induced fission as shown in Figure 6.6 (right panel).

6.1.3 TAC's energy response to neutron capture

The energy response of the TAC to neutron capture events was assessed by means of the 2.28 eV resonance shown in Figure 6.7.

The capture-to-fission ratio of that resonance is close to one, much higher than the ratio in the resolved resonance region, which is typically a factor of 10 lower. The capture and fission components have been separated using the same background subtraction as for the 4.5 eV resonance.

The correction for the fission component was obtained by a linear fit of the fission distribution above the neutron binding energy of ^{233}U of 6.9 MeV, where all counts could be considered as fission events. The resulting TAC response to capture events is shown in Figure 6.8.

The procedure is repeated for several resonances to increase the statistics for the TAC's energy response to capture as shown in Figure 6.9.

6.1.4 TAC's energy response to neutron scattering

Neutrons are scattered by all materials that intersect the beam inside the TAC, in particular by the sample itself but also by the sample canning and the sample holder. In the case of the ^{233}U sample, the titanium canning that had been required for safety reasons gave rise to the largest background contribution,

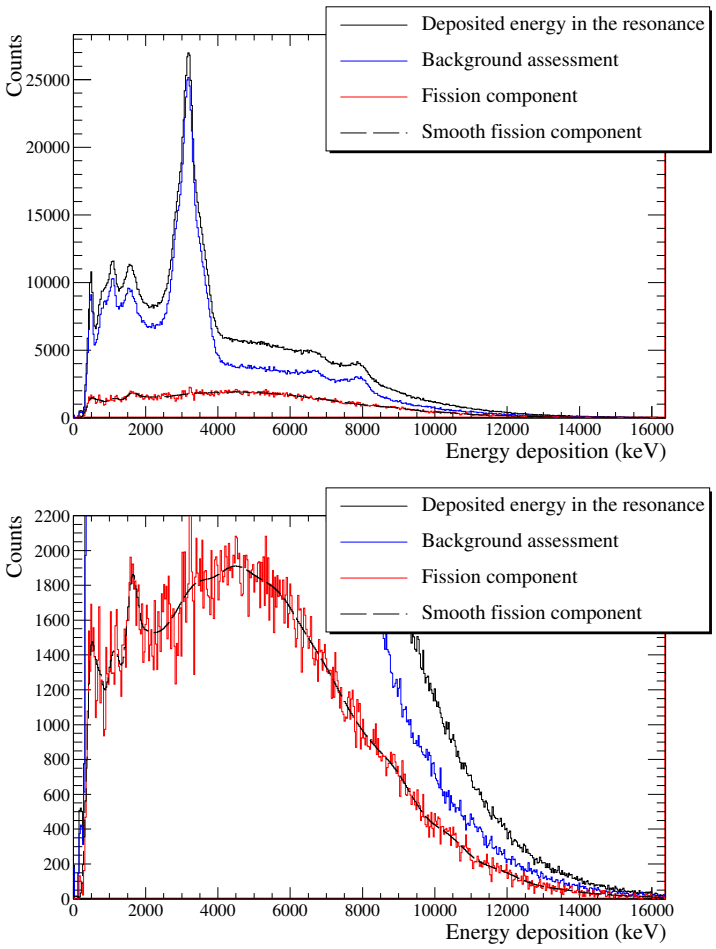

Figure 6.6: TAC's energy response to fission events obtained by subtraction of the time-independent background in the 4.5 eV resonance from the overall deposited energy spectrum. In the bottom panel, a zoom on the Y-axis illustrates the fission component in detail. The solid curve represents the TAC energy response to fission after smoothing.

not only due to the sizable capture and elastic scattering cross sections of the titanium but also due to the large mass. A second, smaller contribution comes from the aluminum backing of the ^{233}U deposit. The respective contributions have been determined for each TOF bin directly by the measured TAC energy response of a titanium canning with a aluminum backing but no uranium.

- Neutron scattering in the materials surrounding the ^{233}U mass (measured directly).
- Neutron scattering in the ^{233}U mass (measured indirectly).

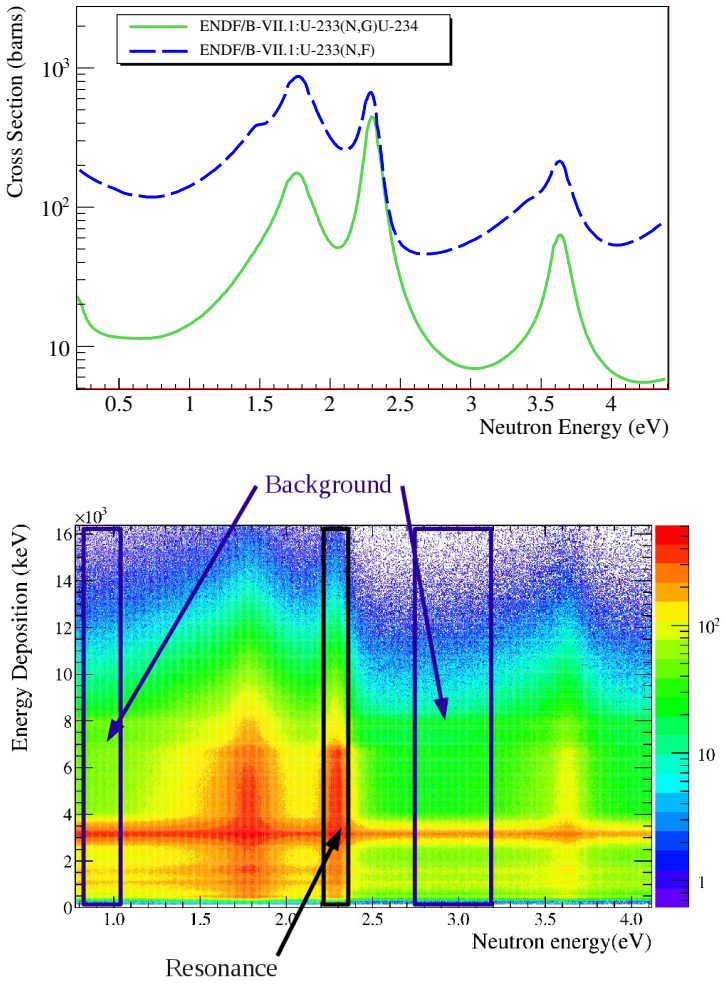

Figure 6.7: The evaluated neutron capture and fission cross sections of ^{233}U from the ENDF/B-VII.1 library [21] in the neutron energy range from 0.5 to 4.5 eV showing the 2.3 eV resonance (top), and the adopted analysis scheme for the determination of the energy deposition pattern of capture events (bottom).

6.1.4.1 TAC's energy response to scattering in the canning assembly

A look at the sample assembly composition shown in Table 5.2 (Section 5.6) help us understand that the titanium canning surrounding the sample used for safety reasons may yield an important contribution, not only due to the magnitude of the titanium neutron elastic and capture cross sections (displayed in Figure 6.10) but also due to the mass of this material intersecting the

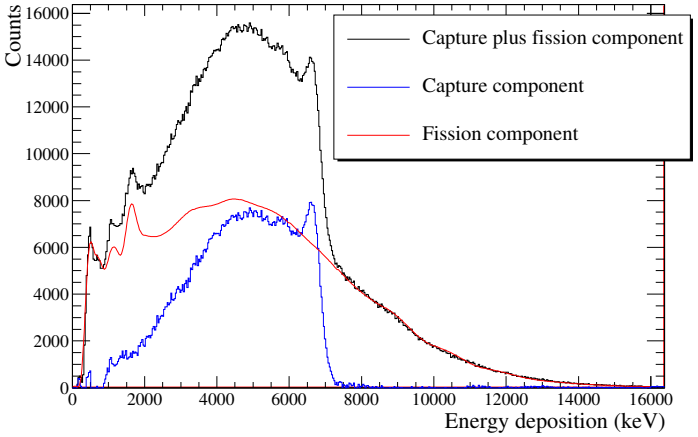

Figure 6.8: TAC's energy response to capture events obtained by subtraction of the fission component from the background-free (fission + capture) deposited energy spectrum in the 2.3 eV resonance.

neutron beam.

The titanium will contribute mainly with neutron scattering but also with capture events having a binding energy of 8142.39 keV from ^{48}Ti [122] with 75% abundance and with neutrons that will be scattered.

Another important contribution is the aluminum that serves as deposition medium for the ^{233}U mass. This contribution will add to the one from titanium although with a smaller effect due to its smaller mass. The total cross section for aluminum behaves very similarly to the titanium in terms of neutron energy range where resonant behavior is present. The total cross section for both nuclides are dominated by elastic scattering and neutron capture, aluminum featuring a higher binding energy (13057.81 keV [122]) for neutron capture in ^{27}Al.

The measured TAC's response to neutron scattering by the sample's canning is displayed in Figure 6.11 as function of the incident neutron energy. Figure 6.12 shows the behavior of the energy deposition spectrum for 4 different values of the incident neutron energy.

Note that the energy spectrum at 2 eV (Figure 6.12 top left panel) show a typical capture shape with binding energy at approximately 8 MeV. This can be attributed either to capture in titanium or in barium present in the BaF_2 crystals.

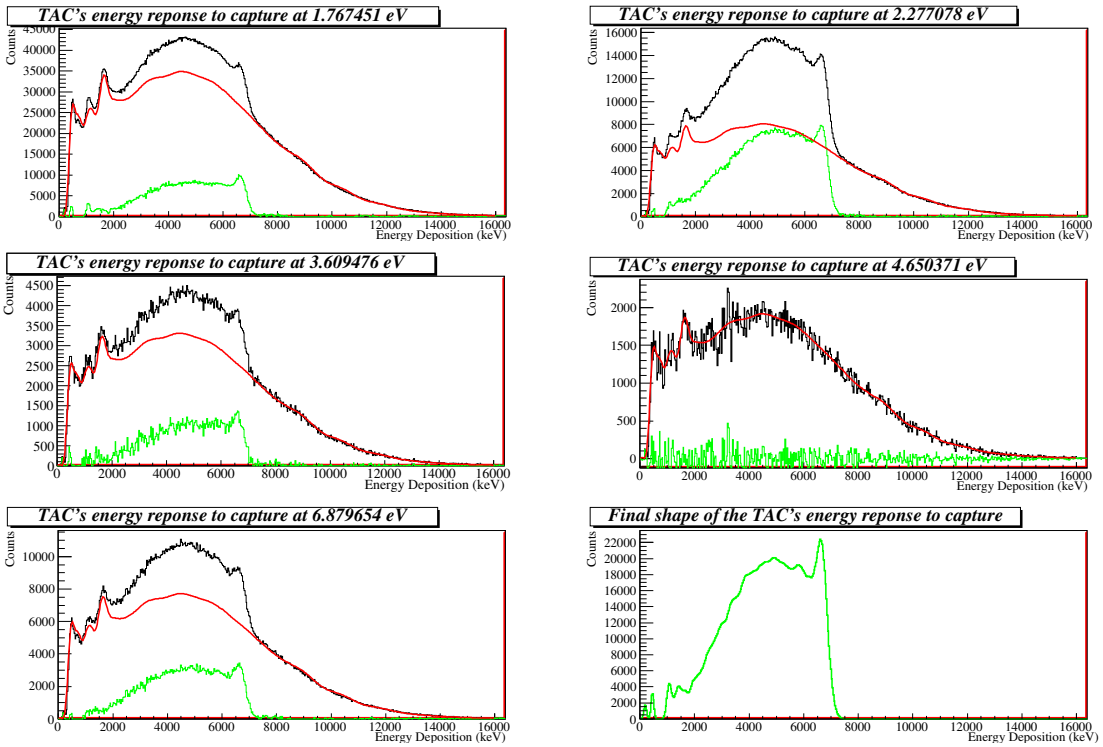

Figure 6.9: Assessment of the TAC's energy response to neutron capture using the already known energy response to fission. The experimental data is in black while the fission response is in red and the assessed capture response is in green.

6.1.4.2 Neutron scattering due to the ^{233}U mass

One of problems encountered during the data analysis of the ^{233}U data was how to account for the scattering cross section of the ^{233}U. One logical way to approach the problem is to measure the scattering of an isotope with similar mass but without the other possible reaction channels open, like fission or capture. While the Ti and Al components can be measured directly with the dummy sample, the contribution from neutron scattering in the ^{233}U sample had to be inferred from a background run with a carbon sample. Lead and Carbon can be considered as pure neutron scatterers in the energy region of interest (1 eV to 1 keV), which was assumed to simulate the scattering effect of ^{233}U. This approximation is justified because it turned out that ^{12}C exhibits the same TAC signature for scattered neutrons as ^{233}U. The description of the total scattering component was obtained by means of the measured data sets for the canning assembly and the carbon sample.

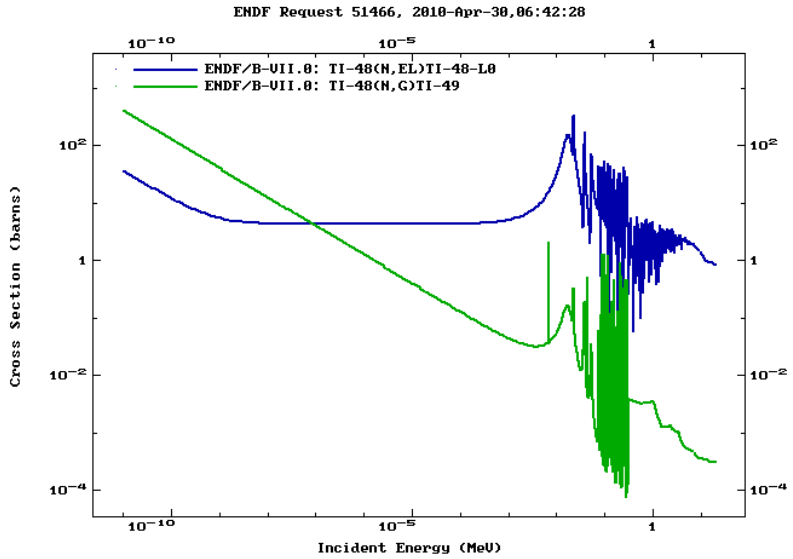

Figure 6.10: ^{48}Ti elastic neutron scattering and neutron capture cross-sections (data extracted from the ENDF/B-VII.1 data library).

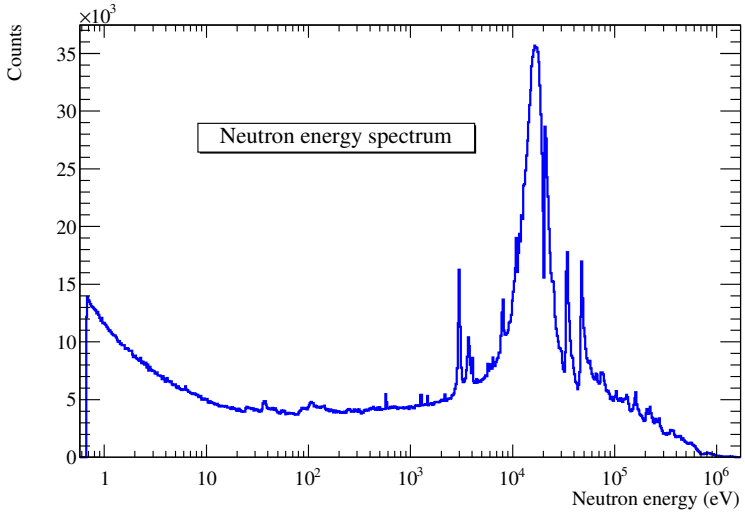

Figure 6.11: Neutron energy spectrum for the canning assembly with multiplicity higher than 1 and single gamma threshold of 150 keV.

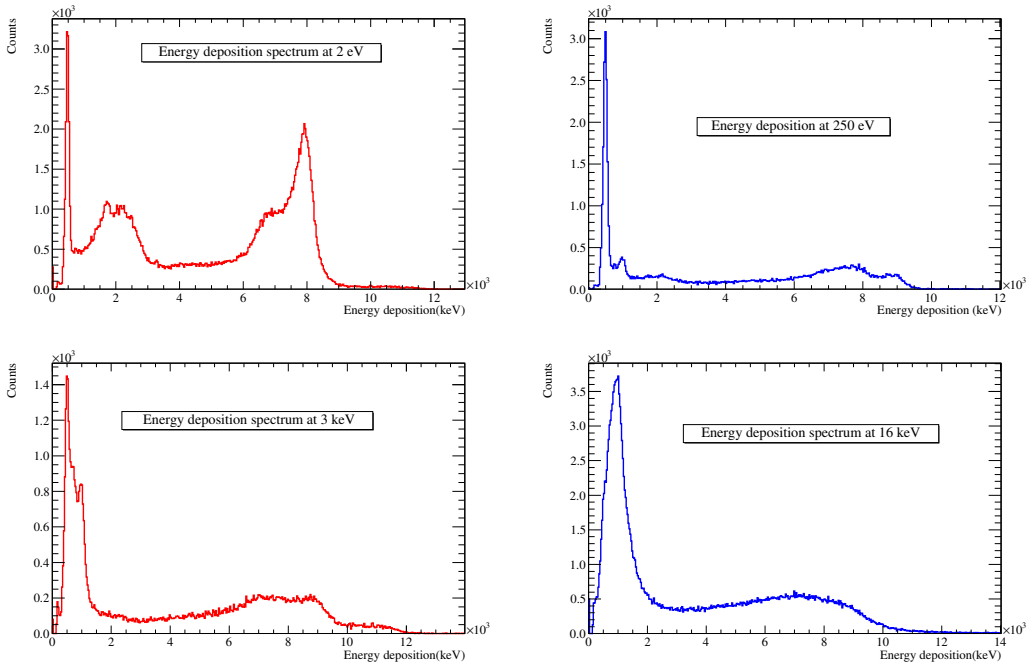

Figure 6.12: Energy deposition due to the canning assembly for different incident neutron energies (2 eV, 250 eV, 3 keV and 16 keV).

6.1.4.3 Neutron scattering due to the ^{233}U mass using the carbon sample

This sample had been measured in the same data acquisition campaign in identical experimental conditions relatively to the ^{233}U measured data.

The incident neutron energy spectrum is shown in Figure 6.13 and the energy deposition spectrum for several selected incident neutron energies is displayed in Figure 6.14

Although, one could perform a more in depth study of the scattering components and associated neutron capture, the full analysis of the titanium, aluminum and ^{233}U scattering footprint in the detection system goes beyond the scope of the present analysis and for the work here discussed, we are only interested in accounting correctly for these contributions and not completely disentangle them in basic components.

For the purpose of the data analysis where the aim is to make a correct description of this component, a mathematical parameterization was avoided, The use of a mathematical parameterization would imply a highly complex mathematical functions with many degrees of freedom and dependencies on the incident neutron energy.

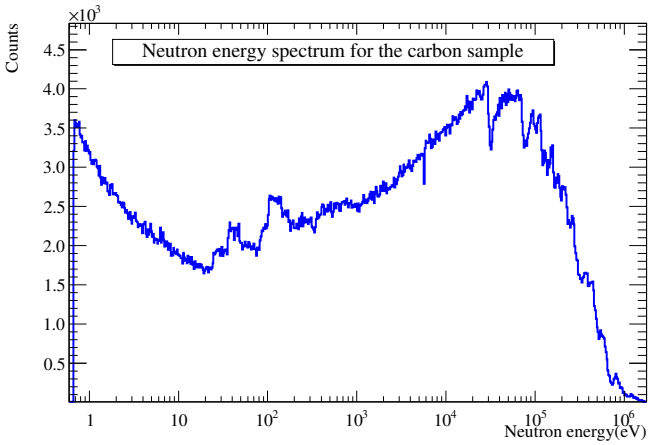

Figure 6.13: Neutron energy spectrum for the carbon sample.

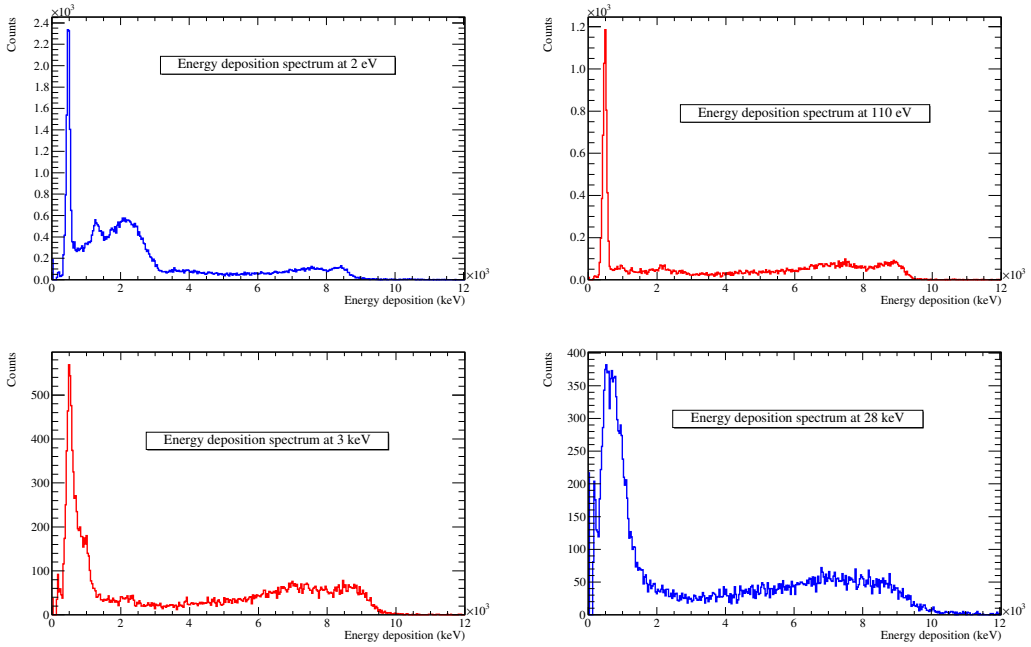

Figure 6.14: Energy deposition due to the carbon sample for different incident neutron energies with multiplicity higher than 1 and single gamma threshold of 150 keV.

Instead, the use of the measured empty sample assembly data set, normalized and corrected for count rate effects was used. With this procedure, the canning contribution will not be subtracted but used together with the

other TAC's responses to reproduce the energy deposition spectrum for each time-of-flight bin.

6.1.5 Sample activity signature in the TAC

The TAC's energy response to sample related activity was assessed by measuring the ^{233}U sample without beam. Figure 6.15 displays the measured spectrum.

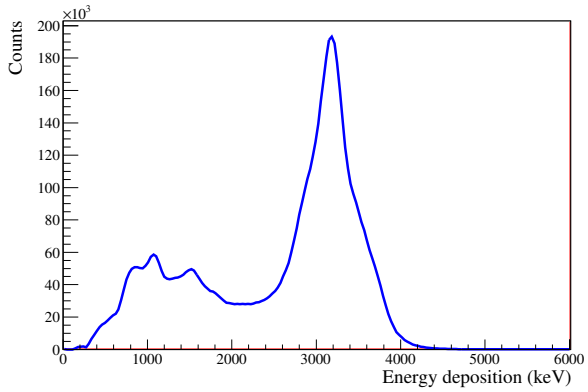

Figure 6.15: The TAC's response to the sample related activity.

6.2 Preparing the data for the decomposition

A source of contamination that is present always is the ambient background of the experimental area. This background will appear in all acquired data and must be removed in order to avoid multiple accounts. The way chosen to avoid multiple accounts for the ambient background was to remove it from all components and also from the ^{233}U data. In this way, its assured that an equal methodology was employed for all components. The subtraction of the ambient background is shown for all individual components in the next section and explained in detail.

The background Time-Of-Flight and Energy Deposition spectra can be seen in Figure 6.16 Important to note that the ambient background of the facility seems to have a higher intensity around 2 MeV.

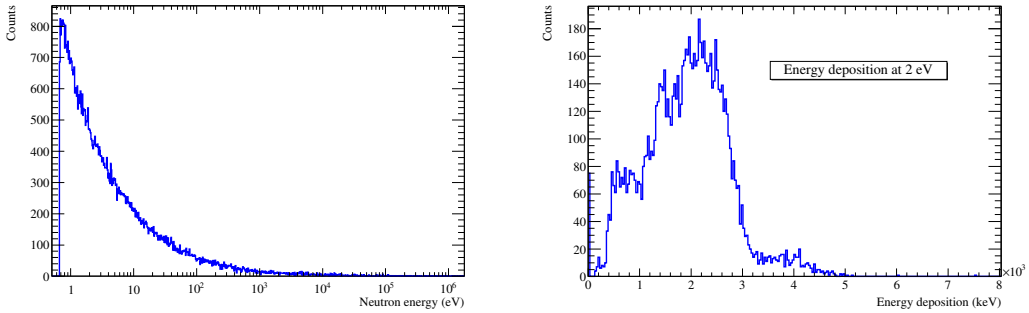

Figure 6.16: Neutron energy spectrum of the ambient background of the facility (left) and energy deposition spectrum (right).

6.2.1 Removing the ambient background from the ^{233}U

The subtraction of the ambient background in the facility from the measured data is done by subtracting each bin of 2D histogram containing the data with the equivalent normalized ambient background bin.

In this case is necessary to normalize by the acquisition time and this is given by the number of proton events in each run. Each individual proton event corresponds to a neutron beam event or to an external trigger event as in the case of measuring the ambient background of the facility. In both cases, the acquisition time of beam or no beam event is the same and dictated by the Flash ADC system used in the data acquisition. Therefore, a normalization by the number of events in the run and by the length in time of the considered bin is necessary.

Figure 6.17, shows the effect that removing the ambient background has in the data corresponding to the ^{233}U sample measurement.

Figure 6.18 shown the difference in the energy deposition spectrum between the original spectrum and the one without the ambient background of the facility.

6.2.2 Removing the ambient background from the Canning

The subtraction of the ambient background of the facility from the canning measurements was done in the same way as for the the ^{233}U sample measurement. The result of the subtraction can be seen in Figure 6.19

The effect of subtracting the ambient background of the facility in the energy deposition spectrum can be seen in Figure 6.19.

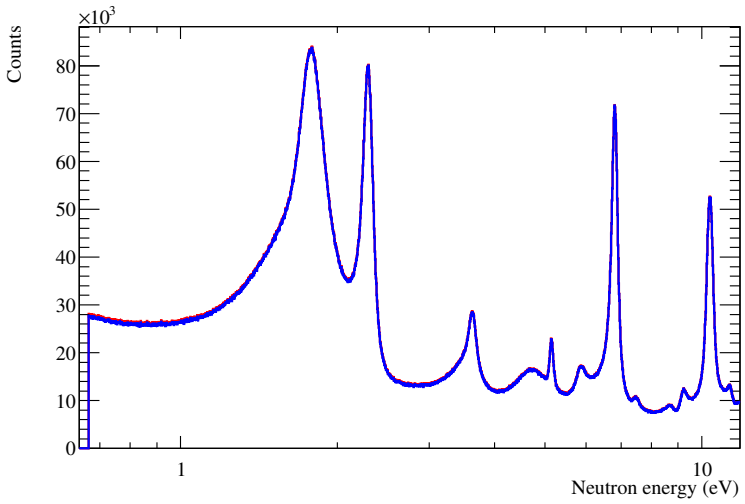

Figure 6.17: Neutron energy spectrum of the ^{233}U sample before (red) and after (blue) subtracting the ambient background of the facility.

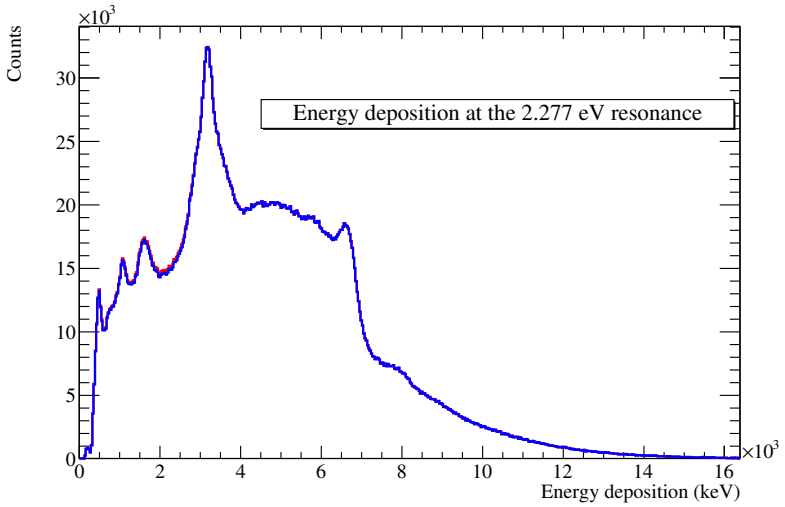

Figure 6.18: Energy deposition spectrum of the ^{233}U sample before (red) and after (blue) subtracting the ambient background of the facility.

The smoothing was done to avoid the significant statistical fluctuation in the energy deposition spectrum. The details of the energy deposition spectrum for the measured canning data, subtraction of the ambient background of the facility can be seen in Figure 6.20.

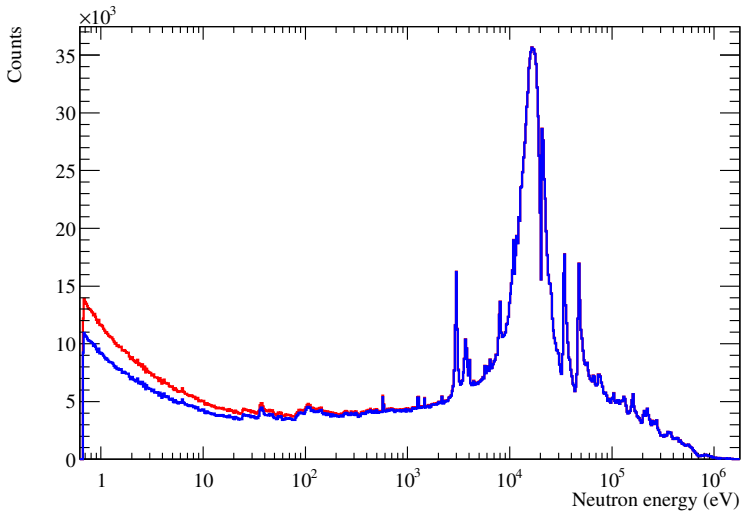

Figure 6.19: Neutron energy spectrum of the canning before (red) and after (blue) subtracting the ambient background of the facility.

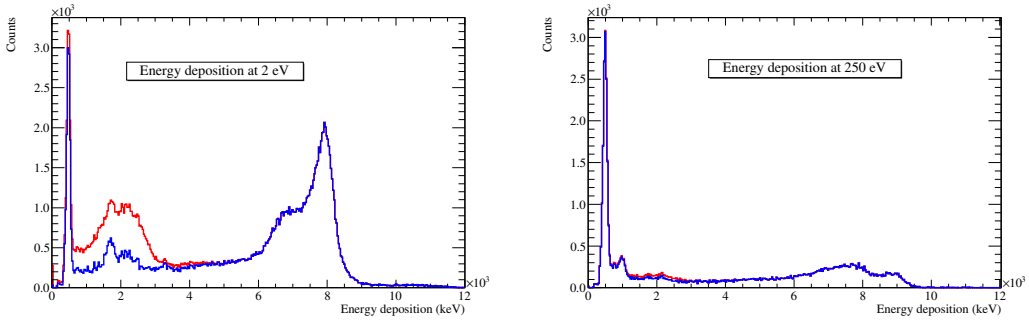

Figure 6.20: Energy deposition spectrum of the canning before (red) and after (blue) subtracting the ambient background of the facility at two different neutron energies: 2 and 250 eV.

6.2.3 Removing the ambient background from the Activity

Figure 6.21 shows the neutron energy spectrum due to the sample activity . The shape is given by the logarithm for of the time displayed in the X Axis. This cause the time bins to be of different sizes along the range. For shorter times, bins are shorter and the corresponding magnitude of the activity is also smaller in comparison with longer time bins which are bigger.

The subtraction of the ambient background of the facility is shown in Fig-

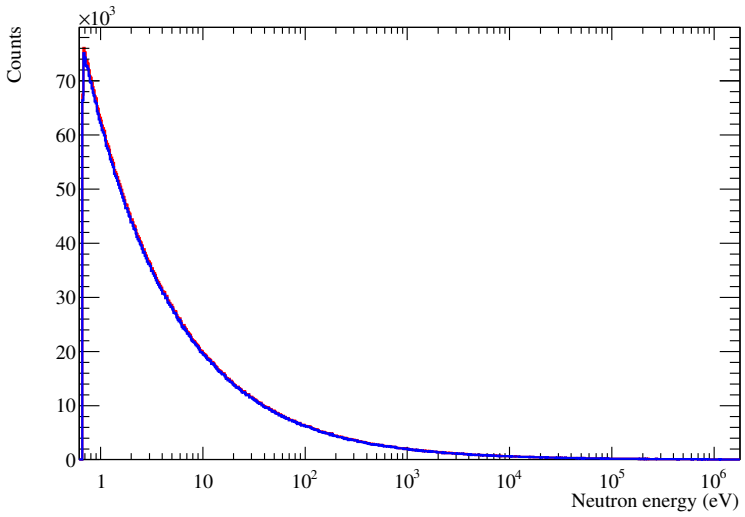

Figure 6.21: Neutron energy spectrum of the sample related activity before (red) and after (blue) subtracting the ambient background of the facility.

ure 6.22 where the black spectrum corresponds to the measured activity data and the red spectrum to the original data minus the ambient background of the facility.

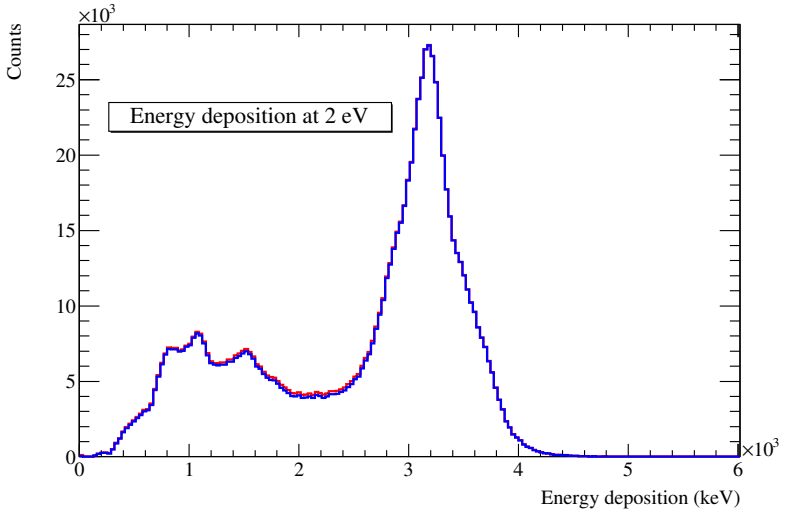

Figure 6.22: Total energy deposition spectrum due to the sample related activity before (red) and after (blue) subtracting the ambient background of the facility.

6.2.4 Removing the ambient background from the Carbon

Figure 6.23 shows the neutron energy spectrum for the carbon sample measured in TOF. The carbon sample exhibits only a scattering cross section free of contaminations.

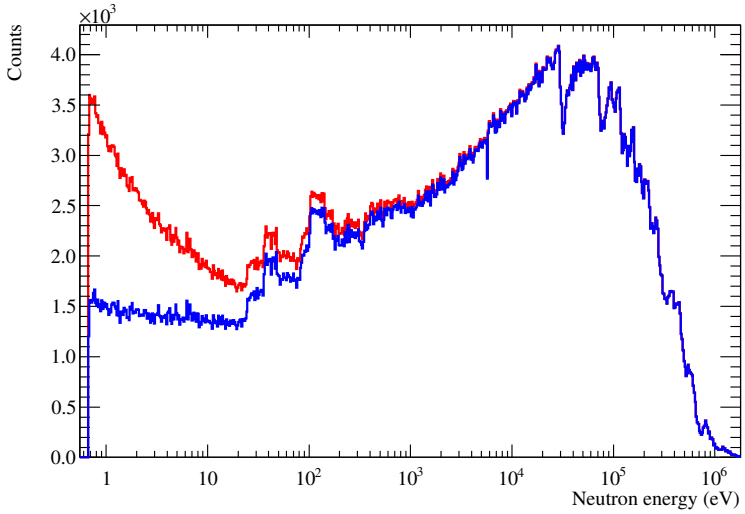

Figure 6.23: Neutron energy spectrum for the carbon sample before (red) and after (blue) subtracting the ambient background of the facility.

In Figure 6.24, the effect of subtracting the ambient background of the facility is shown in the energy deposition spectrum for two different incident neutron energies (2 and 250 eV).

6.3 Spectra decomposition

Using the detailed knowledge of the TAC's response to all contributions arising from neutron interactions in the ^{233}U sample and neutron interactions with structural materials shown in Figure 6.25, the decomposition of the energy deposition spectrum in individual contributions can be undertaken by expressing it as a linear combination of the components assessed before as shown in Eq. (6.1) where the S_i is the normalized to the unit total deposited energy shape for the $i-th$ component and S_{total}, the linear combination of all S_i which is fitted to the experimental total energy deposition spectrum for each neutron energy bin. The coefficients $\alpha, \beta, \gamma, \delta, \epsilon$ determined from the fitting,

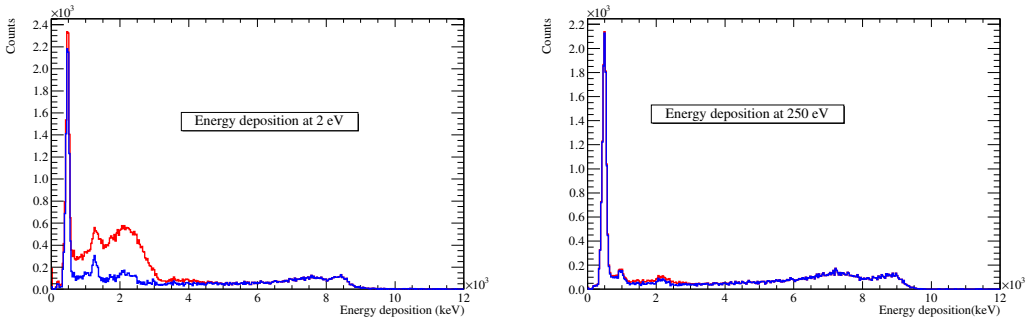

Figure 6.24: Total energy deposition spectrum for the carbon sample before (red) and after (blue) subtracting the ambient background of the facility fro two incident neutron energies: 2 and 250 eV.

depend on the neutron energy E_n and express the number of counts for each $i-th$ component contributing with counts in the TAC for a given neutron energy.

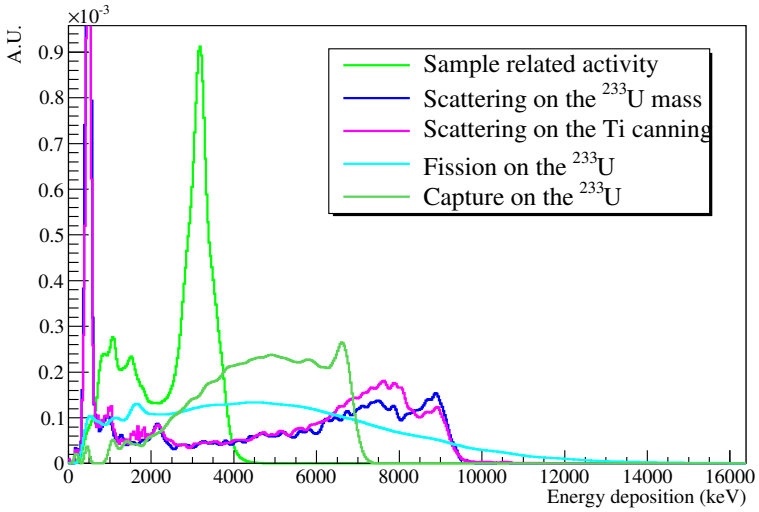

Figure 6.25: TAC's energy response for neutron capture, neutron induced fission, sample related activity, neutron scattering in the ^{233}U and neutron scattering in the sample canning. All responses are normalized to the unit. The neutron scattering in the ^{233}U and the neutron scattering in the sample canning are plotted for a incident neutron energy of 110 eV.

$$S_{total} = \alpha(E_n) \cdot S_{capture} + \beta(E_n) \cdot S_{fission} + \gamma(E_n) \cdot S_{activity} + \\ + \delta(E_n) \cdot S_{canning}(E_n) + \epsilon(E_n) \cdot S_{^{233}U\ scattering}(E_n) \tag{6.1}$$

The decomposition of the total energy deposition spectrum is done performing for each time-of-flight bin, a linear fit using the five components (neutron capture, neutron induced fission, sample activity and neutron scattering in the canning and in the ^{233}U sample) plus a sixth component for the TAC energy response to ^{234}U which is an impurity of the sample. This contribution has been obtained from a corresponding TAC measurement on ^{234}U [123]. The fit is performed thanks to the TLinearFitter class of the ROOT package [120], that uses the normal equation method with Cholesky decomposition along the full range of the energy deposition spectrum.

This decomposition method is valid for the assumptions listed in Sec. 6.1), specially for the assumption that the TAC's response to the γ cascades from capture and fission events are independent of neutron energy. The event selection criteria is chosen as less restrictive as possible, in order to keep a high TAC efficiency that allow to stay almost independent of the cascade de-excitation scheme. In the neutron energy region of interest from 1 eV to a few keV there is neither theoretical nor experimental evidence for a variation of the respective γ-decay patterns. Although the number of nuclear levels available for de-excitation is higher for more energetic neutrons, this is not reflected in the sum energy peak around $S_n + E_n$, because the neutron binding energy, S_n, is of the order of several times 10^6 eV, whereas and the kinetic neutron energy, E_n, is less than 10^4 eV. Accordingly, the shape of the capture spectrum remains fairly constant below 10 keV.

Figure 6.26 shows the total energy spectrum decomposition in the resonance region around 1.76 eV. The fit (red line) of the total energy spectrum is able to reproduce all the visible structures with high fidelity. The same can be said for the 2.23 eV resonance (Figure 6.27) where the neutron capture and neutron induced fission ratio approximates 1.

Figure 6.28 shows the decomposition of the total energy deposition spectrum in the region around the 4.65 eV resonance. This total energy deposition spectrum at this energy, is dominated by the neutron induced fission and was used for assessing the TAC's response to this reaction. Important to note that although the neutron induced fission is dominant, neutron capture is still present and this can be see by the small bump at approximately 6.8 MeV in the fit (red curve) and in the TAC's response to neutron capture (dark green line). This is a good indication that the TAC's response to neutron induced fission was assessed correctly and the neutron capture was well removed.

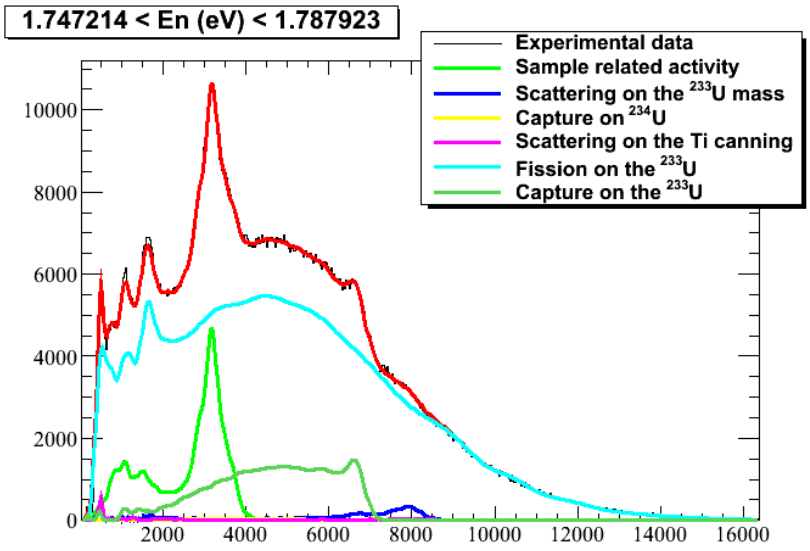

Figure 6.26: Decomposition of the total energy deposition spectrum around the 1.76 eV resonance. The vertical scale is counts and the horizontal scale is Energy deposition in keV.

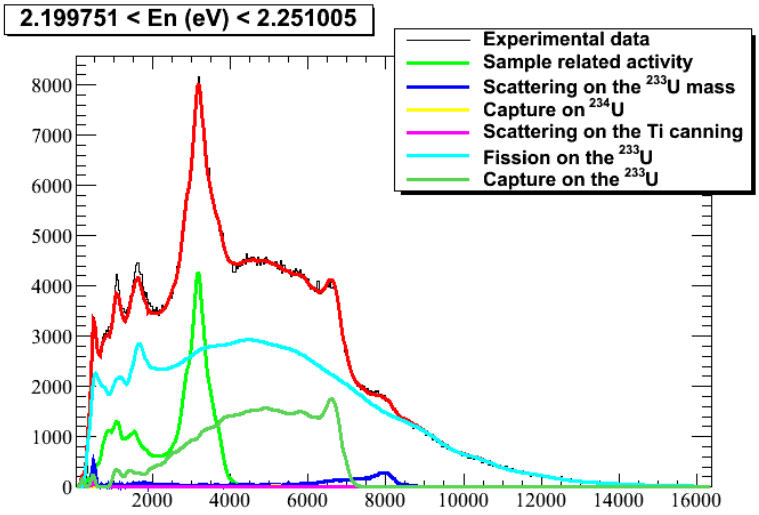

Figure 6.27: Decomposition of the total energy deposition spectrum around the 2.23 eV resonance. The vertical scale is counts and the horizontal scale is Energy deposition in keV.

Figure 6.29, shows the decomposition of the total deposited energy spectrum at the neutron capture resonance at 5.1 eV in the ^{234}U. Once more, the

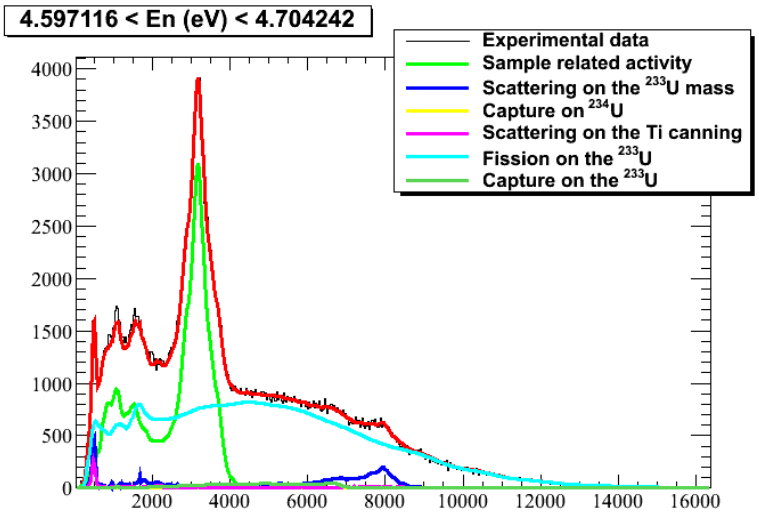

Figure 6.28: Decomposition of the total energy deposition spectrum around the 4.65 eV resonance. The vertical scale is counts and the horizontal scale is Energy deposition in keV.

fit seems to reproduce very well all the structures of the total deposited energy spectrum. The activity peak (light green line) is very well reproduced specially if one takes in account the asymmetric shape.

The result of the fit, S_{total}, is shown for several neutron energy intervals by the red curve in Figure 6.26, 6.27, 6.28 and 6.29 together with the individual components discussed before. The respective experimental data (black) are well reproduced. At low energy, one finds that the background components are dominated by the radioactivity of the sample, whereas neutron scattering has a rather small contribution. However, it is the contrary above a few hundred eV. Note however, the large effect of the ^{234}U contamination in the bottom right panel due to a big capture resonance at this energy.

6.3.1 Decomposition of the total energy deposition spectrum

Using the CSD method we were able to discriminate between the capture and fission components in the total energy spectrum of the TAC. In Figure 6.30 the neutron capture and fission yields obtained with the CSD method are compared in a short energy range with the evaluated cross sections from the ENDF/B-VII.1 library.

The results shown in Figure 6.30 validate the CSD methodology and show

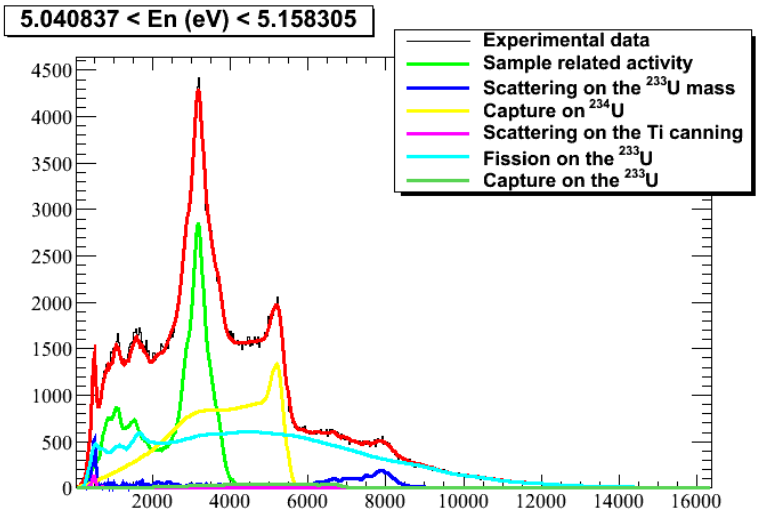

Figure 6.29: Decomposition of the total energy deposition spectrum around the 5.09 eV resonance. The vertical scale is counts and the horizontal scale is Energy deposition in keV.

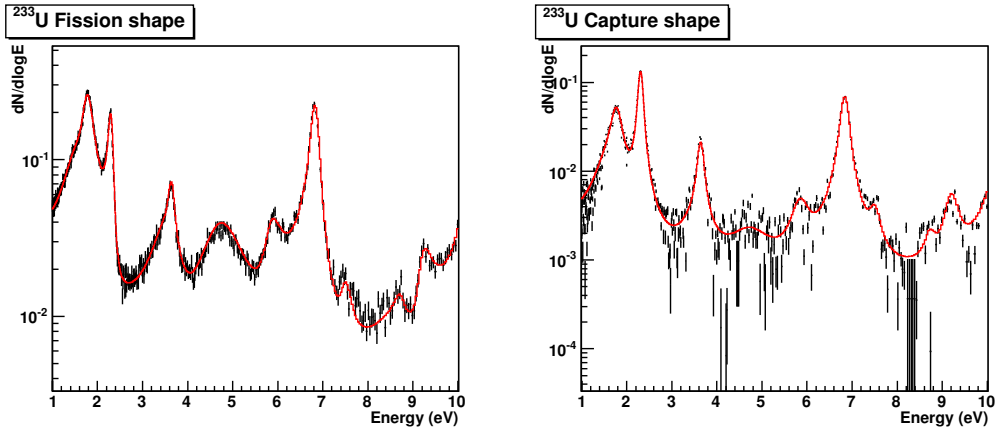

Figure 6.30: Comparison between the neutron capture (right) and neutron induced fission (left) yield with the ENDF/B-VII.1 library. The normalization is arbitrary.

the possibility of performing simultaneous nuclear measurements for neutron capture and neutron induced fission without additional detection systems. Moreover, the simultaneous yield assessment of neutron capture and neutron induced fission, allows the comparison and benchmarking of the results obtained for the neutron induced fission with the CSD methodology with other

measurements done in n_TOF for neutron induced fission using different detection systems [75]. It also provides a way to track systematic uncertainties in the CSD methodology for the assessment of the neutron capture yield.

The drawback of this method is that it depends strongly on the existence of a fission-only resonance to obtain the detector response to fission. It can therefore not be applied alone to all fissile nuclei but the CSD method could be very powerful if used in conjunction with a fission tagging technique. For other fissile nuclei a fission veto device, as for example described in [124], may still be necessary. However, the fission veto technique requires specially prepared thin samples with masses not higher than 300 μg/cm^2. In measurements where such thin samples are not suitable, the CSD methodology may be advisable:

- When much more mass is needed (100 to 500 mg),
- When the sample already exist and can not be manipulated like the case here presented where the it was encapsulated in Ti and Al.

Overall, the CSD methodology provides a solution for measuring the cross sections of isotopes with fission and capture reaction channels open, without the demanding experimental requirements of the fission veto technique and with the added advantage of simultaneously measuring both cross sections in identical conditions.

Chapter 7

Monte Carlo simulations of the experimental setup

In the previous chapters, the detection of neutron induced reactions, event reconstructions and data analysis using the CSD method for discriminating capture and fission events have been discussed.

In this chapter the goal is to study the detection system performance in terms of detection efficiency and of reconstruction efficiency as function of total energy deposition, multiplicity conditions and dead time. An accurate calculation of the detection efficiency can be performed using Monte Carlo simulation tools. To do this, it is necessary an exhaustive study of the detection system response in different experimental conditions. The method consists in reproducing the data analysis results by mocking-up the experimental setup with a Monte Carlo simulation achieving a system parameterization. This is only possible if all the structural characteristics like material isotopic compositions, exact placement of the components and source definitions are known and implemented together with all the physical processes that may occur in the experimental setup including realistic event generators for capture and fission reactions.

The normalizing constants and corrections assessed this way will be used to translate the number of detected fission or capture events for a given incident neutron energy into a neutron energy dependent yield.

7.1 Normalization

In neutron capture yield measurements, the observable quantity is the reaction yield, which is defined as the fraction of neutrons impinging on the sample that undergo a neutron induced reaction. In the case of n_TOF, where the

measurements are performed using a neutron source with a broad energy, the reaction yield $Y(E_n)$ is measured as a function of the time-of-flight which is related with the neutron energy E_n. The $Y(E_n)$ is a function of the total counting rate $T_{count\ rate}(E_n)$, of the detection efficiency ε, of the neutron beam intensity $\phi_n(E_n)$ and of the neutron beam intersection factor N ($0< N <1$) which relates the neutron intensity measured in the monitor with the amount of neutrons impinging in the sample.

$$Y(E_n) = \frac{T_{count\ rate}(E_n)}{\varepsilon \cdot N \cdot \phi_n(E_n)} \tag{7.1}$$

Where the $T_{count\ rate}(E_n)$ is the contributions of the different reactions inducing signals in the detection system such as neutron capture $C_{capture}(E_n)$, neutron induced fission $C_{fission}(E_n)$, neutron scattering $C_{scattering}(E_n)$, sample related activity $C_{activity}$, natural background of the facility $C_{background}(E_n)$, among others.

$$\begin{aligned} T_{count\ rate}(E_n) = C_{capture}(E_n) + C_{fission}(E_n) + \\ C_{scattering}(E_n) + C_{activity}(E_n) + C_{background}(E_n) \end{aligned} \tag{7.2}$$

In order to assess the cross section for a given reaction from the reaction yield, its necessary to normalize it to the sample thickness. The following equation (Eq. (7.3) is only valid if $Y(E_n) << 1$ (thin sample approximation)) show the relation between the reaction yield and cross section for a given reaction (n, x):

$$Y_{(n,x)}(E_n) = S_{thickness} \cdot \sigma_{(n,x)}(E_n) \tag{7.3}$$

Where $S_{thickness}$ is the sample thickness in atoms per barn and $Y(E_n)$ is related with the measured counting rates $C_{(n,x)}(E_n)$ by:

$$Y_{(n,x)}(E_n) = \frac{C_{(n,x)}(E_n)}{\varepsilon_{(n,x)} \cdot N \cdot \phi_n(E_n)} \tag{7.4}$$

The detection efficiency ε of the TAC depends on the multiplicity, deposited energy and on the counting rate and therefore on the measured sample.

7.1.1 Detection and event reconstruction efficiency

The $\varepsilon_{(n,x)}$ defined generally as detection efficiency takes a more complex form in the case of the ^{233}U due to the need to account also for the reconstruction efficiency of an event. This arises from the fact that the TAC has an overall detection efficiency for detecting at least one gamma of a capture or fission

event very close to 100%, but this doesn't imply that all events can be reconstructed. Also, the efficiency for detecting and reconstructing an event has a dependency on the characteristics of the reaction such as energy deposition and multiplicity. Therefore the $\varepsilon^{overall}_{(n,x)}$ for reaction (n,x) which accounts for both detection and event reconstruction efficiency, is defined in the following form:

$$\varepsilon^{overall}_{(n,x)} = \varepsilon^{detection}_{(n,x)} \cdot \varepsilon^{event\ reconstruction}_{(n,x)} \tag{7.5}$$

Important to note that $\varepsilon^{detection}_{(n,x)}$ is a function of the detection system characteristics while the $\varepsilon^{event\ reconstruction}_{(n,x)}$ depends on the data analysis conditions such as multiplicity, energy deposition and single gamma thresholds.

In this chapter, a detailed description of the Monte Carlo studies performed using the GEANT4 toolkit [125, 126] to assess the overall efficiency $\varepsilon^{overall}$ due to the experimental setup and data analysis conditions is done. An estimation of the dead time correction is also performed. The implemented geometry, isotopic constitution of the structural materials and the implementation of different sources are reported. The results obtained with the Monte Carlo simulation program are compared and validated against the experimental data.

7.2 Implemented TAC's geometry

The implemented TAC geometry follows the Computer-Aided Design (CAD) drawings of the engineering design with high fidelity. The simulated geometry includes the 40 BaF_2 crystals with their corresponding ^{10}B enriched carbon fiber capsules, the photomultiplier tubes with their aluminum housings, the aluminum beam pipes with the sample holder, the ^{6}Li enriched neutron moderator/absorber and the aluminum honey-comb structure that holds the complete assembly as shown in Figure 7.1. More details can be found in [103, 123]

Figure 7.1 (right) shows the geometry but without the total number of detection modules to facilitate the understanding of the detection system and the placement of the components.

7.3 Simulation of the sample related activity in the TAC

In any Monte Carlo simulation code, besides the exact description of the geometry, of the materials and of particle transport physics, the accurate source description is mandatory. The following discussion will focus in the source

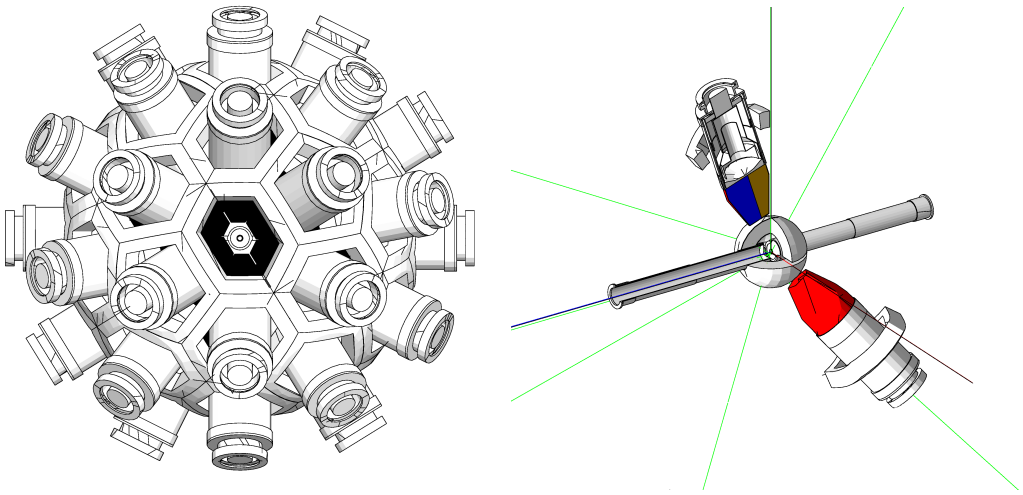

Figure 7.1: TAC's geometry implemented on GEANT4 (left) and simplified geometry of the TAC (right) showing one hexagonal and one pentagonal detector, the neutron absorber, beam pipe, honey comb support structure and sample. The green lines (right) represent the emitted gammas of a capture event.

recreating the gamma arising from the sample related activity. The implementation of the gamma emission due to neutron capture and fission events and will be discussed in the following sections.

As shown in the previous chapter, a byproduct of the CSD method used for decomposing the TAC's total energy deposition spectrum, is the recovery of all reaction rates involved in the measurement and therefore, the activity rate is also recovered. One would expect that the activity rate would be constant in time but as will be shown in Section 7.4, this is not the case and it is related with the dead time. A correct reproduction of the sample related activity with simulation tools permits to perform a direct comparison between the dead time observed experimentally and the one simulated leading to a parameterization of the correction assessed.

The sample related activity event generator was implemented with the following features.

- Creates a branching matrix for the possible excited levels using the parameterization given as input.
- The transition to a new level is sorted randomly according to the branching ratio matrix.
- The process is repeated until the ground state energy is reached.

The input parameterization was retrieved from [122] where the decay level

scheme and branching ratios for the ^{208}Tl is detailed.

The results obtained using the sample related activity event generator and the TAC's simulation code are compared with the experimental data in Figure 7.2. The agreement between the energy deposition spectra is good above the 2 MeV region. Below this region, a contribution from a component that is not included in the simulation code is present in the experimental data. This contribution may be related with the long decay path of the ^{232}Th until the ^{208}Tl which is not considered here.

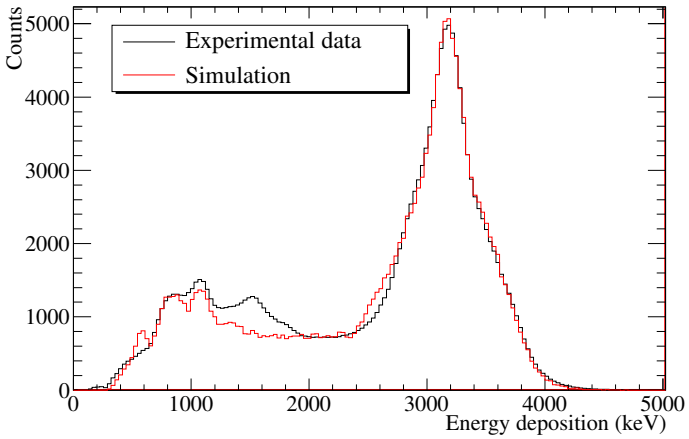

Figure 7.2: Experimental and simulation comparison of the energy deposition for sample related activity events.

The multiplicity distributions for the experimental data and simulation are shown in Figure 7.3 and display a reasonable agreement.

The TAC's event detection and event reconstruction efficiencies for sample related activity are displayed in Table 7.1

Table 7.1: Sample related activity event detection and event reconstruction efficiency results.

Detection efficiency	Reconstruction efficiency	Reconstruction efficiency above 2 MeV
99.2%	82.1%	60.%

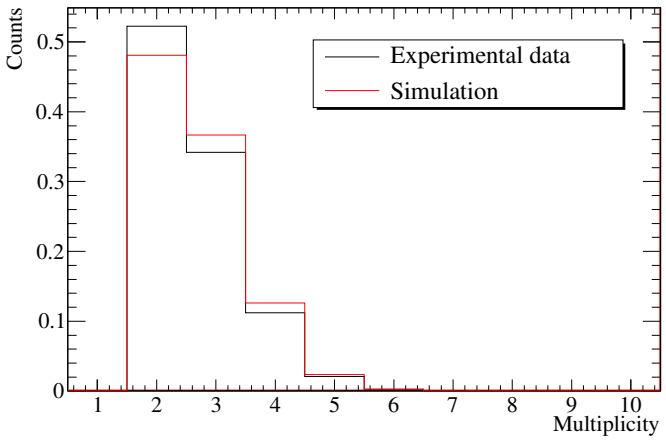

Figure 7.3: Experimental and simulation comparison of the multiplicity distributions for sample related activity events.

7.4 Dead time and pile up effects and corrections

The dead time is by definition the minimum amount of time between two consecutive signals that a detection system is able to detect separately. In some cases the limitation can be set by physics processes in the detector itself and in other cases by the associated electronics.

In the particular case of n_TOF the detector output is sent directly to a Flash ADC avoiding any hardware dead time.

The dead time is then directly related with the time constant of the slow decay (620 ns) component in the detector and the limitations of the pulse shape routine in detecting the overlapping of two or more signals. This limitation was narrowed to the special cases where two signals arrive very close in time or a signal is followed by a small amplitude signal overlapping the first signal.

Also, in ideal conditions the detector (scintillator crystal plus photomultiplier) would give a perfect signal without fluctuations. In real conditions, the fluctuations in the output signal exist and mask sometimes the existence of a second smaller signal overlapping, causing a wrong assessment of the physical quantities. The pulse shape analysis, returns then the sum of the deposited charge by the two signals in one single signal leading to wrong multiplicity assessment. Also, this leads directly to the loss of a signal and overestimation of the energy deposition of the first signal.

Characterizing the behavior of the system regarding dead time is difficult

as the system is somehow nonparalyzable regarding the signal detection but without the loss of charge deposited. This is even more complex as it has a strong dependence with magnitude of the signals involved.

No direct correction is available and direct measurement of the effect is also difficult.

A possible solution is a complete simulation together with the pulse shape routine which would consider the generation of adequate gamma spectra together with simulating real pulses for testing the pulse shape routine.

As a first approach, a trial to measure the dead time affecting the constant sample activity was done.

The sample activity can be considered constant in the time interval that separates the fast neutrons from the thermal neutrons arriving at the experimental area (16 ms).

Any variation in the activity during this period has to do with dead time and the can be related with the variation of the count rate.

Figure 7.4 shows how the activity count rate varies with time. Looking at Figure 7.5 one can see the sharp increase of the count rate for times smaller than 0.1 ms that affects strongly the activity measured in Figure 7.4.

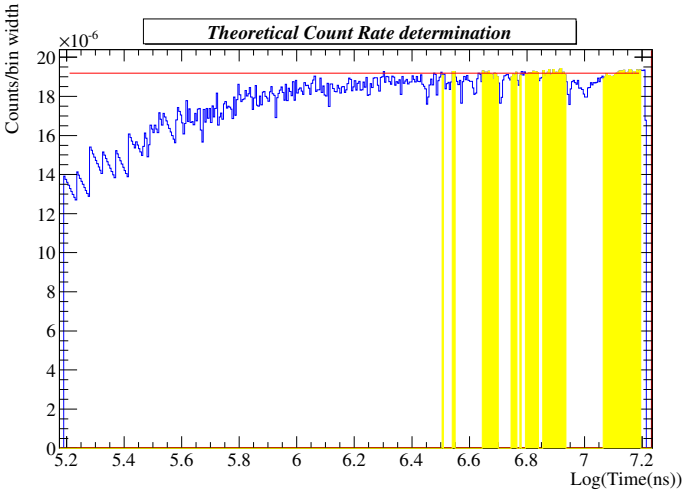

Figure 7.4: Dead time effect on the sample activity. The activity shown (blue) corresponds to the sample activity obtained during the measurement with neutron beam. The nominal activity of the sample (red) is assessed in regions (yellow) where the count rate is below 0.2 MHz and the dead time is negligible.

Figure 7.4 red line consist of a experimental determination of the nominal activity of the sample by assuming that for low overall count rates(>100 counts/s), the dead time will go to zero and the activity measured will depend

uniquely on detection efficiency. The yellow area corresponds to the bins used to assess the nominal sample related activity while the blue line correspond to the sample related activity measured.

The difference between the measured and the nominal sample related activity gives us the dead time correlation with the count rate.

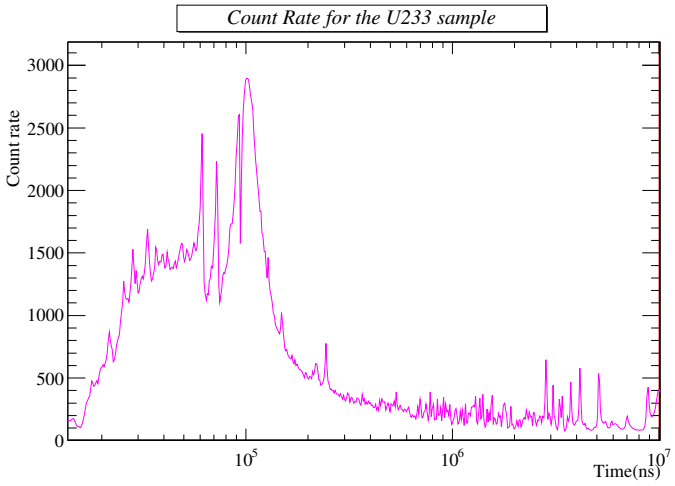

Figure 7.5: Count rate measured for the ^{233}U sample.

Figure 7.6 shows the comparison between experimental data for dead time affecting the sample activity and a simulation for the dead time where we assumed the count rate was due to the fission events only. This assumption is not a exact reproduction of the real conditions but is a good starting approximation as the fission cross section is a factor ∼10 compared with capture and the average multiplicity is higher also. The results show a good agreement taking in account the simplified model used.

The dead time correction factor to be applied to the neutron capture and neutron induced fission components has a dependency on the selection criteria applied in the data analysis (multiplicity >1 and total energy deposition >2 MeV) and will be significantly smaller up to a factor 2 or 3 than the one here shown, due to the multiplicity and total energy deposition these two components being higher and broader respectively than the ones associated with the sample related activity.

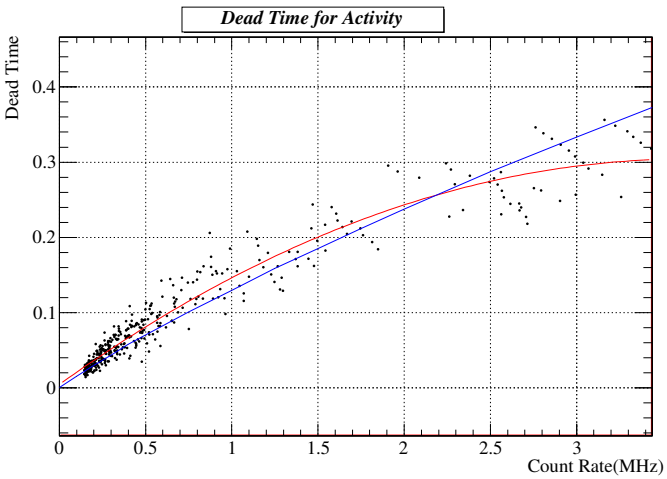

Figure 7.6: Comparison between experimentally assessed dead time correction factor (dots fitted with red line) and simulated (blue line) data.

7.5 Simulation of the capture events on the TAC

The model used in this work for the generation of realistic capture cascades was previously reported in [127, 128] and applied specifically to the TAC measurements in [129]. The model considers two different excitation energy ranges (Figure 7.7):

- The lower energy range where ($E < E_{cut}$) corresponds to the region of known levels (energy, spin and parity) with known transition probabilities. This information is retrieved from the Evaluated Nuclear Structure Data Files (ENSDF) [122] and allows one to calculate the low energy part of the branching ratio matrix. The electron conversion process is modeled for the K, L and M-shells from the tabulated values of fluorescence yields and internal conversion coefficients available in the literature.
- At higher energies ($E > E_{cut}$) the levels and transitions probabilities between levels are calculated using a statistical model. The individual levels are created by sampling the level density distribution given by the Back Shifted Fermi Gas (BSFG) model [130], and the transition probabilities between levels are calculated only for E1 (electric dipole), M1 (magnetic dipole) and E2 (electric quadrupole) transitions from the associated PSF [131].

Starting from the capture level, the algorithm for generating a cascade includes the following features:

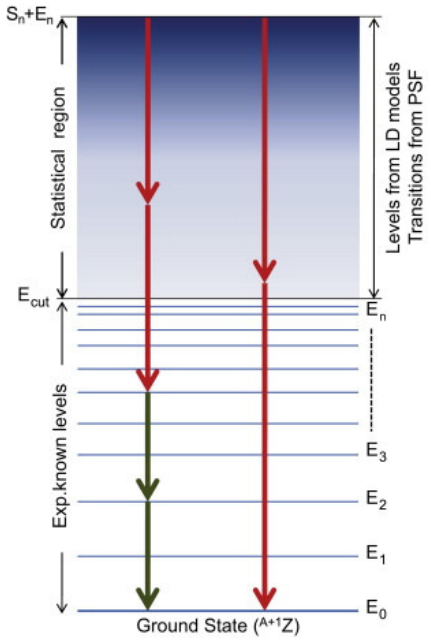

Figure 7.7: Nuclear level scheme used in the neutron capture cascade generator model. The low energy range is known experimentally, while the upper energy range is described from nuclear level density statistical models and parameterized EM (electric and magnetic) transition probabilities.

1. The branching ratio matrix for E1, M1 and E2 transitions is calculated from the known capture level to all levels below using the parameterized PSF.
2. The transition to a new level is sorted randomly according to the branching ratio matrix.
3. If the new level is in the statistical energy range, a new branching ratio matrix is computed. Otherwise the experimental branching ratio matrix is used.
4. The loop returns to step 2 until the ground (or a metastable) state is reached.

The correctness of the model parameters is validated by the comparison of the simulation and the experimental data. The experimental information for low energy ($E_\gamma \lesssim 1$ MeV) and high energy transitions (> 10 MeV) comes from decay and photo-absorption experiments, respectively. In the case of intermediate energy transitions, governing the de-excitation of the compound nucleus from the capture state, the information is very scarce and only the Oslo method and the double step cascade method provide some experimental information [132]. For this reason, the PSF available in the literature are only

a good starting point for the simulation of capture cascades but need to be adjusted in order to reproduce the experimental data. The (n,γ) measurement with the TAC have been shown to be a sensitive way for performing systematic PSF studies [129, 103].

7.5.1 Reproducing the ^{233}U neutron capture cascade: Case 1

The neutron capture generator for the specific case of the $^{233}U(n,\gamma)$ measurement uses the following information as input:

- At low energies and up to 2 MeV, the nuclear levels and transition probabilities found in the ENSDF data base [122];
- At higher excitation energies, the Back Shifted Fermi Gas model for the calculation of the level density with the parameters recommended in the RIPL-2 database [133], and the PSF for the calculation of the transition probabilities with the parameterization of Kopecky et al. [131].

The recommended PSF (see Table 7.2) is described by two standard Lorentzian distributions for E1 transitions and single particle distributions for M1 and E2 transitions.

Table 7.2: Recommended (Case 1) parameterization for the PSF of ^{233}U neutron capture generator.

	$E1_a$	$E1_b$	M1	E2
E (MeV)	11.13	13.94		
Γ	2.26	4.46		
σ_0 (mb)	371	401		
$k_{strength}$			$2{\cdot}10^{-8}$	$5{\cdot}10^{-11}$

A first simulation was performed with the initial PSF and assuming a constant counting rate of 0.7 counts/μs, which corresponds to the experimental counting rate registered at the 2.3 eV resonance. Figure 7.8 shows the distributions of energy deposition and Figure 7.9, the multiplicity distribution resulting from the simulation and compared with the experimental data.

In Figure 7.8 where both experimental data and simulation spectra for the total energy deposition spectrum at the 2.3 eV resonance for events with multiplicity >1 are superimposed, one can see a clear disagreement between spectra. Is also clear that the expected structures of the TAC's response to

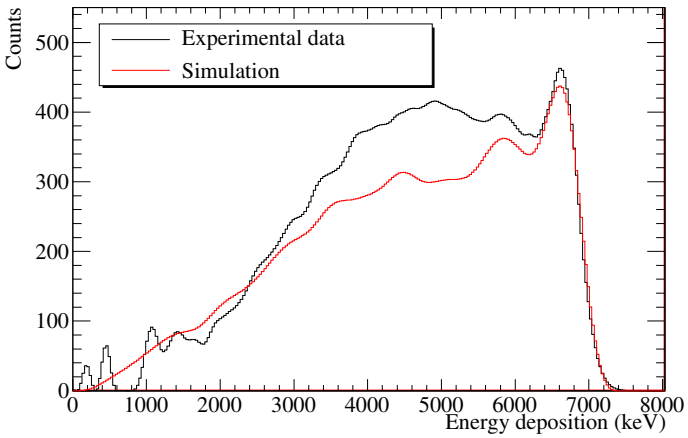

Figure 7.8: Comparison between experimental data and simulation for the neutron capture total energy deposition spectrum at the 2.3 eV resonance for events with multiplicity >1 (Case 1).

capture events are present in the simulation but do not reproduce the assessed experimental data.

As expected, the disagreement is also present in the multiplicity distribution spectrum (shown in Figure 7.9) where multiplicities 2, 6 and higher are favored in the simulation in respect to the experimental data, whereas multiplicities 3 and 4 seem underestimated.

In Figure 7.10 where the single gamma spectrum is displayed, a step in the spectrum is visible around 5 MeV. The physical meaning of this would imply some strange behavior in transition between levels with energies around 5 MeV. A smooth behavior is far more reasonable taking in consideration the level densities.

A possible reason for the disagreement seen in the reproduction of the energy deposition spectrum and multiplicity distribution spectrum can be a mis-assignment of the type of transition during measurement performed. To investigate this possibility, we tried two additional cases where we assign the recommended parameters to different types of transitions.

7.5.2 Reproducing the ^{233}U neutron capture cascade: Case 2

In order to cope with the identified disagreement between simulated and experimental data, which may be attributed to a wrong assignment of a transition type, the recommended PSF where changed in the following way: The E1 tran-

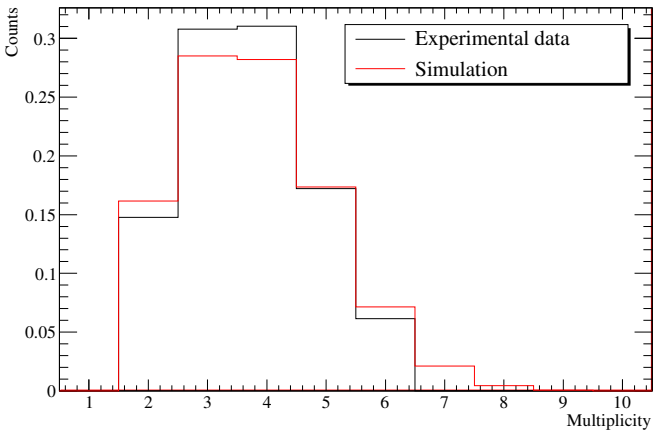

Figure 7.9: Comparison between experimental data and simulation for the neutron capture multiplicity distribution spectrum at the 2.3 eV resonance (Case 1).

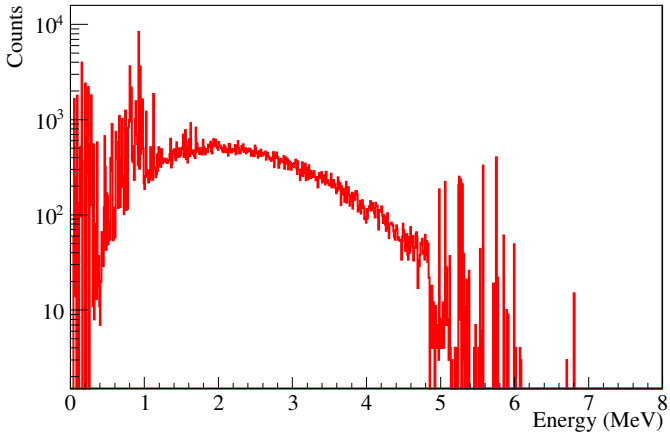

Figure 7.10: Single gamma spectrum for neutron capture events generated with the "captugens" software using the recommended (Case 1) PSF parameters for ^{233}U.

sitions are now described using only one standard Lorentzian distribution, the M1 transitions are described using the a standard Lorentzian distribution and the single particle model was used for E2 transitions. The parameterization used for E1, M1 and E2 can be found in Table 7.3.

The disagreement between the simulation (using the modified PSF) and the experimental data is considerable as observed in Figure 7.11 and no improve-

Table 7.3: Parameterization for the PSF of ^{233}U neutron capture generator (case 2).

	E1	M1	E2
E (MeV)	11.13	13.94	
Γ	2.26	4.46	
σ_0 (mb)	371	401	
$k_{strength}$			$5{\cdot}10^{-11}$

ment can be pointed when comparing with the results found in Figure 7.8.

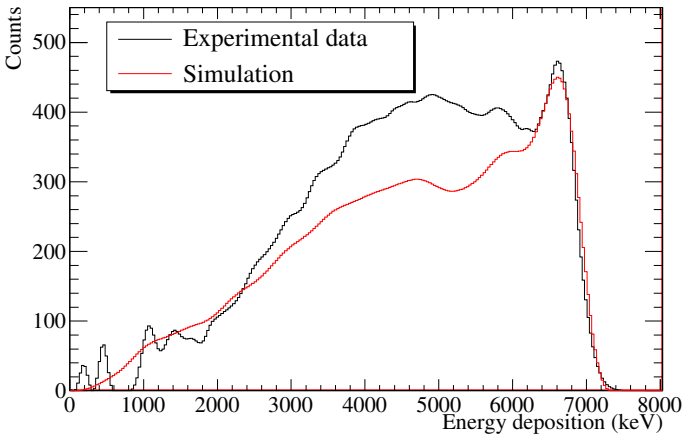

Figure 7.11: Comparison between experimental data and simulation (Case 2) for the energy deposition spectrum at the 2.3 eV resonance.

Looking at the multiplicity distributions spectrum shown in Figure 7.12, its possible to see that some multiplicities are favored and other underestimated just like in the case of the recommended PSF parameterization and overall, no improvement is registered.

In Figure 7.13 where the single gamma spectrum generated with the modified set of parameters is shown, its possible to see that the step around 5 MeV has been mitigated (when compared with Figure 7.10) but is still present.

The results shown in Figures 7.11, 7.12 and 7.13 leads to the conclusion that the modified set of parameter proposed in Table 7.3 is incorrect and doesn't correspond to an improved description of the capture deexcitation cascade.

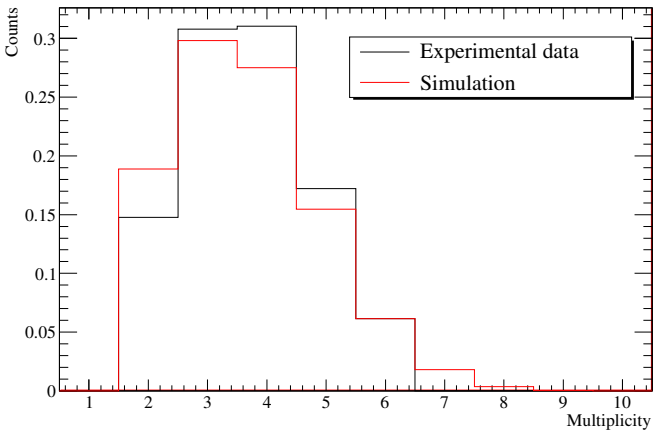

Figure 7.12: Comparison between experimental data and simulation (Case 2) for the multiplicity distribution spectrum at the 2.3 eV resonance.

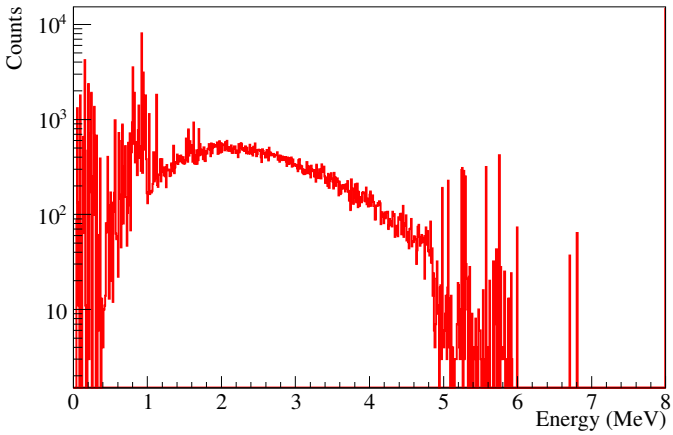

Figure 7.13: Single gamma spectrum for neutron capture events generated with the "captugens" software using the Case 2 PSF parameters for ^{233}U.

7.5.3 Reproducing the ^{233}U neutron capture cascade: Case 3

In this third attempt to reproduce the experimental data with simulations, the recommended PSF where changed in the following way: The E1 transitions are described using one standard Lorentzian distribution, the M1 transitions with a single particle model and E2 transitions were described using a standard Lorentzian distribution. The parameterization for E1,M1 and E2 can be found

in Table 7.4.

Table 7.4: Parameterization for the PSF of ^{233}U neutron capture generator (case 3).

	E1	M1	E2
E (MeV)	11.13		13.94
Γ	2.26		4.46
σ_0 (mb)	371		401
$k_{strength}$		$2{\cdot}10^{-8}$	

The results obtained with the simulation for the energy deposition spectrum in the 2.3 eV resonance using the set of parameters displayed in Table 7.4 can be seen in Figure 7.14 where they are compared with the experimental data. When compared with the results shown in Figure 7.8, it is possible to note a better reproduction of the experimental data but still far from a good agreement.

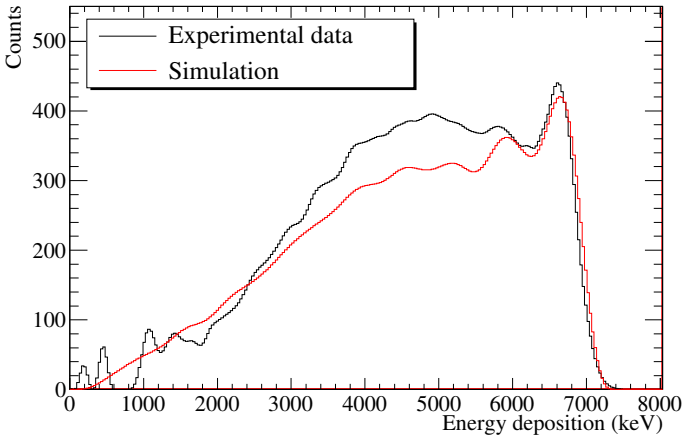

Figure 7.14: Comparison between experimental data and simulation (Case 3) for the energy deposition spectrum at the 2.3 eV resonance.

The multiplicity distribution spectrum shown in Figure 7.15 shows that events with higher multiplicities (7 and above) are more present and the events with multiplicities 3 and 4 are underestimated.

The single gamma spectrum shown in Figure 7.16 displays a smooth transition between all levels.

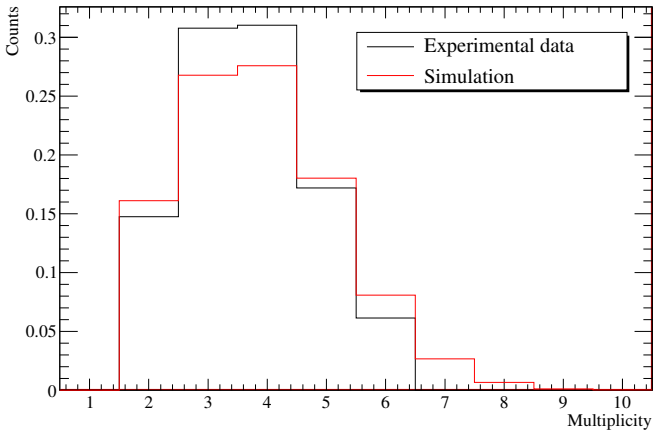

Figure 7.15: Comparison between experimental data and simulation (Case 3) for the multiplicity distribution spectrum at the 2.3 eV resonance.

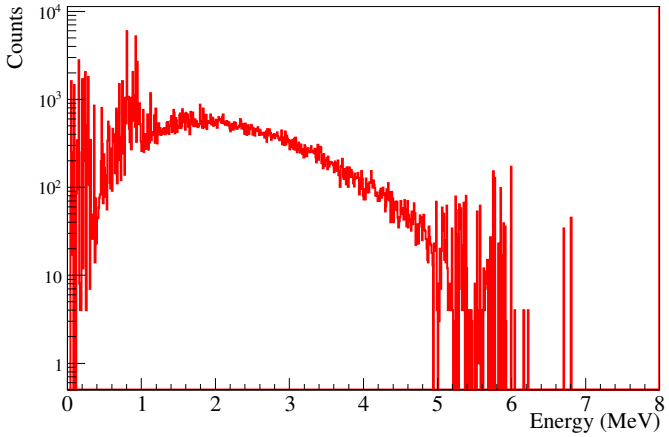

Figure 7.16: Single gamma spectrum for neutron capture events generated with the "captugens" software using the Case 3 PSF parameters for ^{233}U.

7.5.4 Reproducing the ^{233}U neutron capture cascade: Results overview

In the particular case of neutron capture in ^{233}U, information about the known nuclear levels, level densities and electromagnetic intensities are available from nuclear data bases. The use of recommended set of parameters has shown poor agreement with experimental data, leading to the need of tweak and fine-tune the parameters to achieve reasonable agreement, as described in other works

[134] and [123].

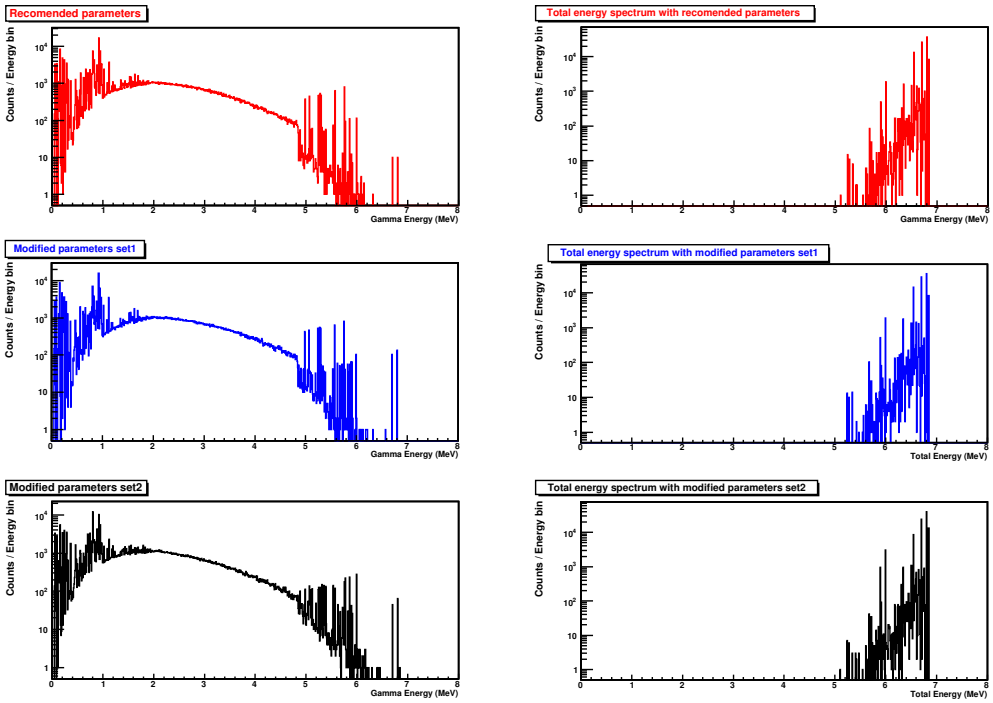

Figure 7.17: Results using different parameterizations for the gamma strength function used in the generation and simulation of the capture events. From left to right, single gamma spectrum and total energy spectrum for each event.

In Figure 7.17 right panels, the effect of the internal conversion is clearly seen in the total energy spectrum where some events show a loss up to almost 2 MeV in respect to the binding energy.

Overall, the results (Figures 7.9, 7.12 and 7.15) suggest that the theory (initial PSF) overestimates the multiplicity of the capture cascades and underestimates the intensity of primary high energy transitions.

The capture event detection and capture event reconstruction efficiencies are displayed in Table 7.5. The capture event detection efficiency is the TAC's efficiency for detecting at least one of the gammas emitted during a capture event and as displayed in Table 7.5 is very close to 100%.

The capture event reconstruction efficiency is the TAC's efficiency for detecting enough gammas rays from one capture event that combined with the analysis conditions such as event multiplicity higher than one and single gamma energy higher than 150 keV, permit the identification of the event as capture. In addition, this efficiency is also calculated for energy deposition

higher than 2 MeV to avoid the contribution of components that seem not accounted and reproduced with the simulation code.

Table 7.5: Capture event detection and event reconstruction efficiency results for the tree parameterizations studied.

Parameterization	Detection efficiency	Reconstruction efficiency (M>1)	Reconstruction efficiency above 2 MeV (M>1)
Test case 1 (recommended)	99.7%	95.2%	88.6%
Test case 2	99.5%	93.6%	86.0%
Test case 3	99.6%	94.8%	88.6%

7.6 Simulation of the fission events on the TAC

Due to the fact that both capture and fission reaction channels are opened in the case of the ^{233}U, and both reactions emit gamma radiation that is detected in the TAC, a full simulation of the detection system must accommodate also a simulation of the fission events. To do so, an algorithm to generate the gammas emitted by fission events with adequate multiplicity and gamma energy was developed.

7.6.1 Implementation of a gamma generator for fission events

The implemented event generator for the neutron induced fission in ^{233}U, followed closely the work presented in [135]. In this work, a simple and direct way to generate the gamma emission spectrum for fission is proposed, based on a negative binomial distribution capable or reproducing the gamma multiplicity spectrum, which is parameterized based in the average number of emitted gammas and distribution width.

The gamma energy is derived from the multiplicity of each event and average gamma energy. Important to note that the proposed fission deexcitation models for reproducing the gamma energy, multiplicity and total energy are based in data dating back to 1973 for ^{233}U and older in some other cases [144, 135, 140, 136] and no other measurement has been performed for validation or improvement (see Table 7.6) of those data.

Table 7.6: Measured properties of gamma rays from fission [135].

Isotope	Total energy (MeV)	Average number	Average energy (MeV)	Reference
^{233}U	6.69±0.3	6.31±0.3	1.06±0.07	Pleasonton (1973) [136]
^{235}U	6.43±0.3	6.51±0.3	0.99±0.09	Pleasonton et al. (1972) [137]
	6.70±0.4	6.69±0.3	0.97±0.05	Verbinski et al. (1973) [138]
	7.2±0.3	7.45±0.32	0.96±0.05	Pelle and Maienschein (1971) [139]
	6.53±0.2	6.60±0.2	0.97±0.04	Average
^{239}Pu	6.73±0.35	6.88±0.35	0.98±0.07	Pleasonton (1973) [136]
	6.82±0.3	7.23±0.3	0.94±0.05	Verbinski et al. (1973) [138]
	6.78±0.2	7.06±0.2	0.95±0.04	Average
^{252}Cf	7.06±0.35	8.32±0.4	0.85±0.06	Pleasonton et al. (1972) [140]
	6.84±0.3	7.80±0.3	0.88±0.04	Verbinski, et al. (1973) [138]
	8.6	10	0.90±0.06	Bowman and Thompson (1958)[141]
	6.7±0.4	n. a.	n. a.	Nardi et al. (1969) [142]
	n. a.	7.5±1.5	0.96±0.08	Val'skii et al. (1969) [143]
	6.95±0.2	7.98±0.2	0.87±0.03	Average

The author in [135] stresses that the methods are only approximate at best and should only be used for sensitivity studies. Measurements of the multiplicity distribution of prompt gamma rays from fission should be performed to determine the adequacy of the models proposed in this article.

The recommended values for the fission parameterization in ^{233}U are:

- 6.69 ± 0.3 MeV for average emitted energy.
- 6.31 ± 0.3 for the average number of emitted gammas.
- 1.07 for the width for negative binomial distribution.

Figure 7.18 shows in red the experimental derived energy deposition spectrum due to fission and in black the simulated energy deposition spectrum due

to fission.

Despite normalization factors, the shape of the simulated spectrum seams to follow quite well the experimental data, except for energies below 2 MeV where some peaks are present in the experimental spectrum. These peaks seam to contaminate the resonant data and appear indistinctly on fission and capture energy deposition spectra as can be seen in Figure 7.14 below 2 MeV. The origin of these peak may be related with the delay gamma emission.

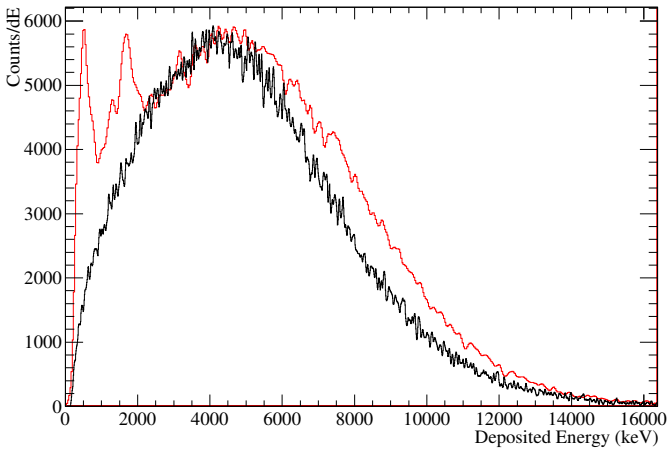

Figure 7.18: Comparison between simulated (black) and measured (red) total energy deposition for fission.

Although the shape above 2 MeV seems to agree in terms of slope, one can see that the distribution width isn't in agreement with the experimental distribution. The recommended values which are based in measurements for ^{252}Cf and ^{235}U, gave consistent results pointing to a width of 1.07 but in the case of the data taken with n_TOF, a higher value seems more appropriated.

The consistency between the two measurements suggests that the relative width of the distribution of the number of prompt fission gamma rays may be independent of the fission process. However, the consistency between the two measurements may also result because the measurements were performed using the same experimental method with the same basic assumptions [135]. Moreover, variations on the width of the measured distribution may occur most likely due to artifacts in the detection system.

Taking these facts in account the parameterization of the fission event generator was fine tuned to reproduce the experimental data and is detailed in Table 7.7.

The results obtained with the simulation using the new parameterization

Table 7.7: Parameterization for the ^{233}U fission event generator.

	Multiplicity	Total gamma energy	Gamma width
Recommended	6.31 ± 0.3	6.69 ± 0.3 (MeV)	1.07
After fine-tuning	7.21	9.49	1.12

can be seen in Figure 7.19.

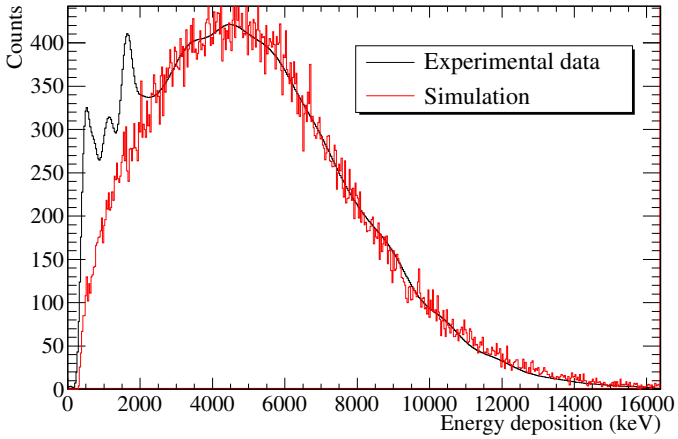

Figure 7.19: Comparison between the simulated energy deposition spectrum for fission with experimental data using a new parameterization for the fission event generator.

A good agreement between experimental data and simulation can be observed for energies above 2 MeV. Below this energy there is clearly a component in the fission spectra that is not considered in the simulation. This component may be related with delayed emission from fission fragments and it seems to affect also the experimental capture spectra (Figure 7.14 below 2 MeV). To avoid the contributions from this component, the efficiency will be determination based on data above 2 MeV, where simulation and experiment agree. Moreover, below this energy the CSD method may not be reliable because of the many components interfering in this region such as sample and room activity, capture events, fission events, in beam gamma scattering, TAC overall neutron sensitivity, among others. In Figure 7.20, where the experimental data

and simulation multiplicity distributions for fission events are plotted together, a good agreement can be observed. for multiplicities higher than 4.

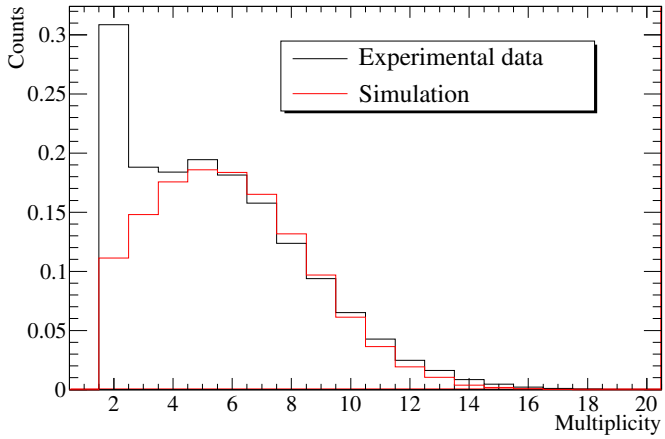

Figure 7.20: Comparison of experimental (black) and simulated (red) multiplicity distributions for fission events.

The assessed event detection and event reconstruction efficiencies are shown in Table 7.8.

Table 7.8: Fission event detection and event reconstruction efficiency results.

Detection efficiency	Reconstruction efficiency (M>1)	Reconstruction efficiency above 2 MeV (M>1)
98.6%	93.%	82.4%

Chapter 8

Results

In this chapter, reaction yields $Yr_{(n,x)}(E_n)$ obtained from the data analysis performed on the ^{233}U data using the CSD will be discussed. The ^{233}U neutron capture and neutron induced fission yields are assessed using the normalization constants obtained in Chapter 7, due to data analysis conditions and event detection efficiency and are compared with the data available in the ENDF/B-VII.1 library. The uncertainties relative to the ^{233}U neutron capture and neutron induced yields will also be discussed.

As introduced in Chapter 7, the relation between counting rates obtained with the data analysis and reaction rates that are used to assess the cross sections, implies the accurate knowledge of the neutron beam intensity and neutron beam intersection factor. The neutron beam intensity has been discussed in Section 4.1.2.3 together withe facility characteristics. The neutron beam intersection factor will be discussed in the following section.

8.1 Neutron beam intersection factor

The neutron beam intersection with the sample is a function of the sample cross section area, beam collimation and neutron energy. The beam collimation system installed along the beam line (see Section 4.1.4.1) dictates the neutron beam spatial profile.

The neutron beam profile or resulting spatial distribution of the neutrons in the beam has been measured with a stripped Micromegas detector [145]. The measurements were performed with the strip electrodes of the Micromegas rotated at different angles (0°, 30°, and 90°) in order to determine the two dimensional beam profile, which is shown in Figure 8.1 in the energy range between 10 eV and 100 eV.

The neutron beam was found to have an approximate Gaussian shape with

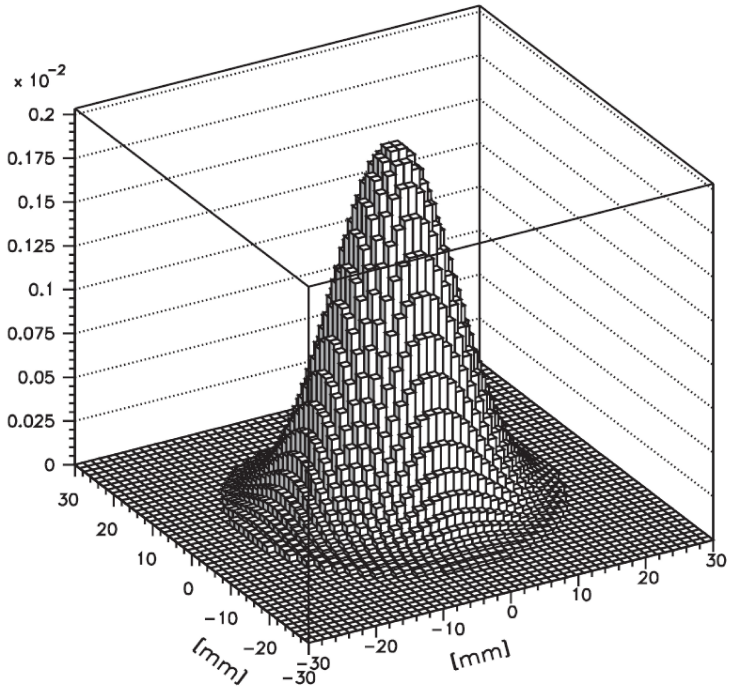

Figure 8.1: Neutron beam spacial profile obtained with the Micromegas detector ([145]).

a width of σ=0.77 cm, which varies slowly with neutron energy. The detailed beam profile and an analytical function for its description are given in [145]. In addition to the measurement with the Micromegas, a complete Monte Carlo simulation of the production and moderation of the neutrons and their transport trough the beam line was performed using the Monte Carlo simulation program FLUKA [146]. The results obtained for the neutron beam intersection factor "N" with the sample ($N = 0.1979$) were validated by comparison with the measurements [145]. It was also established that the sample position has an uncertainty of 0.5 mm. The contribution of this uncertainty in the position will be discussed in Section 8.4.1.

Figure 8.2 shows the simulated results for the beam profile as a function of neutron energy.

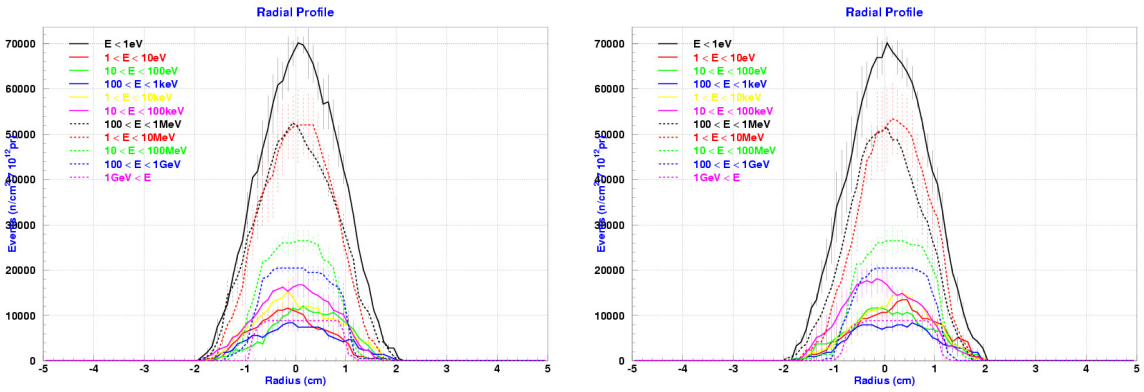

Figure 8.2: Neutron beam profile as function of the neutron energy at 184.6 meters. Vertical (left) and horizontal (right) projections of the beam profile.

8.2 Discussion of the ^{233}U neutron induced fission yield measured at n_TOF

Using the counting for a given reaction assessed with the CSD method to decompose the total energy deposition spectrum, the beam intersection factor, the event reconstruction efficiency and the neutron beam flux, we obtained the dead time correction and the reaction yield using Eq. (7.4). The neutron induced fission yield assessment for the ^{233}U is compared with the data from the ENDF/B-VII.1 library and as can be seen in Figure 8.3 there is a good agreement between n_TOF experimental data and evaluation is present in the energy range between 1 and 10 eV both in linear and logarithm vertical scales.

The agreement in normalization and shape, validates the CSD method to decompose the total energy deposition spectrum and discriminate between competing reactions and also the Monte Carlo study performed to understand the TAC's response to the prompt gamma radiation emitted in fission events.

Figure 8.4 shows the n_TOF neutron induced fission yield measured for the ^{233}U compared with the data from the ENDF/B-VII.1 library in the incident neutron energy range between 1 eV and 1 keV. The is a good agreement over the whole range.

In Figure 8.5 and 8.6 the ^{233}U fission yield is compared with the ENDF/B-VII.1 library in the specific ranges of 10 to 100 eV and 100 eV to 1 keV in both linear and logarithm vertical scale and a good reproduction of the shape is visible. The normalization is also in good agreement.

Above the resolved resonance region (which extends until 600 eV), the data taken in n_TOF shows a number of structures which in the resonance

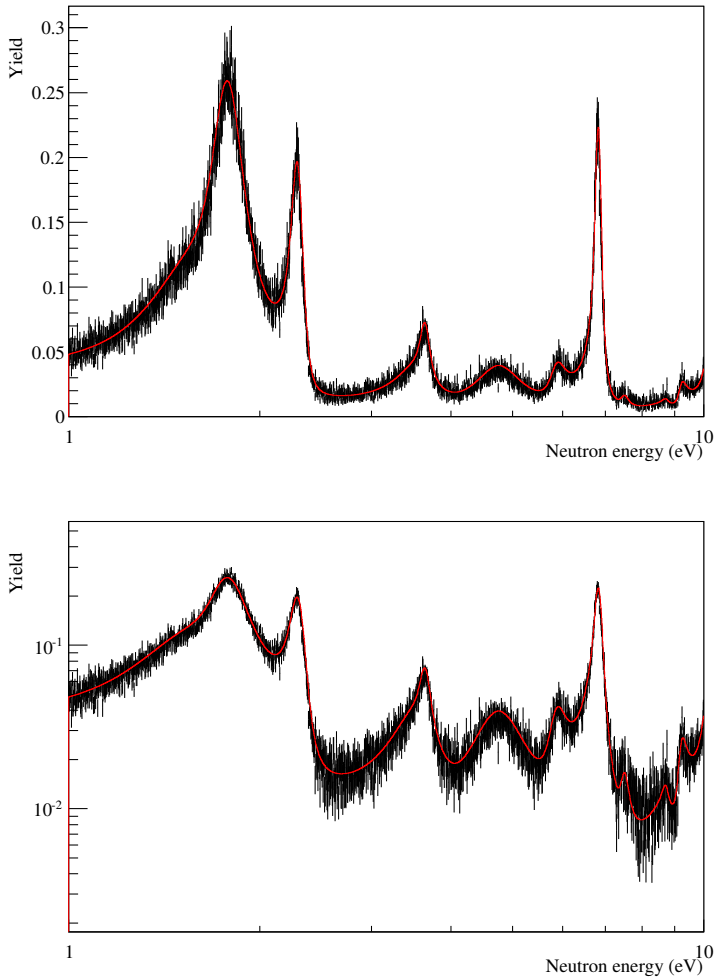

Figure 8.3: Comparison of the ^{233}U neutron induced fission yield measured at n_TOF (black) and the ENDF/B-VII.1 library (red) between 1 and 10 eV.

analysis parameter may not be possible to discriminate due to the great overlap between resonances. The average yield of the ENDF/B-VII.1 library is in good agreement with the structures trend in the n_TOF yield.

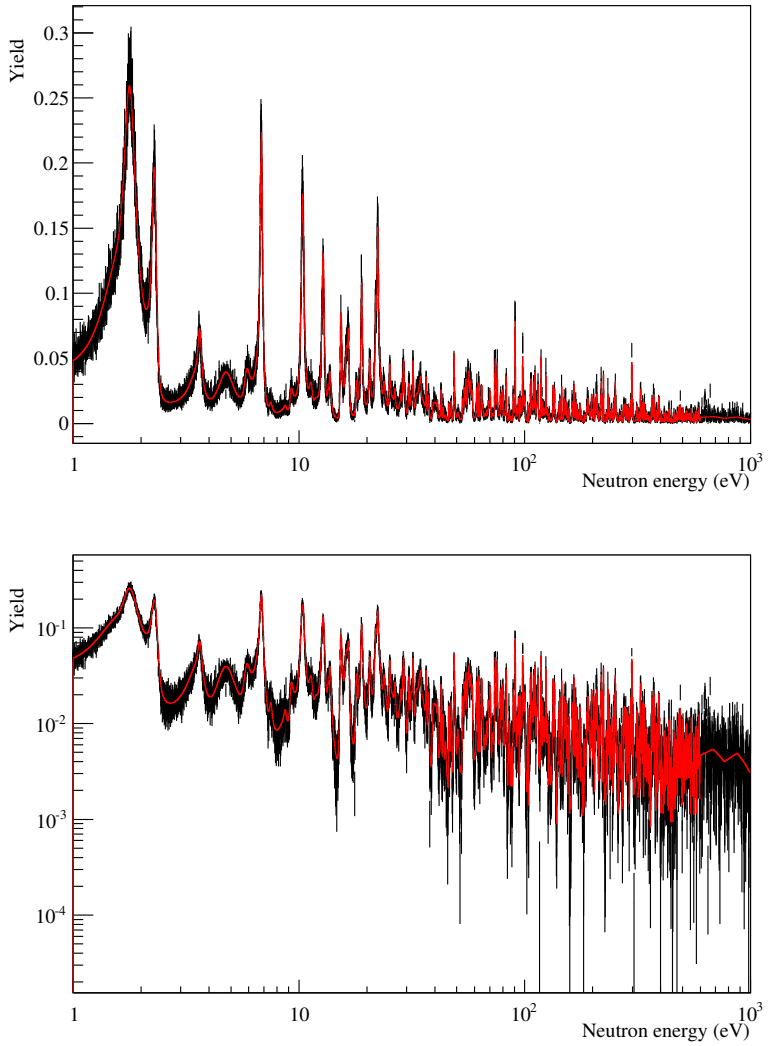

Figure 8.4: Comparison between the ^{233}U neutron induced fission yield measured at n_TOF (black) and the ENDF/B-VII.1 library (red) between 1 eV and 1 keV.

8.3 Discussion of the ^{233}U neutron capture yield measured at n_TOF

The neutron capture yield has been measured in the same way as the neutron induced fission yield and the only difference lies in the event generator used in the Monte Carlo study to reproduce the neutron capture events used in

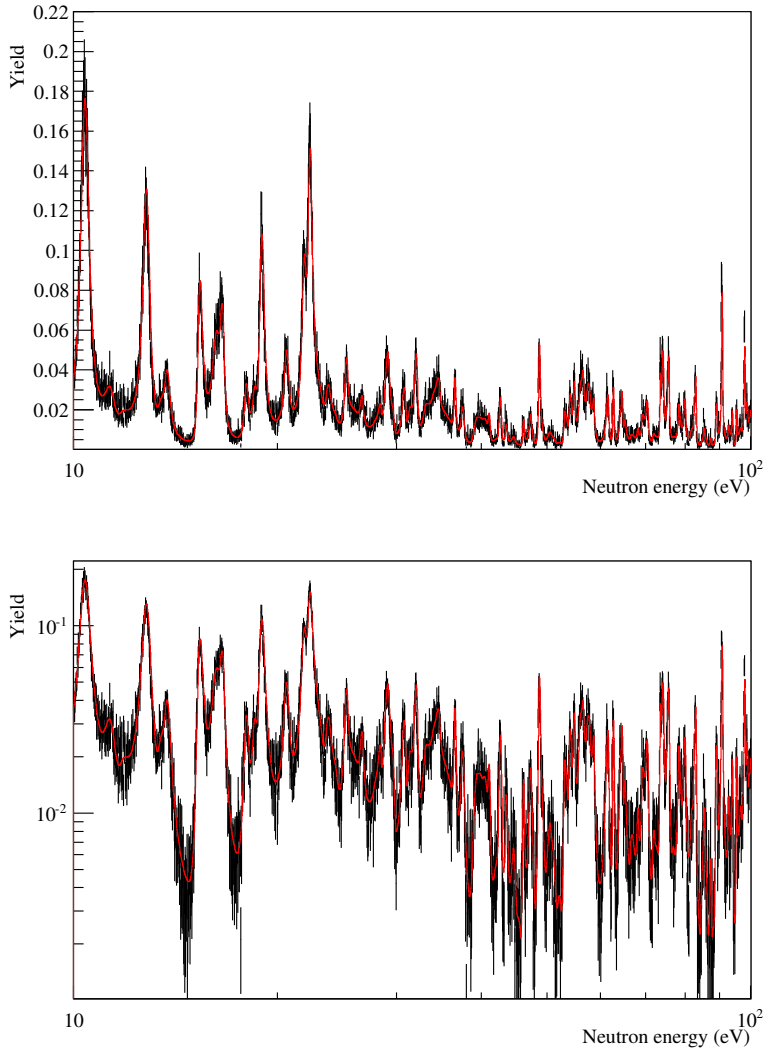

Figure 8.5: Comparison between the ^{233}U neutron induced fission yield measured at n_TOF (black) and the ENDF/B-VII.1 (red) library between 10 and 100 eV.

the event reconstruction efficiency determination. As mentioned in Chapter 7, discrepancies were observed in the comparison between the simulation and experimental energy deposition spectrum in either tried cases.

the agreement between the simulation and the experimental energy deposition spectrum for capture events was not the best in either tried cases. Although the simulations seem to point out that overall, the event reconstruction efficiency does not change dramatically with the parameterizations used,

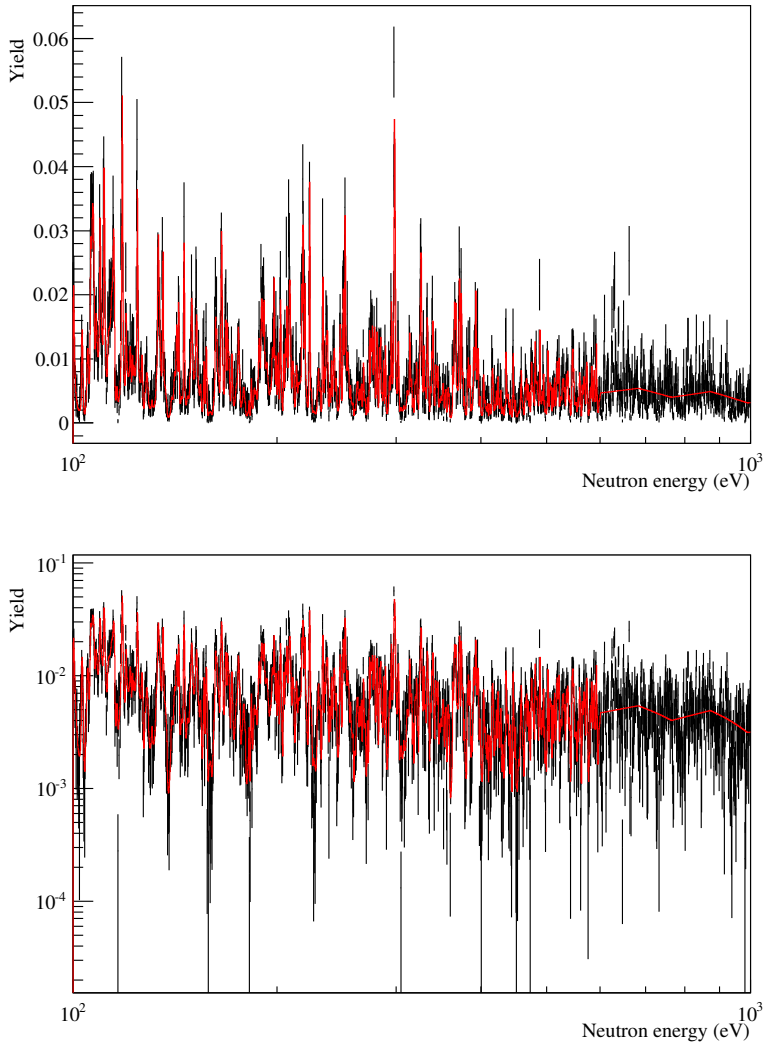

Figure 8.6: Comparison between the ^{233}U neutron induced fission yield measured at n_TOF (black) and the ENDF/B-VII.1 (red) library between 100 eV and 1 keV.

one must consider the uncertainty for this parameter.

Considering the other aspects of the analysis and quantities used in the yield assessment, they are the same used for assessing the neutron induced fission yield and produced a good agreement with ENDF/B-VII.1 library.

Looking at Figure 8.7 where the neutron capture yield measured at n_TOF between 1 and 10 eV is compared with the ENDF/B-VII.1 library, a disagreement of 30% in the normalization is present. The value obtained for both

neutron capture and neutron induced fission event reconstruction efficiency is very close and this is compatible with the fact that both types of events have similar average multiplicity and energy deposition values.

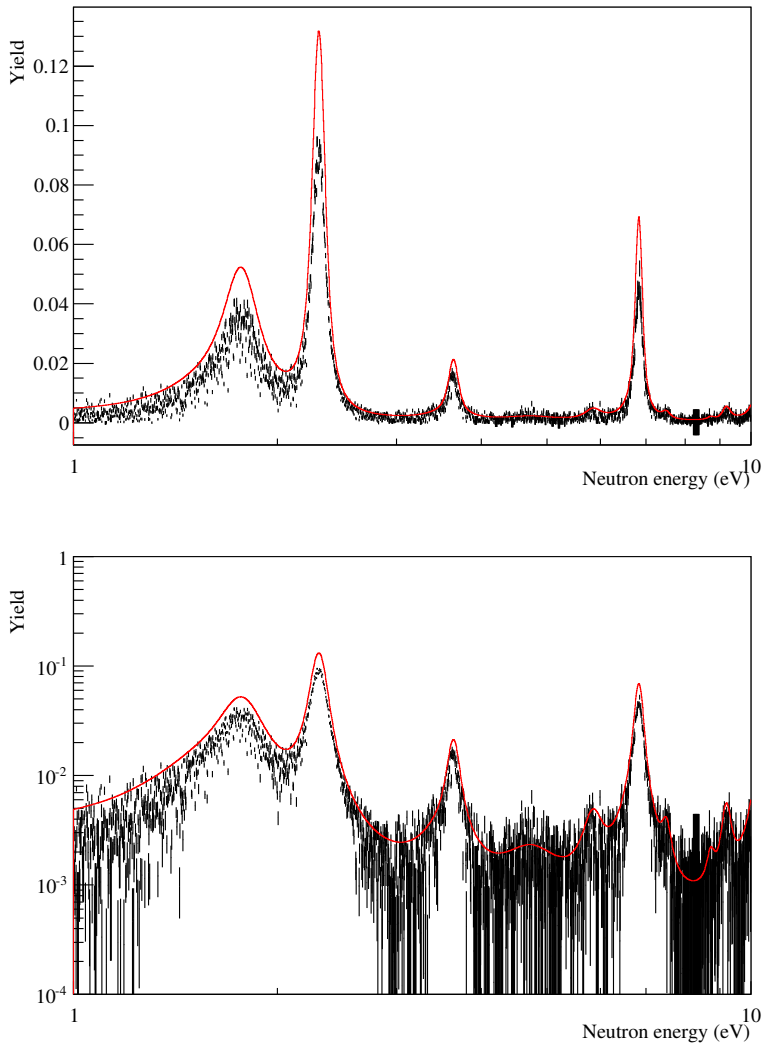

Figure 8.7: Comparison between the ^{233}U neutron capture yield measured at n_TOF (black) and the ENDF/B-VII.1 (red) library between 1 and 10 eV using the assessed normalization factor.

Figure 8.8 shows the neutron capture yield between 1 and 10 eV normalized to the ENDF/B-VII.1 library. The normalization was obtained for the integral of capture yield from the ENDF/B-VII.1 library in the energy range between 1 and 10 eV. A good agreement between yield shapes is visible which validates

the CSD method used.

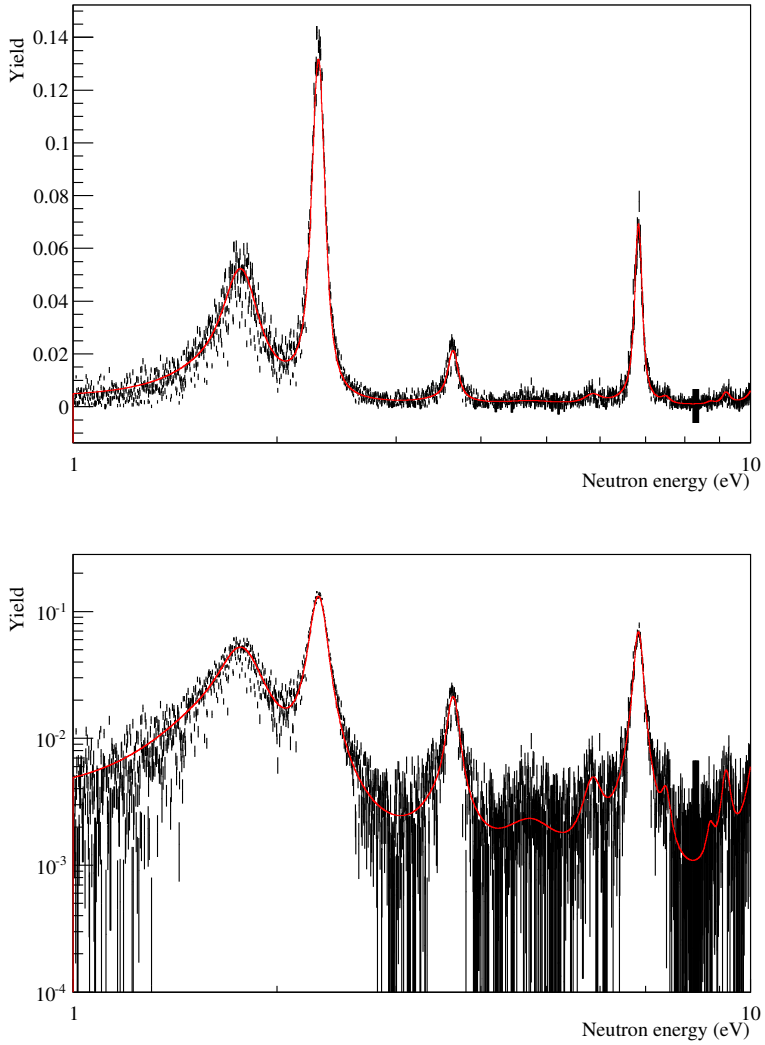

Figure 8.8: Comparison between the ^{233}U neutron capture yield measured at n_TOF (black) and the ENDF/B-VII.1 (red) library between 1 and 10 eV using an arbitrary normalization factor.

The agreement is observed over all the incident neutron energy range displayed in both Figure 8.9 and 8.10 except beyond the resolved resonance region which ends at 600 eV. In the unresolved resonance region, the ENDF/B-VII.1 library is above the yield measured at n_TOF and further investigation is necessary to fully understand the causes.

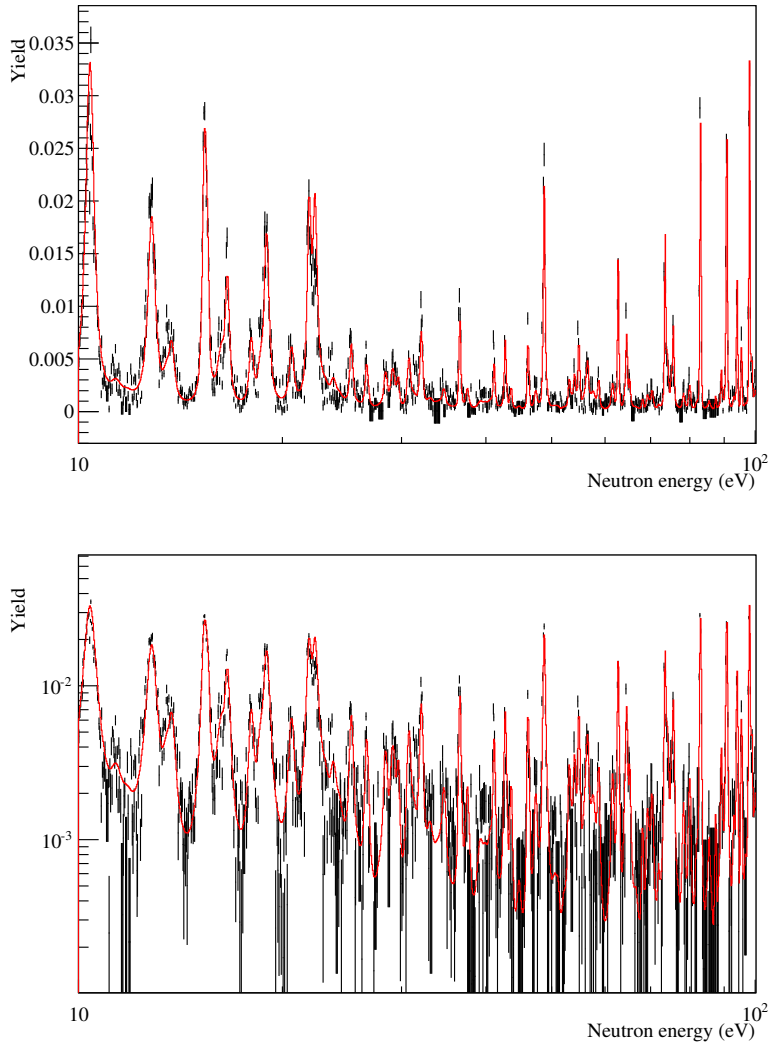

Figure 8.9: Comparison between the ^{233}U neutron capture yield measured at n_TOF (black) and the ENDF/B-VII.1 (red) library between 10 and 100 eV using an arbitrary normalization factor.

The data plotted in Figures 8.9 and 8.10 has bigger bin widths in respect to Figure 8.8 to compensate the inferior statistics.

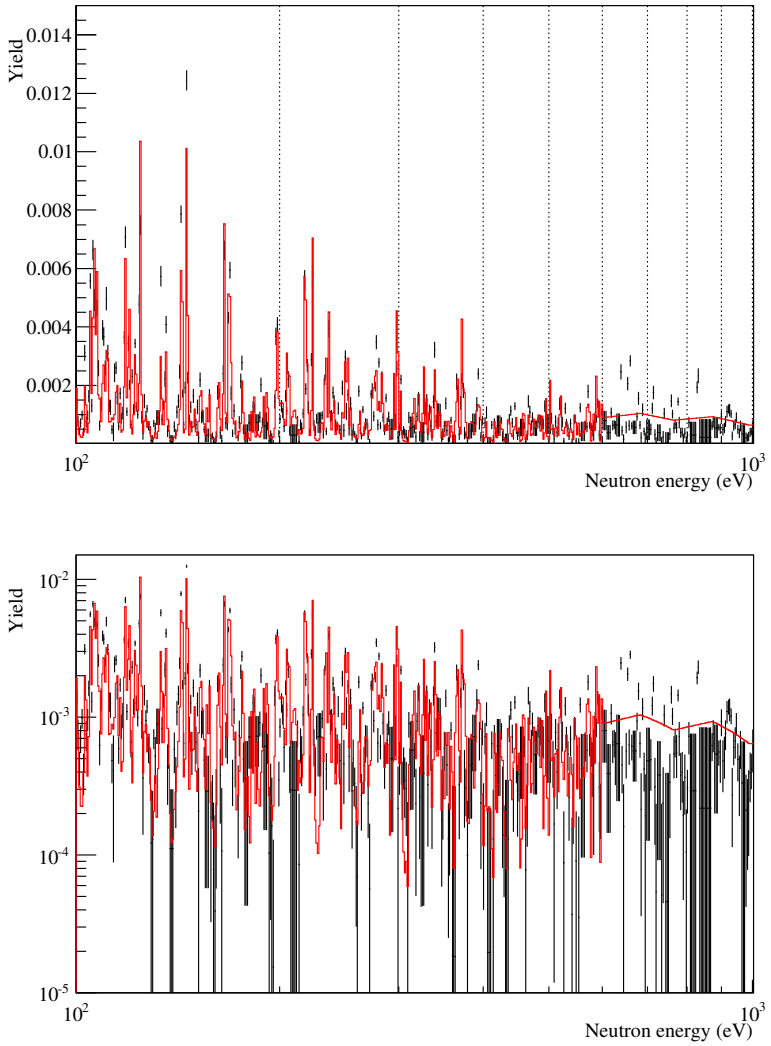

Figure 8.10: Comparison between the ^{233}U neutron capture yield measured at n_TOF (black) and the ENDF/B-VII.1 (red) library between 100 eV and 1 keV using an arbitrary normalization factor.

8.4 Uncertainties in the results

The experimental uncertainties associated to the measurement reported here are exceedingly difficult to evaluated. Uncertainties can be attributed to (i) statistics, (ii) normalization, (iii) correction factors and (iv) sample related. Efforts have been made in order to make the best estimation of these uncertainties but the estimation of the uncertainty associated with the de-

composition of the total deposited energy spectrum depends not only in the statistics of the spectrum but also in the assessed shapes to describe each components contributing with counts in the detection system. The assessment was done by a sensitivity study to the shapes used for the TAC's response.

$$U_{Total} = (U^2_{Beam\ intersection\ factor} + U^2_{Fluxe\ shape} + U^2_{Data\ analysis\ and\ simulations} + U^2_{Sample\ mass})^{1/2} \tag{8.1}$$

The uncertainty "U_{Total}" in the yield is related with the following components:

- Statistical uncertainty in the raw data.
- Determination of the TAC total energy deposition response to neutron capture and fission events.
- The method used to perform the decomposition of the total energy deposition spectrum.
- Event reconstruction efficiency for neutron capture and fission.
- Normalization factors such as beam intersection factor, sample mass and flux characteristics.

While the last components (beam intersection factor, sample mass and flux characteristics) can be determined separately, the remaining components are very difficult to isolate and propagate trough the whole data analysis process specially when using such a complex methodology as is the case with the CSD.

8.4.1 Uncertainty in the beam intersection factor

Using the sample holders detailed in Section 5.6 to place the sample in the center of the beam, it can be assumed that the maximum misalignment of the sample's positioning in the TAC is below 1 mm. Such a displacement would affect the fraction of the beam intercepted by the sample, which has been calculated from the information on the beam profile. Figure 8.11 shows the beam profile in a 2D histogram with the sample positioned in the center. For a maximum misalignment of 0.5 mm, the uncertainty in the fraction of the beam intercepted by the sample is 1% [134]. The uncertainty in the sample diameter is also considered here.

8.4.2 Uncertainty in the sample mass

The uncertainty in the sample mass is given by the sample certificate and no other direct measurement has been performed to validate the 5% uncertainty mentioned.

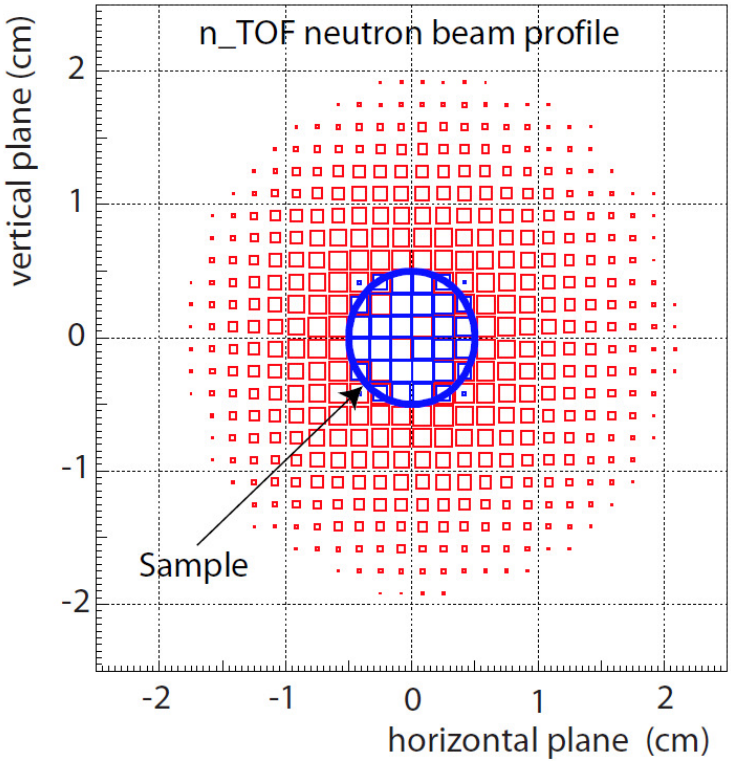

Figure 8.11: Calculation of the beam interception factor with the sample using the beam profile information [134].

8.4.3 Uncertainty in the flux shape and absolute value

The flux uncertainty has two components, one being the flux energy spectrum shape and the other the absolute value. The first is related with the spallation and moderation processes which yield the characteristic shape with the moderation (25 meV) and evaporation (1 MeV) peaks and the almost flat region within the peaks. The second one is related with the neutron to proton production ratio and distance from the neutron source to the experimental area. An extensive and comprehensive study has been performed using different detection systems and analyzing different neutron energy ranges and resonances at different neutron energies [92].

The uncertainty associated with the flux shape and absolute value have been assessed accordingly to the experimental conditions used for the ^{233}U capture cross section measurement with the TAC using a set of two detections systems, detailed in Section 4.1.2.3.

The overall uncertainty for the flux shape and absolute value assessed is 2%.

8.4.4 Uncertainty in the detection efficiency

Considering the neutron capture deexcitation cascade simulation and the 3 studied cases, the fact that different parameterizations yield equivalent descriptions of the neutron capture events, gives us the possibility of using this information to estimate the uncertainty. The uncertainty due to the different parameterizations in the assessed neutron capture event reconstruction efficiency is below 3% corresponding to the biggest variation between simulated cases.

In the case of the simulations performed for the fission event reconstruction efficiency, the parameterization that yielded a good description of the fission events was unique and therefore, the uncertainty based in the systematic variation of the parameters was not assessed. In order to cope with possible uncertainties in the fission event reconstruction efficiency, a 3% uncertainty was considered based on a conservative approach and on the results obtained for the neutron capture event reconstruction efficiency.

8.4.5 Systematic uncertainty in the data analysis

The determination of the uncertainties related with the data analysis using the CSD method is a complex task and due to the decomposition of the total energy deposition spectrum using a linear fit of the previously assessed TAC responses to neutron capture and fission, the correlation of the uncertainties increases and a statistical uncertainty loses meaning.

To address the propagation of possible correlated uncertainties as expected for instances with TAC response to neutron capture which is assess based on the knowledge of the TAC response to fission, a systematic analysis of the uncertainties was performed. The analysis aims at determining the uncertainty in the yield due to:

- the TAC response to neutron capture and fission
- and to the decomposition process of the total energy deposition spectrum.

The uncertainties related with the TAC response to neutron capture and fission were addressed performing a series of yields calculations with different but compatible sets of TAC total energy deposition responses shown in Figure 8.12. The mathematical representation is assessed by fitting the experimental spectrum of the total energy deposition due to neutron capture or neutron induced fission events with a predefined function. This procedure limits the ability to reproduce the fine structures of the experimental spectrum. On the contrary, the use of the experimentally assessed total energy deposition spectrum (histogram representation) either for neutron capture or

neutron induced fission yields a very precise description of the fine structures such as the binding energy peak.

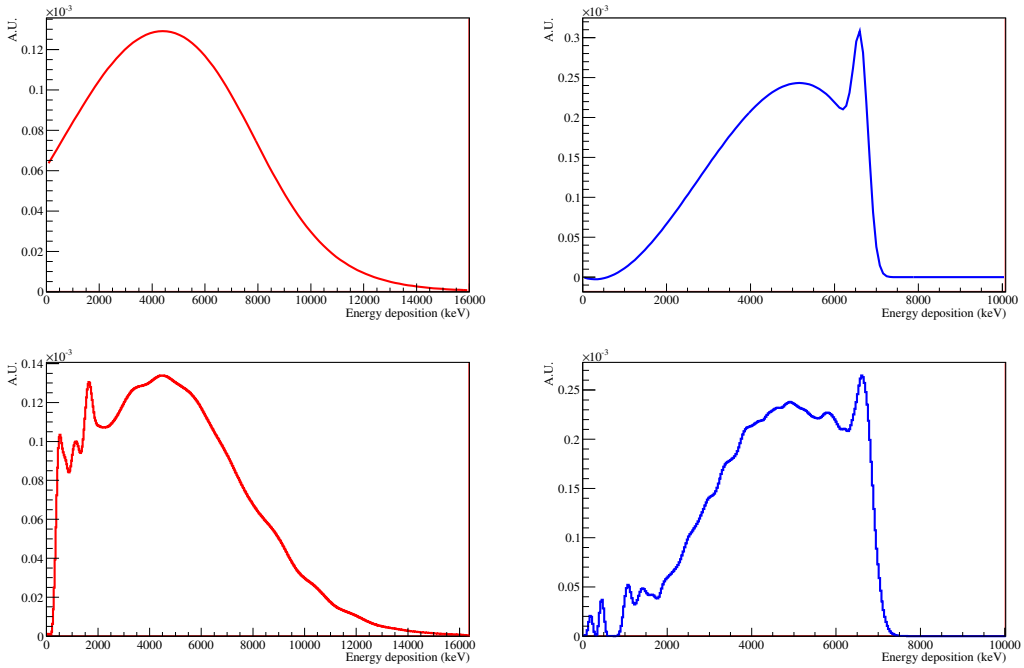

Figure 8.12: Different assessed TAC responses to fission and capture. Mathematical parameterization of the TAC response to fission (top left) and capture (top right). Histogram representation of the TAC response to fission (bottom left) and capture (bottom right).

To understand the effectiveness of the methodology used and the robustness of the developed algorithm and its sensitivity to the inputed TAC responses, different methods to perform the decomposition of the total energy deposition spectrum were studied and the uncertainties related with each method were assessed. The two methods studied consist in the following ways to perform the decomposition:

- one consisting in a two step process where the fission contribution is assess and removed from the total energy deposition spectrum in a first step followed by a second step where all other components are assessed. This poses several advantages such as: (i) the fission is easily assessed (ii) and removing one contribution from the total energy deposition spectrum helps in the assessment of the remaining contributions,
  Nevertheless it has several disadvantages such as: (i) the fission contribution assessment is performed based on the fit of a reduced portion of

the total energy deposition spectrum where its assumed that the only reaction contributing is fission. (ii) consequently, a small uncertainty in the fission contribution assessed in the first step will translate itself into the second step and in the case of the capture which is several times smaller in magnitude, this factor will appear multiplied.

- The second method consists of performing the decomposition of the total energy deposition spectrum in one single step. This method increase the complexity of the process but has advantages such as: (i) the freedom of the fitting algorithm to adjust all TAC responses at the same time and fully reproduce the experimental spectrum (ii) and therefore a smaller probability of propagating uncertainties from one contribution to the others.

Due to the fact that the methodology to perform the decomposition of the total energy spectrum depends directly on the assessed TAC response to the different reactions, the systematic uncertainty analysis has been performed together for this two factors and will be detailed in the next two sections.

8.4.5.1 Two step method

The two step method as mentioned before consists in assessing the fission contribution in a first step and the remaining contributions in the second step. This is only possible because above ∼10 MeV, only fission contributes to the total energy deposition spectrum. From the point of view of the systematic uncertainty analysis, the fission determination has no correlation with the neutron capture and remaining contributions assessed in the second step. Therefore, the systematic uncertainty of the fission yield using the two step method depends solely on the TAC response to fission (Figure 8.12).

The determination of the systematic uncertainties was based on the comparison between two yields extracted with different TAC responses and in the assessment of the difference in percentage for every neutron energy bin in the 1 eV to 1 keV energy region. The difference is plotted in a histogram and the mean and Root Mean Square (RMS) is computed for the distribution. Several cases have been studied and the particular details of each are summarized here:

- Reference: Uses both histogram representations for the TAC response to neutron capture and fission.
- Case 1: Histogram representation of the TAC response to neutron capture and mathematical parameterization of the TAC response to fission.
- Case 2: Used both mathematical parameterization for the TAC response to neutron capture and fission.
- Case 3: Mathematical parameterization of the TAC response to neutron capture and histogram representation of the TAC response to fission.

The results obtained for the fission yield assessment using the two step method for the decomposition of the total energy deposition spectrum for the case 2 condition and comparing it with the reference case are shown in Figure 8.13.

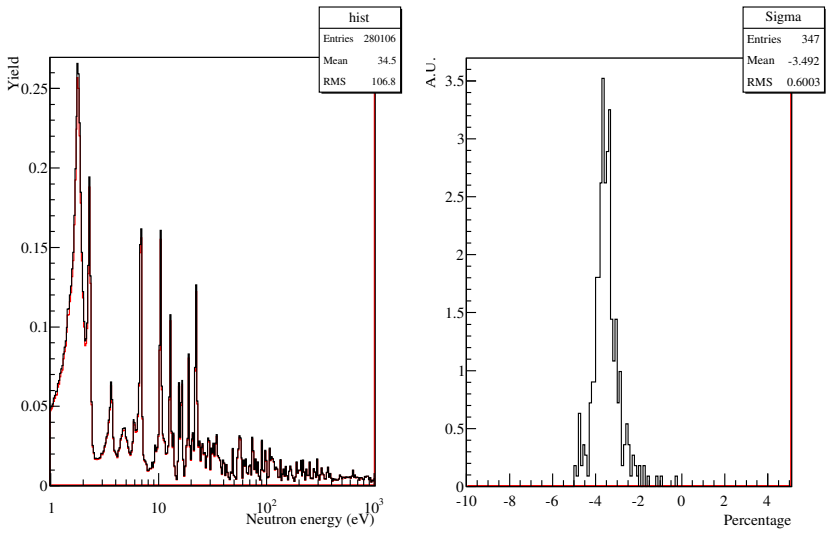

Figure 8.13: Fission yields obtained with the two step methodology (left) for the reference case (black) and case 2 (red) and the computed difference in percentage between yields (right).

The complementary assessment of the uncertainty for the neutron capture yield is shown in Figure 8.14. Note that the assessment of the uncertainty for the neutron capture yield depends on the TAC response to fission and its systematic uncertainty although the contrary is not true due to the two step method employed.

The results obtained for the 3 cases studied are presented in Table 8.1. The zeros for both mean and RMS assessment of case 3 are expected as comparing the assessment of the fission yield under the same conditions should produce no variation.

Before discussing the results showed in Table 8.1, its important to understand the meaning of the mean and RMS of the distribution obtained by comparing two yields assessed in different conditions. The mean in this case give us information about a global difference between the yields and can be interpreted as a over or underestimation of the yield magnitude but also as the global uncertainty. The RMS on the other hand give us information on the point wise variations and can be interpreted as the uncertainty in the determination of each bin content from one method to other. Note also that all results

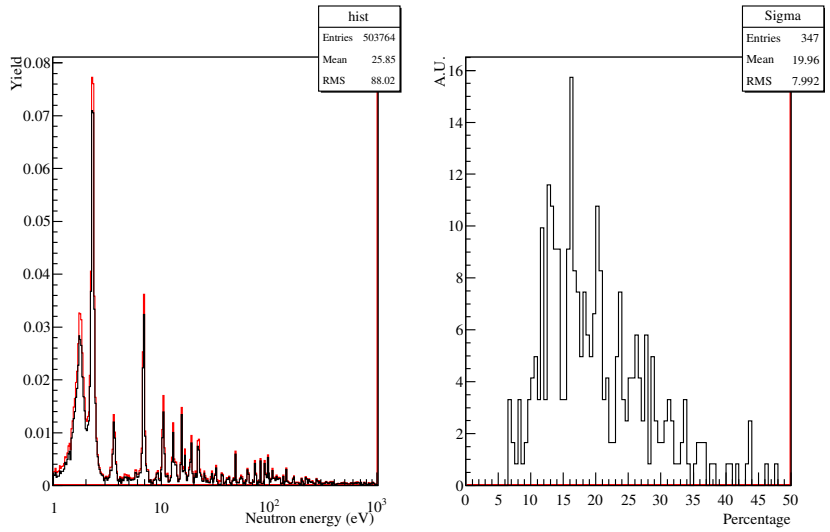

Figure 8.14: Neutron capture yields obtained with the two step methodology (left) for the reference case (black) and case 2 (red) and the computed difference in percentage between yields (right).

Table 8.1: Result obtained for the systematic uncertainty analysis using the two step method.

Reaction	Fission		Capture	
Quantity	Mean	RMS	Mean	RMS
Case 1 (Capture_{Hist}, Fission_{Math})	-3.5%	0.6%	15.4%	9.5%
Case 2 (Capture_{Math}, Fission_{Math})	-3.5%	0.6%	19.7%	8.9%
Case 3 (Capture_{Math}, Fission_{Hist})	0.%	0.%	5.2%	3.0%

were obtained by comparing the different cases with the reference which consists in both histogram representations of the TAC response to neutron capture and fission.

With mean and RMS meanings in mind, when looking at the results obtained in case 1 for the fission yield, the use of a mathematical representation vs an histogram representation of the TAC response to fission, produces an underestimation of the yield in 3.5% but a small uncertainty of 0.6%.

Analyzing the neutron capture yield in case 1, the use of a mathematical representation of the TAC response to fission and a histogram representation of the the TAC response to neutron capture, produces an overestimation of the capture yield by 15.4% versus the reference.

Again, looking at the neutron capture yield but this time for case 2, the yield obtained using both mathematical representations of the TAC response to neutron capture and fission vs the reference yield, shows an overestimation in 19.7% and a significant uncertainty (8.9%). This big uncertainty in capture is due to the fact that capture and fission are extracted separately. The neutron capture cross section is almost one order of magnitude lower in comparison with the neutron induced fission cross section. A 3% deviation in fission gives a 20% deviation in capture.

In case 3 where the capture yield is obtained using an histogram representation of the TAC response to fission and a mathematical representation of the TAC response to neutron capture, produces an overestimation of 5.2% with a uncertainty of 3%.

From the uncertainty study done for the two step method, one can conclude the high dependency of the results on the inputed type of representation used to do the decomposition. This also points out that this method may not be the most adequate.

8.4.5.2 One step method

The one step method consists in performing the decomposition of the total energy deposition spectrum for all components at the same time. Concerning the assessment of the uncertainties, this poses different consequences in comparison with the two step method. In the two step method, being the fission yield assessed prior to the capture yield and other contribution, made it independent of the uncertainty in the remaining contributions. On the other hand, the capture yield showed a great dependence on the type of assessment of the fission yield. This causality relation should be less important in the one step method, due to the fact that the fitting algorithm can play with all TAC responses at the same time without constrains.

Figure 8.15 shows the fission yields obtained for the reference case and case 2 and the computed difference in percentage between yields. The conditions used to assess the different yield have been detailed in Section 8.4.5.1.

The assessment of the uncertainty for the neutron capture yield is shown in Figure 8.16. With this method, the capture yields and its associated uncertainty depends on the fission yield and associated uncertainty and vice versa.

The mutual dependency between the neutron capture and fission yields and respective associated uncertainties reflects itself in the results showed in Table 8.2.

Looking at Table 8.2 were the results obtained for the mean and RMS with the one step method are displayed, one can see that overall, this method has a smaller associated uncertainty in comparison with the two step method. The

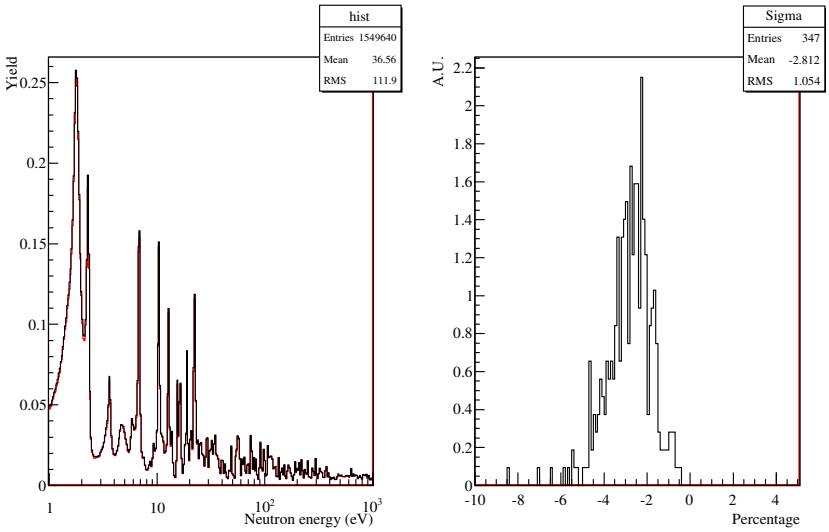

Figure 8.15: Fission yields obtained with the one step methodology (left) for the reference case (black) and case 2 (red) and the computed difference in percentage between yields (right).

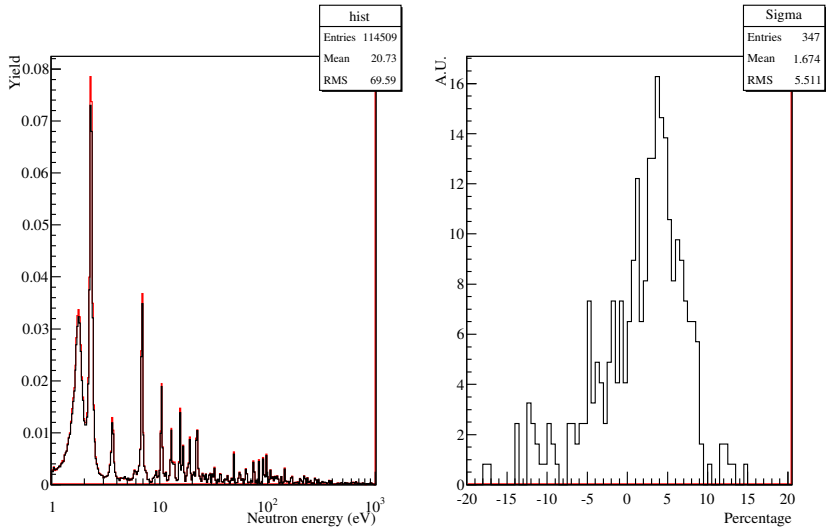

Figure 8.16: Neutron capture yields obtained with the one step methodology (left) for the reference case (black) and case 2 (red) and the computed difference in percentage between yields (right).

smaller uncertainties in the fission yield can be attributed to larger magnitude of the fission cross section and to the larger flexibility that the fitting algorithm

Table 8.2: Result obtained for the systematic uncertainty analysis using the one step method.

Reaction	Fission		Capture	
Quantity	Mean	RMS	Mean	RMS
Case 1 (Capture$_{Hist}$, Fission$_{Math}$)	-1.9%	1.4%	-7.9%	7.6%
Case 2 (Capture$_{Math}$, Fission$_{Math}$)	-2.8%	1.1%	1.7%	8.2%
Case 3 (Capture$_{Math}$, Fission$_{Hist}$)	-0.9%	1.5%	8.7%	6.3%

has to fit all contributions.

Analyzing closely Table 8.2 specially case 1 and 3, the dependence of the capture yield on the fission yield determination is visible.

In case 1, were a mathematical representation of the fission and an histogram representation of the capture, are used as the TAC responses, the fission is underestimated by 1.9% while the capture is underestimated by 7.9%

In case 3 were an histogram representation of capture and a mathematical representation of fission, are used as the TAC responses, the fission is underestimated in 0.9% but the capture yield is now overestimated by 8.7% while the uncertainties are comparable between case 1 and 3.

This can be attributed to two factors:

- The dependence that the TAC response to neutron capture has on the TAC response to fission due to the method used to assess both responses and
- the method used where the fitting algorithm can adjust all the TAC responses to minimize the χ^2.

8.4.6 Total uncertainty

The uncertainties due to the data analysis for the neutron capture and neutron induced fission were assessed by the summation of the modulo of the Mean times the RMS, weighted by the RMS for each case and methodology. In this way we account for both types of uncertainties assessed in a way that reflects the meaning of each one.

$$U = \frac{\sum |Mean_i| * RMS_i}{\sum RMS_i} \tag{8.2}$$

The sources of uncertainty that are propagated to the neutron capture and fission yields are summarized in Table 8.3, where the final uncertainty is

calculated as the square root of the sum of squares of the partial uncertainties (Eq. (8.1)). Accordingly to the study performed and detailed in Section 7.4, the contribution from the calculation of dead-time losses is negligible as well its contribution to the overall uncertainty and therefore not accounted here.

Table 8.3: Uncertainty contributions for neutron capture and fission yields and respective total uncertainties.

	Fission yield	Capture yield
Sample mass	5%	5%
Beam intersection	1%	1%
Flux	2%	2%
Data	2.0%	10.6%
Simulation	3%	3%
Total	6.6%	12.3%

Conclusions

The aim of this work was the determination of the ^{233}U neutron capture cross section. The measurement performed at the n_TOF facility at CERN using the TAC as the detection system and employing the CSD method for discriminating between competing reactions, allowed the simultaneous measurement of both neutron capture and neutron induced fission cross sections.

In order to separate the contributions of neutron capture and neutron induced fission in the TAC, the CSD methodology was developed. This novel methodology is based on the innovative study of the TAC's energy response for all competing reactions, allowing to discriminate between gammas originating from neutron induced fission and those from neutron capture reactions without the need for fission tagging or any additional detection system.

Due to the unique characteristic of the n_TOF facility such as its good energy resolution and high instantaneous neutron fluxes, the measurement of the ^{233}U radioactive sample was possible with an uncertainty of 12.3%.

The neutron capture yield was measured between 1 eV and 1 keV being the measurement limited at higher energies due to the contribution of scattering in the sample's canning and backing materials.

The results obtained and the comparisons made with the ENDF/B-VII.1 library permit to conclude that the neutron induced fission contribution was efficiently discriminated using the CSD method and that the Monte Carlo study performed to assess the detection efficiency and event reconstruction efficiency was successful for reproducing the signature of fission events. In the case of neutron capture, there were discrepancies between the simulated and experimental total energy spectrum which were taken into account in the estimated uncertainty of the yield.

The neutron induced fission yield agrees with the ENDF/B-VII.1 library both in normalization and shape, validating the CSD methodology .

The neutron capture yield shows a disagreement of the order of 30% between the n_TOF normalization and ENDF/B-VII.1 which cannot be attributed to the Monte Carlo modeling and can hardly be explained by the estimated 11.4% total uncertainty or with the data extraction procedure.

It must be emphasized the completely independent nature of the results obtained at n_TOF and the agreement of the neutron induced fission yield, with the ENDF/B-VII.1 library. The same methodology was applied to the assessment of the neutron capture yield. However, in this case a sizable disagreement is observed between the normalization of the neutron capture yield and the ENDF/B-VII.1 library. Such discrepancies may be attributed to:

- limitations in the event reconstruction efficiency methodology used in the work here presented,
- a problem in the measurements used to create the evaluation
- or combined problems in both measurements.

Possible causes for the disagreement in the normalization may be related to the fission veto technique used in the Weston measurement [65]. In his work, the author uses a combination of fission chamber and liquid scintillators as detection system and capture events are selected in the absence of fission fragments detected. The problem with this technique lies in the fact that it is not possible to discriminate between fission delayed gamma emission and gammas arising from the fission neutrons interactions with the structural materials resulting in a situation where the capture contribution is difficult to assess accurately.

In the work described in this thesis, these two components associated with fission events were considered within the scattering components used for the decomposition of the total energy spectrum.

Certain aspects of the measurement and analysis may be improved, namely by means of:

- Performing a measurement without the titanium canning and aluminum backing would increase the count rate of neutron capture relative to scattering reactions. The increase of the ratio of signal to noise would be most visible above the 1 keV region.
- Gaining a better understanding of TAC's response to the delayed gamma emission associated with the fission events, would permit to have a better idea about the correctness of the neutron capture yield assessed.
- Determining the TAC's response to the neutrons produced in fission events and their interaction with the structural materials which is also a possible source of background.
- Developing a better understanding of the neutron capture deexcitation process, would provide a better description of the TAC's response to neutron capture using Monte Carlo methods and therefore a more accurate determination of the event reconstruction efficiency.
- Assessing the resonance parameter analysis to extend the accuracy of the comparison and validation of the results.

Despite all the difficulties associated with the measurement of a radioactive sample with several neutron reaction channels open in the energy range of interest and the challenges of employing a different methodology and associated problems, it must be stressed that the results obtained are of great relevance to the thorium fuel cycle and unveil a possible problem with the data available in the ENDF/B-VII.1 library.

To understand the relevance of the findings reported on this work, one has to look at the neutron induced reactions occurring at the branching point $^{233}U + n$. Three reactions are possible such as neutron capture, neutron induced fission and neutron scattering. From these three reactions, only neutron capture and neutron induced fission lead to the isotopic evolution of the fuel in a nuclear reactor core using ^{232}Th as the main component in a breeding blanket and therefore, bred ^{233}U as fissile elements.

From the point of view of neutronics performance, the desirable reaction is fission, as neutron capture would lead to the formation of ^{234}U which would need to capture a second neutron to reach the fissile ^{235}U. Not only this decreases the reactor neutronics performance but also leads to the formation of trans-uranium actinides which is not desirable also from the point of view of waste management.

In the work here reported, a 30% lower neutron capture yield was assessed at n_TOF in respect to the ENDF/B-VII.1 evaluated data. The fission yield assessed at n_TOF agrees with the ENDF/B-VII.1 over the entire energy range studied both in shape and magnitude.

Besides the implications to the neutron economy of a reactor using ^{232}Th as a fuel, these two facts have an impact on the reaction occurring at the branching point ($^{233}U + n$). Considering the ratio at the branching point between neutron capture and neutron induced fission using the data measured at n_TOF, the ratio is now more favorable to fission in respect to the same ratio obtained with the ENDF/B-VII.1 data.

This has implications in the design and operation of the new Generation IV reactors, leading to a better neutronics performance, production of less trans-uranium actinides, better efficiency, lower radiotoxicity of the spent fuel, increased sustainability and better economics.

Bibliography

[1] C. Rubbia *et al.*, "An energy amplifier for cleaner and inexhaustible nuclear energy production driven by a particle beam accelerator," European Organization for Nuclear Research, Genève, Tech. Rep. CERN CERN-LHC-98-02 (EET), 1998.

[2] International Nuclear Data Committee, "Assessment of nuclear data needs for thorium and other advanced cycles," IAEA, Tech. Rep. INDC(NDS)-408, 1999.

[3] U. Energy Information Administration, "International Energy Outlook 2010," U.S. Energy Information Administration, Tech. Rep., 2010. [Online]. Available: http://www.eia.doe.gov

[4] D. Greneche *et al.*, *RED-IMPACT - Impact of partitioning, transmutation and waste reduction technologies on the final nuclear waste disposal - Synthesis report*, W. V. Lensa, R. Nabbi, and M. Rossbach, Eds. Forschungszentrum Jülich, 2008.

[5] International Atomic Energy Agency, "Classification of radioactive waste," IAEA, Tech. Rep. Safty Series 111-G-1.1, 2004. [Online]. Available: http://newmdb.iaea.org/

[6] International Atomic Energy Agency, "Clearance Levels for Radionuclides in Solid Materials: Application of Exemption Principles," IAEA, Vienna, Tech. Rep. IAEA-TECDOC-8S5, 1996.

[7] Generation IV International Forum, "2009 GIF R&D Outlook for Generation IV Nuclear Energy Systems," 2009. [Online]. Available: http://www.gen-4.org/PDFs/GIF_RD_Outlook_for_Generation_IV_Nuclear_Energy_Systems.pdf

[8] World Nuclear Association: Generation IV Nuclear Reactors. [Online]. Available: http://www.world-nuclear.org/info/inf77.html

[9] G. Jean-Claude *et al.*, "GFR System: Progress of CEA pre-conceptual design studies," in *International Congress on Advances in Nuclear Power Plants*, vol. 5, American Nuclear Society. Seoul, Korea: Curran Associates, Inc., May 2005, p. 1567. [Online]. Available: http://www.gen-4.org/Technology/systems/gfr.htm

[10] L. Cinotti *et al.*, "The ELSY Project," in *Proceeding of the International Conference on the Physics of Reactors (PHYSOR)*, R. Chawla, Ed., Interlaken, Switzerland, September 2008, p. 2419. [Online]. Available: http://www.proceedings.com/10098.html

[11] A. Zaetta *et al.*, "Innovating Core Design for Sodium Cooled Fast Reactors of Fourth Generation," in *International Congress on Advances in Nuclear Power Plants (ICAPP 2007): The Nuclear Renaissance at Work*. Nice, France: Curran Associates, Inc., May 2007, p. 2230. [Online]. Available: http://www.proceedings.com/02165.html

[12] J. Yoo *et al.*, "Conceptual design of compact supercritical water-cooled fast reactor with thermal hydraulic coupling," *Annals of Nuclear Energy*, vol. 33, no. 11–12, pp. 945 – 956, 2006. [Online]. Available: http://www.sciencedirect.com/science/article/pii/S0306454906001320

[13] The Very-High-Temperature Reactor (VHTR). [Online]. Available: http://www.gen-4.org/Technology/systems/vhtr.htm

[14] R. Claude *et al.*, "The Molten Salt Reactor (MSR) in Generation IV - Overview and perspectives," in *Proceedings of the GIF Symposium*. Société Française d'Energie Nucléaire, 2009, pp. 1–7. [Online]. Available: http://publications.jrc.ec.europa.eu/repository/handle/111111111/1510

[15] R. Hargraves and R. Moir. The Liquid Fluoride Thorium Reactor. [Online]. Available: http://www.americanscientist.org/issues/feature/liquid-fluoride-thorium-reactors

[16] Thorium as a nuclear fuel. [Online]. Available: http://www.world-nuclear.org/info/inf62.html

[17] E. Shwageraus *et al.*, "Microheterogeneous Thoria-Urania Fuels for Pressurized Water Reactors," *Nuclear Technology*, vol. 147, pp. 20–36, 2004. [Online]. Available: http://www.new.ans.org/store/j_3512

[18] A. Galperin, A. Radkowsky, and M. Todosow, "A competitive thorium fuel cycle for pressurized water reactors of current technology," International Atomic Energy Agency, Tech. Rep., 2002. [Online]. Available: http://www-pub.iaea.org/MTCD/publications/PDF/te_1319_web.pdf

[19] D. Kerdraon *et al.*, "Characterization and extrapolation of a conceptual experimental accelerator driven system," *Progress in Nuclear Energy*, vol. 42, no. 1, pp. 11 – 24, 2003. [Online]. Available: http://www.sciencedirect.com/science/article/pii/S0149197003800033

[20] International Atomic Energy Agency, "Thorium fuel cycle - Potential benefits and challenges," IAEA, Tech. Rep. IAEA-TECDOC-1450, 2005. [Online]. Available: http://www-pub.iaea.org/MTCD/publications/PDF/TE_1450_web.pdf

[21] M. Chadwick *et al.*, "ENDF/B-VII.1 Nuclear Data for Science and Technology: Cross Sections, Covariances, Fission Product Yields and Decay Data," *Nuclear Data Sheets*, vol. 112, no. 12, pp. 2887 – 2996, 2011, ¡ce:title¿Special Issue on ENDF/B-VII.1 Library¡/ce:title¿. [Online]. Available: http://www.sciencedirect.com/science/article/pii/S009037521100113X

[22] A. Galperin, P. Reichert, and A. Radkowsky, "Thorium fuel for light water reactors - reducing proliferation potential of nuclear power fuel cycle," *Science & Global Security 6*, vol. 3, pp. 265–290, 1997.

[23] David, Sylvain, Huffer, Elisabeth, and Nifenecker, Hervé, "Revisiting the Thorium-Uranium nuclear fuel cycle," *Europhysics News*, vol. 38, no. 2, pp. 24–27, 2007. [Online]. Available: http://dx.doi.org/10.1051/EPN:2007007

[24] S. David *et al.*, "Fast subcritical hybrid reactors for energy production: evolution of physical parameters and induced radiotoxicities," *Nucl. Instrum. Methods Phys. Res. A*, vol. 443, no. 2–3, pp. 510 – 530, 2000. [Online]. Available: http://www.sciencedirect.com/science/article/pii/S0168900299011638

[25] J. M. Beck and L. F. Pincock, "High Temperature Gas-Cooled Reactors Lessons Learned Applicable to the Next Generation Nuclear Plant," Idaho National Laboratory, Tech. Rep. INL/EXT-10-19329, 2011. [Online]. Available: http://www.inl.gov/technicalpublications/Documents/5026001.pdf

[26] S. Şahin *et al.*, "Candu reactor as minor actinide/thorium burner with uniform power density in the fuel bundle," *Annals of Nuclear Energy*, vol. 35, no. 4, pp. 690 – 703, 2008. [Online]. Available: http://www.sciencedirect.com/science/article/pii/S0306454907002046

[27] C. S. Sunny *et al.*, "KAMINI reactor benchmark analysis," *Annals of Nuclear Energy*, vol. 35, no. 4, pp. 570 – 575, 2008. [Online]. Available: http://www.sciencedirect.com/science/article/pii/S0306454907002356

[28] G. L. Olson, R. K. McCardell, and D. B. Illum, "Fuel Summary Report: Shippingport Light Water Breeder Reactor," Idaho National Engineering and Environmental Laboratory, Tech. Rep., 2002. [Online]. Available: http://www.inl.gov/technicalpublications/Documents/2664750.pdf

[29] S. M. *et al.*, "The potential of accelerator-driven systems for transmutation or power production using thorium or uranium fuel cycles," *Nuclear Science and Engineering*, vol. 126, no. 3, pp. 333–340, 1997. [Online]. Available: http://cat.inist.fr/?aModele=afficheN&cpsidt=2757564

[30] J. Chadwick, "Possible Existence of a Neutron," *Nature*, vol. 129, p. 312, 1932. [Online]. Available: http://www.nature.com/nature/journal/v129/n3252/pdf/129312a0.pdf

[31] J. Beringer *et al.*, "Review of Particle Physics," *Phys. Rev. D*, vol. 86, p. 010001, Jul 2012. [Online]. Available: http://link.aps.org/doi/10.1103/PhysRevD.86.010001

[32] K. Krane, *Introductory Nuclear Physics*. Wiley, 1987.

[33] E. P. Wigner, "Resonance Reactions," *Phys. Rev.*, vol. 70, pp. 606–618, Nov 1946. [Online]. Available: http://link.aps.org/doi/10.1103/PhysRev.70.606

[34] N. Bohr, "Neutron Capture and Nuclear Constitution," *Nature*, vol. 137, p. 344, 1936. [Online]. Available: http://www.nature.com/nature/journal/v137/n3461/pdf/137344a0.pdf

[35] G. Breit and E. Wigner, "Capture of Slow Neutrons," *Phys. Rev.*, vol. 49, no. 7, pp. 519–531, 1936.

[36] F. Gunsing, "Neutron Resonance Spectroscopy," Ph.D. dissertation, l'Université Paris 7, 2005.

[37] J. E. Lynn, *The Theory of Neutron Resonance Reactions*. Oxford: Clarendon Press, 1968.

[38] M. L. Mehta and M. Gaudin, "On the Density of Eigenvalues of a Random Matrix," *Nucl. Phys.*, vol. 18, p. 395, 1960.

[39] R. U. Haq, A. Pandey, and O. Bohigas, "Fluctuations properties of nuclear energy levels: Do theory and experiment agree?" *Phys. Rev. Lett.*, vol. 48 (6), p. 1086–1089, 1982.

[40] C. S. O. Bohigas, M. J. Giannoni, "Characterization of chaotic quantum spectra and universality of level fluctuation laws," *Phys. Rev. Lett.*, vol. 52, p. 1–4, 1984.

[41] M. L. Mehta, *Random matrices*. Academic Press Edition, 1991.

[42] C. E. Porter and R. G. Thomas, "Fluctuations of nuclear reaction widths," *Phys. Rev.*, vol. 104 (2), p. 483–491, 1956.

[43] C. Wagemans, "The Nuclear Fission Process," *CRC Press Book*, 1991. [Online]. Available: http://www.crcpress.com/product/isbn/9780849354342

[44] A. Gilbert and A. G. W. Cameron, "A composite nuclear-level density formula with shell corrections," *Canadian Journal of Physics*, vol. 43 (3), pp. 1446–1496, 1965. [Online]. Available: http://adsabs.harvard.edu/abs/1965CaJPh..43.1446G

[45] S. F. Mughabghab, M. Divadeenam, and N. E. Holden, "Neutron cross sections: Neutron resonance parameters and thermal cross sections. Z=1-60," *Academic Press*, 1981.

[46] S. F. Mughabghab, M. Divadeenam and N. E. Holden, "Neutron cross sections: Neutron resonance parameters and thermal cross sections. Z=61-100," *Academic Press*, 1984.

[47] S. I. Sukhoruchkin, Z. N. Soroko, and V. V. Deriglazov, "Low Energy Neutron Physics," *Tables of Neutron Resonance Parameters, Springer, Landolt-Börnstein*, vol. Volume I/16B, 1998.

[48] A. I. Blokhin *et al.*, "Current Status of Russian Evaluated Neutron Data Libraries," in *Proc. International Conference on Nuclear Data for Science and Technology*, vol. 2, Gatlinburg, Tennessee, USA, May 1994, p. 695.

[49] A. Santamarina *et al.*, "The JEFF-3.1.1 Nuclear Data Library," OECD/NEA Data Bank, Tech. Rep. JEFF Report 22, 2009. [Online]. Available: http://www.oecd-nea.org/dbdata/jeff/

[50] K. Shibata *et al.*, "JENDL-4.0: A New Library for Nuclear Science and Engineering," *Journal of Nuclear Science and Technology*, vol. 48, no. 1, pp. 1–30, 2011. [Online]. Available: http://www.tandfonline.com/doi/abs/10.1080/18811248.2011.9711675

[51] Z. G. Ge *et al.*, "The Updated Version of Chinese Evaluated Nuclear Data Library (CENDL-3.1)," in *Proc. International Conference on Nuclear Data for Science and Technology*, Jeju Island, Korea, April 2010, (in press).

[52] E. P. Wigner and L. Eisenbud, "Higher Angular Momenta and Long Range Interaction in Resonance Reactions," *Phys. Rev.*, vol. 72, pp. 29–41, Jul 1947. [Online]. Available: http://link.aps.org/doi/10.1103/PhysRev.72.29

[53] A. M. Lane and R. G. Thomas, "R-Matrix Theory of Nuclear Reactions," *Rev. Mod. Phys.*, vol. 30, pp. 257–353, Apr 1958. [Online]. Available: http://link.aps.org/doi/10.1103/RevModPhys.30.257

[54] F. H. Fröhner, "Evaluation and analysis of nuclear resonance data," *Tech. Rep. JEFF Report 18, OECD/NEA*, 2000.

[55] J. Humblet and L. Rosenfeld, "Theory of nuclear reactions: I. Resonant states and collision matrix," *Nucl. Phys.*, vol. 26 (4), p. 529–578, 1961.

[56] E. Vogt, "Theory of low energy nuclear reactions," *Rev. Mod. Phys.*, vol. 34 (4), p. 723–747, 1962.

[57] F. Schmittroth and W. Tobocman, "Comparison of the R-matrix nuclear reaction theories," *Phys. Rev. C*, vol. 3, p. 1010–1019, 1971.

[58] D. B. Adler and F. T. Adler, "Uniqueness of R-matrix parameters in the analysis of low-energy neutron cross sections of fissile nuclei," *Phys. Rev. C*, vol. 6, p. 986–1001, 1972.

[59] C. Chandler and W. Tobocman, "R-matrix method for nuclear reaction theory," *Phys. Rev. C*, vol. 19, p. 1660–1666, 1979.

[60] T. A. Brody, "Random-matrix physics: spectrum and strength fluctuations," *Rev. Mod. Phys.*, vol. 53, no. 3, pp. 385–479, Jul 1981. [Online]. Available: http://link.aps.org/doi/10.1103/RevModPhys.53.385

[61] J. Humblet, "K-matrix analysis of resonance nuclear reactions," *Phys. Rev. C*, vol. 42 (4), p. 1582–1591, 1990.

[62] A. A. Luk'yanov and N. B. Yaneva, "Multilevel parametrization of resonance neutron cross sections," *Rev. Mod. Phys.*, vol. 28, p. 331–347, 1997.

[63] C. R. Brune, "Alternative parametrization of R-matrix theory," *Phys. Rev. C*, vol. 66, p. 044611, 2002.

[64] E. Bauge, J. P. Delaroche, and M. Giro, "Lane-consistent, semimicroscopic nucleon-nucleus optical model," *Phys. Rev. C*, vol. 63, p. 024607, 2001.

[65] L. Weston *et al.*, "Measurement of the Fission and Capture Cross Section for ^{233}U in the Energy Region 0.4 to 2000 eV," *Nuclear Science and Engineering*, vol. 34, pp. 1–12, 1968.

[66] L. C. Leal *et al.*, "Evaluation of the ^{233}U Neutron Cross Sections in the Resolved Resonance Energy Range." [Online]. Available: http://www.ornl.gov/~webworks/cppr/y2001/pres/111576.pdf

[67] D. C. Larson, "The Oak Ridge Electron Linear Accelerator Pulsed Neutron Source." [Online]. Available: http://www.phy.ornl.gov/orela/orela.html/

[68] K. H. Guber, "New High-Resolution Fission Cross-Section Measurements of ^{233}U in the 0.4 eV to 700 keV Energy Range," *Nuclear Science and Engineering*, vol. 135, p. 141, 2000. [Online]. Available: http://www.ans.org/pubs/journals/nse/vv-135

[69] M. S. Moore and C. W. Reich, "Multilevel Analysis of the Slow Neutron Cross Sections of U^{233}," *Phys. Rev.*, vol. 118, no. 3, pp. 718–724, May 1960. [Online]. Available: http://prola.aps.org/abstract/PR/v118/i3/p718_1

[70] N. J. Pattenden and J. A. Harve, "Measurement of the Total Cross Section of U^{233} from 0.07 to 10,000 eV," *Nuclear Science and Engineering*, vol. 17, p. 404, 1963.

[71] J. Blons, "High Resolution Measurements of Neutron-Induced Fission Cross Sections for ^{233}U, ^{235}U, ^{239}Pu and ^{241}Pu Below 30 keV," *Nuclear Science and Engineering*, vol. 51, p. 423, 1973.

[72] A. J. Deruytter and C. Wagemans, "Measurement and Normalization of the Relative Uranium-233 Fission Cross Section in the Low Resonance Region," *Nuclear Science and Engineering*, vol. 54, p. 423, 1974.

[73] J. A. Harvey, C. L. Moore, and N. W. Hill, "Neutron total cross section of ^{233}U from 0.01 to 1.0 eV," Oak Ridge National Lab., TN (USA), Tech. Rep. CONF-791058-73, Jan 1979.

[74] C. Wagemans, "Subthermal Fission Cross-section Measurements for ^{233}U, ^{235}U and ^{239}Pu," *MITO*, vol. 91, 1988. [Online]. Available: http://wwwndc.jaea.go.jp/1988Mito/

[75] M. Calviani and the n_TOF Collaboration, "High-accuracy ^{233}U(n, fission) cross-section measurement at the white-neutron source n_TOF from near-thermal to 1 MeV neutron energy," *Phys. Rev. C*, vol. 80, no. 4, p. 044604, 2009. [Online]. Available: http://link.aps.org/doi/10.1103/PhysRevC.80.044604

[76] S. Ganesan, "New Reactor Concepts and New Nuclear Data Needed to Develop Them," in *Proceedings of the International Conference on Nuclear Data for Science and Technology*, R. Haight, Ed., Santa Fe, USA, 2004, 2004, p. 1411–1416.

[77] D. Karadimos *et al.*, "Analysis of the FIC detector data at the n_TOF facility," *Nucl. Instrum. Methods Phys. Res. B*, vol. 268, no. 16, pp. 2556 – 2562, 2010. [Online]. Available: http://www.sciencedirect.com/science/article/pii/S0168583X10004246

[78] E. Berthoumieux, "Simultaneous measurement of the neutron capture and fission yields of ^{233}U," in *International Conference on Nuclear Data for Science and Technology*, no. 152, 2007. [Online]. Available: http://nd2007.edpsciences.org/index.php?option=com_article&access=doi&doi=10.1051/ndata:07665&Itemid=129

[79] "Experimental Nuclear Reaction Data." [Online]. Available: http://www-nds.iaea.org/exfor/exfor.htm

[80] F. Brooks *et al.*, "Eta and Neutron Cross Sections of ^{239}Pu and ^{233}U," United Kingdom Atomic Energy Research Establisment, Harwell, Berks., England, Tech. Rep. AERE-M-1709, 1966.

[81] T. A. Bredeweg *et al.*, "Simultaneous measurement of (n, γ) and (n, fission) cross sections with the DANCE 4π BaF_2 array," *Nucl. Instrum. Methods Phys. Res. B*, vol. 261, no. 1-2, pp. 986 – 989, 2007. [Online]. Available: http://www.sciencedirect.com/science/article/B6TJN-4NJWNJB-P/2/f8326e12381ea8583997e1acfc2d347a

[82] T. Bredeweg *et al.*, "Recent actinide nuclear data efforts with the DANCE 4π BaF_2 array," in *International Conference on Nuclear Data for Science and Technology*, 2007. [Online]. Available: http://nd2007.edpsciences.org/index.php?option=com_article&access=standard&Itemid=129&url=/articles/ndata/abs/2007/01/ndata07592/ndata07592.html

[83] R. A. Macri *et al.*, "Fission measurements with DANCE," in *Nuclei Proceedings of the Fourth International Conference: Fission And Properties Of Neutron-Rich*, J. H. Hamilton, A. V. Ramayya, and H. K. Carter, Eds., Sanibel Island, USA, November 2007, pp. 440–447. [Online]. Available: http://www.worldscientific.com/doi/abs/10.1142/9789812833433_0052

[84] P. Schillebeeckx *et al.*, "Neutron Resonance Spectroscopy at GELINA," *Journal of the Korean Physical Society*, vol. 59, pp. 1563–1568, 2011. [Online]. Available: http://irmm.jrc.ec.europa.eu/about_IRMM/laboratories/Pages/gelina_neutron_time_of_flight_facility.aspx

[85] M. Flaska *et al.*, "Modeling of the GELINA neutron target using coupled electron–photon–neutron transport with the MCNP4C3 code," *Nuclear Instruments and Methods in Physics Research Section A: Accelerators, Spectrometers, Detectors and Associated Equipment*, vol. 531, no. 3, pp. 392 – 406, 2004. [Online]. Available: http://www.sciencedirect.com/science/article/pii/S016890020401109X

[86] I. Companis *et al.*, "Measurement of neutron capture and fission cross sections of ^{233}U in the resonance region," *EPJ Web of Conferences*, vol. 21, p. 10002, 2012. [Online]. Available: http://dx.doi.org/10.1051/epjconf/20122110002

[87] K. H. Guber *et al.*, "High-Resolution Transmission Measurements of ^{233}U Using a Cooled Sample at the Temperature T = 11 K," *Nuclear Science and Engineering*, vol. 139, no. 2, pp. 111–117, 2011. [Online]. Available: http://www.new.ans.org/pubs/journals/nse/a_2226

[88] D. Tarrío *et al.*, "Neutron-induced fission cross section of ^{nat}Pb and ^{209}Bi from threshold to 1 GeV: An improved parametrization," *Phys. Rev. C*, vol. 83, no. 4, p. 044620, 2011. [Online]. Available: http://prc.aps.org/abstract/PRC/v83/i4/e044620

[89] V. G. Pronyaev *et al.*, "An International Evaluation of the Neutron Cross Section Standards," IAEA, Tech. Rep., 2006. [Online]. Available: http://www.oecd-nea.org/science/docs/2006/nsc-wpec-doc2006-380.pdf

[90] P. Talou *et al.*, "The Nuclear Reaction Code McGNASH," *AIP Conference Proceedings*, vol. 769, no. 1, pp. 1132–1135, 2005. [Online]. Available: http://link.aip.org/link/?APC/769/1132/1

[91] J. C. Hopkins and B. C. Diven, "Neutron Capture to Fission Ratios in ^{233}U, ^{235}U and ^{239}Pu," *Nuclear Science and Engineering*, vol. 12, p. 169, 1962.

[92] The n_TOF Collaboration, "CERN n_TOF Facility: Performance Report," CERN, Tech. Rep. CERN INTC-2002-037, 2003.

[93] J. Cugnon, "Cascade models and particle production: A comparison," University of Liège, Particle Production in Highly Excited Matter, NATO Science Series B 303 (1993) 271-293 ULG-PNT-91-6-G, 1991.

[94] Physikalisch-Technische Bundesanstalt. [Online]. Available: www.ptb.de

[95] R. Plag *et al.*, "An optimized C6D6 detector for studies of resonance-dominated (n,γ) cross-sections," *Nucl. Instrum. Methods Phys. Res. A*, vol. 496, no. 2–3, pp. 425 – 436, 2003. [Online]. Available: http://www.sciencedirect.com/science/article/pii/S0168900202017497

[96] G. Lorusso *et al.*, "Time-energy relation of the n_TOF neutron beam: energy standards revisited," *Nucl. Instrum. Methods Phys. Res. A*, vol. 532, no. 3, pp. 622 – 630, 2004. [Online]. Available: http://www.sciencedirect.com/science/article/pii/S0168900204013221

[97] W. E. Lamb, "Capture of neutrons by atoms in a crystal lattice," *Phys. Rev.*, vol. 55, p. 190, 1939.

[98] A. Meister, "Calculations on lattice vibration effects in the doppler broadening of the 0.18 eV Cd neutron resonance cross section," JRC-IRMM, Tech. Rep. CE/R/VG/78/94, 1994.

[99] D. G. Naberejnev, C. Mounier, and R. Sanchez, "The influence of crystalline binding on resonant absorption and reaction rates," *Nucl. Sci. Eng.*, vol. 131, p. 220, 1999.

[100] C. Coceva *et al.*, "On the Figure of Merit in Neutron Time-of-Flight Measurements," *Nucl. Instrum. Methods Phys. Res. A*, vol. 489, p. 346, 2002.

[101] C. Guerrero *et al.*, "The n_TOF Total Absorption Calorimeter for neutron capture measurementsat CERN," *Nucl. Instrum. Methods Phys.*

Res. A, vol. 608, no. 3, pp. 424 – 433, 2009. [Online]. Available: http://www.sciencedirect.com/science/article/pii/S016890020901465X

[102] S. Derenzo and W. Moses, "Experimental efforts and results for finding new heavy scintillators," in *Proceedings of the CRYSTAL 2000 International Workshop on Heavy Scintillators for Scientific and Industrial Applications*, Chamonix, France, Sept. 22-26 1992, pp. 125–135.

[103] C. Guerrero *et al.*, "The n_TOF Total Absorption Calorimeter response to γ-ray cascades following neutron capture in minor actinides," *AIP Conference Proceedings*, vol. 1090, pp. 372–375, 2009.

[104] C. Borcea *et al.*, "The Neutron Time of Flight Facility at CERN," *Nuclear Science and Technology*, vol. Suppl. 2, p. 653, 2002.

[105] S. Andriamonje *et al.*, "Neutron TOF Facility (PS 213)," CERN, Tech. Rep. CERN/INTC/2000-004, 2000.

[106] V. Vlachoudis *et al.*, "Monte Carlo simulation of the neutron time of flight facility at CERN," in *Proceedings of the Monte Carlo 2000 Conference*, ser. Advanced Monte Carlo for Radiation Physics, Particle Transport Simulation and Applications, A. Kling *et al.*, Eds. Lisbon, Portugal: Springer-Verlag, October 2000, p. 1175.

[107] A. Fassò *et al.*, "FLUKA: A Multi-Particle Transport Code," CERN, Tech. Rep. CERN-2005-10, INFN/TC_50/11, SLAC-R-773, 2005.

[108] N. M. Larson, "SAMMY—Multilevel R-Matrix Fits to Neutron and Charged-Particle Cross-Section Data Using Bayes' Equations," Oak Ridge National Laboratory, Tech. Rep. ORNL/TM-9179/R8, 2008.

[109] *Improved Intranuclear Cascade Models for the Codes CEM2k and LAQGSM*, ser. Proc. Int. Conf. Nuclear Data for Science and Technology, vol. 769, no. 1188. American Institute of Physics, October 2005.

[110] J. S. Hendricks *et al.*, "Monte Carlo N-Particle Transport Code Version 2.6e," Los Alamos National Laboratory, Tech. Rep. LA-UR-08-2216, 2008.

[111] S. Furihata, "Statistical analysis of light fragment production from medium energy proton-induced reactions," *Nucl. Instrum. Methods Phys. Res. B*, vol. 171, no. 3, pp. 251 – 258, 2000. [Online]. Available: http://www.sciencedirect.com/science/article/pii/S0168583X00003323

[112] S. Furihata, "The GEM Code - The Generalized Evaporation Model and the Fission Model," in *Proceedings of the Monte Carlo 2000 Conference*, ser. Advanced Monte Carlo for Radiation Physics, Particle Transport Simulation and Applications, A. Kling *et al.*, Eds. Lisbon, Portugal: Springer-Verlag, October 2000, p. 1045.

[113] T. Booth, "A Sample Problem for Variance Reduction in MCNP," Los Alamos National Laboratory, Tech. Rep. LA-10363-MS, 1985.

[114] K. Wisshak *et al.*, "The Karlsruhe 4π Barium Fluoride Detector," *Nucl. Instr. and Meth*, vol. A292, pp. 595–618, 1990.

[115] The n_TOF Collaboration, "Measurement of the neutron capture cross sections of ^{233}U, ^{237}Np, ^{240,242}Pu, ^{241,243}Am and ^{245}Cm with a Total Absorption Calorimeter at n_TOF," CERN, Tech. Rep. CERN/INTC-2003-036, 2003. [Online]. Available: http://cdsweb.cern.ch/record/678357/files/intc-2003-036.pdf

[116] S. Jastaniah and P. Sellin, "Digital Pulse Shape Algorithms for Scintillation Based Neutron Detectors," *IEEE Trans. Nucl. Sci.*, vol. 49, p. 1824, 2002.

[117] N. V. Kornilov *et al.*, "Neutron spectroscopy with fast waveform digitizer," *Nucl. Instrum. Methods Phys. Res. A*, vol. 497, pp. 467–478, 2003.

[118] Numerical Recipes, Chapter:15.5. [Online]. Available: http://apps.nrbook.com/rollover/index.html

[119] M. Bräger, "Redesign and Functional Extension of the Robotic Tape Queueing System within the CASTOR HSM," Ph.D. dissertation, Fachhochschule Wiesbaden, University of Applied Sciences, 2005. [Online]. Available: http://castorold.web.cern.ch/castorold/docs.htm

[120] R. Brun and F. Rademakers, "ROOT - An object oriented data analysis framework," *Nucl. Instrum. Methods Phys. Res. A*, vol. 389, no. 1–2, pp. 81 – 86, 1997. [Online]. Available: http://www.sciencedirect.com/science/article/pii/S016890029700048X

[121] C. Carrapico *et al.*, "Neutron induced capture and fission discrimination using Calorimetric Shape Decomposition," Accepted for publication in Nucl. Instrum. Methods Phys. Res. A (August 2012).

[122] "ENSDF Evaluated Nuclear Structure Data File." [Online]. Available: http://www.nndc.bnl.gov/ensdf/

[123] W. Dridi, "Mesure de la section efficace de capture neutronique de l' ^{234}U a n_TOF au CERN pour les reacteurs nucleaires de Generation IV," Ph.D. dissertation, Université d'Évry Val d'Essonne, Ecole Doctorale Sitevry, 2006. [Online]. Available: http://cdsweb.cern.ch/collection/n_TOF%20Theses?ln=en

[124] C. Guerrero *et al.*, "Simultaneous measurement of neutron-induced capture and fission reactions at CERN," *The European Physical Journal A - Hadrons and Nuclei*, vol. 48, pp. 1–9, 2012, 10.1140/epja/i2012-12029-2. [Online]. Available: http://dx.doi.org/10.1140/epja/i2012-12029-2

[125] S. Agostinelli *et al.*, "Geant4 - a simulation toolkit," *Nucl. Instrum. Methods Phys. Res. A*, vol. 506, no. 3, pp. 250 – 303, 2003. [Online]. Available: http://www.sciencedirect.com/science/article/pii/S0168900203013688

[126] J. Allison *et al.*, "Geant4 developments and applications," *Nuclear Science, IEEE Transactions on*, vol. 53, no. 1, pp. 270 –278, feb. 2006.

[127] J. Taín, "Accuracy of the pulse height weighting technique for capture cross-section measurements," IFIC, CSIC-Univ. Valencia, Tech. Rep., 2000.

[128] J. Tain *et al.*, "Accuracy of the Pulse Height Weighting Technique for Capture Cross Section Measurements," in *Proceedings of the International Conference "Nuclear Data for Science and Technology"*, Tsukuba - Japan, October 2001.

[129] C. Guerrero *et al.*, "Application of Photon Strength Functions to (n,γ) measurements with the n_TOF TAC," in *Proc. of the Workshop on Photon Strength Functions and Related Topics*, vol. 006, Prague, Czech Republic, June 2007.

[130] W. Dilg *et al.*, "Level density parameters for the back-shifted fermi gas model in the mass range 40 <A <250," *Nuclear Physics A*, vol. 217, pp. 269–298, Dec 1973. [Online]. Available: http://www.sciencedirect.com/science/article/B6TVB-47196MP-TK/2/2be3f2f76a057567b3d0907f6708f79a

[131] J. Kopecky and M. Uhl, "Test of γ-ray strength functions in nuclear reaction model calculations," *Phys. Rev. C*, vol. 41, no. 5, pp. 1941–1955, May 1990. [Online]. Available: http://prc.aps.org/abstract/PRC/v41/i5/p1941_1

[132] M. Krtička and F. Bečvář, "What do we really know about photon strength functions?" *Journal of Physics G: Nuclear and Particle Physics*, vol. 35, p. 014025, 2008.

[133] T. Belgya *et al.*, "Reference Input Parameter Library," RIPL-2. IAEA-TECDOC-1506 (IAEA, Vienna), 2006. [Online]. Available: http://www-nds.iaea.org/RIPL-2/

[134] C. G. G. Sánchez, "Measurements of the ^{237}Np and ^{240}Pu neutron capture cross sections at the CERN n_TOF Facility," Ph.D. dissertation, Universidad Complutense de Madrid, Departamento de Física Atómica, Molecular y Nuclear, 2008. [Online]. Available: http://cdsweb.cern.ch/collection/n_TOF%20Theses?ln=en

[135] T. E. Valentine, "Evaluation of prompt fission gamma rays for use in simulating nuclear safeguard measurements," *Annals of Nuclear Energy*, vol. 28, no. 3, pp. 191 – 201, 2001. [Online]. Available: http://www.sciencedirect.com/science/article/B6V1R-415RGFK-1/2/161cb9c036664f12e5d9eabbfb1fd505

[136] F. Pleasonton, "Prompt γ-rays emitted in the thermal-neutron induced fission of ^{233}U and ^{239}Pu," *Nuclear Physics A*, vol. 213, no. 2, pp. 413 – 425, 1973. [Online]. Available: http://www.sciencedirect.com/science/article/B6TVB-471XC25-F0/2/0062946edd461fb5432026ecf2c90e8f

[137] F. Pleasonton, R. Ferguson, and H. Schmitt, "Prompt gamma rays emitted in the thermal-neutron induced fission of ^{235}U," *Physics Review C*, vol. 6, pp. 1023–103, 1972.

[138] V. Verbinski, H. Weber, and R. E. Sund, "Prompt gamma rays from ^{235}(U,n,f), ^{239}Pu(n,f) and spontaneous fission of ^{252}Cf," *Physics Review C*, vol. 7, pp. 1173–1185, 1973.

[139] R. Pelle and F. Maienschein, "Spectrum of photons emitted in coincidence with fission of ^{235}U by thermal neutrons," *Physics Review C*, vol. 3, pp. 373–390, 1971.

[140] F. Pleasonton, R. Ferguson, and H. Schmitt, "Prompt gamma Rays Emitted in the Thermal-Neutron Induced Fission of ^{233}U, ^{235}U, and ^{239}Pu

and the Spontaneous Fission of ^{252}Cf," Oak Ridge National Laboratory, Tech. Rep. ORNL-4844, 1972.

[141] H. Bowman and S. Thompson, "Prompt radiation in the spontaneous fission of Cf-252," in *Proceedings 2nd International Conference on Peaceful Uses of Atomic Energy*, vol. 15, United Nations, Geneva, 1958, p. 12.

[142] E. Nardi, A. Gavron, and Z. Fraenkel, "Total energy associated with prompt gamma ray emission in spontaneous fission of ^{252}Cf," *Physics Review C*, vol. 8, pp. 2293–2297, 1973.

[143] G. V. Val'skii *et al.*, "Some characteristics of the g radiation accompanying fission of ^{252}Cf," *Soviet Journal of Nuclear Physics*, vol. 10, pp. 137–141, 1969.

[144] P. Singer *et al.*, "High-energy γ-rays in α-accompanied spontaneous fission of ^{252}Cf," *Zeitschrift für Physik A Hadrons and Nuclei*, vol. 359, pp. 41–45, 1997, 10.1007/s002180050365. [Online]. Available: http://dx.doi.org/10.1007/s002180050365

[145] J. Pancin *et al.*, "Measurement of the n_TOF beam profile with a micromegas detector," *Nucl. Instrum. Methods Phys. Res. A*, vol. 524, no. 1–3, pp. 102 – 114, 2004. [Online]. Available: http://www.sciencedirect.com/science/article/pii/S0168900204001512

[146] A. Fassò *et al.*, "FLUKA92," in *Proceedings of the Workshop on Simulating Accelerator Radiation Environment*, no. Los Alamos Report LA-12835-C (1994), 1993. [Online]. Available: http://www.fluka.org/content/publications/1993_santafe.pdf